DEVELOPMENT AND CHARACTERIZATION OF ULTRASOUND CONTRAST MICROBUBBLES TARGETED TO DYSFUNCTIONAL ENDOTHELIUM

by

Gregory Eugene Robert Weller

B.S. in Biomedical Engineering, Johns Hopkins University, 1995

Submitted to the Graduate Faculty of

the School of Engineering in partial fulfillment of

the requirements for the degree of

Doctor of Philosophy

University of Pittsburgh

2003

UNIVERSITY OF PITTSBURGH

SCHOOL OF ENGINEERING

This dissertation was presented

by

Gregory Eugene Robert Weller

It was defended on

March 26, 2003

and approved by

Harvey S. Borovetz, Ph.D.
Professor, Departments of Bioengineering and Surgery

William J. Federspiel, Ph.D.
Associate Professor, Departments of Bioengineering, Surgery, and Chemical Engineering

Michael K. K. Wong, M.D., Ph.D.
Assistant Professor, Department of Medicine, Pittsburgh Cancer Institute

Flordeliza S. Villanueva, M.D.
Dissertation Co-Director
Associate Professor, Department of Medicine, Cardiovascular Institute

William R. Wagner, Ph.D.
Dissertation Co-Director
Associate Professor, Departments of Bioengineering, Surgery, and Chemical Engineering

© Copyright by Gregory E. R. Weller

2003

ABSTRACT

DEVELOPMENT AND CHARACTERIZATION

OF ULTRASOUND CONTRAST MICROBUBBLES

TARGETED TO DYSFUNCTIONAL ENDOTHELIUM

Gregory E. R. Weller, Ph.D.

University of Pittsburgh, 2003

Endothelial dysfunction is characterized by the upregulation of leukocyte adhesion molecules, including intercellular adhesion molecule-1 (ICAM-1), and has been identified in numerous disease processes including inflammation, atherosclerosis, transplant rejection, and neoplasia, yet current clinical techniques to assess endothelial dysfunction are limited. An ultrasound-based molecular imaging technique to detect cell surface markers of endothelial dysfunction may offer non-invasive assessment of associated disease processes.

Lipid-based ultrasound contrast microbubbles were targeted to ICAM-1 by conjugation with anti-ICAM-1 antibodies. These targeted microbubbles should selectively adhere to dysfunctional endothelium overexpressing ICAM-1, producing stronger and more persistent contrast enhancement during ultrasound imaging. Previous results from our laboratory demonstrated that ICAM-1-targeted microbubbles preferentially adhere to inflammatory versus normal endothelium *in vitro* under static conditions.

In the current studies, we first verified that ICAM-1 was upregulated in a variety of inflammatory models using immunohistochemistry. Next, various parameters that modulate adhesion of targeted microbubbles to dysfunctional endothelium were investigated. We quantified and demonstrated control over the final antibody density on the microbubble. Using a parallel plate perfusion chamber and a radial flow chamber, ICAM-1-targeted microbubble adhesion to cultured human endothelium was shown to be greater to inflammatory than non-inflammatory cells, and linearly dependent on microbubble antibody density, wall shear rate, and endothelial ICAM-1 density.

In vivo experiments using a rat heart transplant model demonstrated that ultrasound imaging using ICAM-1-targeted microbubbles can non-invasively detect acute cardiac allograft rejection. Using a mouse subcutaneous tumor model, we demonstrated that ultrasound imaging using microbubbles targeted via a tumor endothelium-specific binding peptide can non-invasively identify tumor vasculature.

These data have implications for the development of targeted contrast agents capable of identifying endothelial molecular markers of disease, and offer promise for the optimization and clinical application of a targeted, contrast-enhanced ultrasound imaging technique for the diagnosis and monitoring of disease states associated with endothelial dysfunction.

DESCRIPTORS

Adhesion

Cell adhesion molecules

Contrast Media

Endothelium

Inflammation

Molecular Imaging

Myocardial contrast echocardiography

Targeted Imaging

Ultrasound

ACKNOWLEDGEMENTS

The work presented in this dissertation would not have been possible without the encouragement, assistance, and support of numerous individuals. My co-advisors, Drs. Villanueva and Wagner, were outstanding paragons of curiosity, thoughtful scientific reasoning, and commitment to research endeavors. They taught by example many of the ideals that I believe are critical to a successful and meaningful research career as a physician-scientist.

I would also like to thank the remaining members of my thesis committee, Drs. Borovetz, Federspiel, and Wong, for their advice and expertise during this long process. Financial support in the form of a pre-doctoral fellowship from the Pennsylvania-Delaware affiliate of the American Heart Association was greatly appreciated.

The excellent surgical skills of Dr. Erxiong Lu enabled many successful experiments, and his camaraderie and sense of humor were highly valued. The laboratory and logistical assistance of two technicians, Maris Pina Fenyus and Melissa Csikari, was invaluable. I'd also like to thank Dave Fischer for his surgical and anesthetic expertise, sense of humor, and uncanny ability to locate and acquire any needed equipment.

A number of undergraduates worked with me as summer research interns. Tamla Simmons, Neshat Rowghani, Kim Karavitch, Kendra Krutilla, and Margrit Rosado made essential contributions. The Center for Biologic Imaging offered important training in fluorescent microscopy and immunohistochemistry. Dr. Jon Wu offered the use of his excellent laser flow visualization system, and was very helpful and generous in modifying the setup for my

needs. I would like to thank Dr. Clayton Wiley for his progressive leadership of the MD/PhD Program here at Pitt. I am very appreciative of the exhilarating and productive collaboration with Dr. Michael Wong and Dr. Ruth Modzelewski.

Lastly, I'd like to thank my family and friends for their continued encouragement during my research years. My parents have always encouraged me in whatever goals I pursue, and my friends, although often teasing that after all these years I still don't have a real job, always offered thoughtful advice and support.

I owe my thanks especially to my beautiful wife Wendy. During my time here at Pitt, she has acquired a professional degree, worked diligently at her new career, turned our house into our home, been my best friend, and been an excellent mother to our wonderful baby daughter. Thank you for letting me pursue this very difficult and time-consuming training. I am very grateful for your love and support. Thank you for everything.

TABLE OF CONTENTS

ABSTRACT iv

ACKNOWLEDGEMENTS vii

LIST OF TABLES xvi

LIST OF FIGURES xvii

NOMENCLATURE xxiv

1.0 INTRODUCTION 1

1.1 Endothelial Dysfunction 1

1.1.1 Leukocyte Adhesion Molecules 2

1.1.2 ICAM-1 4

1.2 Atherosclerosis 5

1.2.1 Imaging of Endothelial Dysfunction in Atherosclerosis 7

1.3 Organ Transplant Rejection 8

1.3.1 Assessment of Transplant Rejection 10

1.4 Tumor Angiogenesis 11

1.5 Contrast Echocardiography 15

1.5.1 Contrast-Enhanced Ultrasound 15

1.5.2 Ultrasound and Microbubble Physics 18

1.6 Previous Research in Targeted Imaging of Endothelial Function 19

1.6.1 Targeted Ultrasound Agents 20
1.7 Specific Aims 25
2.0 INTERROGATION OF TISSUE FOR TARGET MOLECULE 28
2.1 Introduction 28
2.2 Methods 29
2.2.1 Human myocardium 29
2.2.2 Rabbit LPS-stimulated Myocardium 29
2.2.3 Rat Acutely Rejecting Allograft Myocardium 30
2.3 Results 31
2.3.1 Human Myocardium 31
2.3.2 Rabbit LPS-Stimulated Myocardium 34
2.3.3 Rat Acutely Rejecting Allograft Myocardium 34
2.4 Discussion 37
3.0 CONTROL OF MICROBUBBLE ANTIBODY DENSITY 39
3.1 Introduction 39
3.2 Methods 40
3.2.1 Microbubble Preparation 40
3.2.2 Streptavidin and Antibody Quantification 42
3.2.3 Statistics 43
3.3 Results 44
3.4 Discussion 47
4.0 EFFECT OF ANTIBODY DENSITY ON TARGETED MICROBUBBLE ADHESION .. 50
4.1 Introduction 50

4.2 Methods 51
4.2.1 Microbubble Preparation 51
4.2.2 Cell Culture 52
4.2.3 Quantification of ICAM-1 Expression 52
4.2.4 Parallel Perfusion Apparatus 53
4.2.4.1 Fluid Dynamical Analysis 55
4.2.5 Microbubble Perfusion 57
4.2.6 Statistics 58
4.2.7 Mathematical Adhesion Modeling 59
4.3 Results 64
4.3.1 Endothelial ICAM-1 Expression 64
4.3.2 Endothelial ICAM-1 Expression 66
4.4 Discussion 71
5.0 EFFECT OF WALL SHEAR CONDITIONS ON TARGETED MICROBUBBLE ADHESION 76
5.1 Introduction 76
5.2 Methods 77
5.2.1 Microbubble Preparation 77
5.2.2 Cell Culture 77
5.2.3 Microbubble Perfusion 77
5.2.4 Statistics 78
5.3 Results 78
5.4 Discussion 82

6.0 EFFECT OF ENDOTHELIAL TARGET DENSITY ON TARGETED MICROBUBBLE ADHESION 85
6.1 Introduction 85
6.2 Methods 86
6.2.1 Microbubble Preparation 86
6.2.2 Cell Culture 86
6.2.3 Quantification of ICAM-1 Expression 87
6.2.4 Radial Flow Chamber 88
6.2.4.1 Fluid Dynamical Analysis. 92
6.2.5 Radial Flow Chamber Validation 94
6.2.6 Microbubble Perfusion 97
6.2.7 Statistics 98
6.3 Results 98
6.4 Discussion 99
7.0 APPLICATIONS IN TRANSPLANT REJECTION 103
7.1 Introduction 103
7.2 Methods 105
7.2.1 Targeted Microbubbles 105
7.2.2 Cell Culture 105
7.2.3 Quantification of Rat EC ICAM-1 Expression 106
7.2.4 *In Vitro* Microbubble Perfusions 106
7.2.5 Heterotopic Rat Heart Transplant Model 107
7.2.6 Verification of Acute Rejection 109

7.2.6.1 Histological Rejection Grading. 109

7.2.6.2 Immunohistochemical ICAM-1 Scoring. 110

7.2.7 Myocardial Contrast Echocardiography 111

7.2.8 Ultrasound Imaging Protocol 112

7.2.9 Statistics 114

7.3 Results 115

7.3.1 In Vitro Experiments 115

7.3.2 In Vivo Experiments 119

7.3.2.1 Histology. 119

7.3.2.2 Myocardial Contrast Echocardiography. 123

7.4 Discussion 128

7.4.1 Targeted Adhesion to Cultured Rat Endothelium 128

7.4.2 Ultrasound Detection of Allograft Rejection 129

7.4.3 Comparison with Previous Studies 132

7.4.4 Limitations 133

7.4.5 Summary 136

8.0 APPLICATIONS IN TUMOR ANGIOGENESIS 137

8.1 Introduction 137

8.1.1 MW3 Tumor-Binding Peptide 138

8.2 Methods 143

8.2.1 Targeted Microbubbles 143

8.2.2 Cell Culture 146

8.2.3 In Vitro Microbubble Perfusions 146

8.2.4 Mouse Tumor Model 147

8.2.5 Contrast Echocardiography 147

8.2.6 Ultrasound Imaging Protocol 148

8.2.7 Statistics 150

8.3 Results 150

8.3.1 In Vitro Experiments 150

8.3.2 In Vivo Experiments 152

8.4 Discussion 156

8.4.1 Targeted Adhesion to Tumor Endothelium 157

8.4.2 Ultrasound Imaging of Tumor Angiogenesis 158

8.4.3 Comparison to Previous Studies 160

8.4.4 Limitations 161

8.4.5 Summary 163

9.0 FUTURE WORK 164

9.1 Planned Future Work 164

9.1.1 Multi-targeted MBs 164

9.1.2 Tissue Controls for *In Vivo* Tumor Imaging 166

9.1.3 Additional Angiogenesis Imaging 166

9.2 Recommendations for Additional Future Work 167

10.0 CONCLUSIONS 169

APPENDIX A 172

APPENDIX B 174

APPENDIX C 176

APPENDIX D 177

APPENDIX E 182

APPENDIX F 187

APPENDIX G 188

APPENDIX H 190

APPENDIX I 192

APPENDIX J 193

APPENDIX K 194

BIBLIOGRAPHY 207

LIST OF TABLES

Table 7-1 ISHLT criteria for the scoring of acute transplant rejection. Modified from [230]. 110

Table 7-2 Graft myocardial videointensity (VI) measurements for ICAM-1-targeted microbubbles (MB_{ICAM}) and isotype control microbubbles ($MB_{Control}$) for each of the 15 completely analyzed rats. Mean VI's were calculated as the average pixel intensity within the left ventricular region of interest in the first frame at 3:00 minus the average intensity in the first frame at 3:20. The $VI_{targeted}$ index is defined in the text. 126

Table 8-1 Tumor videointensity (VI) measurements for microbubbles targeted via the tumor-binding peptide MW3 (MB_{MW3}) and glycine control microbubbles ($MB_{Glycine}$) for each of the 7 completely analyzed mice. Mean VI Differences were calculated as the average pixel intensity within the region of interest encompassing the tumor in the 120 sec frame minus the average intensity in the 135 sec frame. 155

LIST OF FIGURES

Figure 1-1 Steps in leukocyte adhesion to activated endothelium. Adapted from [76]..... 4

Figure 1-2 Short-axis myocardial contrast echocardiography images in a canine model of coronary artery stenosis. Myocardium is visible as a doughnut-shaped ring encircling the contrast-filled left ventricular cavity. The top image shows homogeneous myocardial perfusion seen under normal coronary flow conditions. The bottom image, acquired during adenosine administration to increase coronary flow, shows a perfusion defect in a region of the myocardium affected by the coronary stenosis. Courtesy of Dr. Flordeliza S. Villanueva. 17

Figure 1-3 Adherence of different species of microbubbles to normal vs. activated endothelium *in vitro*. Adherence of anti-ICAM-1 MBs to activated ECs was significantly higher than all other conditions ($p<0.001$). From [95]. 21

Figure 1-4 Fluorescein-tagged microbubbles (green) targeted against ICAM-1 adhere to activated human coronary artery endothelial cells. Cytoskeletal actin is stained red and nuclei are stained blue. Courtesy of Dr. Flordeliza S. Villanueva. The color version of this figure is shown in Appendix K-1. 22

Figure 2-1 Immunohistochemical ICAM-1 expression in human cardiac explant tissue from a transplantation patient with severe ischemic cardiomyopathy. Images show staining with an anti-ICAM-1 monoclonal antibody (top), and an isotype control antibody (bottom). ICAM-1 is stained red, and was seen in larger vessels (large arrow) as well as capillaries (small arrows). The color version of this figure is shown in Appendix K-2. 32

Figure 2-2 Immunohistochemical ICAM-1 expression in human cardiac autopsy specimens from a patient with known ischemic disease (top) and a patient with normal heart tissue (bottom). ICAM-1 is stained red, and was seen in larger vessels as well as microcirculatory vessels. The color version of this figure is shown in Appendix K-3..... 33

Figure 2-3 Immunohistochemical ICAM-1 staining of two normal (upper panels) and two lipopolysaccharide-stimulated (lower panels) rabbit myocardial tissue specimens. ICAM-1 is stained red. The color version of this figure is shown in Appendix K-4. 35

Figure 2-4 Immunohistochemical ICAM-1 staining of normal (panel A) and acutely rejecting (panel B) rat myocardium. ICAM-1 is stained reddish-brown. The normal tissue showed only a small amount of constitutively expressed vascular ICAM-1, whereas the rejecting tissue showed dramatic upregulation of endothelial ICAM-1 expression in the microcirculation. The color version of this figure is shown in Appendix K-5. 36

Figure 3-1 Sample particle size distribution data for a representative batch of lipid microbubbles. Mean microbubble diameter was 3.4 ± 1.2 μm. 41

Figure 3-2 Schematic of antibody conjugation to microbubbles, using avidin/biotin bridging. (Not to scale). 42

Figure 3-3 Streptavidin density on the microbubble surface (y-axis) as measured by quantitative flow cytometry vs. streptavidin concentration (x-axis). Biotinylated microbubbles were incubated with various concentrations of PE-labeled streptavidin (0.001 – 100 μg/mL). Microbubble streptavidin density varied sigmoidally over a range of about 4 magnitudes, from 50 to 170,000 molecules per microbubble. 44

Figure 3-4 Antibody density on the microbubble surface (y-axis) as measured by quantitative flow cytometry vs. streptavidin concentration (x-axis). Biotinylated microbubbles were exposed to various concentrations of streptavidin (0.1 – 10 μg/mL, indicated as a percentage, with 100% corresponding to 10 μg/mL) followed by PE-labeled, biotinylated anti-ICAM-1 monoclonal antibody. Maximum surface antibody density was 60,000 ± 5,000 antibodies per microbubble. (Mean ± SD). 46

Figure 4-1 Schematic of the parallel plate perfusion chamber. A solution of microbubbles is perfused under controllable shear conditions across a monolayer of cultured endothelial cells grown on a coverslip. Wall shear rate is uniform over the experimental surface. (Not to scale). 54

Figure 4-2 Parallel perfusion chamber, side view and top view. 55

Figure 4-3 Hydrodynamic forces acting on a surface-adherent particle. Modified from [204]. 59

Figure 4-4 Relationship between antibody density and adhesion strength. 63

Figure 4-5 Flow cytometry sample data using cultured human coronary artery ECs with fluorescently-labeled ICAM-1. Cells were either normal or inflamed with interleukin. Calibrated standard microsphere peaks (from microspheres with 3 distinct levels of fluorochrome) used for quantitative calculations are shown as black-filled histograms. Inflammatory EC expression of ICAM-1 was approximately 20 times greater than normal ECs. 65

Figure 4-6 Expression of ICAM-1 on normal versus IL-1β-activated ECs, in terms of number of ICAM-1 molecules per cell. Interleukin activation upregulated ICAM-1 approximately 20-fold from constitutive levels. (Mean ± SD). 66

Figure 4-7 *In vitro* adherence of various microbubble species to normal versus inflammatory ECs. Adherence of bare and non-specific IgG microbubbles was minimal. Adherence of ICAM-1-targeted microbubbles increased with increased antibody surface density ($p<0.01$). Adherence of ICAM-1-targeted microbubbles was significantly greater to activated versus normal ECs ($p<0.001$). (Mean ± SD). 68

Figure 4-8 *In vitro* adherence of MB_{ICAM} to normal and inflammatory ECs vs. MB antibody density. MB adherence to both cell types increased with increased antibody surface density ($p<0.01$). (Mean ± SD)..... 69

Figure 4-9 Brightfield micrographs of inflammatory ECs following exposure to microbubbles carrying nonspecific IgG, or various densities anti-ICAM-1 antibody. Each image shows approximately 6-8 ECs in the background, and adhered microbubbles (arrows). There was only minimal adherence of nonspecific IgG-containing microbubbles. With the anti-ICAM-MBs, adhesion increases with increasing antibody density..... 70

Figure 5-1 *In vitro* adhesion of maximally-targeted (100% antibody density) anti-ICAM-1 microbubbles to normal versus inflammatory human ECs under various wall shear conditions. Adherence was significantly greater to activated versus normal ECs. Microbubble adherence was clearly shear-dependent, with binding decreasing with increasing shear rate. (Mean ± SD)..... 80

Figure 5-2 Brightfield micrographs of inflammatory ECs following perfusion with maximally-targeted (100% antibody density) anti-ICAM-1 microbubbles at flow rates corresponding to 5 different wall shear rates between 100 s^{-1} and 500 s^{-1}. Each image shows approximately 6-8 ECs in the background, and adhered microbubbles (arrows). As the shear rate under which the microbubble binding interactions occur increases, adhesion to ECs decreased... 81

Figure 6-1 Dose-response relationship between interleukin-1β and ICAM-1 expression on cultured endothelial cells. 87

Figure 6-2 Schematic of the radial flow perfusion chamber. A solution of microbubbles is perfused under controllable shear conditions across a monolayer of cultured endothelial cells grown on a coverslip. Wall shear rate varies inversely with radius from the central inlet, and microbubble adherence primarily occurs outside of a "critical shear radius" which corresponds to a "critical shear rate" above which microbubbles do not adhere. (Not to scale). 90

Figure 6-3 Radial flow perfusion chamber, side view and top view. The color version of this figure is shown in Appendix K-6..... 91

Figure 6-4 Microbubble adhesion pattern in the radial flow chamber. Microbubbles adhere primarily outside of a critical shear radius, observable at low microscopic magnification as a critical shear ring..... 91

Figure 6-5 Radial position vs. velocity as measured using laser velocimetry. There is general agreement between the predicted inverse relationship and the experimental data. 95

Figure 6-6 Volumetric flow rate (Q) vs. critical shear radius validation data. 97

Figure 6-7 Endothelial ICAM-1 expression versus targeted MB adhesion strength. Four different concentrations of interleukin-1 were used to activated cultured ECs to four different levels of inflammation. The critical shear rates of ICAM-1-targeted MB adhesion were measured in a radial flow chamber. (Mean ± SD). 99

Figure 6-8 Possible relationships between degree of endothelial inflammation and targeted MB adhesion. 102

Figure 7-1 Heterotopic heart transplantation in the rat, using the method of Ono and Lindsey [227]. The explanted donor heart is implanted into the abdomen of the recipient animal, and the donor aorta is anastomosed end-to-side to the recipient abdominal aorta (left image). The donor pulmonary artery is then anastomosed to the recipient inferior vena cava (right image). Drawings from [227]..... 108

Figure 7-2 Protocol for the *in vivo* ultrasound contrast imaging of transplanted hearts in rats. Microbubbles (either MB_{ICAM} or $MB_{Control}$) were injected at time zero. Ultrasound pulses were given at 3 min and 3 min 20 sec post-injection. The videointensity of the tumor region of interest at 3:20 was subtracted from the videointensity at 3:00 to achieve the acoustic signal attributable only to adhered microbubbles. 114

Figure 7-3 Flow cytometry sample data using cultured rat ECs with fluorescently-labeled ICAM-1. Inflammatory cultured rat ECs expressed substantially more ICAM-1 than normal ECs. 115

Figure 7-4 Mean fluorescence intensity of ICAM-1-labeled ECs. ICAM-1 expression was approximately 8 times higher on IL-1β-activated ECs than normal ECs. (Mean ± SD). .. 116

Figure 7-5 *In vitro* adherence of targeted microbubbles to cultured rat endothelial cells. Adherence of control microbubbles ($MB_{Control}$) was minimal to both cell types, whereas adhesion of ICAM-1-targeted microbubbles (MB_{ICAM}) was significantly higher to interleukin-activated cells than normal cells (Mean ± SD)..... 117

Figure 7-6 Brightfield micrographs of IL-1β-activated (left panels) and normal (right panels) cultured rat ECs after exposure to ICAM-1-targeted microbubbles (MB_{ICAM}, upper panels) and isotype control microbubbles ($MB_{Control}$, lower panels). Each image shows approximately 6-8 ECs in the background, and adhered microbubbles (arrows). There was significantly greater adhesion of MB_{ICAM} to activated versus normal ECs. Adhesion of $MB_{Control}$ to both cell types was minimal. 118

Figure 7-7 Brightfield micrographs of examples of isograft (panel A) and allograft (panel B) rat myocardium stained with hematoxylin and eosin. The isograft tissue was histologically normal, while the allograft tissue was characterized by indicators of acute rejection including edema, lymphocytic infiltration, and myocyte damage. The color version of this figure is shown in Appendix K-7. 120

Figure 7-8 Endothelial ICAM-1 expression in BN→L allograft and L→L isograft rat hearts versus post-op day. ICAM-1 expression was scored by blinded observers on a scale of 0 (constitutive ICAM-1 only) to 4 (most positive). The qualitative ICAM-1 score increased more quickly in the allografts than isografts ($p<0.01$), and at post-op day 5 was significantly higher for allograft than isograft rats ($p<0.005$). (Mean ± SD). 121

Figure 7-9 Brightfield micrographs of isograft (panel A) and allograft (panel B) rat myocardium stained for ICAM-1 (reddish-brown). The isograft tissue showed only a small amount of

constitutively expressed vascular ICAM-1, whereas the rejecting allograft tissue showed dramatic upregulation of endothelial ICAM-1 expression in the microcirculation. (Same as Figure 2-4). The color version of this figure is shown in Appendix K-8. 122

Figure 7-10 Background-subtracted, color-coded ultraharmonic ultrasound images acquired after injection of ICAM-1-targeted microbubbles (MB_{ICAM}) in the donor myocardium of a rejecting allograft rat (upper panels) and control isograft rat (lower panels). Gradations from red → orange → yellow → white denote increasing opacification. Ultrasound contrast enhancement by MB_{ICAM} in the rejecting myocardium (panel A) was greater than in the control myocardium (panel C). There was minimal contrast in both hearts at 3:20. The color version of this figure is shown in Appendix K-9. 124

Figure 7-11 Corresponding ultrasound images acquired after injection of isotype control microbubbles ($MB_{Control}$) in the donor myocardium of the same rejecting (upper panels) and control (lower panels) rats as in Figure 7-10. Gradations from red → orange → yellow → white denote increasing opacification. Ultrasound contrast enhancement by $MB_{Control}$ was minimal in both rejecting and normal myocardium. The color version of this figure is shown in Appendix K-10. 125

Figure 7-12 Mean $VI_{targeted}$ for control (isograft) vs. rejecting (allograft) donor hearts (n = 7 and 8, respectively). The $VI_{targeted}$ compares the signal due to adhered MB_{ICAM} with the signal due to adhered $MB_{Control}$ to give a measure of the signal attributable to specific microbubble adhesion to vascular ICAM-1. The $VI_{targeted}$ for allograft rats was significantly higher than the $VI_{targeted}$ for isograft rats. (Mean ± SD). 127

Figure 8-1 Fluorescent micrographs showing that the peptide MW3 (left panels) binds strongly to cultured angiogenic tumor-derived endothelial cells (TDEC, upper panels), but not to control cells (NIH3T3, lower panels). A control peptide composed only of glycines (right panels) shows only minimal binding to both cell types. Courtesy of Dr. Michael K. K. Wong. 140

Figure 8-2 Fluorescent micrographs of PC3 (upper panels) and Clone C (lower panels) tumors harvested from mice following *in vivo* intravenous injection of fluorescently-labeled MW3 (left panels) or glycine control peptide (right panels). In comparison to the glycine control, MW3 binds strongly to the tumor vasculature. Courtesy of Dr. Michael K. K. Wong. 142

Figure 8-3 Schematic of microbubble conjugation to cyclic peptide containing the MW3 tumor-binding sequence. (Not to scale). 144

Figure 8-4 Schematic of microbubble conjugation to cyclic peptide containing a glycine control sequence. (Not to scale). 145

Figure 8-5 Protocol for the *in vivo* ultrasound contrast imaging of tumors in mice. Microbubbles (either MB_{MW3} or $MB_{Glycine}$) were injected at time zero. Ultrasound pulses were given at 120 and 135 sec post-injection. The videointensity of the tumor region of interest at 135 sec was subtracted from the videointensity at 120 sec to achieve the acoustic signal attributable only to adhered microbubbles. 149

Figure 8-6 Brightfield micrographs of cultured tumor derived endothelial cells (TDEC, upper panels) and normal human coronary artery endothelial cells (HCAEC, lower panels) after exposure to microbubbles conjugated to MW3 (left panels) or a glycine control peptide (right panels). More MB_{MW3} adhered to the tumor-derived cells than to the normal cells. Only a few control microbubbles adhered to either cell type. 151

Figure 8-7 *In vitro* adherence of targeted microbubbles to cultured tumor-derived endothelial cells (TDEC) and normal human coronary artery endothelial cells (HCAEC). Adherence of control microbubbles (Glycine) was minimal to both cell types, whereas adhesion of microbubbles targeted via the tripeptide Arg-Arg-Leu (MW3) was significantly higher to tumor-derived cells than normal cells (Mean ± SD). 152

Figure 8-8 Background-subtracted, color-coded ultrasound images taken 120 seconds after injection of microbubbles conjugated to MW3 (left image) or glycine control peptide (right image) into a mouse bearing a Clone C tumor. The region within the tumor has been color-coded. Gradations from red → orange → yellow → white denote increasing opacification. MB_{MW3} resulted in greater contrast enhancement. The color version of this figure is shown in Appendix K-11. 153

Figure 8-9 Background-subtracted, color-coded ultrasound images taken 120 seconds after injection of microbubbles conjugated to MW3 (left image) or glycine control peptide (right image) into a mouse bearing a PC3 tumor. The region within the tumor has been color-coded. Gradations from red → orange → yellow → white denote increasing opacification. MB_{MW3} resulted in greater contrast enhancement. The color version of this figure is shown in Appendix K-12. 154

Figure 8-10 Videointensity due to adhered microbubbles (120 sec signal – 135 sec signal). Intensity due to adhesion of microbubbles targeted via MW3 was significantly greater than that due to adhesion of control glycine microbubbles. (n=7 each). (Mean ± SD). 156

Figure 9-1 Adhesion strength of microbubbles targeted via conjugation with anti-ICAM-1 antibodies only, a 50/50 mix of anti-ICAM-1 and anti-VCAM-1 antibodies, or anti-VCAM-1 antibodies only, respectively. 165

Appendix K-1 Color version of Figure 1-4 195

Appendix K-2 Color version of Figure 2-1 196

Appendix K-3 Color version of Figure 2-2 197

Appendix K-4 Color version of Figure 2-3 198

Appendix K-5 Color version of Figure 2-4 199

Appendix K-6 Color version of Figure 6-3 200

Appendix K-7 Color version of Figure 7-7 201

Appendix K-8 Color version of Figure 7-9..... 202

Appendix K-9 Color version of Figure 7-10..... 203

Appendix K-10 Color version of Figure 7-11..... 204

Appendix K-11 Color version of Figure 8-8..... 205

Appendix K-12 Color version of Figure 8-9..... 205

NOMENCLATURE

a	Radius of contact area between surface and adherent sphere
BN	Brown Norway strain rat
c	Numerical constant
C	Total number of receptor/ligand bonds
CT	Computed tomography
∂	Partial derivative operator
e	Natural logarithm base
EC	Endothelial cell
EDTA	Ethylenediaminetetraacetate
FACS	Fluorescence-activated cell sorting
F_b	Bond force
F_s	Fluid force
F_T	Total fluid force
g	Gravitational constant
γ	Bond range of interaction
$\dot{\gamma}$	Shear rate
∇	Gradient operator
h	Channel height (gap height)
HCAEC	Human coronary artery endothelial cell
Hz	Hertz
ICAM-1	Intercellular adhesion molecule-1
IgG	Immunoglobulin G
IL-1β	Interleukin-1-beta
ISHLT	International Society for Heart and Lung Transplantation
IVC	Inferior vena cava
K	Receptor-ligand affinity constant k_f/k_r
k_b	Boltzmann's constant
k_f	Forward rate constant
k_r	Reverse rate constant
L	Lewis strain rat
LAM	Leukocyte adhesion molecule
LPS	Bacterial lipopolysaccharide
μ	Dynamic viscosity
M-199	Medium-199
MB	Microbubble
$MB_{Control}$	Microbubble conjugated to an isotype control antibody
$MB_{Glycine}$	Microbubble conjugated to a glycine control peptide
MB_{ICAM}	Microbubble conjugated to an anti-ICAM-1 monoclonal antibody

MB_{MW3}	Microbubble conjugated to the peptide MW3
MCE	Myocardial contrast echocardiography
MHz	Megahertz
MI	Mechanical index
min	Minutes
MRI	Magnetic resonance imaging
MRS	Magnetic resonance spectroscopy
MW3	The tumor endothelium-specific binding peptide Arg-Arg-Leu
N_b	Bond density
N_L	Ligand density
N_R	Receptor density
ρ	Density
ρ_B	Sphere radius
P	Pressure
PBS	Phosphate buffered saline
PE	Phycoerythrin
PEG	Polyethylene glycol
PET	Positron emission tomography
PMMA	Polymethylmethacrylate
Q	Volumetric flow rate
r	Radius
RBC	Red blood cell
S_c	Critical shear stress
SD	Standard deviation
sec	Seconds
τ	Shear stress
t	Time
T	Temperature
Tq	Torque
TDEC	Tumor-derived endothelial cells
TNF	Tumor necrosis factor
V	Velocity
VCAM-1	Vascular cell adhesion molecule-1
VI	Acoustic videointensity
$VI_{targeted}$	An index of relative videointensity, defined in Section 7.2.7
w	Channel width

1.0 INTRODUCTION

1.1 Endothelial Dysfunction

The endothelial lining of blood vessels has numerous beneficial functions in the healthy state. In this normal role, the endothelium provides an anti-thrombotic luminal surface, regulates vasodilation and vasoconstriction, modulates thrombosis, regulates vascular smooth muscle proliferation, and regulates vascular permeability [1, 2]. Implications at the endothelial surface include inhibition of coagulation, inhibition of vasoconstriction, and discouragement of adhesion and subsequent migration of leukocytes. These active functions serve to maintain the healthy homeostasis of the vascular bed.

In disease states, however, the endothelium changes roles to become an active promoter of thrombosis, smooth muscle growth, and leukocyte adhesion and diapedesis [1,2]. Production of the vasodilating substances nitric oxide (a.k.a. endothelium-derived relaxing factor) and prostacyclin is reduced [1, 3]. Production of procoagulants including tissue factor increases, which, in conjunction with the decrease in vasodilator secretion, creates a prothrombotic surface [4]. Endothelial secretion of growth factors increases, encouraging smooth muscle cell proliferation [5]. Endothelial cell (EC) surface expression of leukocyte adhesion molecules (LAMs) is upregulated, to encourage leukocyte capture and migration [6, 7]. These responses to insult collectively have been termed “endothelial dysfunction”, which has been identified as a component of ischemia, inflammation, hypertension, diabetes, atherosclerosis, tissue injury, transplant rejection, and neoplasia [1, 8-15].

1.1.1 Leukocyte Adhesion Molecules

Of particular relevance to the work presented herein is the overexpression of leukocyte adhesion molecules during endothelial dysfunction. A key function of inflammatory endothelium is to encourage the binding of circulating leukocytes to allow for their emigration through the endothelial layer into the underlying tissue. This phenomenon, as described by Dr. Timothy Springer, is a multistep process [16-18]. First, a group of adhesion molecules on the endothelial surface called selectins weakly bind circulating leukocytes, with labile attachments that result in transient adhesion and leukocyte "rolling" along the endothelium (see Figure 1-1). Second, leukocytes are now close enough such that chemoattractants can signal to G-protein receptors on the leukocytes, activating integrin adhesiveness. Third, immunoglobulin superfamily receptors on the endothelium bind strongly to integrins expressed on the leukocyte surface, halting the rolling, and firmly adhering the cell to the endothelium. After the activated white cells are arrested on the luminal surface, they diapedese between adjoining ECs and migrate into the affected tissue, following chemoattractant gradients.

The selectins are a family of vascular adhesion molecules that mediate the initial weak attachment of leukocytes to endothelial cells, allowing the leukocytes to roll along the vascular wall [16, 19]. Ligands for the selectins include sialyl Lewis-x, a carbohydrate determinant found on a number of hematopoietic cells [20]. L-selectin, found on leukocytes, E-selectin, found on ECs, and P-selectin, found on platelets and ECs, form weak, labile tethers (fast on- and off-rates) with their respective ligands, allowing for the transient capture and rolling of leukocytes along the EC layer in the direction of blood flow [21, 22].

The immunoglobulin superfamily is a group of cell surface receptors that includes intercellular adhesion molecule-1 (ICAM-1), intercellular adhesion molecule-2 (ICAM-2), vascular cell adhesion molecule (VCAM-1), and platelet-endothelial cell adhesion molecule (PECAM) [20]. These receptors are all transmembrane glycoproteins that have immunoglobulin-like extracellular domains. These endothelial receptors bind to integrin ligands on activated leukocytes to firmly bind rolling leukocytes and allow for extrusion into the underlying tissue.

Upregulation of endothelial cell surface LAMs has been observed in atherosclerosis [12, 23], diabetes [24], arterial thrombosis [25], organ transplant rejection [26, 15], neoplasia [14], ischemia [27, 28], tissue injury [29], ischemia/reperfusion [13], hypertension [30], inflammatory myopathies [31], dilated cardiomyopathy [32], and chronic heart failure [33].

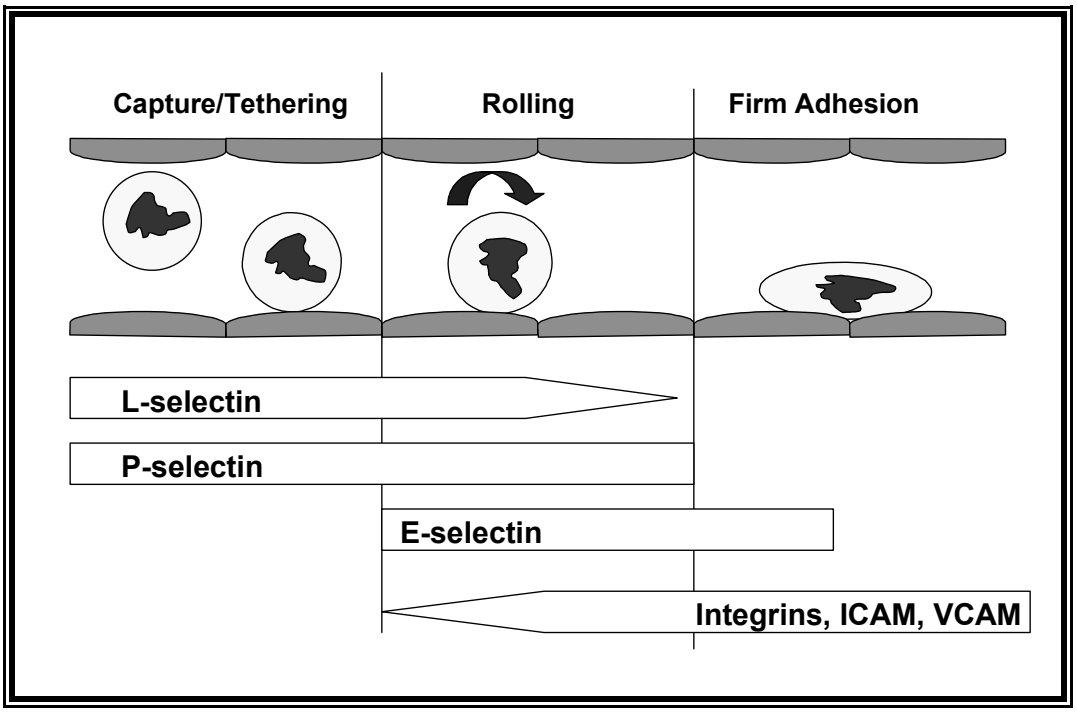

Figure 1-1 Steps in leukocyte adhesion to activated endothelium. Adapted from [76].

1.1.2 ICAM-1

Much of the work presented herein focuses on the well-characterized leukocyte adhesion molecule ICAM-1 (CD54). A member of the immunoglobulin superfamily, it is most heavily expressed on activated leukocytes and endothelial cells, although it can also be expressed on other cells, including fibroblasts, monocytes, mast cells, smooth muscle cells, and epithelial cells [34]. ICAM-1 functions mainly to achieve specific, reversible cell-cell adhesion, thus supporting activation of the T cell-mediated immune system and mediating inflammation [34]. It contains 5 immunoglobulin-like domains and has a molecular weight between 80 and 114 kDa [35, 36]. Its structure has been determined by X-ray crystallography [37, 38]. Its ligands are the integrins

Mac-1 (CD11b/CD18) and leukocyte function associated antigen (LFA-1; CD11a/CD18), which are both present on leukocytes but have different binding kinetics and signaling functions [39-43]. ICAM-1 is transcriptionally regulated, and is upregulated by inflammatory cytokines [44].

ICAM-1 is overexpressed during inflammation, sepsis, wound healing, ischemia/reperfusion injury, atherosclerosis, asthma, organ transplant rejection, melanoma and other solid tumors, and hematological malignancies [20, 34, 45]. ICAM-1 also serves as a receptor for rhinoviruses, a leading cause of upper respiratory tract infections, and has been considered as a potential target for respiratory infection treatment and prophylaxis [38, 46]. It is expressed constitutively on normal endothelial cells at a low level, and upregulated on ECs both *in vitro* and *in vivo* by agents including interleukin-1 (IL-1), bacterial endotoxins, and tumor necrosis factor (TNF) [20, 29, 34, 47-49]. ICAM-1 is downregulated by nitric oxide [50].

1.2 Atherosclerosis

The pathogenesis of atherosclerosis is a lifelong process, beginning long before clinical consequences manifest. Fatty streaks, intimal aggregations of lipid-laden macrophages and T lymphocytes, can be found in young adults, adolescents, infants, and even some fetuses [51, 52]. As Dr. Russell Ross asserts, atherosclerosis is an inflammatory disease, one that is more complex than the simple accumulation of lipid products within the vessel wall [12]. The "response-to-injury" model states that, long before ischemic flow limitations occur, the atherosclerotic process is set into motion by the vascular response to insult: endothelial dysfunction [12, 53, 54]. As described in Section 1.1, endothelium expressing an inflammatory, dysfunctional phenotype changes its vascular roles to become prothrombotic and vasoconstrictive, and actively encourages smooth muscle cell proliferation and leukocyte adhesion and transmigration.

Monocytes that migrate across the endothelial barrier into the underlying tissue become macrophages and ingest lipid, resulting in foam cells that contribute to the formation of the initial fatty streaks [11, 55]. As the recruited lymphocytes and macrophages multiply in the tissue, they secrete pro-inflammatory factors such as cytokines, growth factors, and chemokines that lead to further cell influx and proliferation, and tissue damage [12]. This cycle eventually allows the initial fatty streak lesions to progress over time to the more advanced fibrofatty lesions, and finally to the fibrous plaque stage [11].

Thus, endothelial dysfunction is a key event in the pathogenesis of atherosclerotic disease. One aspect of this phenomenon that is of particular interest to the work in this dissertation is the overexpression of LAMs on the activated endothelial surface. Increased levels of ICAM-1 have been found on the endothelium of atherosclerotic plaques in many studies [23, 56-58]. ICAM-1, VCAM-1, e-selectin, and p-selectin are upregulated on the endothelium over atherosclerotic plaques in human coronary arteries [23, 56, 58, 59]. ICAM-1 is also overexpressed by the smooth muscle cells of human arterial plaques, and has been identified on early fatty streaks [57, 60]. Serum levels of soluble ICAM-1 and soluble VCAM-1 have been shown to correlate with cardiovascular risk factors and atherosclerotic disease [61, 62]. Atherogenic lipoproteins have been shown to upregulate endothelial ICAM-1 *in vitro* [63]. ICAM-1 has been shown to be a key factor for the progression of transplant-related arteriosclerosis in a murine model [64], and arteriolar ICAM-1 expression in human cardiac allografts correlates with risk for developing transplant-related coronary arteriosclerosis [65].

The pathophysiological characteristics of atherosclerosis, including LAM overexpression, have been shown to exist not only in large vessels such as the aorta and epicardial coronary arteries, but also in the small vessels of the microcirculation [66-68]. This is an important

finding, as contrast-enhanced ultrasound images not the large vessels, but the rather the microcirculation, as will be discussed in Section 1.5.

1.2.1 Imaging of Endothelial Dysfunction in Atherosclerosis

The current gold standard for the diagnosis of atherosclerosis is coronary catheterization with X-ray angiography. This technique identifies physical vessel abnormalities (stenoses) that cause flow limitations. The limitations of angiography include invasiveness, inter-observer variability, and an imperfect correlation with functional flow limitations [69]. Additionally, angiography is only able to detect late-stage disease, once it has resulted in vessel shape changes. An non-invasive technique has been introduced that assesses flow-mediated brachial artery vasoactivity by ultrasonically measuring brachial artery diameter changes in response to temporary flow occlusion [70]. This technique, however, is only indirectly related to coronary endothelial function, and relies on measurements of small changes in vessel diameter that approach the spatial resolution limits of ultrasound imaging [71]. Imaging techniques including computed tomography (CT) and magnetic resonance imaging (MRI) have been employed to measure vessel wall thickness, lumen area, and fibrous plaque components, but none has progressed to clinical application [72, 73]. Intravascular ultrasound has been employed to measure thickening of the vascular intima and media, but this technique has poor sensitivity with mild disease, and assesses only structural vascular changes [74, 75].

Molecular imaging of atherosclerotic endothelial dysfunction may provide for the detection of the disease process prior to structural vessel changes or clinical manifestations. Reported techniques include scintigraphy using radiolabeled antibodies against oxidized low-density lipoprotein (LDL) in a hyperlipidemic rabbit model [77, 78], radiolabeled anti-myosin

antibodies to image disease-associated myocyte necrosis [79], and (although not targeted the endothelium) radiolabeled antibody specific for proliferating smooth muscle cells [80]. Magnetic particles targeted via anti-E-selectin antibodies have been used for MRI assessment of inflammatory cultured human ECs [81]. Drug delivery liposomes linked to anti-ICAM-1 antibodies have been shown to specifically adhere to human endothelium *in vitro* [82].

Ultrasound imaging of molecular markers associated with atherosclerosis has been described in a number of reports. Further details are provided in Section 1.6. Briefly, non-targeted contrast agents can be used to image inflammation after being phagocytosed by activated blood-borne leukocytes, which then adhere to dysfunctional endothelium [83, 84]. Echogenic liposomes conjugated to anti-fibrinogen or anti-ICAM-1 antibodies have been used to image thrombi or atherosclerotic lesions in a porcine model [85-89]. Thrombus has also been ultrasonically imaged using antibody targeting and avidin/biotin binding [90-92]. Activated platelets have been targeted using contrast agents linked to receptor-specific binding peptides [93, 94]. Inflammation has been targeted using agents linked to anti-ICAM-1 or anti-P-selectin antibodies [95, 96], as well as agents targeted to activated leukocytes [97, 98].

1.3 Organ Transplant Rejection

As in the case of atherosclerosis discussed earlier, endothelial dysfunction is a critical step in the pathogenesis of acute transplant rejection. Organ transplant rejection is caused by an immunologic response to non-self tissue. Hyperacute rejection is caused by preexisting host antibodies specific for antigens on the graft tissue, and occurs within the first 24 hours post-transplantation; acute rejection is due to the cell-mediated immunity actions of helper and cytotoxic T lymphocytes, and occurs within a few weeks; chronic rejection can be caused by

both humoral and cell-mediated mechanisms, and occurs months to years post-transplantation [99].

Acute rejection is a leading cause of death in heart transplant patients, responsible for up to 20% of deaths in the first post-transplant year and up to 15% thereafter [100]. Cell-mediated immune reactions lead to an infiltration of T lymphocytes and macrophages into the graft tissue, where cytotoxic T cells destroy targeted graft cells, and numerous cytokines are released that promote T-cell proliferation, macrophage activation, and endothelial dysfunction [99].

The upregulation of a variety of LAMs has been demonstrated in a number of allograft models. The expression of ICAM-1 and VCAM-1 correlates with the extent of acute rejection in rabbit cardiac allografts [101]. Endothelial VCAM-1 and E-selectin as well as tubular ICAM-1 are all upregulated in murine models of renal transplant rejection [102, 103]. There are conflicting reports concerning endothelial ICAM-1 upregulation in renal allograft rejection [102, 104, 105]. In rat heterotopic heart transplantation models of acute and chronic rejection, ICAM-1 is overexpressed by the graft myocardial endothelium [106, 107].

Similar results have been found regarding human transplantation. Vascular endothelial growth factor has been identified in rejecting human cardiac allografts [108]. Microvascular ICAM-1, VCAM-1, and E-selectin are overexpressed during rejection of cardiac and pulmonary allografts [15, 26, 109-112].

A number of studies have targeted these upregulated adhesion molecules for the prevention or treatment of transplant rejection. Antibodies against ICAM-1 have been reported to cause attenuation of graft rejection and increase cardiac graft survival in mouse and rat models [113, 114]. Antibodies against E-selectin and P-selectin have had similar protective effects in a rat cardiac rejection model [115]. Blockade of the leukocyte ligands for ICAM-1 via

administration of anti-CD18 antibodies has led to a reduction in graft rejection in a rabbit cardiac transplant model [116, 117]. Donor hearts from knockout mice with deficient ICAM-1 and P-selectin expression demonstrate less rejection than normal donor hearts [118]. Rat donor hearts transfected with antisense anti-ICAM-1 oligodeoxynucleotide has been shown to inhibit ICAM-1 expression and thus improve graft survival [119]. Rat donor cardiac allografts treated with the drug sulfasalazine to inhibit ICAM-1 and VCAM-1 expression showed decreased reperfusion injury, thus helping to reduce rejection [120].

1.3.1 Assessment of Transplant Rejection

The current gold standard for the assessment of cardiac transplant rejection is endomyocardial biopsy, a procedure that is invasive and not without risk. However, numerous non-invasive techniques for the assessment of acute rejection have been reported, some of which image endothelial dysfunction.

Non-targeted radiologic approaches have been reported for the assessment of transplant rejection. MRI has been used to detect anatomic and hemodynamic changes in rejecting rat kidney and heart allografts, as well as macrophage accumulation in rat cardiac transplants [121-123]. Magnetic resonance spectroscopy (MRS) has been used to detect rejection of rat cardiac transplant by measuring energy-rich phosphates [124]. Positron emission tomography (PET) has been used to detect changes in glucose metabolism in rejecting rat cardiac transplants [125, 126]. Acoustic changes due to altered cardiac hemodynamic function and wall morphology in rejecting human cardiac allografts have been detected with ultrasound [127, 128].

Targeted imaging techniques have been reported as well. A scintigraphic technique using ^{99m}technecium-labeled annexin-V to image rejection-associated apoptosis has been demonstrated

in a rat heterotopic cardiac transplant model as well as in a human cardiac allograft study [129-131]. Major histocompatibility complex class II antigens have been targeted with ^{123}I-labeled antibodies to scintigraphically image rejection in a rat cardiac transplant model [132, 133]. Radiolabeled antibodies have also been used to target the adhesion molecule ICAM-1 in this rat cardiac model, as well as a rat model of pulmonary rejection [134-136].

1.4 Tumor Angiogenesis

New blood vessels are created through two processes. Vasculogenesis, the *in situ* differentiation and proliferation of vascular networks, occurs during embryonic development [137]. Angiogenesis, the formation of new blood vessels by sprouting from existing vascular trees, i.e. recruitment, occurs during wound repair, menstruation, retinopathy, response to ischemia, and neoplasia [138-140].

A fundamental concept upon which much cancer research is based is that angiogenesis is a requirement for the growth of solid tumors beyond a few millimeters' diameter [138, 141]. The new vascular supply is necessary for the tumor mass to progress to the large, malignant stage capable of metastasizing to other parts of the body. Accordingly, an avenue of anticancer therapy that is being increasingly pursued is the inhibition of angiogenesis [138]. If the formation of a blood supply for a solid tumor can be blocked, then the tumor will not be capable of growing beyond a small, non-metastatic cluster of transformed cells.

Based on the above concepts, anti-angiogenic therapy may be able to prevent tumor progression to a more clinically severe state, by attacking the angiogenic vascular endothelium rather than the actual tumor cells. An advantage that anti-angiogenic therapies may have over more established chemotherapy is that they may have fewer drug resistance difficulties than are

seen with chemotherapy, because the mutation rate of endothelial cells (targeted by anti-angiogenics) in a tumor is generally much lower than that of the tumor cells themselves (targeted by conventional chemotherapy) [142].

The effects of chemotherapy can be monitored using conventional imaging methods that follow tumor size or other anatomic measures as the response variables. CT can measure response variables such as tumor blood flow, blood volume, and vascular permeability [143, 144]. MRI can measure tumor blood volume and vascular permeability [143, 145, 146]. For example, dynamic contrast enhanced MRI has been used to measure tumor size and vascular permeability in response to anti-VEGF anti-angiogenic therapy in human glioblastoma multiforme tumors in nude rats [147]. Ultrasound can also measure these same three parameters: tumor blood flow, volume, and vascularity [143, 148]. Doppler ultrasound has been used, for example, to monitor response to antivascular therapy in human melanomas in athymic mice [149]. Tumor vascularity as measured by Doppler ultrasound has been correlated with an *ex vivo* index of angiogenesis generated by measuring microvessel density in cervical cancer specimens harvested from human patients [150]. Doppler US measurements of tumor vascularity have also been correlated with immunohistochemical identification of molecular tumor markers such as cyclooxygenase-2 (COX-2) [151]. However, this study failed to demonstrate any correlations with other molecular markers, including VEGF, basic fibroblast growth factor (bFGF), and CD31.

To complement the use of anti-angiogenic therapy, techniques for imaging angiogenesis are needed. Because anti-angiogenic treatments are generally cytostatic rather than cytotoxic, the conventional imaging methods discussed above are not optimal for monitoring such therapy [146]. A *functional* evaluation of the therapeutic effect on the vasculature is warranted, not just

an anatomic assessment of the tumor volume or blood flow [143]. Since the degree of angiogenesis is an indicator of the malignant potential of a solid tumor, a technique to assess the functional status of the tumor endothelium would be of great utility for the assessment and monitoring of tumors [152, 153].

For such an endeavor, molecular imaging techniques have been proffered as a possible solution. For example, in a human case study, tumor vitamin B_{12} metabolism was imaged in breast cancer using radiolabeled adenosylcobalamin [154]. Using *in vivo* phage display, Rajotte *et al* have shown that endothelium from various vascular beds express varied molecular surface markers, a concept they refer to as "molecular heterogeneity" [155]. Others have also demonstrated that this concept Ruoslahti *et al* call "vascular addressing" applies to angiogenic tumor endothelium [156, 157]. Dr. Judah Folkman has been a pioneer in angiogenesis research, and refers to an "angiogenic zip code" [158].

The fact that tumor angiogenic endothelium expresses specific endothelial molecular markers has important implications for molecular imaging of tumor angiogenesis. Agents that bind to tumor angiogenesis-specific markers could yield effective imaging and drug delivery techniques. A well-characterized example is the endothelial integrin $\alpha_v ß_3$, which is selectively expressed on angiogenic endothelium [159]. A group led by Dr. David Cheresh has published extensively in this area, including a study in which rabbit carcinomas were imaged *in vivo* using MRI with a magnetic liposome contrast agent targeted to $\alpha_v ß_3$ via conjugation with a monoclonal antibody [160]. Lipid-based particles targeted to $\alpha_v ß_3$ by have been shown to selectively adhere to angiogenic vessels in tumor-bearing mice, and when the particles were loaded with a mutant Raf gene that is known to inhibit angiogenesis, tumor regression resulted [161]. Ultrasound

contrast agents have been targeted to α_v integrins via conjugation with anti-α_v antibodies, and shown to adhere preferentially to growth factor-stimulated angiogenic endothelium [162].

Numerous small peptides have been identified that specifically interact *in vivo* with various types of endothelial cells, including angiogenic endothelium [155, 163, 164]. Dr. Ruoslahti's group has targeted tumor vasculature using angiogenesis-specific peptides containing the asparagine-glycine-arginine (NGR) or arginine-glycine-aspartate (RGD) sequence [165, 166]. In one study, peptides containing the NGR sequence were shown to specifically target tumor endothelium *in vitro* and *in vivo* by binding to aminopeptidase N (CD13), a receptor for NGR [165]. In another study, peptides with the RGD and NGR adhesion sequences were linked to doxorubicin (a chemotherapeutic agent with anti-angiogenic activity) and injected into nude mice bearing human breast tumors, resulting in increased therapeutic drug effect [166]. Targeting of the anticancer agent tumor necrosis factor α (TNF-α) to CD13 via conjugation with an NGR-containing peptide has enhanced its therapeutic effects [167]. The sequence histidine-tryptophan-glycine-phenylalanine (HWGF) has also been used to target angiogenesis. In a study by Koivunen *et al*, tumors were targeted using the HWGF sequence, which also functions to inhibit metalloproteinase activity (a requirement for angiogenesis), demonstrating specific tumor targeting and simultaneous inhibition of tumor growth in mice [168]. The peptide sequence RGD is found naturally in vitronectin and fibronectin, and is known to bind to the tumor-specific $\alpha_v\beta_3$ integrin [169]. A study by Haubner *et al* used positron emission tomography (PET) to image tumors in mice using $^{F}18$-labeled glycopeptides containing the RGD sequence [170]. Janssen *et al* also used RGD-containing peptides to bind to the $\alpha_v\beta_3$ integrin on tumor endothelium, and demonstrated scintigraphic imaging of human ovarian carcinomas in nude

mice [171]. Other studies, however, have encountered difficulty getting enough radiolabeled RGD peptide to bind to tumor endothelium to allow *in vivo* imaging [172, 173].

1.5 Contrast Echocardiography

1.5.1 Contrast-Enhanced Ultrasound

Myocardial contrast echocardiography (MCE) is an ultrasound imaging technology that makes use of injectable contrast agents to enhance the ultrasonic signal received from the coronary microcirculation during echocardiographic imaging. The contrast agents are suspensions of gas-filled microbubbles (MBs) a few micrometers in diameter that increase the backscattering of transmitted ultrasonic energy, resulting in increased acoustic intensity, or contrast enhancement. Microbubble shells have been composed of proteins, lipids, and polysaccharides. Since the *in vivo* bloodstream kinetics of these MBs are very similar to red blood cells in terms of myocardial transit rates, these contrast agents can serve as blood flow tracers [174, 175]. Thus, MCE using contrast MBs can offer the *in vivo,* real-time, non-invasive assessment of myocardial perfusion, and can be used to assess ischemic risk areas, infarct size, and collateral blood flow [176, 177, 242-244]. This contrast-enhanced ultrasound technique images the whole myocardial vascular bed, not just individual large epicardial vessels, predominantly imaging the microcirculation [177].

Examples of contrast-enhanced ultrasound images of canine myocardium are shown in Figure 1-2. In this model of coronary artery stenosis, the images are in short-axis view, such that the myocardium is visible as a doughnut-shaped ring encircling the contrast-filled left ventricular cavity. The top image was acquired during normal coronary artery flow conditions, showing homogeneous perfusion throughout the myocardium. The bottom image is of the same heart

during an adenosine stress test in which coronary flow increases, showing a perfusion defect in the region of the myocardium affected by the flow limitation (stenosis).

Under normal conditions, microbubbles do not adhere to the endothelium, allowing them to act as blood tracers. In an early canine echocardiographic study of cardioplegia-perfused hearts, however, it was observed that the albumin microbubbles used as the contrast agent appeared to persist in the coronary microvasculature, resulting in persistent acoustic opacification [178]. This shift in microbubble behavior away from normal RBC kinetics implied that the microbubbles may have adhered to the cardioplegia-perfused endothelium. Since cardioplegia is known to injure ECs, causing endothelial dysfunction, it was reasonable to predict that this persistent myocardial contrast was due to microbubble adherence to dysfunctional endothelium [179, 180]. Villanueva *et al* later demonstrated that albumin microbubbles adhere to inflammatory endothelial extracellular matrix [181]. These early observations were the initial catalysts for the development of targeted microbubble contrast agents that specifically adhere to markers of dysfunctional endothelium, to allow ultrasonic imaging of the functional status of the endothelium.

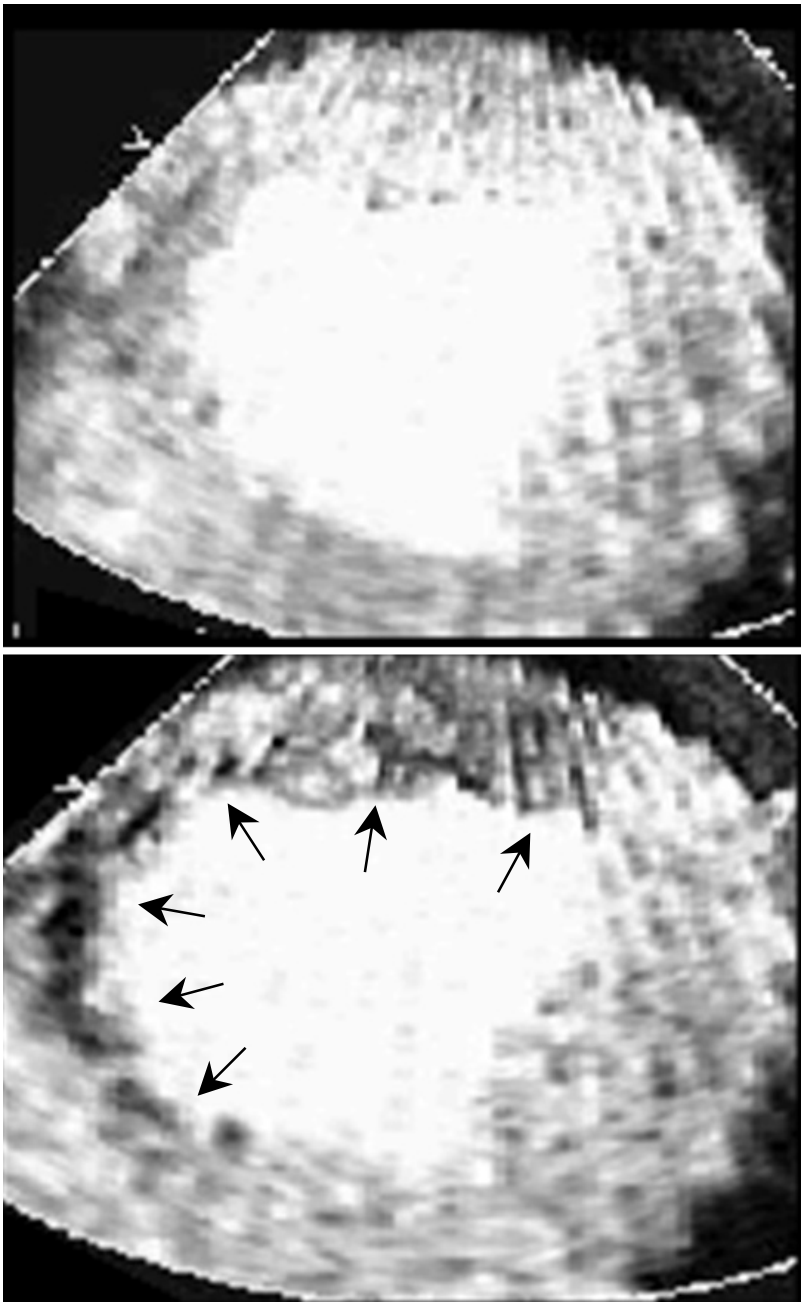

Figure 1-2 Short-axis myocardial contrast echocardiography images in a canine model of coronary artery stenosis. Myocardium is visible as a doughnut-shaped ring encircling the contrast-filled left ventricular cavity. The top image shows homogeneous myocardial perfusion seen under normal coronary flow conditions. The bottom image, acquired during adenosine administration to increase coronary flow, shows a perfusion defect in a region of the myocardium affected by the coronary stenosis. Courtesy of Dr. Flordeliza S. Villanueva.

1.5.2 Ultrasound and Microbubble Physics

Ultrasound propagates through a medium as a periodic wave with a certain frequency, amplitude, and velocity. When the wave encounters an interface between media of different densities, part of the acoustic energy is reflected back to the transducer, and is measured by the ultrasound machine.

When contrast microbubbles are subjected to an ultrasound field, they alternately compress and expand due to the alternately positive and negative acoustic pressure [182]. Clinically relevant frequencies induce oscillations on the order of one million Hz [183]. These oscillations produces acoustic waves that propagate radially from the microbubble. This backscattered energy is measured by the ultrasound transducer.

An interesting property of microbubbles is that their acoustic backscattering response is not linear; they do not respond to incident ultrasound transmissions of different amplitudes in a proportional manner [184]. As the ultrasound energy is increased towards the upper end of the clinically relevant transmission range, microbubble oscillations become nonlinear. The contraction at positive acoustic pressure and the expansion at negative pressure are unequal, resulting in the scattering of additional frequency components by the oscillating microbubble. These additional components include harmonics (energy peaks at multiples of the fundamental frequency), subharmonics (fractions of the fundamental frequency) and ultraharmonics (peaks at non-integer multiples of the fundamental frequency) [184, 185].

Many modern ultrasound machines are capable of not only fundamental imaging (sending out acoustic waves and receiving scattered energy from microbubbles at the same

frequency), but also 2nd harmonic imaging (sending at one frequency and receiving at twice that frequency). Such harmonic imaging can be advantageous because it enhances the signal from the nonlinear contrast agents while suppressing the signal from the more linearly responsive surrounding tissue [186]. Transducers capable of imaging at 2nd harmonic, subharmonic, and ultraharmonic frequencies have been developed [187]. Another technique is power harmonic Doppler imaging, which can further increase the signal-to-noise ratio for contrast microbubbles by being sensitive to Doppler shifts, which are created by the movement or collapse of microbubbles within the bloodstream. The most recent development is pulse inversion imaging. In this technique, two successive mirror-image (180º phase rotated) ultrasound pulses are transmitted [186]. Tissue with linear response characteristics will return two mirror-image echoes that sum to zero. Nonlinear contrast microbubbles, however, will return non-mirror-image (asymmetric) echoes with a non-zero sum, thus allowing for a much stronger signal to be measured from the contrast agent than from the surrounding tissue.

1.6 Previous Research in Targeted Imaging of Endothelial Function

As discussed in the previous sections, numerous reports have been published describing non-targeted and targeted assessment of endothelial dysfunction related to inflammatory disease processes, using a variety of imaging modalities including ultrasound, scintigraphy, MRI, MRS, PET, and CT. In this section, the reported techniques employing targeted ultrasound agents will be further detailed.

1.6.1 Targeted Ultrasound Agents

Ultrasound contrast microbubbles targeted to molecular markers associated with endothelial dysfunction have been described in a number of reports.

Key previous work in our laboratory from Villanueva *et al* described lipid-based echogenic microbubbles targeted to ICAM-1 via covalent linkage with anti-ICAM-1 antibodies [95]. Control microbubbles were produced with either no antibodies at all (bare) or with non-specific isotype control antibodies. Microbubbles were statically dwelled for 3 min over a monolayer of cultured human endothelial cells mounted in a parallel plate perfusion chamber, then washed with MB-free medium for 3 min at the very low wall shear rate of 25 s^{-1}. The cells were either normal, or inflammatory via incubation with interleukin-1ß. As shown in Figure 1-3, adhesion of both species of control MBs was minimal to both normal and inflammatory ECs, while adhesion of ICAM-1-targeted MBs was approximately 40 times higher to inflammatory than normal endothelium. A fluorescent photomicrograph showing targeted microbubbles adhered to inflammatory endothelium is shown in Figure 1-4. The findings in this study constituted the first proof-of-principle that ultrasound contrast microbubbles specifically targeted to inflammatory molecular markers will preferentially adhere to endothelium overexpressing that target.

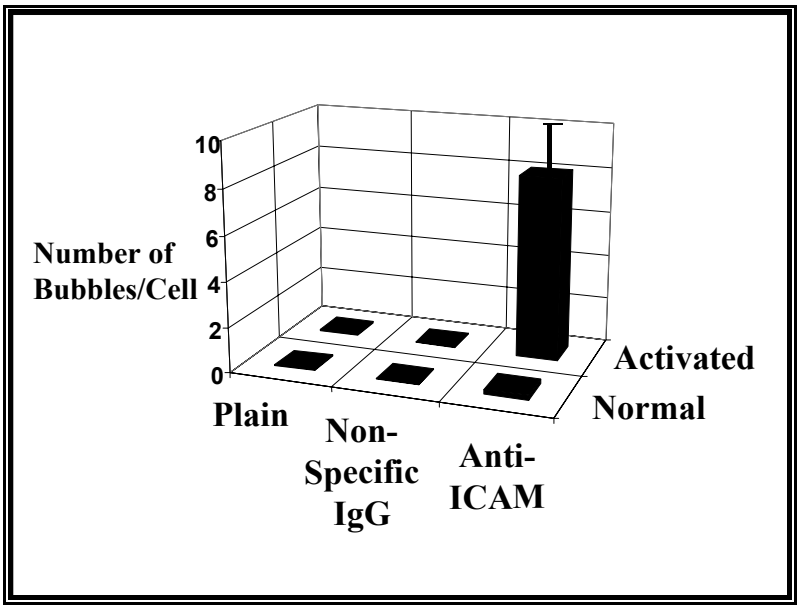

Figure 1-3 Adherence of different species of microbubbles to normal vs. activated endothelium *in vitro*. Adherence of anti-ICAM-1 MBs to activated ECs was significantly higher than all other conditions ($p<0.001$). From [95].

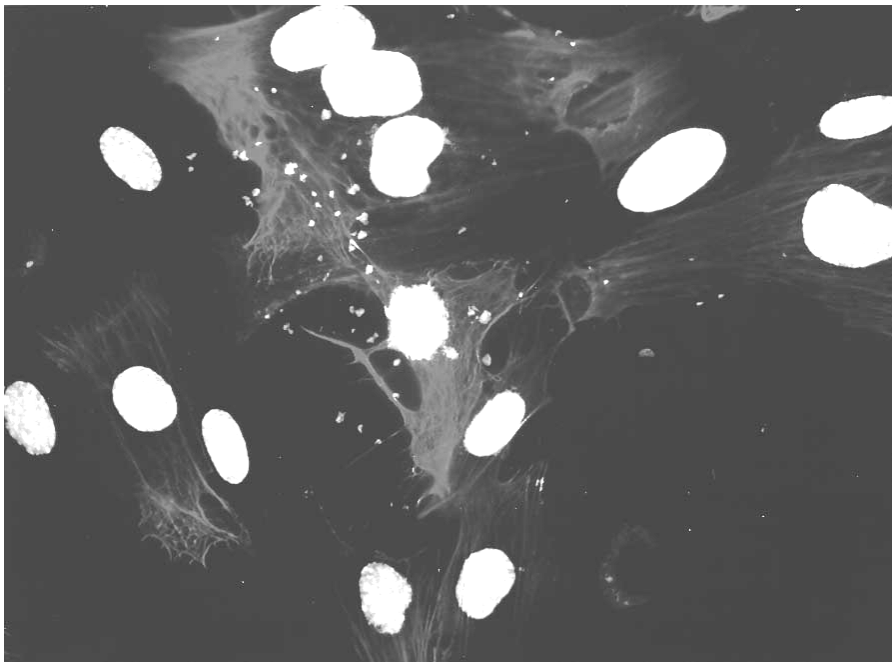

Figure 1-4 Fluorescein-tagged microbubbles (green) targeted against ICAM-1 adhere to activated human coronary artery endothelial cells. Cytoskeletal actin is stained red and nuclei are stained blue. Courtesy of Dr. Flordeliza S. Villanueva. The color version of this figure is shown in Appendix K-1.

Since then, Dr. Jonathan Lindner's group at the University of Virginia has been active in the field. Using intravital microscopy of inflamed, exteriorized murine cremaster muscle, they demonstrated that non-targeted ultrasound contrast microbubbles can bind to activated blood-borne leukocytes, which naturally adhere to dysfunctional endothelium [83]. This attachment was mediated by β_2 integrins or complement, depending on the microbubble composition. This group later demonstrated that microbubbles adhered to leukocytes can be phagocytosed, and that

these phagocytosed MBs remain intact and acoustically active [84]. They again used the murine cremaster intravital microscopy preparation, in this case to demonstrate the ultrasonic detection of phagocytosed MBs inside leukocytes adherent to the inflammatory endothelium. The acoustic intensity generated by adhered microbubbles was greater for TNF-α-stimulated versus normal endothelium.

Based on the idea that microbubble adherence to leukocytes is mediated by complement, and that complement activation can be accelerated by phophatidylserine, Lindner *et al* next investigated microbubbles targeted to activated leukocytes via incorporation of phophatidylserine into the MB shell [97]. Using a murine cremaster intravital microscopy preparation and an *in vivo* murine model of renal ischemia/reperfusion injury, they demonstrated that the acoustic contrast enhancement from phophatidylserine-MBs was higher in the inflammatory kidneys than in normal control kidneys, and the signal from phophatidylserine-MBs was higher than that from control MBs containing no phophatidylserine. Later, Christiansen *et al* at Virginia reported that contrast-enhanced ultrasound using phophatidylserine-containing MBs can detect post-ischemic inflammation in a canine model of myocardial reperfusion injury [98]. Together, these studies published between 2000 and 2002 demonstrated that endothelial dysfunction can be ultrasonically imaged by targeting MBs to activated leukocytes.

In 2001, Dr. Lindner reported an investigation of MBs targeted to endothelial dysfunction via anti-P-selectin antibodies [96]. Again using an intravital microscopy preparation, as well as a murine model of renal ischemia/reperfusion injury, they demonstrated that P-selectin-targeted MBs preferentially adhere to the endothelium or adherent platelet/leukocyte aggregates of

inflammatory versus normal tissue, and that this differential binding can be visualized with ultrasound.

Most recently, in 2003, this group reported that microbubbles targeted to α_v integrins via surface-bound antibodies adhere to FGF-stimulated vessels overexpressing α_v integrins using an *in vivo* Matrigel model of angiogenesis [162]. Ultrasound was used to visualize the resulting contrast enhancement, demonstrating the feasibility of ultrasonic imaging of angiogenesis.

Thrombus has also been imaged using acoustically-active contrast agents. Lanza *et al* pre-targeted *in vivo* and *in vitro* models of thrombus with biotinylated anti-fibrin antibodies, then exposed them to avidin, and then to a biotinylated fluorocarbon microemulsion contrast agent [90-92, 188]. This pre-labeling technique allowed ultrasonic visualization of the coated thrombi. This technique requires multiple steps and local administration of binding reagents, as opposed to the more direct technique using contrast agents specifically targeted to the markers of interest.

Thrombus has also been imaged by targeting activated platelets. Unger *et al* and Wu *et al* have used MBs linked to peptides that specifically bind to GPIIb/IIIa receptors on activated platelets [93-94]. These agents specifically adhere to thrombi, and result in acoustic contrast enhancement for ultrasonic visualization.

Using *in vitro* and *in vivo* models of atherosclerotic lesions, Demos *et al* have reported that echogenic liposomes conjugated to anti-fibrinogen or anti-ICAM-1 antibodies adhere to thrombi or fibrous components of atheroma. [85-89]. The adhered contrast agent enabled the *in vivo* ultrasonic imaging of an atherosclerotic arterial injury model using intravascular and transvascular ultrasound techniques.

1.7 Specific Aims

The objective of this dissertation is to investigate the **general hypothesis that contrast-enhanced ultrasound using microbubbles targeted to specific endothelial cell surface epitopes can image these molecular markers of endothelial dysfunction**. Targeted microbubbles that adhere to markers on the endothelial surface would be expected cause persistent acoustic contrast enhancement that can be visualized with ultrasound. Such a molecular imaging technique may allow for the non-invasive ultrasonic diagnosis and monitoring of disease processes associated with endothelial dysfunction.

The majority of this work will focus on microbubbles targeted to the inflammatory adhesion molecule ICAM-1. Accordingly, work presented in Chapter 2 will investigate the **hypothesis that the target molecule, ICAM-1, is upregulated on the microcirculatory endothelium of tissues experiencing endothelial dysfunction**. Because myocardial contrast echocardiography images mainly microbubbles in the microcirculation, we need to demonstrate that ICAM-1 is overexpressed on dysfunctional endothelium not just in large blood vessels, such as the epicardial coronary arteries, but also in arterioles, capillaries, and/or venules. Myocardial tissue specimens from human ischemic hearts, and animal models of inflammation and acute transplant rejection will be interrogated immunohistochemically for endothelial ICAM-1 expression.

Chapter 3 will present experiments studying the **hypothesis that the antibody density on the microbubble surface can be controlled by modifying the antibody/microbubble conjugation protocol**. By varying the reagent concentrations in the antibody conjugation

process, MBs will be linked to varying amounts of anti-ICAM-1 antibody, which will be measured via quantitative flow cytometry.

These studies are a necessary prelude to the work in Chapter 4, which investigates the **hypothesis that adhesion of targeted microbubbles to cultured endothelium is dependent on microbubble antibody density**. The amount of targeting antibody on the MB surface is an important design parameter, that is expected to strongly modulate the adhesion characteristics of the targeted agent. A parallel plate perfusion chamber will be used to investigate the adhesion of MBs with various antibody densities to normal and inflammatory cultured endothelium. Results will be interpreted in terms of previously reported mathematical models of specific particle/substrate adhesion.

Chapter 5 will examine the **hypotheses that ICAM-1-targeted microbubbles can adhere to inflammatory endothelium from shear flow, and that the level of adhesion is dependent on wall shear rate**. Physiologic shear conditions vary widely throughout the circulation, and can be expected to strongly affect targeted MB adhesion, but previous work with ICAM-1-targeted microbubbles has investigated adhesion only under static conditions. In anticipation of *in vivo* experiments, the effect of physiologically-relevant shear rates on the adhesion of ICAM-1-targeted MBs to cultured endothelium will be tested using the parallel plate perfusion chamber.

Work examining the **hypothesis that targeted microbubble adhesion to cultured endothelium is dependent on the cell surface density of the target molecule (ICAM-1)** will be presented in Chapter 6. A radial flow perfusion chamber will be used to investigate the *in vitro* adhesion strength of ICAM-1-targeted MBs to variably-stimulated endothelial cells exhibiting various levels of inflammation (as measured by ICAM-1 expression). The effect of

endothelial ICAM-1 density on MB adhesion is critical to the development of this molecular imaging technique as a clinically useful tool. We need to determine whether our targeted imaging system can potentially differentiate between various degrees of endothelial dysfunction, or will be limited to distinguishing only between normal and fulminant disease.

Chapter 7 presents our first *in vivo* data using ICAM-1-targeted MBs. A rat heterotopic heart transplant model will be utilized to investigate the **hypothesis that ultrasound using contrast microbubbles targeted to ICAM-1 can non-invasively detect acute cardiac allograft rejection**. The rejection status of allograft (rejecting) hearts and isograft (non-rejecting) hearts will be assessed by applying clinical grading criteria, and myocardial ICAM-1 expression will be assessed using immunohistochemistry. Targeted microbubbles will be injected intravenously into the rats, and the donor hearts will be imaged with external ultrasound. The images will be analyzed for myocardial acoustic intensity resulting from adhered microbubbles, and comparisons between rejection groups will be made.

Additional *in vivo* experiments presented in Chapter 8 will examine the hypothesis that **ultrasound using contrast microbubbles targeted to tumor angiogenesis can non-invasively detect tumor vasculature**. Moving away from our ICAM-1 motif, microbubbles will be targeted via conjugation with a tumor endothelium-specific binding peptide. These MBs will be injected intravenously into mice bearing subcutaneous solid tumors, and external ultrasound imaging will be performed. Acoustic intensity within the tumor will be quantified, and comparisons made between targeted MBs and control MBs.

2.0 INTERROGATION OF TISSUE FOR TARGET MOLECULE

2.1 Introduction

As described in Chapter 1, numerous studies have found that various LAMs are upregulated in tissues experiencing disease processes characterized by endothelial dysfunction, including inflammation, atherosclerosis, and allograft rejection [26, 45, 60]. Of particular relevance to the studies presented in this dissertation is the overexpression of ICAM-1 on dysfunctional microvascular endothelium.

In the present study, two aims were pursued. First, since reports of ischemic myocardium have been limited to investigations of LAM expression in large vessels, we studied normal and ischemic human myocardial tissue to demonstrate that ICAM-1 is upregulated in the microcirculation, not just large coronary vessels, of the ischemic heart. We hypothesized that ICAM-1 is overexpressed in the microcirculation of diseased tissue as compared to normal tissue. Second, in anticipation of targeted contrast experiments using *in vivo* animal models, rabbit lipopolysaccharide-stimulated myocardial tissue as well as rat acutely rejecting cardiac allograft tissue were interrogated for ICAM-1. Here, we similarly hypothesized that ICAM-1 is overexpressed in the microcirculation of diseased tissue as compared to normal tissue.

2.2 Methods

2.2.1 Human myocardium

Experiments using human cardiac tissue were approved by the Institutional Review Board at the University of Pittsburgh. Frozen myocardial specimens harvested at autopsy from human patients with known ischemic heart disease (n=4), as well normal cardiac autopsy specimens (n=3), were obtained from the National Disease Research Interchange (NDRI, Philadelphia, PA). Frozen specimens of explanted native ischemic heart tissue (n=4) from human cardiac transplant patients were courtesy of Dr. Charles McTiernan (University of Pittsburgh), and additional normal cardiac specimens (n=6) were courtesy of Dr. Warren Rosenblum (University of Pittsburgh).

Myocardial specimens were cut into 5 μm-thick sections, and stained for ICAM-1 using a monoclonal antibody against human ICAM-1 (R6.5, courtesy of Dr. Robert Rothlein, Boehringer Ingelheim) and an immunoperoxidase amplification kit (Vectastain Elite, Vector Labs, Burlingame, CA) using 3-amino-9-ethylcarbazole (AEC) as the precipitating chromogen. The full staining protocol is given in Appendix I.

2.2.2 Rabbit LPS-stimulated Myocardium

All animal experiments were approved by the Institutional Animal Care and Use Committee at the University of Pittsburgh. New Zealand White rabbits (3-5 kg) were anesthetized with intramuscular ketamine (40 mg/kg) and xylazine (7 mg/kg). A 20-gauge intravenous access catheter was placed in the marginal ear vein. In selected animals, bacterial lipopolysaccharide (LPS) from E. coli 0111:B4 (Sigma, St. Louis, MO) was administered as an intravenous bolus (2 mg diluted in 1 mL normal saline) to stimulate inflammation. Six hours

later, the abdomen was opened, the aorta was cannulated with an 18-gauge catheter, a heparin bolus was administered through the aortic catheter, and the animal was sacrificed with an anesthesia overdose. A nick was cut into the inferior vena cava, and saline was flushed in a retrograde manner through the aorta to the vena cava to clear blood from the coronary circulation. The heart was harvested, and frozen in liquid nitrogen.

Inflammatory (n=4) and normal (n=3) myocardial specimens were cut into 5 μm-thick sections, and stained for ICAM-1 using the murine anti-rabbit monoclonal antibody Rb2/3 (courtesy of Dr. Myron Cybulsky) and the immunoperoxidase amplification kit and chromogen described above.

2.2.3 Rat Acutely Rejecting Allograft Myocardium

Abdominal heterotopic heart transplantation was performed on Brown Norway and Lewis rats, as described in detail in Section 7.2.5. Depending on the strain of the donor and recipient rat, the cardiac allograft will either remain healthy, or will experience acute rejection.

Samples of myocardial tissue from normal (n=3) and rejecting (n=3) transplanted donor hearts were harvested 5 days after transplantation surgery (see Section 7.2.5) and frozen in liquid nitrogen. Specimens were mounted on glass microscope slides and interrogated for ICAM-1 using a polymer-based immunoperoxidase staining kit (Envision K-1390, Dako, Carpinteria, CA) and a biotinylated primary anti-rat-ICAM-1 antibody (clone 1A29, Pharmingen, San Diego, CA). The full staining protocol is given in Appendix J.

2.3 Results

2.3.1 Human Myocardium

Endothelial ICAM-1 stained positively in both the ischemic cardiomyopathy explant tissue and the ischemically-diseased autopsy tissue. Figure 2-1 shows brightfield micrographs of the explant tissue stained with the anti-ICAM-1 antibody (top) and an isotype-matched nonsense antibody as a negative control (bottom). ICAM-1 staining was found on the endothelium of both larger vessels and the microcirculatory vessels in these tissues.

Specimens of normal, non-ischemic myocardium also stained positively for ICAM-1. Again, both larger vessels and the microcirculatory vessels expressed the adhesion molecule. As seen in Figure 2-2, there was no apparent difference in ICAM-1 expression between specimens from patients with known ischemic disease (top) and normal heart specimens (bottom).

Similar results were found for E-selectin expression in these human specimens. All three tissue types stained positively in both large and small blood vessels, and no differences between tissue types could be appreciated.

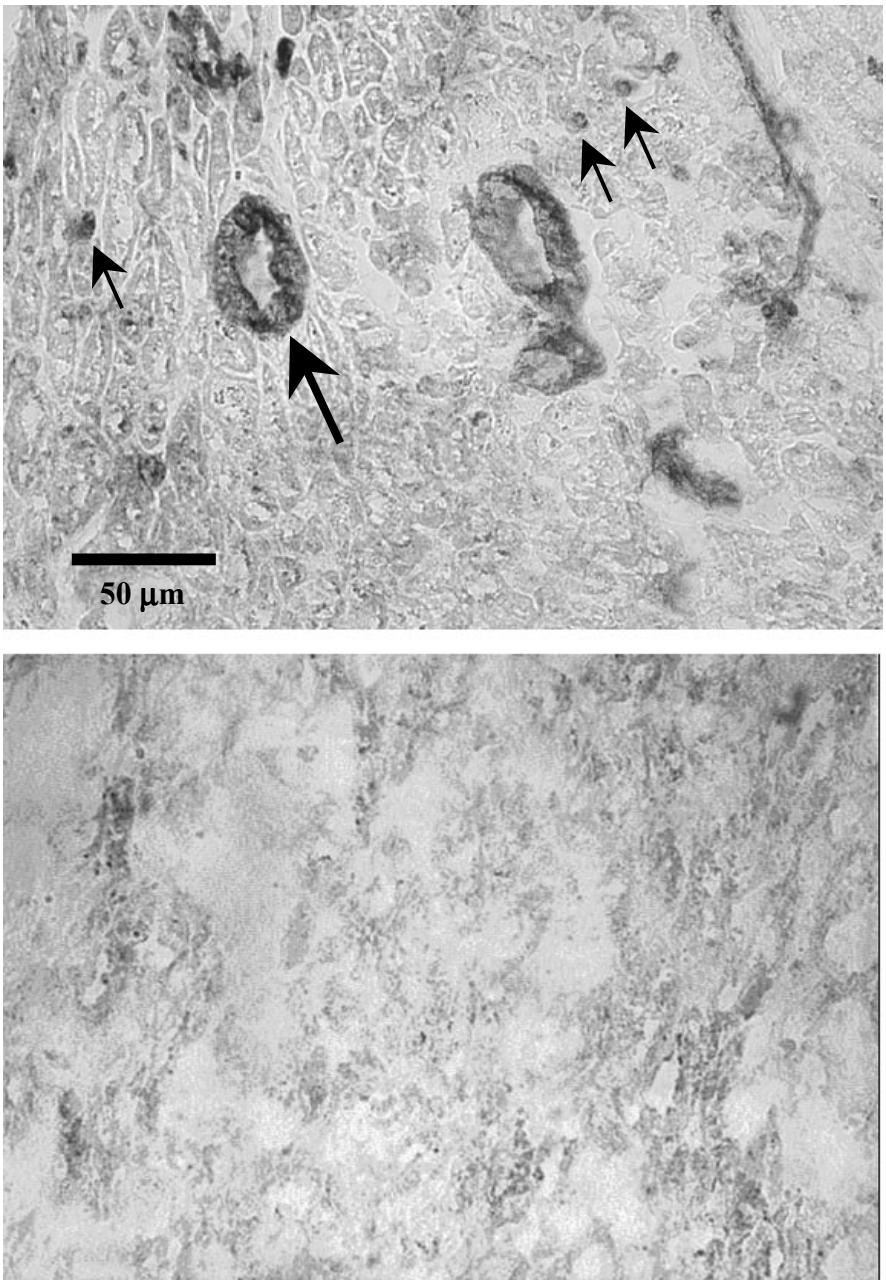

Figure 2-1 Immunohistochemical ICAM-1 expression in human cardiac explant tissue from a transplantation patient with severe ischemic cardiomyopathy. Images show staining with an anti-ICAM-1 monoclonal antibody (top), and an isotype control antibody (bottom). ICAM-1 is stained red, and was seen in larger vessels (large arrow) as well as capillaries (small arrows). The color version of this figure is shown in Appendix K-2.

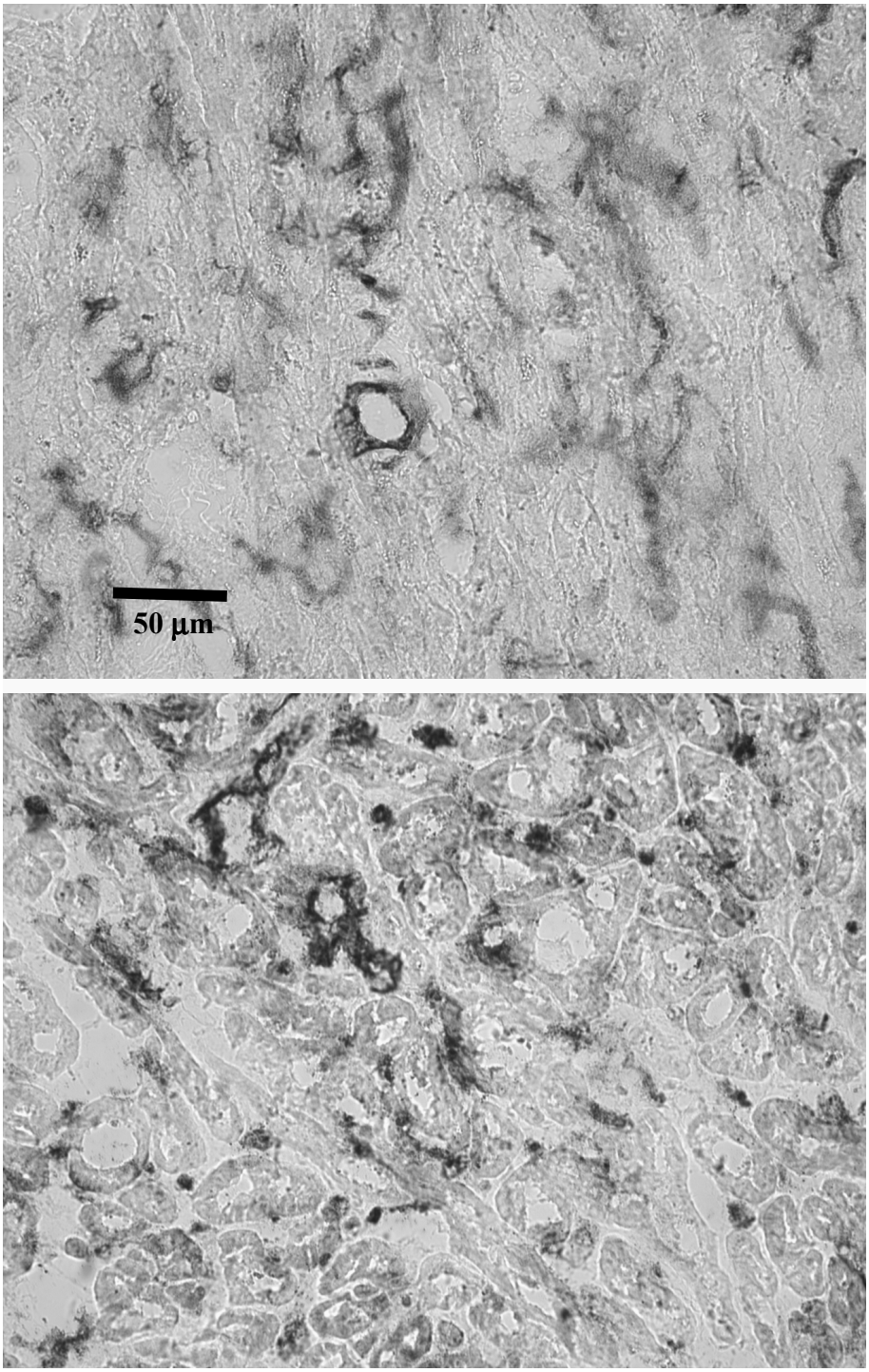

Figure 2-2 Immunohistochemical ICAM-1 expression in human cardiac autopsy specimens from a patient with known ischemic disease (top) and a patient with normal heart tissue (bottom). ICAM-1 is stained red, and was seen in larger vessels as well as microcirculatory vessels. The color version of this figure is shown in Appendix K-3.

2.3.2 Rabbit LPS-Stimulated Myocardium

Brightfield micrographs of ICAM-1-stained rabbit myocardium are shown in Figure 2-3. In normal rabbit tissue, endothelial ICAM-1 was apparent on some larger vessels, but not in any small arterioles, capillaries, or venules. This pattern was consistent for all normal specimens.

In the LPS-stimulated rabbit specimens, ICAM-1 was expressed in both larger vessels and microcirculatory vessels. In all LPS-activated samples, almost all of the capillaries were stained positively.

2.3.3 Rat Acutely Rejecting Allograft Myocardium

Figure 2-4 shows brightfield micrographs of rat cardiac transplant tissue (post-op day 5) stained for ICAM-1 using an anti-rat-ICAM-1 antibody. The normal tissue has only minimal ICAM-1 expression, whereas the rejecting myocardium shows intense staining of the capillaries.

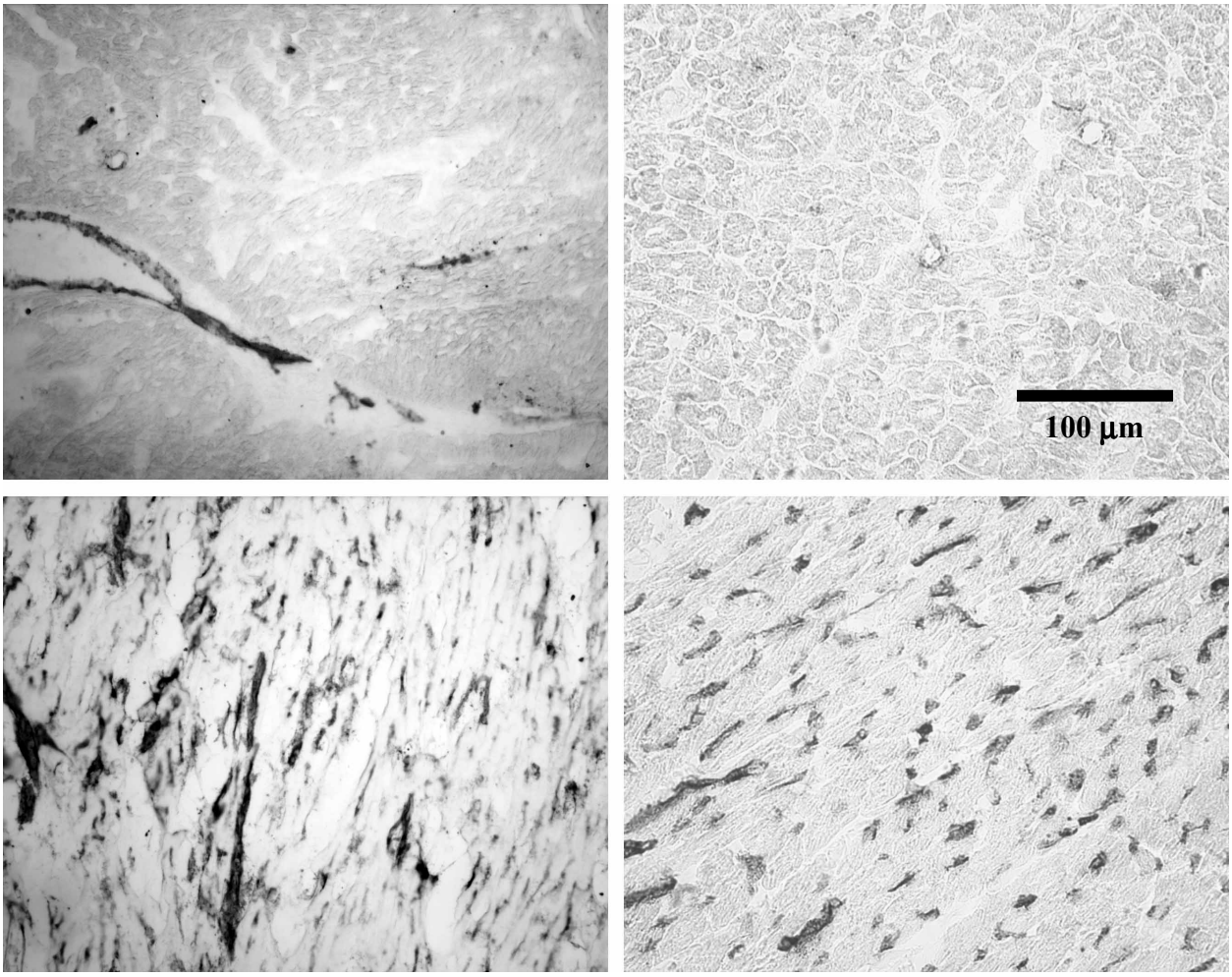

Figure 2-3 Immunohistochemical ICAM-1 staining of two normal (upper panels) and two lipopolysaccharide-stimulated (lower panels) rabbit myocardial tissue specimens. ICAM-1 is stained red. The color version of this figure is shown in Appendix K-4.

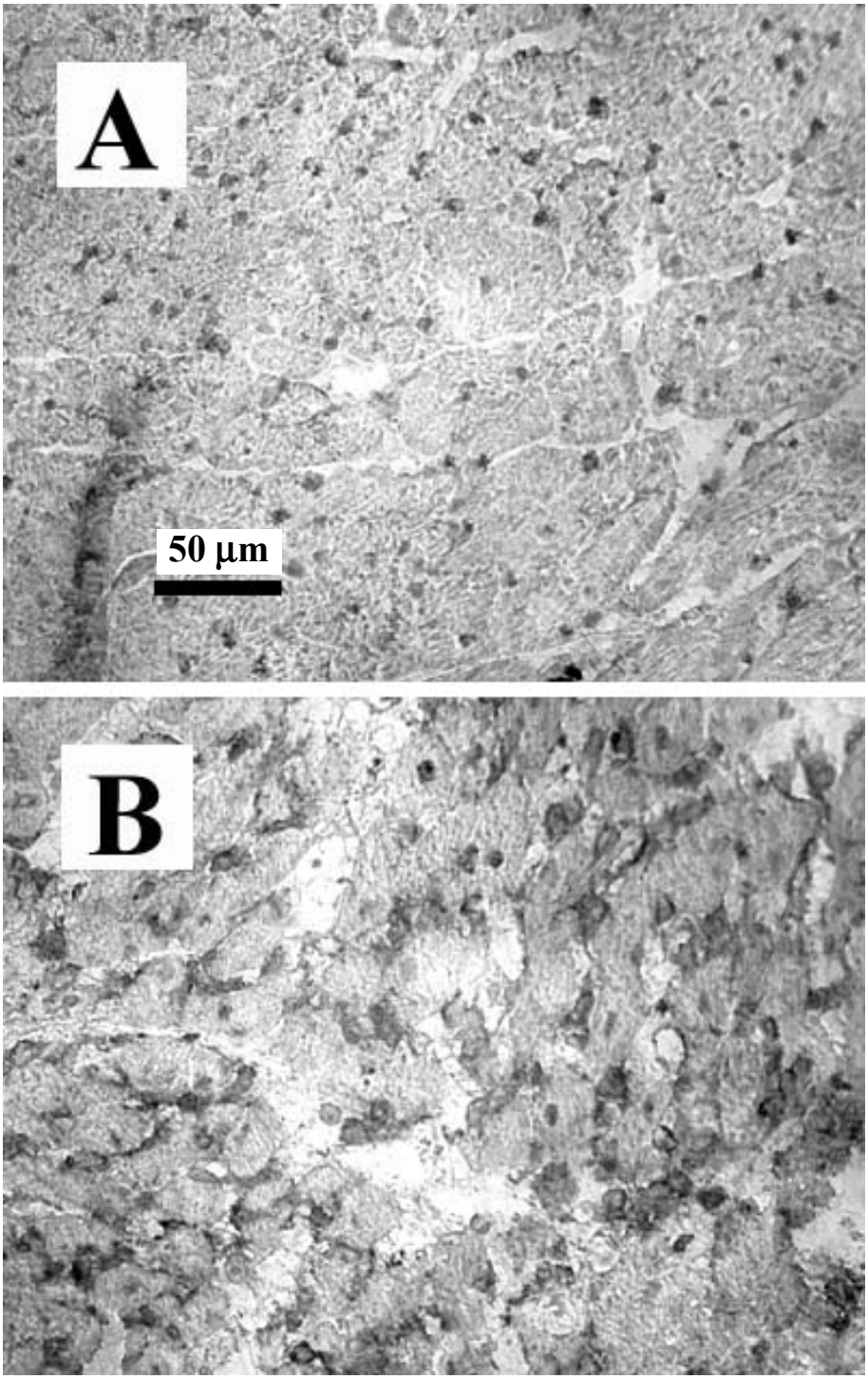

Figure 2-4 Immunohistochemical ICAM-1 staining of normal (panel A) and acutely rejecting (panel B) rat myocardium. ICAM-1 is stained reddish-brown. The normal tissue showed only a small amount of constitutively expressed vascular ICAM-1, whereas the rejecting tissue showed dramatic upregulation of endothelial ICAM-1 expression in the microcirculation. The color version of this figure is shown in Appendix K-5.

2.4 Discussion

An important step in the development of our acoustic agent targeted to endothelial dysfunction is to learn whether our target molecule is differentially expressed by the microcirculatory endothelium of diseased versus normal tissue. This knowledge is useful because such a targeted contrast imaging technique is based on the premise that the presence and/or severity of the disease process correlates with endothelial target expression. Since contrast-enhanced ultrasound images predominantly the microcirculation, it is the smallest blood vessels that are of most interest here.

The data from human specimens failed to demonstrate any difference in ICAM-1 expression between normal myocardial tissue and diseased tissue presumably experiencing endothelial dysfunction. All human cardiac samples stained equally positively for ICAM-1 and E-selectin in both microcirculatory vessels as well as larger vessels. Thus, our hypothesis that the ischemic myocardial vasculature expresses upregulated levels of LAMs was not validated. A major limitation of this study that may be influencing the results is that all of the normal tissue samples (as well as the NDRI ischemically-diseased samples) were acquired during autopsy, between 6 and 10 hours post-mortem. During this time, myocardial endothelial cells may have upregulated adhesion molecule expression in response to local tissue necrosis. Such a phenomenon may account for the observed intense LAM staining even in normal specimens.

The rabbit studies demonstrated that inflammatory myocardium upregulates the expression of endothelial ICAM-1. All specimens displayed ICAM-1 on larger vessels, but only the LPS-stimulated model of inflammation expressed ICAM-1 in the microcirculation. Based of these data, inflammatory tissue can be distinguished from normal tissue by the presence of

capillary ICAM-1 expression, indicating that this may be a suitable animal model for *in vivo* tests of targeted contrast-enhanced ultrasound.

Rat heterotopic cardiac transplantation is a useful model because the rejection status of the donor heart can be predicted based on the donor and recipient strains. Heterostrain allografts produce fulminant acute rejection within a few days, whereas homostrain isografts remain predominantly healthy. Five days after surgery, the isograft myocardial tissue specimens showed only minimal ICAM-1 expression, whereas the acute rejection of the allografts manifested as strongly upregulated microcirculatory endothelial ICAM-1 expression, which agrees with previous reports [106, 107]. These data demonstrate that our laboratory has successfully implemented this model of acute transplant rejection, and that it is a suitable model for *in vivo* tests of ICAM-1-targeted contrast-enhanced ultrasound.

3.0 CONTROL OF MICROBUBBLE ANTIBODY DENSITY

3.1 Introduction

Our laboratory has previously shown that ultrasound contrast microbubbles specifically targeted to ICAM-1 via conjugation with anti-ICAM-1 monoclonal antibodies bind preferentially to activated ECs overexpressing ICAM-1 [95]. However, in this proof-of-principle report, in which the antibodies were conjugated to the microbubble shell via covalent amide linkages, the microbubbles were not thoroughly characterized. In particular, the antibody density on the microbubble surface (the number of antibody molecules bound to the lipid shell) was not quantified or controlled. The reported results demonstrating preferential adhesion of the ICAM-1-targeted agent to activated ECs were of immense value in proving the feasibility of such a targeted ultrasound contrast agent, but in the present studies, we endeavored to thoroughly investigate key parameters that may affect targeted microbubble adhesion to dysfunctional endothelium.

The first of these parameters that we chose to study was the antibody surface density. This study was performed in anticipation of subsequent experiments investigating of the effect of antibody density on targeted microbubble adhesion, which would require the ability not only to quantify, but also to control the antibody density. We chose to effect antibody/microbubble conjugation using avidin/biotin bridging. We hypothesized that by varying aspects of the conjugation protocol (in particular, the avidin concentration), we could control the resulting antibody density. Our goals were to quantify the amount of targeting agent on the microbubble

surface, in terms of number of antibodies per MB, determine the maximum antibody density achievable, and demonstrate controlled production of variably-targeted agents, i.e. MBs with differing antibody densities.

3.2 Methods

3.2.1 Microbubble Preparation

Biotinylated, lipid-based, perfluorocarbon-filled microbubbles, referred to as MP1950, were produced by our collaborator Dr. Alexander Klibanov, first at Mallinckrodt, Inc. (St. Louis, MO) and then the University of Virginia [189-191]. The phospholipids phosphatidylcholine and biotinylated phosphatidylethanolamine were dispersed along with the surfactant polyethyleneglycol (PEG) stearate in an organic solvent. The solvent was evaporated and replaced with a saline buffer, and the mixture was sonicated in the presence of decafluorobutane gas. The sonication dispersed the gas in the form of microbubbles within the saline solution. The phoshpholipids and PEG stearate deposited on the gas microbubble surface, thus forming lipid shells encapsulating perfluorobutane and carrying the biotin label. The microbubble synthesis protocol is detailed in Appendix F. Microbubble diameter as measured by electrozone sensing (Multisizer-II, Beckman-Coulter) was 3.4 ± 1.2 μm. Sample particle size distribution data (Coulter counter data) from a representative batch of microbubbles is shown in Figure 3-1. These biotin-carrying lipid microbubbles, which are stable in solution at 4º C for a few months, were sent to our laboratory at the University of Pittsburgh for conjugation with the targeting molecule and adhesion experiments.

Antibody conjugation to the shell was effected via multi-step avidin-biotin bridging chemistry. First, samples of biotinylated microbubbles were washed twice by centrifugation (100 x g for 2 min) to remove unbound lipid from the solution. Second, the microbubbles were incubated in a solution of streptavidin (Molecular Probes, Eugene, OR) in phosphate-buffered saline (PBS, Sigma, St. Louis, MO). Unbound streptavidin was removed by washing as above. Third, the microbubbles were incubated in a solution of biotinylated monoclonal antibody (100 μg/mL) in PBS, and washed again. Thus, the antibody was conjugated to the lipid shell via a biotin-streptavidin-biotin link, as shown in Figure 3-2. The antibody used was a mouse anti-human-ICAM-1 monoclonal IgG (clone RR1/1, Chemicon, Temecula, CA). The final antibody densities on the microbubble shells were controlled by varying the concentration of the streptavidin solution between 0.1 and 10 μg/mL, and using the same saturating concentration of biotinylated antibody for all preparations.

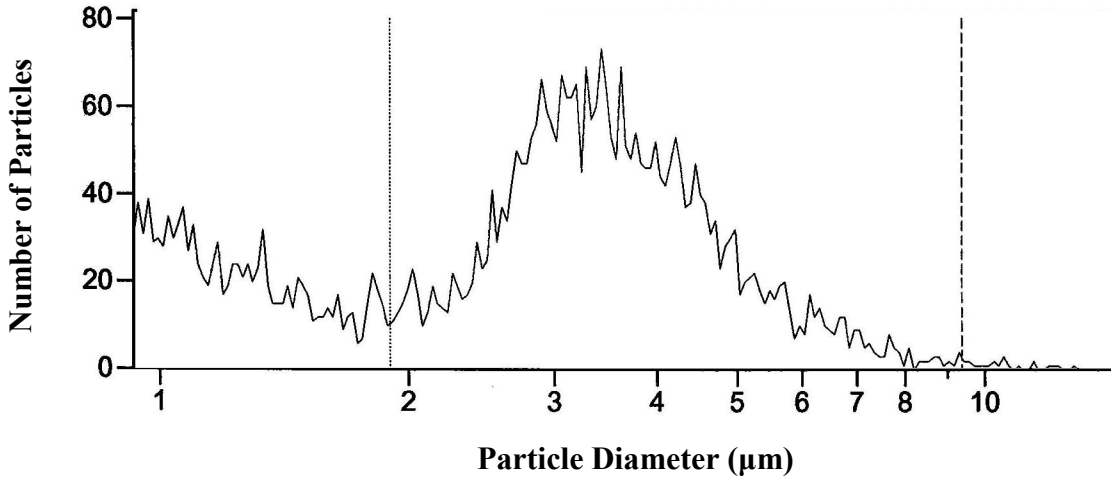

Figure 3-1 Sample particle size distribution data for a representative batch of lipid microbubbles. Mean microbubble diameter was 3.4 ± 1.2 μm.

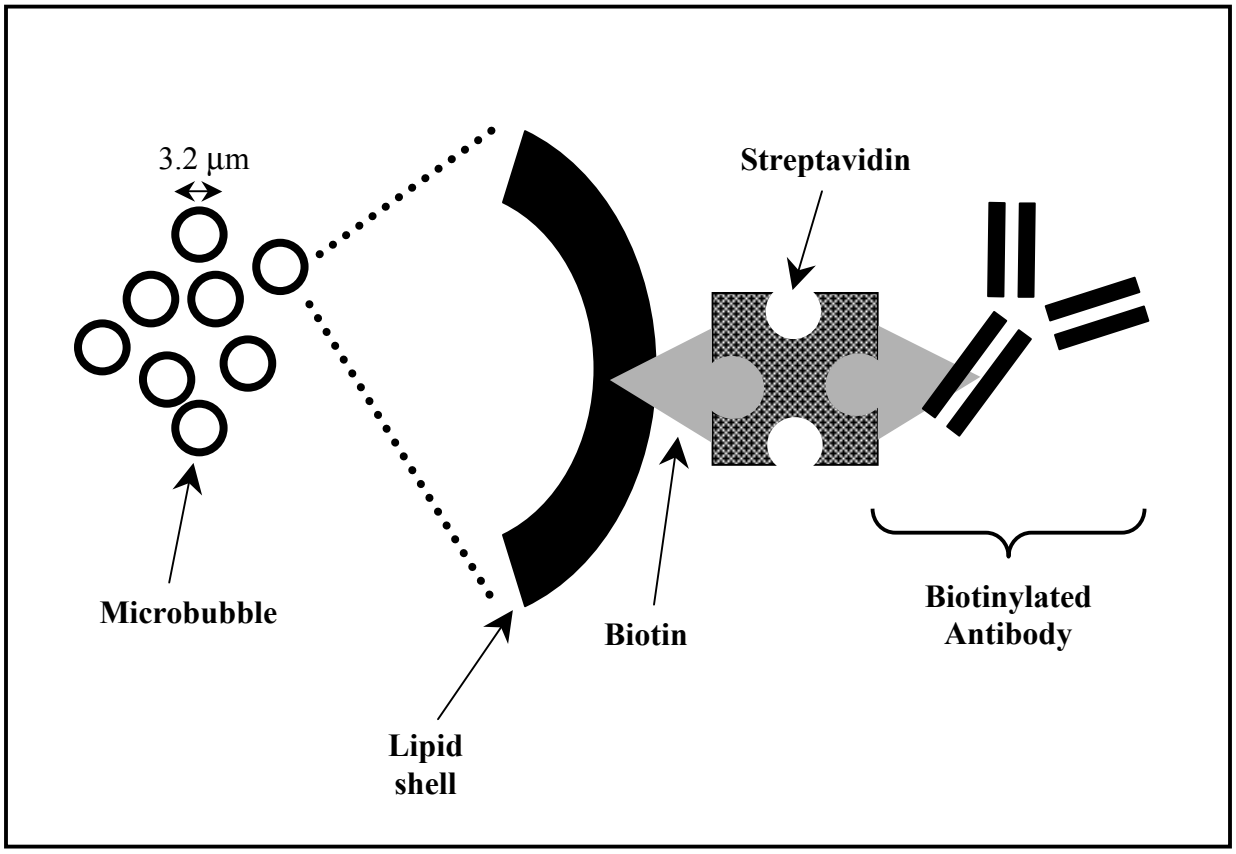

Figure 3-2 Schematic of antibody conjugation to microbubbles, using avidin/biotin bridging. (Not to scale).

3.2.2 Streptavidin and Antibody Quantification

Quantitative flow cytometry was used to measure the streptavidin and antibody densities on the microbubble shell. To quantify streptavidin coverage, microbubbles were linked to streptavidin as above except with the substitution of phycoerythrin (PE)-labeled streptavidin (BD Pharmingen, San Diego, CA). Variable concentrations of PE-streptavidin were used, between

0.1 and 10 μg/mL. Samples of these microbubbles (n=28) in PBS were analyzed for fluorescence (FACScan, Becton-Dickinson, Franklin Lakes, NJ) with 10,000 events per sample and compared to fluorescent standard beads with a known amount of fluorescent molecules on their surface (Quantum R-PE, Bangs Labs, Fishers, IN).

To quantify antibody coverage, microbubbles were linked to unlabeled streptavidin followed by PE-labeled anti-ICAM-1 antibody. Antibodies with both biotin and fluorescent tags were not commercially available, so the biotinylated anti-ICAM-1 antibody used above was conjugated to PE using the PhycoLink kit from Prozyme, Inc (San Leandro, CA). The detailed protocol is given in Appendix H. In brief, the antibody was first centrifuged through an ultrafilter to increase its concentration. The antibody was then reduced using dithiothreitol (from the kit), exposing free sulfhydryls on the antibody. The kit included R-PE previously activated with succinimidyl 4-[N-maleimidomethyl]-cyclohexane-1-carboxylate (SMCC) to introduce maleimide groups. This activated R-PE was incubated with the reduced antibody, allowing the maleimide groups and free sulfhydryl to react, thus covalently conjugating the R-PE to the antibody. The resulting conjugate was then exchanged into storage buffer. As with the streptavidin quantification above, samples of microbubbles (n=24) were analyzed with a flow cytometer and compared to fluorescent standard beads with a known amount of fluorescent molecules on their surface.

3.2.3 Statistics

Results are expressed as mean ± standard deviation.

3.3 Results

Flow cytometric data from samples of microbubbles incubated in various concentrations of PE-labeled streptavidin are shown in Figure 3-3. Measured streptavidin surface density on the microbubbles is expressed on a log scale as the number of streptavidin molecules per microbubble, and varied in a sigmoidal manner over a range of about 4 magnitudes, from 50 to 170,000 molecules per microbubble.

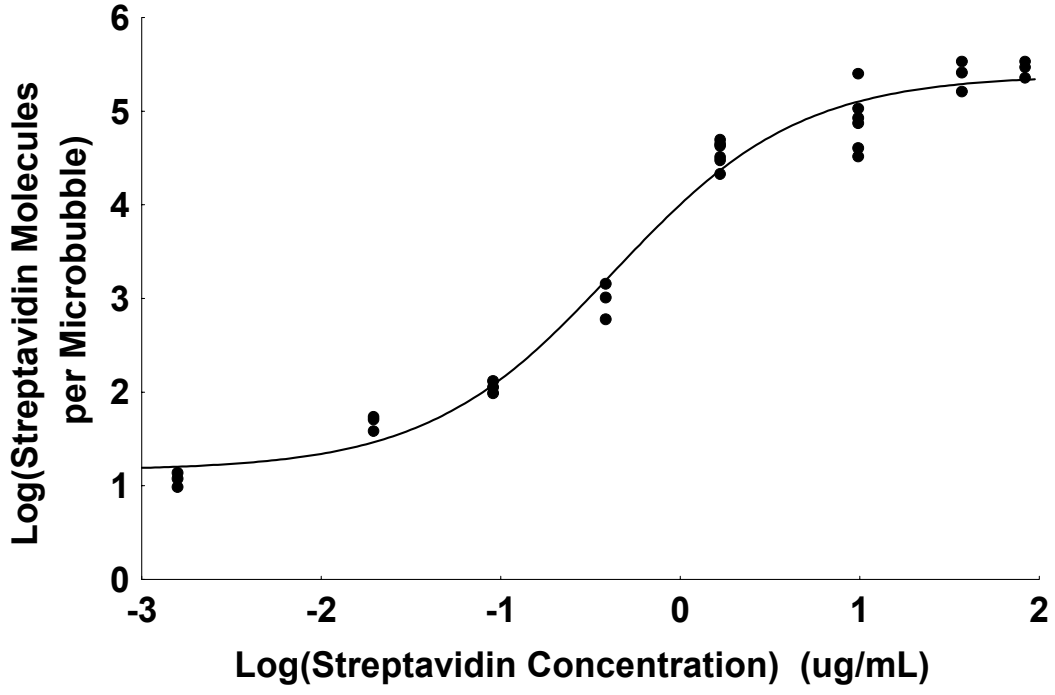

Figure 3-3 Streptavidin density on the microbubble surface (y-axis) as measured by quantitative flow cytometry vs. streptavidin concentration (x-axis). Biotinylated microbubbles were incubated with various concentrations of PE-labeled streptavidin (0.001 – 100 μg/mL). Microbubble streptavidin density varied sigmoidally over a range of about 4 magnitudes, from 50 to 170,000 molecules per microbubble.

Figure 3-4 shows resulting antibody densities from microbubbles incubated in various concentrations of streptavidin (0.1 – 10 μg/mL, indicated as a percentage, with 100% corresponding to 10 μg/mL), followed by incubation in a constant 1:10 dilution of PE-labeled, biotinylated anti-ICAM-1 antibody. Measured antibody surface density is expressed as number of antibodies per microbubble, and ranged from 60,000 antibodies per microbubble on the maximally-targeted 100% microbubbles, to 700 antibodies per microbubble on the 1% microbubbles. Standard deviations of antibody density for each species of microbubble were between 5 and 11% of the mean. Two additional data points (not shown in the Figure) were incubated at 200% and 1000% streptavidin, and also resulted in approximately 60,000 antibodies per microbubble, suggesting that antibody density is saturated at 100%.

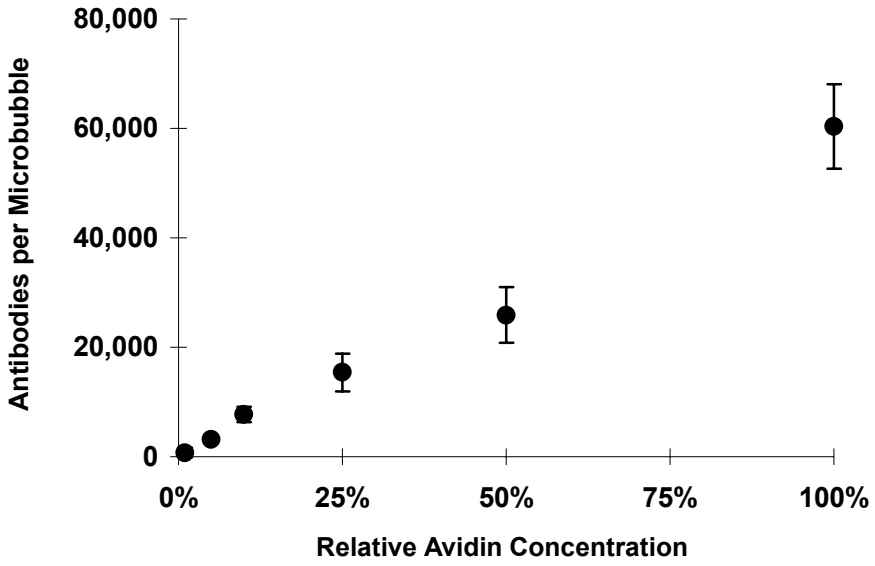

Figure 3-4 Antibody density on the microbubble surface (y-axis) as measured by quantitative flow cytometry vs. streptavidin concentration (x-axis). Biotinylated microbubbles were exposed to various concentrations of streptavidin (0.1 – 10 μg/mL, indicated as a percentage, with 100% corresponding to 10 μg/mL) followed by PE-labeled, biotinylated anti-ICAM-1 monoclonal antibody. Maximum surface antibody density was 60,000 ± 5,000 antibodies per microbubble. (Mean ± SD).

3.4 Discussion

The main findings of this study were that the maximum microbubble antibody density achievable using our avidin/biotin bridging protocol was 60,000 Ab/MB, and that microbubbles with differing antibody densities could be produced, in the range between 700 and 60,000 Ab/MB.

Avidin/biotin chemistry was chosen to link the biotinylated MBs with biotinylated antibodies due to the extremely equilibrium high association constant of avidin-biotin binding, approximately 10^{15} M^{-1} [192, 193]. While biotin has only one binding site for avidin, avidin has four binding sites for biotin, allowing it to serve as a bridge between biotinylated entities [194]. This pair has the strongest known non-covalent, biologic binding interaction [195]. Formation of the avidin/biotin bond is extremely quick, and is highly resistant to many physiochemical factors, including organic solvents, extremes of temperature, and pH variations [195]. The extremely low dissociation rate of such binding approximates covalent binding. Additionally, biotinylated phospholipids as well as numerous biotinylated antibodies are commercially available. A potential problem with natural avidin is that its glycoprotein composition has been shown to cause some non-specific cellular binding [195, 196]. Streptavidin, a bacterial analog of avidin obtained from Streptomyces avidinii, was chosen for our protocol because it generally has lower non-specific binding than regular avidin, due to its non-glycosylated nature. Streptavidin is known to contain the sequence arginine-tyrosine-aspartate (RYD), an analog of a well-characterized binding motif found in fibronectin, which can also cause some non-specific adhesion [197]. However, studies presented in Chapter 4 will demonstrate that this potential confounder does not result in non-specific targeted microbubble binding. The biotin-binding site is buried more deeply within streptavidin than within natural avidin, and the equilibrium

association constant for streptavidin is slightly lower than that for natural avidin, at about 10^{14} M^{-1} [198].

To control the final antibody density, the protocol could have been modified at either of two steps. Either the concentration of the streptavidin incubation solution could have been adjusted (leaving constant the concentration of the antibody incubation solution), or the concentration of the antibody incubation solution could have been adjusted (leaving constant the concentration of the streptavidin incubation solution). The former would result in MBs with varied streptavidin densities, that would then be maximally conjugated with a saturating solution of biotinylated antibody. The latter would result in MBs with a maximum number of streptavidin molecules, that would then be only partially occupied with antibody. The former procedure was chosen over the latter primarily because the latter may result in a MB with exposed, unoccupied streptavidins. Since many tissues contain endogenous biotin, such available streptavidins on the MB surface may allow for higher background binding that is not ICAM-dependent.

The multi-step streptavidin/biotin conjugation process utilized to link the targeting antibody to the microbubble shell allows for production quality control. By varying the concentration of the streptavidin solution to which biotinylated microbubbles were exposed, and then keeping the concentration of biotinylated antibody constant, the final antibody surface density on the microbubbles could be controlled. We were able to produce microbubbles with different antibody densities ranging from 700 antibodies per microbubble (1% of maximum antibody coverage) to a maximum of 60,000 antibodies per microbubble (100%).

Many other reports describing ultrasound contrast agents targeted to various molecular markers of disease have not quantified the density of the targeting molecule on the contrast agent surface [87, 90, 95, 96, 191]. It is reasonable to expect that as the density of the targeting

molecule on the microbubble surface increases, the adhesion of that microbubble to its target would increase as well. Another possibility, however, is that adhesion would increase with increase antibody density only up to a point at which steric hindrance between the tightly-packed antibodies actually leads to decreased antigen binding and thus decreased adhesion. In either case, it would be prudent to quantify the targeting molecule density. To gain greater insight into the effect of antibody density on MB adhesion, it was necessary to first produce MBs with varying antibody densities, allowing us to proceed to the adhesion experiments.

4.0 EFFECT OF ANTIBODY DENSITY ON TARGETED MICROBUBBLE ADHESION

4.1 Introduction

As discussed in Chapter 3, one parameter of key importance that has often been overlooked is the density of the targeting molecule on the particle (microbubble, microsphere, liposome, etc.) surface. In the previous chapter, we demonstrated that the antibody density could be controlled by modulating the reagent concentrations during the antibody conjugation process. In the work presented in this chapter, we endeavored to investigate the effect of antibody density on targeted microbubble adhesion to dysfunctional endothelium.

Achieving control over the binding characteristics of the microbubbles is a critical step towards optimizing the design of a targeted ultrasound contrast agent capable of function-specific imaging of the endothelium. We hypothesized that modulation of the antibody density would permit regulation of microbubble adhesion to endothelium. Our goal was to quantify the adhesion of ICAM-1-targeted microbubbles with varied surface antibody densities, to both normal and inflammatory cultured ECs. Accordingly, our hypothesis was tested using a parallel plate perfusion chamber in which various species of targeted microbubbles were perfused across cultured human coronary artery ECs to quantify their adhesion.

4.2 Methods

4.2.1 Microbubble Preparation

Lipid-based, perfluorocarbon-filled microbubbles (MP1950) were conjugated to monoclonal antibody on the shell as the ligand for endothelial adhesion. Antibody conjugation to the shell was effected via multi-step avidin-biotin bridging chemistry, as described in Chapter 3. Briefly, biotinylated MBs were washed by centrifugation to remove unbound lipid, incubated in a solution of streptavidin, washed to remove unbound streptavidin, incubated in a solution of biotinylated monoclonal antibody, and washed again. Thus the antibody was conjugated to the lipid shell via a biotin-streptavidin-biotin link. The final antibody densities on the microbubble shells were controlled by varying the concentration of the streptavidin solution between 0.1 and 10 μg/mL.

Three different microbubble species were prepared, containing either mouse anti-human-ICAM-1 IgG monoclonal antibody (clone RR1/1, Chemicon, Temecula, CA), nonspecific mouse IgG antibody (Caltag, Burlingame, CA) as a negative control, or nothing (bare microbubbles) on the shell as an additional negative control. Among the anti-ICAM-1 microbubbles, six different levels of antibody surface density were investigated: 1%, 5%, 10%, 50%, 75%, and 100% of maximum antibody coverage.

Flow cytometry was used to quantify the antibody densities on the microbubble shells as described in Section 3.2.2.

4.2.2 Cell Culture

Human coronary artery ECs (Cambrex Corp., East Rutherford, NJ) were grown to confluency on 25 mm x 75 mm glass coverslips in endothelial basal medium (Cambrex Corp.) with 5% fetal bovine serum. Only second through fifth passage cells were used (subculturing procedure presented in Appendix C). Selected coverslips of ECs were made inflammatory by activation with 100 U/mL human recombinant interleukin-1β (IL-1β) (Pierce Endogen, Rockford, IL), which is known to upregulate ICAM-1 endothelial expression [48], for 5 hours immediately prior to the experiment.

4.2.3 Quantification of ICAM-1 Expression

Flow cytometry was used to quantify ICAM-1 expression on the EC surface (n = 6 per condition). Endothelial cell monolayers were lifted into solution by treatment with trypsin and EDTA, and washed by centrifugation in PBS. The ECs were diluted slightly in PBS and incubated with biotinylated anti-human-ICAM-1 monoclonal IgG antibody (the same clone as used on the microbubbles) or biotinylated nonspecific IgG antibody at 1:24 dilution for 30 min. The cells were then washed with PBS, and incubated with a 1:20 dilution of PE-labeled streptavidin (BD Pharmingen, San Diego, CA) for 20 min. The cells were washed, fixed in 1% paraformaldehyde (reagent preparation described in Appendix A) in PBS, and analyzed for fluorescence on the flow cytometer. ICAM-1 density was calculated by comparing the fluorescence signal due to binding of the anti-ICAM-1 antibody to ECs with the signal due to binding of the same antibody to Quantum Simply Cellular standard beads (Bangs Labs, Fishers, IN) [199-201]. These goat-anti-mouse IgG-coated beads have calibrated surface binding capacities for mouse-derived IgG, and provide a linear calibration plot for number of binding

sites versus fluorescence intensity, allowing measurement of the number of ICAM-1 sites on normal and interleukin-activated ECs.

4.2.4 Parallel Perfusion Apparatus

A rectangular parallel plate perfusion chamber was used to examine adhesion of microbubbles to cultured ECs [202, 203]. Figure 4-1 shows a diagram of this perfusion chamber, which comprises a transparent polymethylmethacrylate (PMMA) block, a silastic rubber gasket, and a standard 25 mm x 75 mm glass coverslip. A groove measuring 3.5 cm in length x 0.75 cm in width x 200 μm in depth was cut into the PMMA block as a flow path for perfusate, as seen in Figure 4-1. Inlet and outlet ports were drilled through the PMMA block to either end of the flow path, beginning as cylindrical tubes and widening to entrance and exit slits almost the width of the perfusion groove (about 1 cm). The distal ends of the inlet and outlet ports were adapted to Luer locks, and connected to Tygon® tubing. The coverslip (with confluent monolayer of ECs) was mounted over the groove with the cells facing the inside, such that a 200 μm high gap was formed over the ECs. The coverslip was secured with the silastic gasket and vacuum system, and forms one wall of a closed system in which solutions of MBs in culture medium (M-199, Sigma, St. Louis, MO) were perfused through the 200-μm-high gap across the EC monolayer. The exit port was connected to a nonpulsatile syringe pump (Harvard Apparatus, Holliston, MA) in withdrawal mode. Photographs of the parallel plate perfusion apparatus are shown in Figure 4-2.

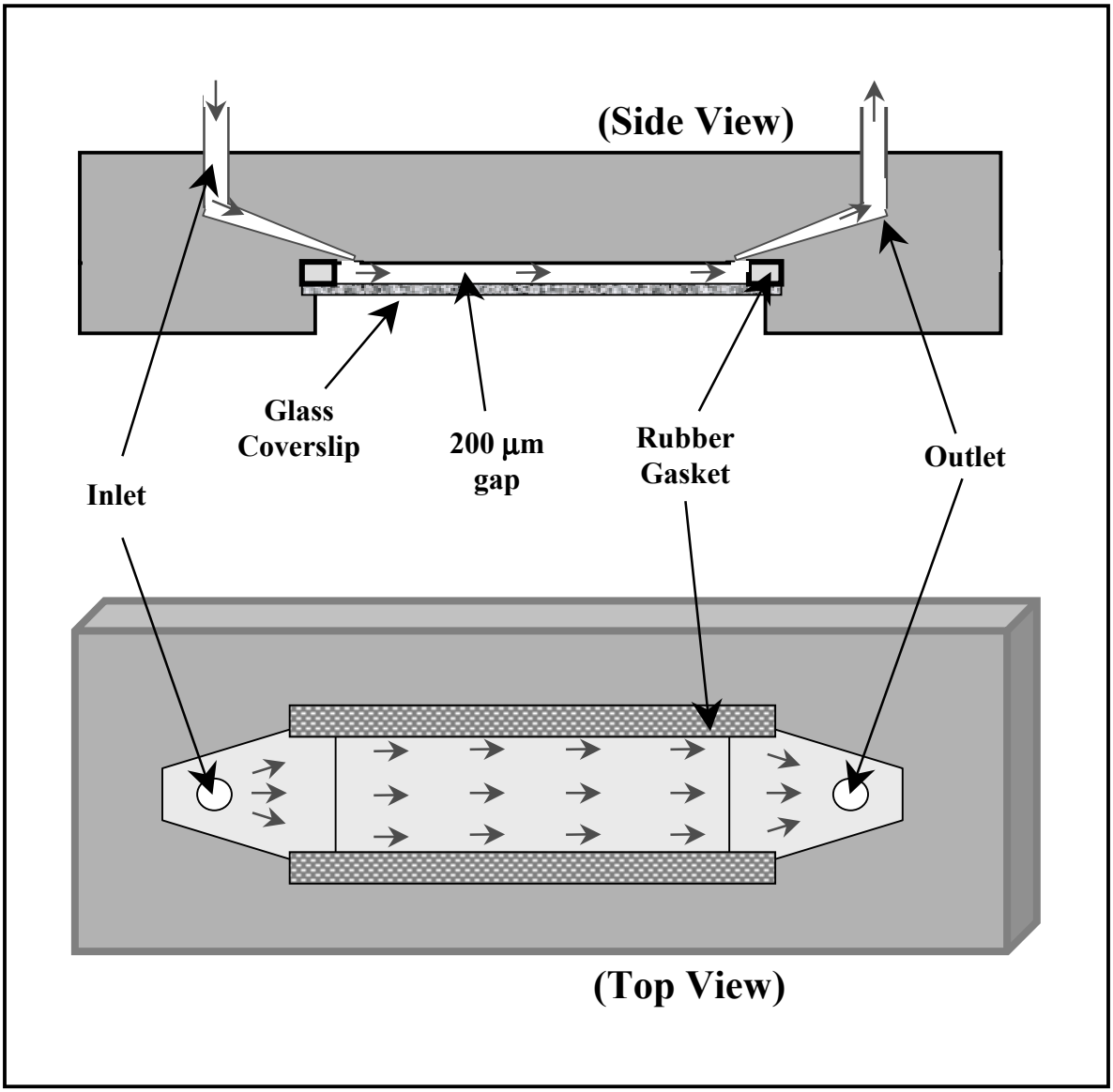

Figure 4-1 Schematic of the parallel plate perfusion chamber. A solution of microbubbles is perfused under controllable shear conditions across a monolayer of cultured endothelial cells grown on a coverslip. Wall shear rate is uniform over the experimental surface. (Not to scale).

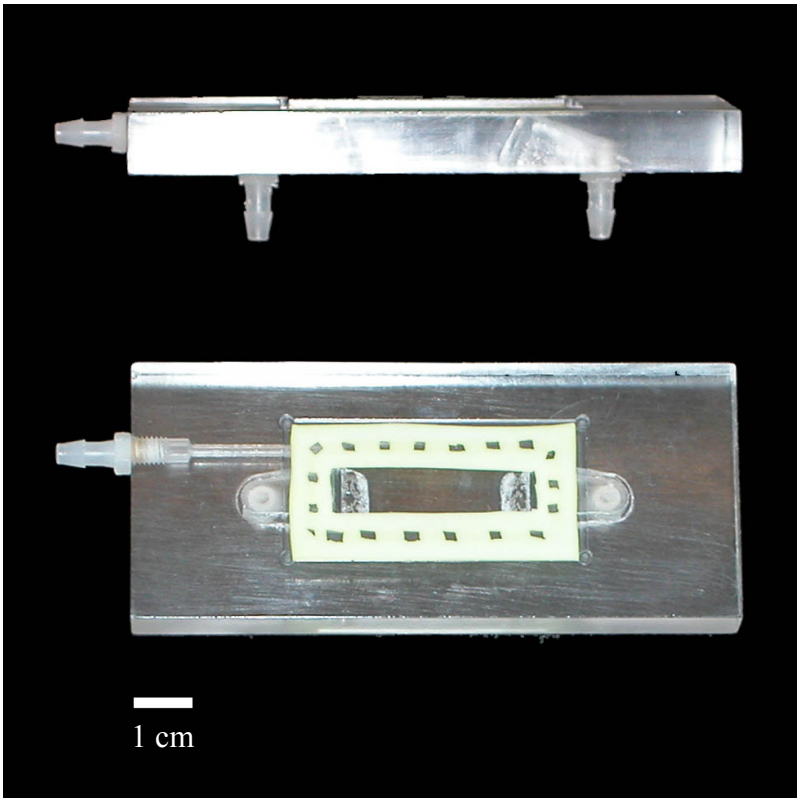

Figure 4-2 Parallel perfusion chamber, side view and top view.

4.2.4.1 Fluid Dynamical Analysis. Under laminar flow conditions, flow through the chamber is well-characterized, with a uniform wall shear rate for the length of the perfusion gap. The wall shear rate can be calculated based on the Navier-Stokes equation, with the volumetric flow rate as the key adjustable parameter. A more detailed derivation is presented in Appendix D.

Briefly, assuming that the culture medium perfusate acts in a Newtonian manner, is an incompressible fluid, and has a constant viscosity, the Navier-Stokes equation (Equation 4-1) can be employed:

Equation 4-1 Navier-Stokes equation

$$\rho[\frac{\partial \bar{V}}{\partial t} + (\bar{V} \bullet \nabla)\bar{V}] = -\nabla P + \mu \nabla^2 \bar{V} + \rho \bar{g}$$

where ρ is density, V is velocity, t is time, P is pressure, g is gravity, μ is viscosity, and ∇ is the gradient operator.

Flow is treated as being between infinitely wide flat plates, such that flow velocity in the x-direction is a function only of y, where x is in the direction of flow, y varies along the gap between the PMMA surface and the coverslip, z is in the direction of channel width.

Assuming steady flow (no unsteady acceleration) and low Reynolds number (no convective acceleration), and neglecting the effects of gravity, the Navier-Stokes equation (Equation 4-1) reduces to its x-component, and since the velocities in the y and z directions are zero, and V_x does not vary with z, the following in obtained:

Equation 4-2

$$0 = \frac{-\partial P}{\partial x} + \mu \frac{\partial^2 V_x}{\partial y^2}$$

Treating V_x as a function of y, and evaluating using no-slip boundary conditions at the walls ($V_x = 0$ at y = 0 and h, where h is the gap height of 200 μm) results in:

Equation 4-3

$$V_x = \frac{1}{2\mu}\frac{\partial P}{\partial x}(y^2 - hy)$$

Volumetric flow rate is defined in rectangular coordinates as the double integral of the x-direction velocity with respect to y and z, so by integrating over the gap (y = 0 to h), we get an expression for volumetric flow rate:

Equation 4-4

$$Q = \frac{w}{2\mu}\frac{\partial P}{\partial x}\frac{h^3}{6}$$

Combining Equation 4-3 and Equation 4-4 gives an expression for the perfusate velocity in the x direction:

Equation 4-5

$$V_x = \frac{6Q}{wh^3}(hy - y^2)$$

We are most interested in the shear component acting on the y-surface (the coverslip) in the x-direction, so we start with the shear stress τ_{yx} (under laminar flow conditions) given by Newton's law of viscosity as viscosity times the partial derivative of V_x with respect to y. Differentiating Equation 4-5 with respect to y, evaluating at the coverslip surface (y=0), and translating into shear rate (shear rate = shear stress / viscosity) gives the shear rate equation for the parallel flow chamber:

Equation 4-6 Wall shear rate equation for the parallel perfusion chamber

$$\overset{\circ}{\gamma} = \frac{6Q}{wh^2}$$

Equation 4-6 gives the wall shear rate as a function of volumetric flow rate Q, gap height h, and chamber width w. Thus, at a given flow rate, the wall shear rate is constant over the experimental surface of the coverslip, and can be easily calculated.

4.2.5 Microbubble Perfusion

Coverslips of ECs (n = 42) were briefly incubated with quinacrine dihydrochloride (Sigma, St. Louis, MO) or alexa phalloidin (Molecular Probes) as a fluorescent label and

mounted in the perfusion chamber. The vacuum seal was applied, and the chamber was primed with 37°C culture medium. A solution of microbubbles (10^6 MBs/mL, 0.2 mL volume) in culture medium was injected into the chamber and dwelled statically for 3 min. Because of the natural buoyancy of the microbubbles, the chamber was oriented with the ECs forming the roof of the chamber, to maximize microbubble exposure to cells. To wash away unbound microbubbles, the chamber was perfused for an additional 3 min with bubble-free culture medium at a flow rate corresponding to 100 s^{-1} wall shear rate. Each coverslip of ECs was either normal or IL-1β-activated, and was perfused with a single microbubble species.

Following perfusions, the chamber was mounted on an inverted epifluorescent microscope (Axiovert 35, Zeiss, Thornwood, NY), and microscopic brightfield images at 1000X were recorded digitally via a CCD camera (CCD-1300-Y, Princeton Instruments, Monmouth Junction, NJ) and imaging software (IPLab, Scanalytics Inc., Fairfax, VA). The number of cells and adherent MBs was quantified for each image, and averaged over the 20 fields to results in a single measure (mean adhered MBs/EC) per coverslip.

4.2.6 Statistics

Results are expressed as mean ± standard deviation. Data were analyzed with factorial ANOVA with two levels of cell activation (activated versus normal) in the first factor and 6 levels of microbubble antibody density (1%, 5%, 10%, 50%, 75%, 100%) in the second factor. Covariates taken into account include microbubble batch and EC passage number. When significant differences were found, post-hoc comparisons were made using Tukey's test. Statistical significance was defined as $p<0.05$.

4.2.7 Mathematical Adhesion Modeling

Adhesion of the targeted MBs to the endothelial surface can be mathematically modeled as receptor-mediated adhesion of spherical particles to a ligand-bearing substrate. Specifically, experimental results will be interpreted in terms of a model consisting of a solid sphere with multiple receptors on the surface, suspended in a shear flow field, and binding to a surface with multiple ligands. Particle adherence requires that the total adhesive force must balance the hydrodynamic force and torque imposed on that particle, as seen in Figure 4-3.

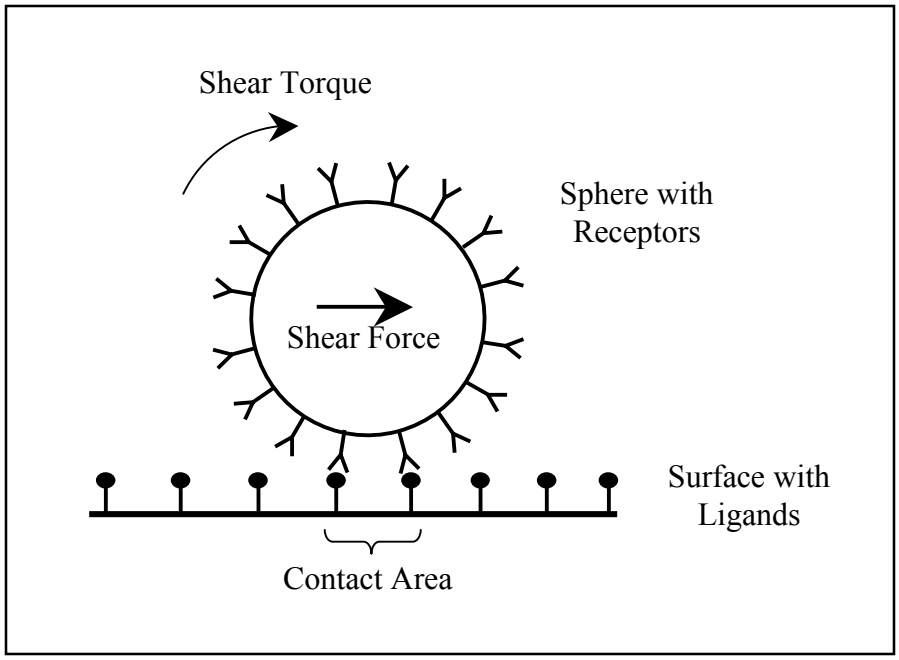

Figure 4-3 Hydrodynamic forces acting on a surface-adherent particle. Modified from [204].

Based on equations by Goldman *et al* [205], describing the hydrodynamic forces acting on a stationary sphere, and Hammer *et al* [206], describing receptor-mediated cell adhesion, Cozens-Roberts *et al* [204] developed an expression (Equation 4-15) for the fluid force acting on a sphere adhering to a planar surface.

Briefly, beginning with an expression from Hammer *et al* [206] for the total fluid force acting on an adherent sphere:

Equation 4-7

$$F_T = \{F_s^2 + (9\pi^2/16a^2)[Tq^2 + 2TqF_s\rho_B + (F_s\rho_B)^2]\}^{1/2}$$

(where F_T is the total fluid force, F_s is the shear force acting on the sphere, a is the radius of the contact area between the surface and the adherent sphere, Tq is the torque acting on the sphere, and ρ_B is the sphere radius), Cozens-Roberts *et al* [204] combine Equation 4-7 with two expressions by Goldman *et al* [205] that show that the fluid force (F_s) and torque (Tq) exerted on the adherent sphere are linearly proportional to the wall shear stress:

Equation 4-8 Fluid force exerted on adherent sphere

$$F_s \propto 6\pi S_c\rho_B$$

Equation 4-9 Torque exerted on adherent sphere

$$Tq \propto 4\pi S_c(\rho_B)^3$$

(where S_c is the critical shear stress), to result in an expression describing the total fluid force acting on the adherent sphere:

Equation 4-10 Total fluid force acting on an adherent sphere.

$$F_T \propto S_c \rho_B^3 / a$$

Next, starting with a basic equation describing receptor/ligand bond formation kinetics:

Equation 4-11 Description of bond formation kinetics.

$$(dN_b/dt) = k_f(N_L - N_b)(N_R - N_b) - k_r N_b$$

(where N_b is the bond density, N_L is the ligand density, N_R is the receptor density, k_f is the forward rate constant, and k_r is the reverse rate constant), Bell [207] made a correction to the reverse rate constant to account for the effects of the external shear force on the specific bonds, and described the bond force (F_b) as:

Equation 4-12 Bond force

$$F_b \approx (0.7k_bT/\gamma)\ln(KN_L)$$

(where k_b is Boltzmann's constant, T is temperature, γ is the range of interaction (about 5×10^{-8} cm for antibody/antigen bond), and K is the receptor-ligand affinity constant k_f/k_r).

Cozens-Roberts *et al* [204] next describe the total number of receptor-ligand (antibody/antigen) bonds (C) necessary to balance the hydrodynamic forces, where $C = F_T/F_b$, by combining Equation 4-10 and Equation 4-12 to achieve:

Equation 4-13 Number of required receptor-ligand interactions

$$C \propto (\gamma/k_bT)[S_c/\ln(KN_L)](\rho_B^3/a)$$

Hammer *et al* [206] modified this to develop an expression for the total receptor density needed to balance the hydrodynamic forces:

Equation 4-14 Total receptor density

$$N_R = (\gamma F_T / k_bT)(e / \pi a^2 KN_L)$$

(where e the natural logarithm base).

By substituting Equation 4-10 into Equation 4-14 and rearranging, the following equation describing between the relationship receptor and ligand densities and the maximum shear stress under which the sphere can adhere (S_c) is obtained:

Equation 4-15 Critical shear stress equation

$$S_c \approx \beta N_L N_R$$

where

Equation 4-16

$$\beta = (K/33e)(k_bT/\gamma)(a/\rho_B)^3$$

This equation shows that the critical shear stress S_c, the maximum shear stress under which the sphere can successfully adhere, is proportional to β (which is dependent on the

receptor-ligand affinity, the contact area, and the sphere size), the ligand density, and the receptor density. The critical shear stress can be interpreted as a measure of particle adhesion strength; it represents the balance between the adhesive receptor/ligand interaction forces acting to bind the sphere, and the fluid dynamical forces acting to move the sphere [208].

According to Equation 4-15, varying the antibody density (N_R) on the microbubbles should lead to a linearly proportional change in MB adhesion strength. Changes in the ligand (endothelial ICAM-1) density (N_L) should similarly result in linearly proportional changes in MB adhesion strength.

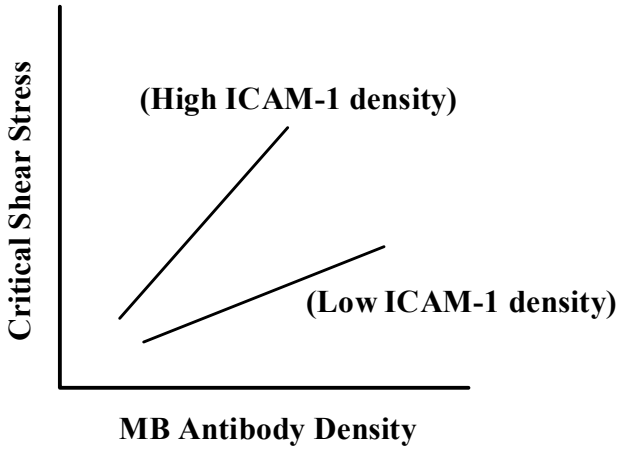

Figure 4-4 Relationship between antibody density and adhesion strength.

In this chapter, the effect of MB antibody density on targeted adhesion to endothelium is being considered. Based on the above model, the relationship between antibody density and critical shear stress should resemble that seen in Figure 4-4, in which the measure of adhesion strength is linearly proportional to MB antibody density. If the ligand density N_L is modified from a low level to a higher level, then the slope of the relationship should increase. In the case of the present study, this entails investigating adhesion at two different ICAM-1 densities, corresponding to two different levels of activation: normal and inflammatory.

4.3 Results

4.3.1 Endothelial ICAM-1 Expression

Sample quantitative flow cytometric measurements of ICAM-1 expression on normal and IL-1β-activated ECs are shown in Figure 4-5. Quantitative results are shown in Figure 4-6. Interleukin activation increased the expression of ICAM-1 approximately 20-fold, from 37,000 ± 3,000 ICAM-1 sites per cell on normal ECs to 760,000 ± 12,000 sites per cell on inflammatory ECs.

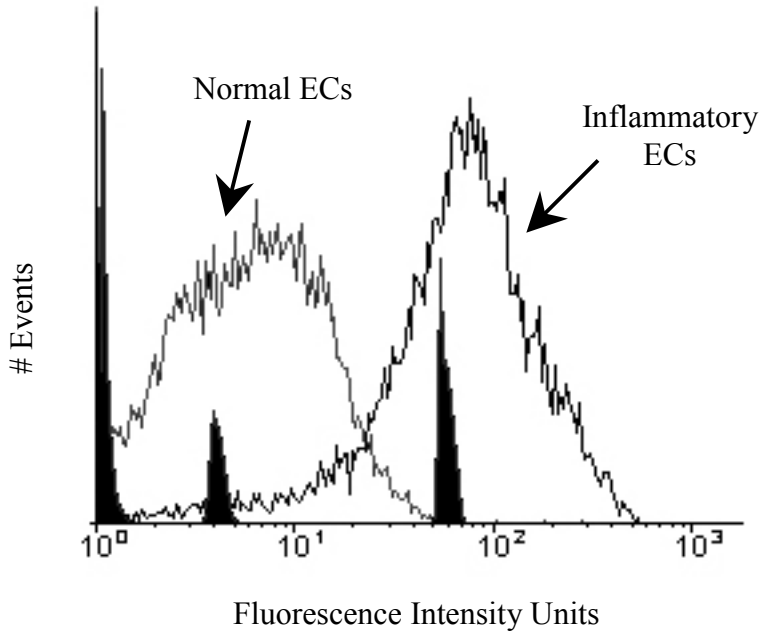

Figure 4-5 Flow cytometry sample data using cultured human coronary artery ECs with fluorescently-labeled ICAM-1. Cells were either normal or inflamed with interleukin. Calibrated standard microsphere peaks (from microspheres with 3 distinct levels of fluorochrome) used for quantitative calculations are shown as black-filled histograms. Inflammatory EC expression of ICAM-1 was approximately 20 times greater than normal ECs.

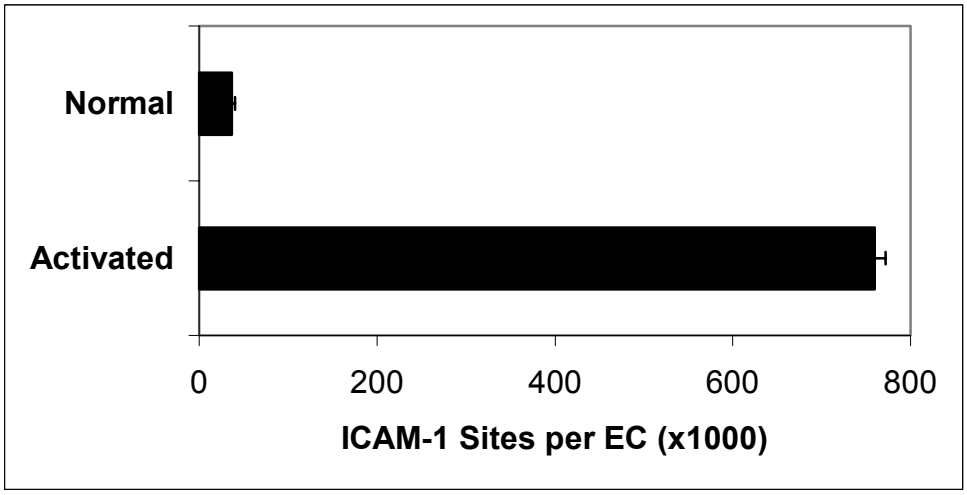

Figure 4-6 Expression of ICAM-1 on normal versus IL-1β-activated ECs, in terms of number of ICAM-1 molecules per cell. Interleukin activation upregulated ICAM-1 approximately 20-fold from constitutive levels. (Mean ± SD).

4.3.2 Endothelial ICAM-1 Expression

Data from coverslips exposed to a static incubation of microbubbles followed by a bubble-free wash at 100 s^{-1} are shown in Figure 4-7. Adhesion is expressed as the number of adhered microbubbles normalized to the number of ECs. Binding of bare microbubbles was minimal to both normal (0.04 ± 0.02 MBs/EC) and activated (0.09 ± 0.07 MBs/EC) endothelium. Similarly, binding of microbubbles containing non-specific IgG was minimal to both normal (0.01 ± 0.00 MBs/EC) and activated (0.05 ± 0.01 MBs/EC) cells. Among the microbubbles targeted to ICAM-1, adhesion increased with increasing antibody density to both normal (1% = 0.12 ± 0.04; 5% = 0.21 ± 0.06; 10% = 0.6 ± 0.2; 50% = 1.4 ± 0.2; 75% = 3.6 ± 1.6; 100% = 4.8 ±

1.8 MBs/EC) and activated ECs (1% = 0.08 ± 0.02; 5% = 0.3 ± 0.2; 10% = 0.9 ± 0.4; 50% = 5.3 ± 1.5; 75% = 7.4 ± 1.7; 100% = 9.2 ± 1.9 MBs/EC). Adherence of ICAM-1-targeted MBs was greater to activated than normal ECs ($p<0.01$), and increased with increasing antibody density ($p<0.01$). There was a significant interaction between microbubble antibody density and EC condition [$F_{(5,34)}=4.15$], with the EC condition effect (ICAM-1 expression effect) becoming stronger as the microbubble antibody density increased. Adhesion was significantly greater to activated than normal ECs within the 100%, 75%, and 50% groups ($p<0.01$ for each). By post-hoc analysis it was determined that a greater number of 100% microbubbles adhered to ECs versus 75%, a greater number of 75% microbubbles versus 50%, and a greater number of 50% microbubbles versus 10%.

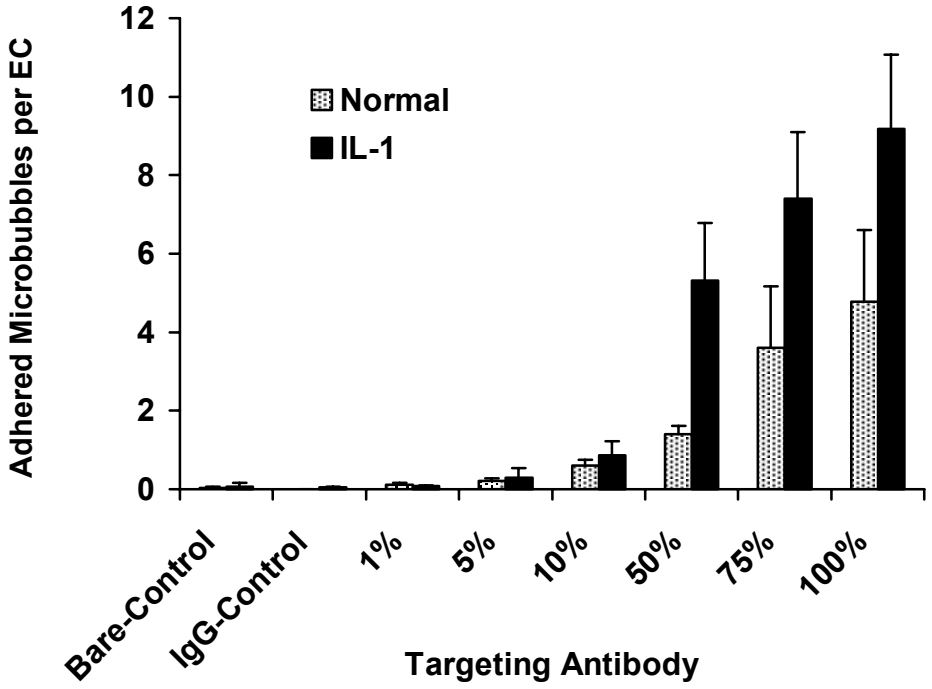

Figure 4-7 *In vitro* adherence of various microbubble species to normal versus inflammatory ECs. Adherence of bare and non-specific IgG microbubbles was minimal. Adherence of ICAM-1-targeted microbubbles increased with increased antibody surface density ($p<0.01$). Adherence of ICAM-1-targeted microbubbles was significantly greater to activated versus normal ECs ($p<0.001$). (Mean ± SD).

ICAM-1-targeted MB adherence as a function of antibody density is shown in Figure 4-8. MB adhesion to both types of cells increased with increasing antibody density. The slope of the linear fit was significantly higher for the inflammatory ECs than for the normal ECs ($p<0.01$).

Brightfield micrographs of coverslips of ECs perfused with the each of the various species of microbubbles are shown in Figure 4-9.

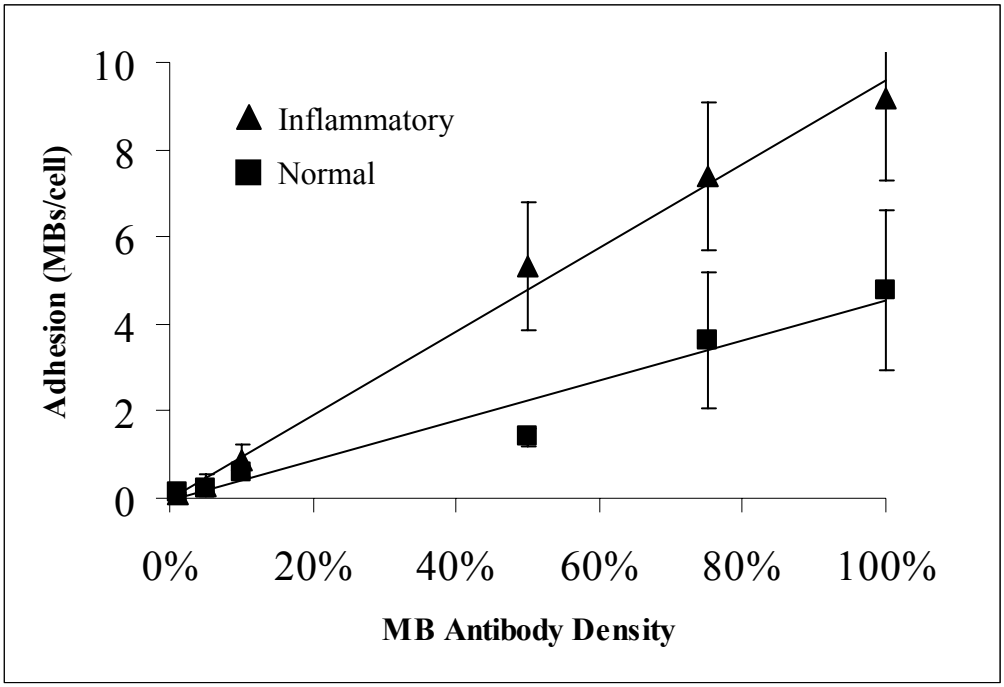

Figure 4-8 *In vitro* adherence of MB_{ICAM} to normal and inflammatory ECs vs. MB antibody density. MB adherence to both cell types increased with increased antibody surface density ($p<0.01$). (Mean ± SD).

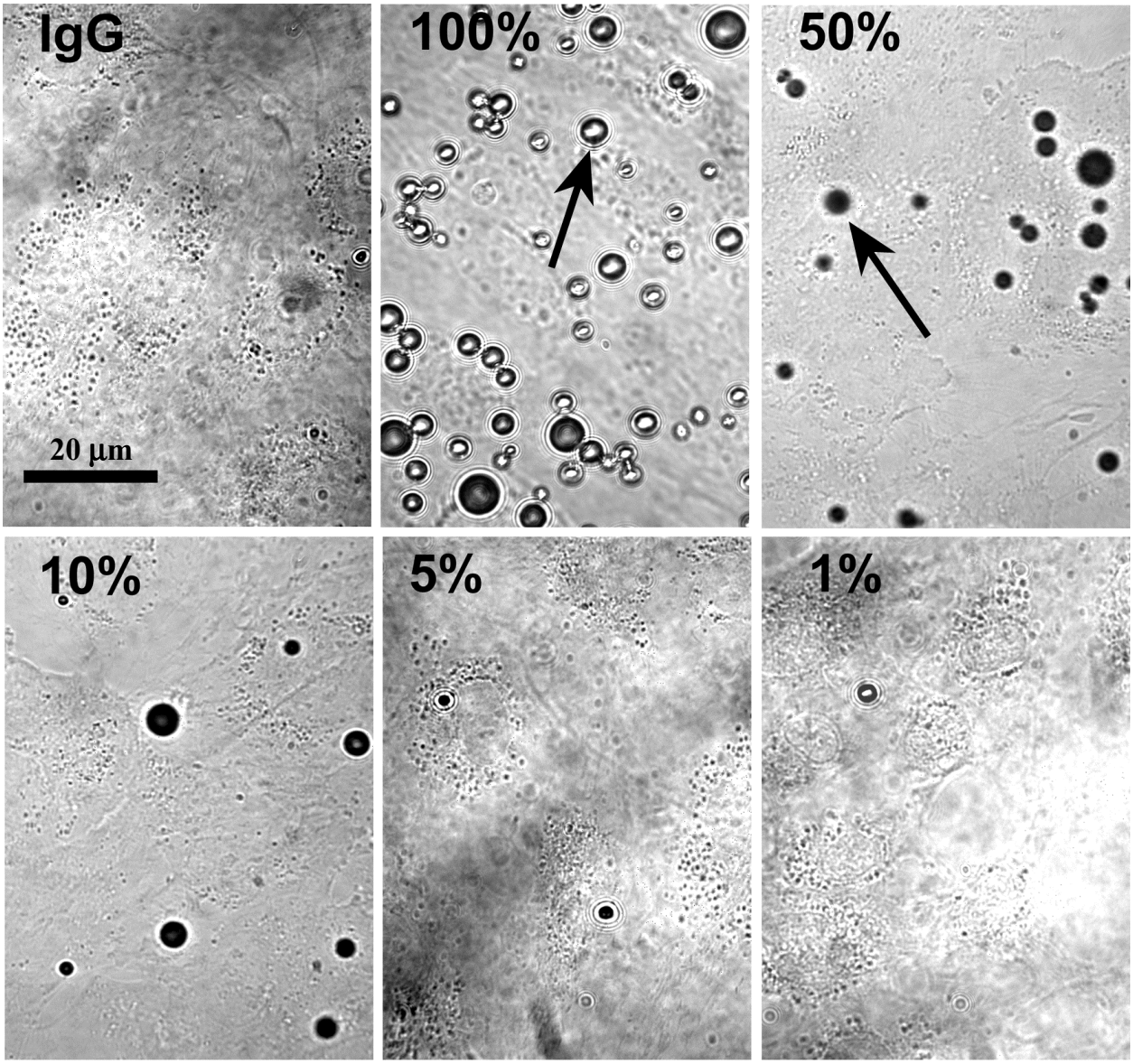

Figure 4-9 Brightfield micrographs of inflammatory ECs following exposure to microbubbles carrying nonspecific IgG, or various densities anti-ICAM-1 antibody. Each image shows approximately 6-8 ECs in the background, and adhered microbubbles (arrows). There was only minimal adherence of nonspecific IgG-containing microbubbles. With the anti-ICAM-MBs, adhesion increases with increasing antibody density.

4.4 Discussion

The main finding of this study was that the adhesion of ICAM-1-targeted MBs is dependent on the MB antibody surface density. This microbubble parameter has been largely overlooked in the targeted imaging literature, and yet our data show that this variable can have an enormous impact on the resulting adhesion characteristics of the agent.

The parallel plate perfusion chamber, in which a uniform shear field is maintained across the entire experimental surface, has been widely utilized to study *in vitro* cellular adhesive events under controlled fluid shear conditions [209]. This device is well-suited for the investigation of adhesive events at the endothelium, and has been employed to study a variety of adhesive phenomena, including the binding interactions of specific leukocyte adhesion molecules [210], the effect of flow on leukocyte adhesion to endothelium [202], and endothelial adhesion of red blood cells [211] and tumor cells [212]. In the current studies, this apparatus was used to evaluate the density of anti-ICAM-1 antibody on the microbubble surface, a key parameter that may modulate targeted microbubble adhesion to dysfunctional endothelium.

Negative control MBs showed minimal adhesion to both cell types. The low adherence of bare microbubbles (with no streptavidin and no antibody on the shell) demonstrates that the lipid shell itself is not responsible for adhesion of the targeted agent. Similarly, the minimal adhesion of microbubbles conjugated to a nonspecific control antibody confirms that unoccupied streptavidin is not responsible for adhesion, and that the adhesion of the ICAM-1-targeted agent is due to the specificity of the antibody/antigen binding interactions.

Microbubble surface antibody density had a significant positive, linear relationship with adhesion to ECs, demonstrating that this parameter should be carefully quantified when

investigating targeted agents. As the antibody density increases towards its maximum, there is the potential for a counter-intuitive decrease in resulting microbubble adherence to endothelial ICAM-1, due to steric hindrance between neighboring antibodies. If the antibodies are packed too closely together on the microbubble shell, they may not have the freedom of movement (molecular range of motion) necessary to allow maximal binding to the endothelial target molecule. However, this phenomenon was not observed in our experiments, as MB adhesion to ECs increased with each step-wise increase in antibody density, and did not reach a plateau or decrease. Nonetheless, this design parameter should be closely monitored when attempting to optimize adhesion of a targeted agent.

Quantitative flow cytometry was used to measure ICAM-1 expression on normal and interleukin-activated ECs. These data established that, first, there is constitutive ICAM-1 expression of 37,000 ICAM-1 sites per cell on resting ECs, and, second, that incubation with IL-1β upregulates this ICAM-1 expression approximately 20-fold to 760,000 sites per cell. These results are on the same order as figures reported for ICAM-1 expression on human umbilical vein ECs (HUVECs): 180,000 on resting ECs and 1,000,000 sites on TNF-α-stimulated ECs, as determined using radio-iodinated anti-ICAM-1 antibodies [213]. The constitutive ICAM-1 expression likely accounts for the observed adherence of ICAM-1-targeted MBs to normal ECs. This adherence to resting ECs, however, was not proportional to the measured ICAM-1 expression, but rather was higher than might be anticipated based on ICAM-1 levels, i.e. inflammatory ECs had 20 times as much ICAM-1, but only 2 to 3 times as much MB adhesion. This may indicate that, even at expression levels found on normal ECs, the ICAM-1 density may already be above the ideal range of expression for eliciting differential binding of targeted agents to normal versus inflamed endothelium. Other potential molecular targets (such as other LAMs)

may have more ideal expression characteristics, and should be subjected to similar *in vitro* investigations.

These data concerning the effect of antibody density on MB adhesion to endothelial ICAM-1 can be interpreted in terms of the mathematical model of receptor/ligand interaction-mediated adhesion of a sphere to a surface presented in Section 4.2.7. In particular, by comparing the theoretical relationship shown in Figure 4-4 with the experimental data shown in Figure 4-8, it can be seen that the model of Cozens-Roberts *et al* [204] properly predicted the interactions between these variables. For both normal and inflammatory cells, the adhesion response to changes in antibody density were linear (S_c linearly proportional to N_R). As the ligand density N_L (endothelial ICAM-1 density) changed from low on the normal cells to high in the inflammatory condition, the slope of the relationship increased. These results further support the notion that the adhesion characteristics of our LAM-targeted microbubbles to dysfunctional endothelium can be modeled in this manner [214]. Furthermore, this agreement between experimental and theoretical results has implications for the contribution of such modeling to the optimization of MB design parameters. Specifically, these initial results demonstrate that such models may be of great utility in predicting the effects of changes in various parameters, including antibody (ligand) density, ligand tether length, MB size, and receptor-ligand pairing. Such model-based predictions may allow for the design of efficient experiments, and may offer insight into the relative importance of, and interactions between, these various parameters.

In Figure 4-9 it can be seen that some microbubble aggregates can form on the endothelial surface. Although the presence of these aggregates may indicate between-microbubble interactions, we have not observed inter-microbubble adhesion to be a common event. In several experiments, perfused MBs were observed microscopically in real time, and

only single MBs were observed flowing in the perfusate (no aggregates were seen), suggesting that any aggregation occurs only on the EC surface. Additionally, while a grape-like three-dimensional cluster of microbubbles would indicate strong inter-microbubble interactions, the aggregates visible in the micrographs in Figure 4-9 are only two-dimensional; each of the MBs in an aggregate independently contacts the cell surface. Thus we believe that the aggregates are most likely due to fluid dynamic effects based on the three-dimensional topography of the EC surface, and do not represent substantial inter-microbubble interaction.

Heterogeneity of microbubble size is also apparent in Figure 4-9. This apparent heterogeneity is due to two factors. First, as shown in Figure 3-1, microbubble diameter was not uniform, but rather was normally distributed around the mean of 3.4 μm. Second, optical effects on the microscope images create additional apparent size heterogeneity: depending on the exact spatial position of each microbubble, its apparent size may vary depending on the chosen focal plane.

Limitations of these studies include the approximations that are common with *in vitro* experiments. Cultured ECs were utilized as an imprecise model for *in vivo* endothelium. The perfusate was culture medium, and included no blood cells. Constitutive expression of ICAM-1 on normal ECs may be lower on cells cultured under static conditions, as ours were prior to experimenting, versus those cultured under physiologic shear conditions [215]. In addition, MBs were exposed to the ECs under static conditions, rather than physiologic shear conditions, to optimize attachment.

Optimization of a targeted ultrasound contrast agent requires investigation of many parameters, including the density of the targeting molecule on the microbubble surface. A microbubble targeted to a cell surface marker of endothelial dysfunction such as ICAM-1 may

offer a non-invasive, real-time, direct tool for the assessment of endothelial function, potentially allowing for the early diagnosis of inflammatory disease processes.

5.0 EFFECT OF WALL SHEAR CONDITIONS ON TARGETED MICROBUBBLE ADHESION

5.1 Introduction

As stated earlier, achieving control over the binding characteristics of the microbubbles is a critical step towards optimizing the design of a targeted ultrasound contrast agent capable of function-specific imaging of the endothelium. In addition to the microbubble surface antibody density, another parameter we endeavored to investigate was the adhesion response to different local shear environments. In the previous chapter, we demonstrated that targeted microbubble adhesion was highly dependent upon the antibody density. In the work presented in this chapter, we investigated the effect of wall shear rate on microbubble adhesion to dysfunctional endothelium.

We hypothesized that ICAM-1-targeted microbubble adhesion is inversely dependent upon the shear rate conditions at the endothelial surface. Our goal was to quantify the adhesion of ICAM-1-targeted microbubbles to inflammatory cultured ECs under various shear conditions, to determine the ability of this contrast agent to adhere to ICAM-1-expressing endothelium under physiologically relevant flow conditions similar to those present in the coronary microcirculation. As before, this hypothesis was tested using a parallel plate perfusion apparatus in which targeted microbubbles were perfused across cultured human coronary artery ECs to investigate their adhesion.

5.2 Methods

5.2.1 Microbubble Preparation

Lipid-based, perfluorocarbon-filled microbubbles (MP1950) were conjugated to anti-human-ICAM-1 IgG monoclonal antibodies as the ligands for endothelial adhesion. Antibody conjugation to the shell was effected via multi-step avidin-biotin bridging chemistry, as described in Chapter 3. MB surface antibody density was maximal (100% MBs), carrying approximately 60,000 Ab/MB (see Chapter 3).

5.2.2 Cell Culture

Cell culture of human coronary artery ECs was undertaken as described in Section 4.2.2. Briefly, the ECs were grown to confluency on 25 mm x 75 mm glass coverslips, and selected coverslips of ECs were made inflammatory by activation with 100 U/mL IL-1β for 5 hours immediately prior to the experiment.

5.2.3 Microbubble Perfusion

Coverslips of ECs (n = 4-8 per condition, total = 71) were briefly incubated with quinacrine dihydrochloride as a fluorescent label and mounted in the perfusion chamber, as described in Sections 4.2.4. As before, the chamber was oriented with the ECs forming the roof of the chamber, due to the natural buoyancy of the microbubbles. Solutions of microbubbles (2 x 10^5 MBs/mL, 1-5 mL volume) were actively perfused through the system at flow rates corresponding to one of 5 different wall shear rates (100, 175, 250, 375, 500 s^{-1}) for 3 min, followed by a 3 min bubble-free wash at the same flow rate. Each coverslip of ECs was either

normal or IL-1β-activated, and was perfused at a single shear rate. Immediately following each perfusion, the chamber was mounted on an inverted epifluorescent microscope, and microscopic brightfield images in 20 random fields of view were recorded digitally at 1000X. The number of cells and adherent MBs was quantified, and averaged over the 20 fields to results in a single measure (mean adhered MBs/EC) per coverslip.

5.2.4 Statistics

Results are expressed as mean ± standard deviation. Data were analyzed with factorial ANOVA with two levels of cell activation (activated versus normal) in the first factor and 5 levels of wall shear rate (100, 175, 250, 375, 500 $s^{-}1$) in the second factor. Covariates taken into account include microbubble batch and EC passage number. When significant differences were found, post-hoc comparisons were made using Tukey's test. Statistical significance was defined as $p<0.05$.

5.3 Results

Data from coverslips perfused with maximally-targeted (100% antibody density) anti-ICAM-1 microbubbles at flow rates corresponding to various wall shear rates followed by a bubble-free wash at matching shear rates are shown in Figure 5-1. Adhesion is expressed as the number of adherent microbubbles normalized to the number of ECs. Adhesion to ECs decreased with increasing wall shear rate to both normal (100 s^{-1} = 0.8 ± 1.7; 175 s^{-1} = 0.6 ± 0.4;

250 s^{-1} = 0.4 ± 0.4; 350 s^{-1} = 0.2 ± 0.1; 500 s^{-1} = 0.04 ± 0.02 MBs/EC) and activated ECs (100 s^{-1} = 3.0 ± 2.7; 175 s^{-1} = 2.6 ± 0.8; 250 s^{-1} = 2.1 ± 1.3; 350 s^{-1} = 1.2 ± 0.9; 500 s^{-1} = 0.5 ± 0.1 MBs/EC). Adhesion of anti-ICAM-1 MBs was greater to activated than normal ECs ($p<0.001$), and decreased with increasing wall shear rate ($p=0.02$). The ratio of adherence to activated ECs versus adherence to normal ECs was 6 at 100 s^{-1} and 21 at 500 s^{-1} ($p=0.22$ for comparison of ratios). By post-hoc analysis, adhesion significantly decreased between 250 and 350 s^{-1} ($p<0.01$), and between 350 and 500 s^{-1} ($p<0.01$).

Figure 5-2 shows brightfield micrographs of coverslips of IL-1β-activated ECs perfused with anti-ICAM-1 microbubbles at flow rates corresponding to wall shear rates of 100 s^{-1}, 175 s^{-1}, 250 s^{-1}, 350 s^{-1}, and 500 s^{-1}. The endothelial cell monolayer is seen in the background, with approximately 6-8 ECs per image. As the shear rate under which microbubble binding interactions occur is increased, adhesion to ECs decreased ($p = 0.02$).

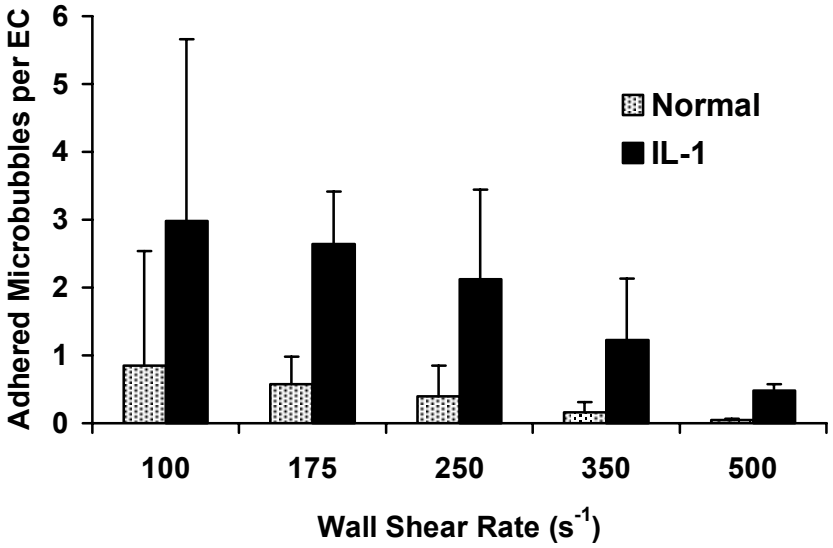

Figure 5-1 *In vitro* adhesion of maximally-targeted (100% antibody density) anti-ICAM-1 microbubbles to normal versus inflammatory human ECs under various wall shear conditions. Adherence was significantly greater to activated versus normal ECs. Microbubble adherence was clearly shear-dependent, with binding decreasing with increasing shear rate. (Mean ± SD).

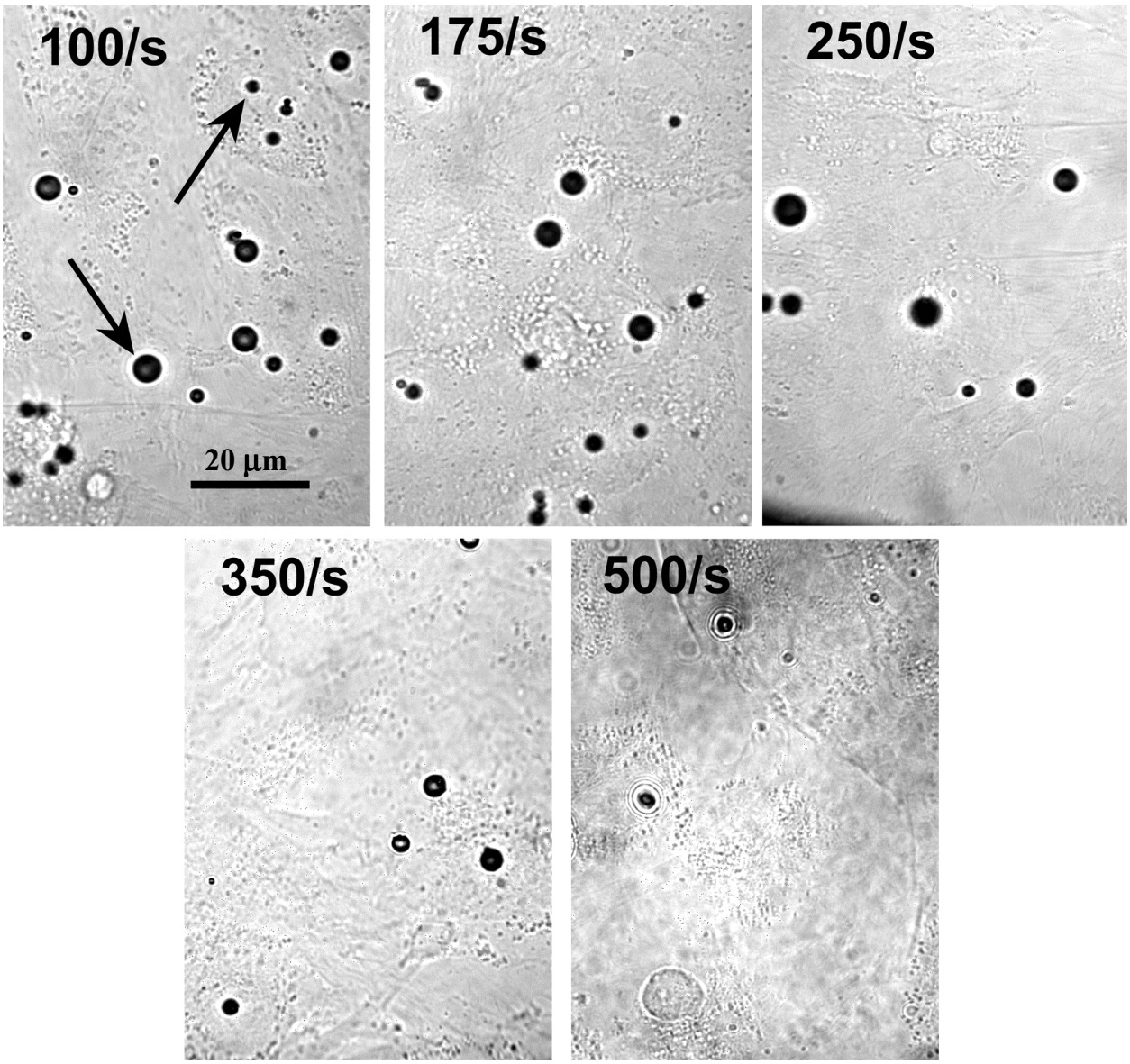

Figure 5-2 Brightfield micrographs of inflammatory ECs following perfusion with maximally-targeted (100% antibody density) anti-ICAM-1 microbubbles at flow rates corresponding to 5 different wall shear rates between 100 s^{-1} and 500 s^{-1}. Each image shows approximately 6-8 ECs in the background, and adhered microbubbles (arrows). As the shear rate under which the microbubble binding interactions occur increases, adhesion to ECs decreased.

5.4 Discussion

The main finding of this study was that the adhesion of ICAM-1-targeted microbubbles is dependent on local shear conditions. Since the *in vivo* application of targeted MBs would require their adhesion to endothelium from vascular shear flow, it was important to quantify the effect of physiologic shear conditions on MB binding.

In developing a targeted imaging agent, two potentially conflicting factors need to be considered: the *absolute* adhesion measured as bound microbubbles per cell, and the *differential* adhesion between normal and disease (inflammatory) conditions. High absolute adhesion is necessary to ensure that bound MBs can provide adequate acoustic signal for ultrasound imaging, and differential adhesion is necessary to allow distinction between normal and diseased tissues. Based on data presented in Chapter 4, the 100% antibody density microbubbles were chosen for the investigation of adhesion under shear conditions because, although the adhesion *differential* was greater with the 50% microbubbles than with the 100% microbubbles, the 100% microbubbles demonstrate the highest *absolute* adhesion, and are thus likely to offer the highest acoustic intensity for ultrasound imaging.

Wall shear rates vary throughout the *in vivo* vascular system, ranging between 50 and 2000 s^{-1} [216]. It is thus important to study the adherence of new targeted agents under a wide range of shear conditions. Our maximally targeted anti-ICAM-1 microbubbles demonstrated a significant negative relationship with wall shear rate in the range studied. Between 100 s^{-1} and 500 s^{-1}, adhesion decreased by more than 80% to activated ECs and more than 90% to normal ECs. The ratio of adherence to activated versus normal ECs was higher at 500 s^{-1} than 100 s^{-1}, but the trend did not reach statistical significance.

These experiments were designed to investigate mainly microbubble attachment, rather than detachment. Binding kinetics for attachment versus detachment can be substantially different, due to recruitment of additional antibody/antigen linkages, flattening of the adhered MB against the EC surface, and differing antibody on-rates and off-rates [214, 217, 218]. In our study, we quantified MBs that adhered during the 3 min MB perfusion across the coverslip and remained adhered after the 3 min MB-free wash (which was intended to remove unbound MBs). We did not observe the attachment and detachment of individual MBs, as would be required for the detailed measurement of MB binding kinetics. However, anecdotal evidence suggests that adhered microbubbles remain adhered for at least 15 min. In several experiments, the MB-free wash was extended from 3 min to 15 min, which yielded no change in microbubble retention, suggesting that adhered microbubbles remain intact and bound to the endothelial surface for at least 15 min even under shear flow.

Limitations of these studies include the approximations that are common with *in vitro* experiments. Cultured ECs were utilized as an imprecise model for *in vivo* endothelium. Constitutive expression of ICAM-1 on normal ECs may be lower on cells cultured under static conditions, as ours were prior to experimenting, versus those cultured under physiologic shear conditions [215]. Microbubbles with normally distributed sizes were studied, but microbubbles of different diameters would be expected to have varied binding strengths, due to different antibody quantities, surface contact areas, and resistance to drag. A single, commercially-available antibody clone was used as the targeting agent, whereas others with different binding kinetics may elicit different MB adhesion characteristics. Lastly, flow through the perfusion chamber was nonpulsatile, and included no blood components. The lack of other blood cells may mean that these data underestimate the adhesion that would occur *in vivo*, because the

presence of other particles in the bloodstream may encourage MB adhesion to the endothelium [219].

Optimization of a targeted ultrasound contrast agent requires investigation of many parameters, including the adhesive response to various physiologic shear conditions. Microbubbles targeted to a cell surface marker of endothelial dysfunction such as ICAM-1 may allow for the ultrasonic assessment of endothelial function, offering non-invasive diagnosis and monitoring of inflammatory disease processes.

6.0 EFFECT OF ENDOTHELIAL TARGET DENSITY ON TARGETED MICROBUBBLE ADHESION

6.1 Introduction

In Chapters 4 and 5, data were presented demonstrating that targeted microbubble adhesion is highly dependent upon the antibody density and the local wall shear conditions. In the work discussed in the present chapter, we continued these efforts to characterize the binding of targeted microbubbles to dysfunctional endothelium by studying the effect of endothelial target density on MB adhesion. We investigated ICAM-1-targeted microbubble adhesion to variably inflamed endothelium, covering the entire spectrum of inflammatory status, as measured by ICAM-1 expression, from the normal status to fulminant dysfunction. Describing the relationship between target density and contrast agent adhesion has important implications for the eventual application of this function-specific imaging technique in the clinical setting.

Specifically, we hypothesized that ICAM-1-targeted microbubble adhesion is dependent upon the level of ICAM-1 expression on the endothelial surface. Our goal was to quantify the adhesion of targeted microbubbles to cultured ECs expressing various levels of ICAM-1, to determine the relationship between the severity of endothelial dysfunction (level of inflammation) and MB adhesion. This hypothesis was tested using a radial flow perfusion apparatus in which targeted microbubbles were perfused across cultured human coronary artery ECs to investigate their adhesion strength.

6.2 Methods

6.2.1 Microbubble Preparation

Lipid-based, perfluorocarbon-filled microbubbles (MP1950) were conjugated to mouse anti-human-ICAM-1 IgG monoclonal antibody on the shell as the ligand for endothelial adhesion. Antibody conjugation was effected via multi-step avidin-biotin bridging chemistry, as described in Chapter 3. MB surface antibody density was maximal (100% MBs), carrying approximately 60,000 Ab/MB (see Chapter 3).

6.2.2 Cell Culture

Cell culture of human coronary artery ECs was undertaken as described in Section 4.2.2. Cells were grown to confluency on 45 mm x 50 mm glass coverslips, and selected coverslips of ECs were made inflammatory by activation with various amounts of IL-1β (0, 0.5, 2, or 100 U/mL) for 5 hours immediately prior to the experiment, resulting in four groups of coverslips with varying degrees of inflammation: normal, low, medium, and high. These particular dosages of IL-1β were chosen based on a study of the dose-response association between IL-1β and human coronary artery ICAM-1 expression measured by quantitative flow cytometry. This study, not reported in detail in this dissertation, demonstrated a standard sigmoidal dose-response relationship, as seen in Figure 6-1.

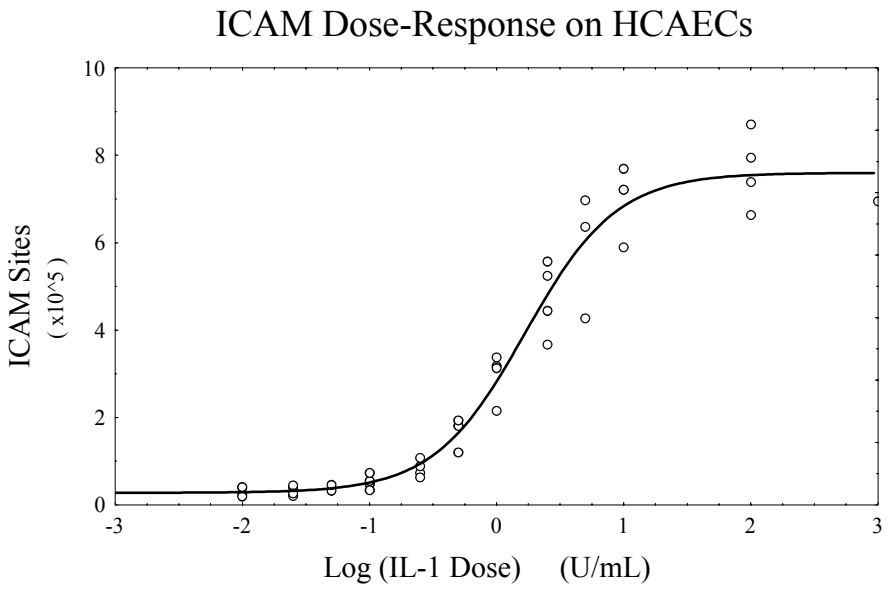

Figure 6-1 Dose-response relationship between interleukin-1β and ICAM-1 expression on cultured endothelial cells.

6.2.3 Quantification of ICAM-1 Expression

Flow cytometry was used to quantify ICAM-1 expression on the EC surface for non-perfused samples from each of the four inflammatory groups, using the procedure described in Section 4.2.3. Briefly, endothelial cell monolayers grown on glass coverslips as above were labeled with biotinylated anti-human-ICAM-1 monoclonal IgG antibody (the same clone as used on the microbubbles) followed by PE-labeled streptavidin, then analyzed for fluorescence. Comparisons with Quantum Simply Cellular standard beads were used to correlate fluorescence intensity with the quantity of ICAM-1 sites.

6.2.4 Radial Flow Chamber

A radial flow perfusion chamber was used to examine adhesion of microbubbles to cultured ECs [204, 220-222]. Similar in concept to the parallel perfusion chamber, this radial apparatus differs by allowing the investigation of a wide range of shear rates in a single experiment, by generating position-dependent shear flow. Figure 6-2 shows a diagram of our design, modified from Cozens-Roberts *et al* [204]. It comprises a transparent PMMA block, 2 rubber gaskets, and a 45 mm x 50 mm glass coverslip. Multiple circular grooves were cut into the block, as seen in Figure 6-2. Starting from the center and moving outwards radially: an inlet port was drilled in the center of the chamber; a shallow disk-shaped groove 500 μm in depth was made as a path for perfusate, a deep circular groove was cut as a fluid reservoir to minimize flow disturbances; three outlet ports spaced 120º apart were drilled through the bottom of the reservoir; and a narrow, shallow groove was made for a vacuum seal, and connected to a horizontal hole drilled as a vacuum port. The distal ends of the inlet and outlet ports were adapted to Luer locks, and connected to Tygon® tubing. A coverslip (with confluent monolayer of ECs) was mounted over the grooves with the cells facing the inside, such that a 500 μm gap was formed between the ECs and the experimental zone. The coverslip was secured with the rubber gaskets and vacuum system, and forms one wall of a closed system. The 3 exit ports were connected together with a 4-way adapter, which was then connected to a nonpulsatile syringe pump in withdrawal mode. Photographs of the radial flow perfusion apparatus are shown in Figure 6-3.

As shown by the arrows in Figure 6-2, a solution of MBs in culture medium (M-199) is perfused in the inlet, flows radially across the 500 μm high experimental zone, flows into the reservoir, and then exits through the 3 outlet ports. As the cross-sectional area of flow increases

with increasing radius from the central inlet, the perfusate velocity and wall shear rate decrease. Over the experimental zone, a range of shear rates covering approximately a single order of magnitude is produced.

Microbubble perfusion experiments result in two zones on the experimental area of the coverslip: an inner region, where velocity and shear are high and MBs cannot adhere, and an outer region, where velocity and shear are low and MBs can successfully adhere, as seen in Figure 6-4. The boundary between these two regions is the margin of MB attachment is observable at low microscopic magnifications, and is designated the "critical shear ring", located at the "critical shear radius". The adhesion strength of the targeted MBs can be measured in terms of the "critical shear rate", calculated at the critical shear radius.

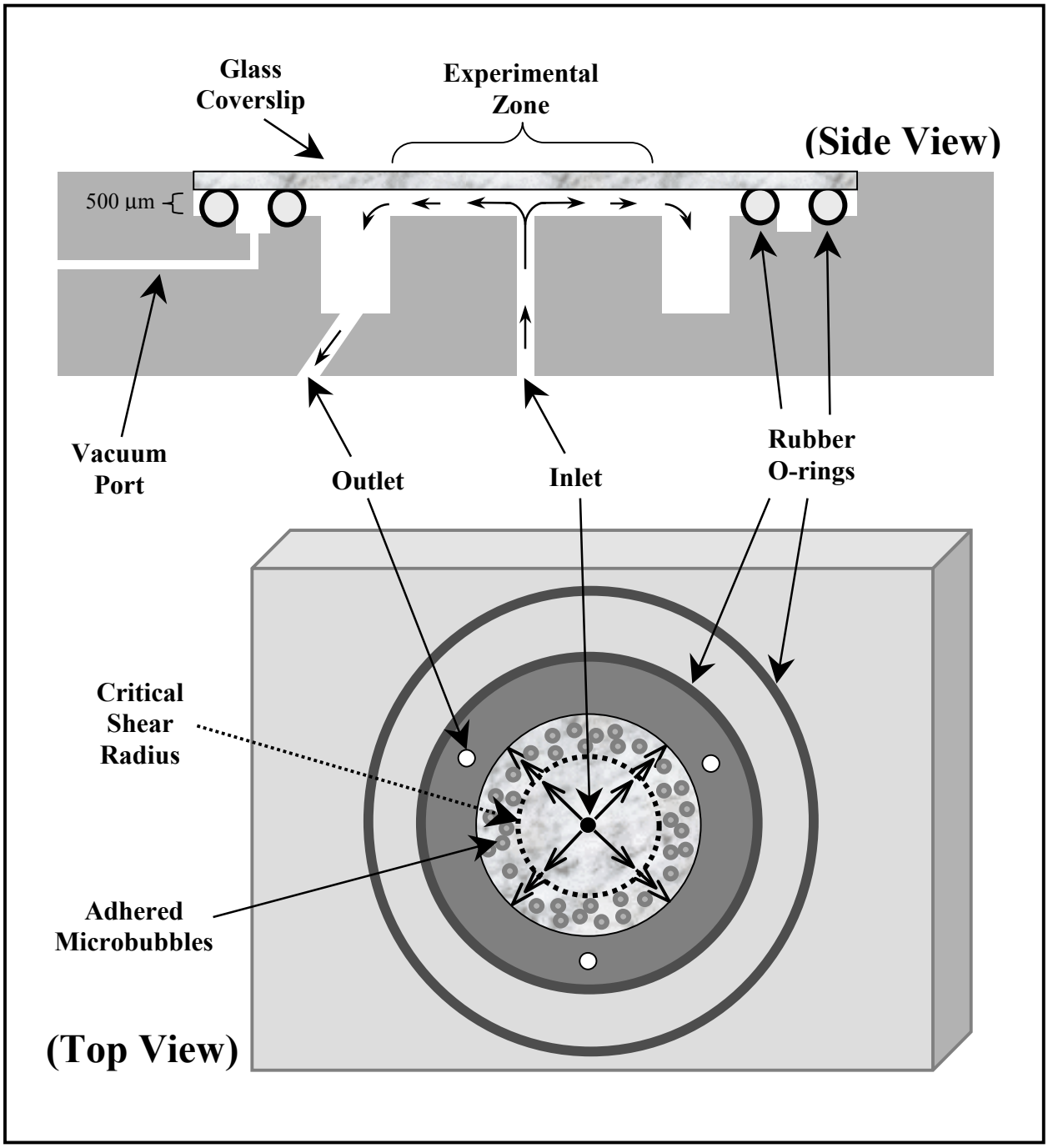

Figure 6-2 Schematic of the radial flow perfusion chamber. A solution of microbubbles is perfused under controllable shear conditions across a monolayer of cultured endothelial cells grown on a coverslip. Wall shear rate varies inversely with radius from the central inlet, and microbubble adherence primarily occurs outside of a "critical shear radius" which corresponds to a "critical shear rate" above which microbubbles do not adhere. (Not to scale).

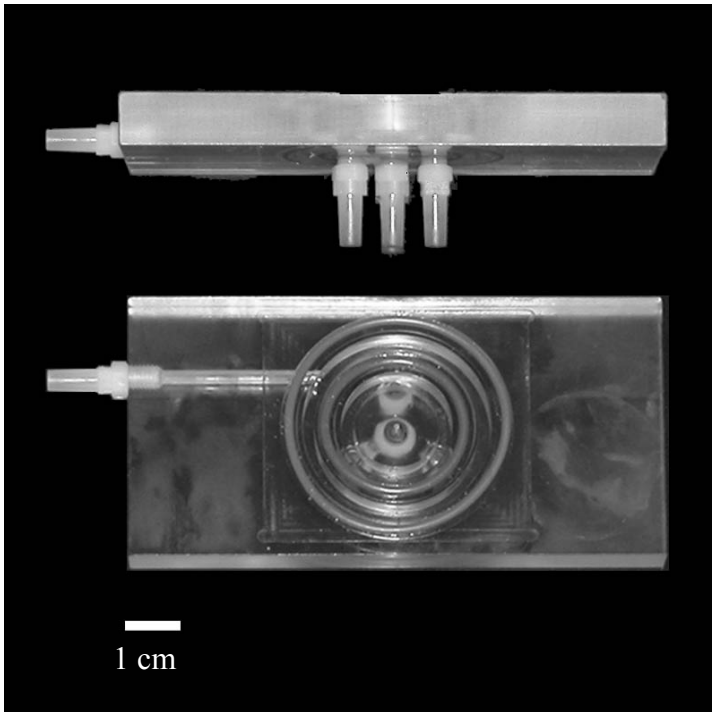

Figure 6-3 Radial flow perfusion chamber, side view and top view. The color version of this figure is shown in Appendix K-6.

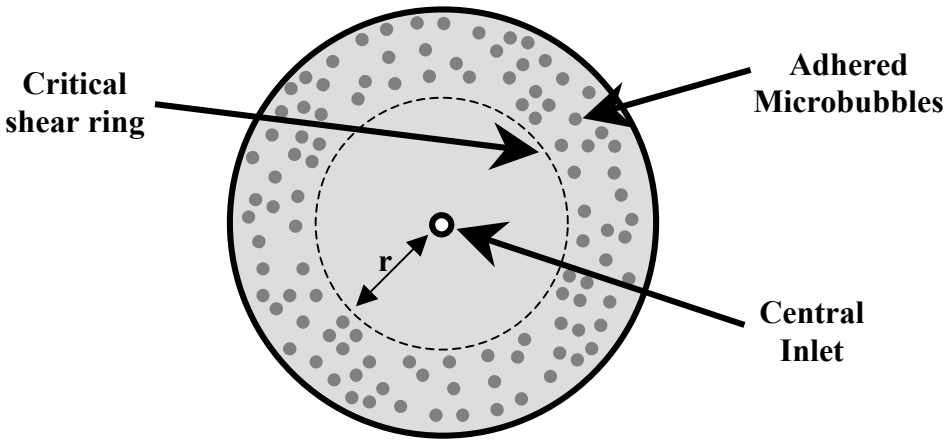

Figure 6-4 Microbubble adhesion pattern in the radial flow chamber. Microbubbles adhere primarily outside of a critical shear radius, observable at low microscopic magnification as a critical shear ring.

6.2.4.1 Fluid Dynamical Analysis. Under laminar flow conditions, flow through the chamber in the experimental zone is well-characterized, with wall shear rates that vary inversely with radius. The positional wall shear rate can be calculated based on the Navier-Stokes equation, with the volumetric flow rate and radius as the key variables. A more detailed derivation is presented in Appendix E.

Briefly, using the same assumptions as with the parallel plate chamber, the Navier-Stokes equation (Equation 4-1) can be employed. Again assuming steady flow and low Reynolds number, the equation in cylindrical coordinates (r = radial position, θ = angle, z = axial position) reduces to its r-component:

Equation 6-1 r-component of Navier-Stokes equation

$$0 = \frac{-\partial P}{\partial r} + \mu \left[\frac{\partial}{\partial r} \left(\frac{1}{r} \frac{\partial}{\partial r} (r V_r) \right) + \frac{\partial^2 V_r}{\partial z^2} \right]$$

From the continuity equation, assuming that the velocities in the circumferential (θ) and axial (z) directions are zero, we have:

Equation 6-2

$$\frac{1}{r} \frac{\partial}{\partial r} (r V_r) = 0$$

and thus

Equation 6-3

$$0 = \frac{-\partial P}{\partial r} + \mu \frac{\partial^2 V_r}{\partial z^2}$$

Treating rV_r as a function of z, and evaluating using no-slip boundary conditions at the walls results in:

Equation 6-4

$$V_r = \frac{1}{2\mu}\frac{\partial P}{\partial r}(z^2 - hz)$$

Volumetric flow rate is defined in cylindrical coordinates as the integral of the r-direction velocity times the circumference with respect to z, so by integrating over the gap (z = 0 to h), an expression for volumetric flow rate is obtained:

Equation 6-5

$$Q = \frac{-1}{6}\frac{\pi r}{\mu}\frac{\partial P}{\partial r}h^3$$

Combining Equation 6-4 and Equation 6-5 gives an expression for the perfusate velocity in the radial direction:

Equation 6-6

$$V_r = \frac{3Q}{\pi r h^3}(hz - z^2)$$

We are most interested in the shear component acting on the z-surface (the coverslip) in the r-direction, so we start with the shear stress τ_{zr} (under laminar flow conditions) given by Newton's law of viscosity as viscosity times the partial derivative of V_r with respect to z. Differentiating Equation 6-6 with respect to z, evaluating at the coverslip surface (z=0), and translating into shear rate (shear rate = shear stress / viscosity) gives the shear rate equation for the radial flow chamber:

Equation 6-7 Wall shear rate equation for the radial flow chamber

$$\dot{\gamma} = \frac{3Q}{\pi r h^2}$$

Equation 6-7 thus gives the wall shear rate as a function of volumetric flow rate Q, gap height h, and radial position r. Thus, at a given flow rate, the wall shear rate varies inversely with radius over the experimental surface of the coverslip [223]. Using this equation, the observed critical shear radius for each perfusion can be translated into a critical shear rate, a measure of MB adhesion strength.

6.2.5 Radial Flow Chamber Validation

Following construction of the radial flow chamber, tests were performed to validate that flow through its experimental zone met specifications. The goal was to demonstrate that the spatial distribution of velocity and thus of wall shear rate followed the theoretical predictions, and that critical shear rings were observable, radially symmetric, and able to be manipulated as suggested by Equation 6-7.

First, an ion argon laser flow visualization system was used to produce a velocity map of the experimental zone of the radial flow chamber. A solution of fluorescent beads was perfused through the chamber under laser illumination while digital images of the coverslip surface of the chamber were recorded by a high resolution CCD camera. Using a relatively long exposure time of 500 milliseconds, images were obtained in which the fluorescent flow tracers were observed as radial streaks, the lengths of which were proportional to the bead velocities. The length and position of these streaks was measured (n = 80) to develop a velocity map of the chamber experimental area. Figure 6-5 shows measured velocity versus radial position. There is general

agreement between a power fit of the data and the y ~ 1/x relationship predicted by the wall shear rate equation above.

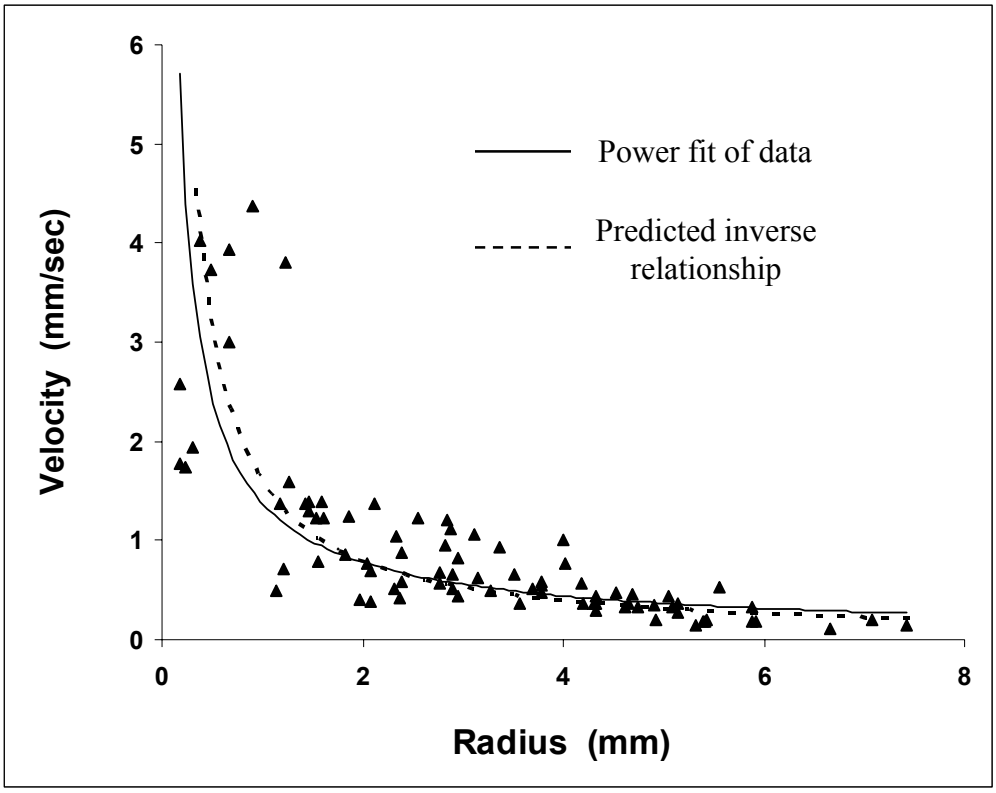

Figure 6-5 Radial position vs. velocity as measured using laser velocimetry. There is general agreement between the predicted inverse relationship and the experimental data.

An additional set of validation tests was performed to verify that MBs perfused through the radial flow chamber would adhere in patterns with well-defined critical shear rings. Solutions of non-targeted Optison (Amersham Health Inc., Princeton, NJ), a commercially available, protein-based ultrasound contrast agent that tends to adhere to glass coverslips, were perfused through the chamber at various volumetric flow rates. Based on Equation 6-7, the critical radius is expected to be linearly proportional to the flow rate Q for a given microbubble species. As seen in Figure 6-6, the relationship between flow rate and critical radius was substantially linear ($r = 0.97$). However, the linear fit had a nonzero y-intercept, a discrepancy from the prediction of Equation 6-7. This same discrepancy has been noted by others, and it has been interpreted as an artifact caused by hydrodynamic effects from the inlet [204, 220, 221]. These groups have made adjustments for this effect by correcting measured shear ring data by the value of the discrepant y-intercept. This adjustment has likewise been made for the current study, using a value of 0.45 mm. Due to potential inlet transition effects, data were acquired only for radii between 1.0 and 8.0 mm.

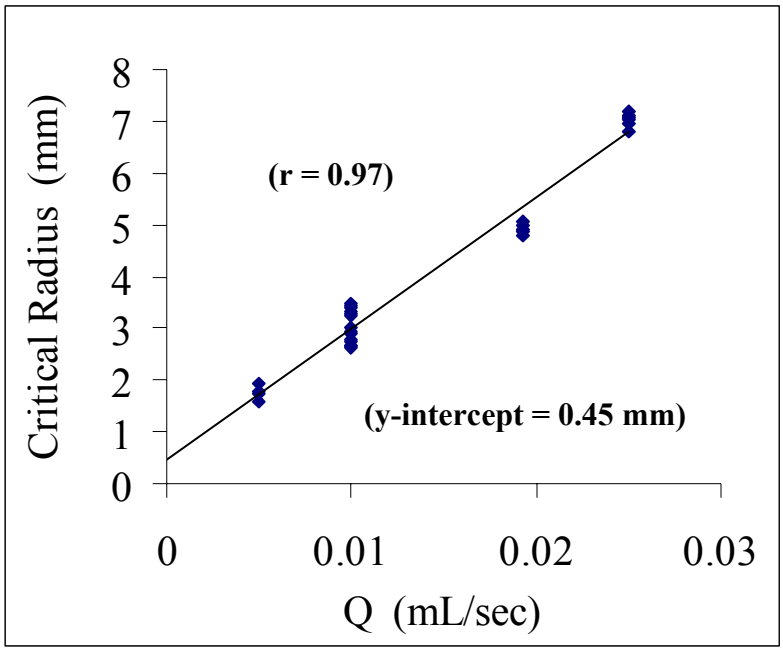

Figure 6-6 Volumetric flow rate (Q) vs. critical shear radius validation data.

6.2.6 Microbubble Perfusion

Coverslips of ECs (n = 3-4 per condition) were briefly incubated with quinacrine dihydrochloride as a fluorescent label and mounted in the radial flow chamber, as described in Sections 6.2.4. As with the parallel plate apparatus, the radial chamber was oriented with the ECs forming the roof of the chamber, due to the natural buoyancy of the microbubbles. A solution of microbubbles (8 x 10^4 MBs/mL) was actively perfused through the system in a diverging manner for 3 min, followed by a 5 min bubble-free wash at the same flow rate. Each coverslip of ECs was activated to a single level of inflammation (normal, low, medium, high). Immediately following each perfusion, the chamber was mounted on an inverted epifluorescent

microscope, and the critical shear radius was measured twice in each of four cardinal directions, and translated into the critical shear rate using Equation 6-7.

6.2.7 Statistics

Results are expressed as mean ± standard deviation. Data were analyzed with ANOVA with four levels of EC activation (levels of ICAM-1 expression). When significant differences were found, post-hoc comparisons were made using Tukey's test. Statistical significance was defined as $p<0.05$.

6.3 Results

A summary of the data obtained in the radial flow chamber is shown in Figure 6-7. Endothelial ICAM-1 expression is on the x-axis, and is reported as a percentage of the maximal level of 750,000 ICAM-1 sites per EC. The critical shear rate as calculated from the measured critical shear radii is on the y-axis.

Endothelial surface ICAM-1 densities were: normal (constitutive) = 35,000 ± 10,000; low = 230,000 ± 30,000; medium = 440,000 ± 40,000; and high = 750,000 ± 55,000 ICAM-1 sites per EC. The critical shear rate for targeted MBs increased with increasing degree of inflammation: normal = 380 ± 110; low = 515 ± 80; medium = 745 ± 60; and high = 960 ± 130 s^{-1} ($p < 0.001$). There were significant differences in MB adhesion between the low and medium inflammation levels, and between the medium and high levels ($p<0.02$ each). The relationship between critical shear rate and ICAM-1 expression was both positive and linear ($r > 0.99$).

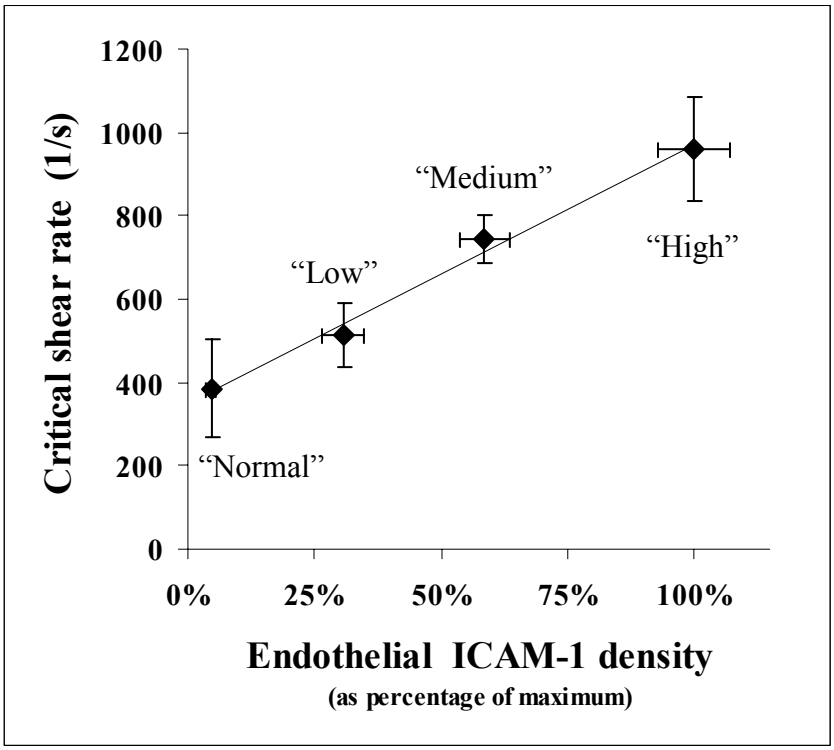

Figure 6-7 Endothelial ICAM-1 expression versus targeted MB adhesion strength. Four different concentrations of interleukin-1 were used to activated cultured ECs to four different levels of inflammation. The critical shear rates of ICAM-1-targeted MB adhesion were measured in a radial flow chamber. (Mean ± SD).

6.4 Discussion

First suggested by Fowler and McKay, the radial flow chamber has since become widely used to study cell attachment and detachment phenomena [220]. It is a particularly useful device for the study of cell-substrate adhesion phenomena because it allows investigation over a wide range of shear conditions simultaneously. In our version of the design, a range of wall shear

rates almost a full magnitude wide could be produced in the experimental zone of the coverslip in each perfusion experiment, allowing the efficient investigation of the adhesion strength of our targeted microbubble agent to variably inflamed cultured endothelium.

The data demonstrated a positive relationship between endothelial ICAM-1 expression and targeted MB adhesion strength, which agrees with our earlier data showing greater binding to maximally inflammatory ECs than to resting ECs. The mathematical model of Cozens-Roberts *et al*, which states that (see Section 4.2.7):

$$S_c \approx \beta N_L N_R$$

where S_c is the critical shear stress, β is in our case a constant term, N_L is the ligand (ICAM-1) density, and N_R is the receptor (anti-ICAM-1 antibody) density, predicts that the relationship between ICAM-1 expression and targeted MB adhesion is both linear and proportional.

As seen in Figure 6-7, our data showed that the experimental relationship was linear, as predicted, but was not proportional, i.e. the linear fit did not go through the origin. This discrepancy manifests in our *in vitro* ICAM-1-targeted system as low to moderate MB adhesion to resting ECs expressing only constitutive amounts of ICAM-1. Similar discrepancies in which the linear fit had a nonzero y-intercept have been reported [204]. Ideally, targeted MB adhesion to normal endothelium would be close to zero, maximizing the difference between binding to normal versus dysfunctional tissue.

As seen in Equation 4-16, the β term in the above model is dependent on the size of the microbubble. Specifically, the β term is proportional to the contact area (a), and inversely proportional to the cube of the MB radius (ρ_B). Since the interaction contact area (a) is roughly proportional to the square of ρ_B, this implies that the β term, and thus S_c, may be expected to be roughly inversely proportional to ρ_B. Thus smaller MBs may be capable of binding to the

endothelium at higher shear rates than larger microbubbles. In our radial flow chamber experiments detailed in this chapter, however, an obvious relationship between microbubble size and critical radius was not observed. The critical shear rings were generally fairly distinct, and no obvious radial gradient of microbubble size was seen. With respect to the Cozens-Roberts model above, this lack of size effect may be due to an unexpected effect of MB size on microbubble antibody density (in terms of antibodies per microbubble surface area), or may be due to heterogeneous microbubble shell flexibilities, a factor that is not considered by the above model.

Our data suggest that the adhesion strength of targeted microbubbles was linearly dependent on the degree of endothelial inflammation, which has important implications for the application of this imaging technique in a clinical setting. In previous chapters, data have been presented that demonstrated preferential adhesion of our targeted contrast agent to inflammatory versus normal endothelium. A key limitation of such studies, however, is that the *in vivo* range of endothelial dysfunction severity may be narrower than with the *in vitro* models. In other words, the previous *in vitro* adhesion experiments neglected to investigate MB adhesion in the spectrum of inflammation lying *between* "normal" and maximally "inflammatory". In the current study, we have generated data to illuminate this region. Various potential relationships between adhesion strength and degree of inflammation are shown in Figure 6-8. In case A, the targeted MB imaging system would be able to differentiate between normal tissue and a low level of disease, but would not be able to distinguish between low, moderate, or severe disease. In case C, we would not be able to differentiate normal from low or moderate disease. The fact that the observed relationship was linear (case B) indicates that contrast-enhanced echocardiography using targeted agents may be able to differentiate between various degrees of

endothelial dysfunction, and thus detect not only the presence, but also the severity of inflammatory disease processes.

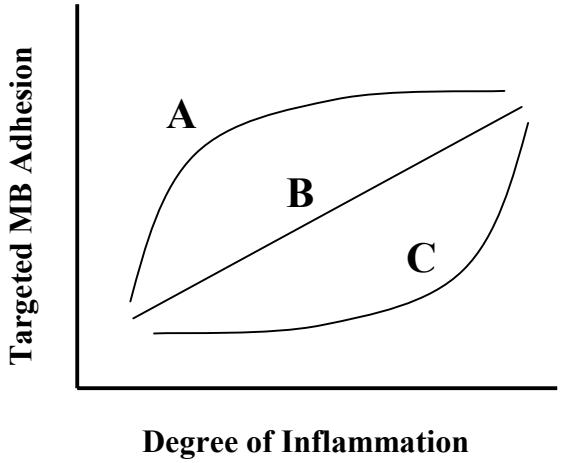

Figure 6-8 Possible relationships between degree of endothelial inflammation and targeted MB adhesion.

7.0 APPLICATIONS IN TRANSPLANT REJECTION

7.1 Introduction

Work discussed in Chapters 4, 5, and 6 demonstrated that ultrasound contrast agents targeted to ICAM-1 via conjugation with anti-ICAM-1 antibodies preferentially bind to inflammatory versus resting cultured human endothelial cells *in vitro*. We have also demonstrated that the *in vitro* adhesion of targeted MBs depends upon a number of parameters, including microbubble antibody density, local shear conditions, and endothelial target (ICAM-1) density. Our next goal was to determine whether the phenomenon of selective adherence of our targeted agent to dysfunctional endothelium would occur *in vivo*, and whether the preferential adherence could be detected via external ultrasound.

We initiated this critical next step in the development of our targeted ultrasound agent by investigating the potential for non-invasive assessment of organ transplant rejection. Although several noninvasive tools to diagnose rejection have been reported [129, 131, 133, 134], each of these has limitations that prevent their widespread clinical implementation, and the current gold standard for the assessment of rejection remains endomyocardial biopsy, a procedure that is invasive and not without risk. The development of a non-invasive, clinically viable technique for the diagnosis and monitoring of allograft rejection would thus be of great value to post-transplant patients.

As discussed earlier in Section 1.3, a critical event in the pathogenesis of organ transplant rejection is endothelial dysfunction, which is characterized by the upregulation of leukocyte

adhesion molecules (LAMs) including ICAM-1. A technique that offers direct, non-invasive clinical assessment of the inflammatory status of the endothelium as indicated by the level of ICAM-1 expression may thus allow diagnostic evaluation of the rejection process.

In the current study, we endeavored to investigate targeted ultrasound contrast MBs as a non-invasive imaging technique for the detection of transplant rejection. We hypothesized that MBs targeted to ICAM-1 would allow for the diagnosis of fulminant acute cardiac allograft rejection. Specifically, we hypothesized that ICAM-1-targeted MBs would preferentially adhere to the microcirculatory endothelium of rejecting grafts vs. non-rejecting grafts in a rat model of cardiac transplantation, and that this selective binding could be detected via ultrasound imaging. We tested these hypotheses using both *in vitro* and *in vivo* models.

First, because our previous experience with targeted MBs was with *human* endothelium, it was necessary to verify that microbubbles could be targeted to *rat* ICAM-1, prior to engaging in the more technically difficult *in vivo* studies. Accordingly, *in vitro* tests were performed to demonstrate that MBs conjugated to anti-rat-ICAM-1 antibodies would selectively adhere to inflammatory versus normal cultured rat ECs.

Second, abdominal heterotopic heart transplantation was performed in rats, and targeted microbubbles were injected into the animals during simultaneous myocardial contrast echocardiography of the donor heart to determine if this targeted agent was capable of identifying rejecting myocardium. Abdominal rat heterotopic heart transplantation was chosen as our *in vivo* model of acute cardiac allograft rejection for a number of reasons: (1) the model is well characterized and prevalent in the literature, (2) the model is known to produce fulminant acute rejection in hetero-strain transplants, and very little rejection in homo-strain transplants, (3) heterotopic transplantation is much less burdensome on the recipient animal than is homotopic

transplantation, thus allowing for less peri-operative mortality, (4) the transplanted heart is functional, although unloaded, and continues beating after being placed in the donor animal, and (5) the rat heart is large enough to allow the acquisition of adequate ultrasound images.

7.2 Methods

7.2.1 Targeted Microbubbles

Biotinylated lipid-based microbubbles (MP1950) were conjugated to antibodies via avidin/biotin bridging as described earlier (see Chapter 3). Microbubbles were linked to either nonspecific mouse IgG antibody (Caltag, Burlingame, CA), or mouse anti-rat-ICAM-1 IgG monoclonal antibody (clone 1A29, Pharmingen, San Diego, CA), a clone that has been heavily used in ICAM-1 literature [224-226]. Microbubbles with 1A29 were designated MB_{ICAM}, and those with the control antibody were designated $MB_{Control}$. Antibody density on the microbubble shell was measured by quantitative flow cytometry (as previously described in Chapter 3) to be $60 \pm 5 \times 10^3$ and $62 \pm 5 \times 10^3$ antibodies per microbubble for MB_{ICAM} and $MB_{Control}$, respectively. Microbubble diameter was 3.4 ± 1.2 μm.

7.2.2 Cell Culture

Rat heart microvessel ECs (VEC Technologies, Rensselaer, NY) were grown to confluence on glass coverslips in endothelial basal medium supplemented with 5% fetal bovine serum. Only second, third, or fourth passage cells were used. Selected coverslips of ECs were made inflammatory by incubation with 100 U/mL interleukin-1β for 5 hours immediately prior to microbubble perfusion.

7.2.3 Quantification of Rat EC ICAM-1 Expression

Flow cytometry was used to quantify ICAM-1 expression on the rat EC surface, as described in Section 4.2.3. Briefly, trypsinized ECs were incubated with biotinylated anti-rat-ICAM-1 monoclonal IgG antibody (clone 1A29, the same as used for MB_{ICAM}) or biotinylated nonspecific IgG antibody (the same as used for $MB_{Control}$) followed by PE-labeled streptavidin. The cells were washed, fixed, and fluorescence quantified via flow cytometry (n = 5 per condition).

7.2.4 *In Vitro* Microbubble Perfusions

The rectangular parallel plate perfusion chamber was again used to examine adhesion of microbubbles to cultured ECs. The general setup was as described in Chapter 4. Coverslips of ECs (n = 3-6 per condition) were briefly incubated with quinacrine dihydrochloride (50 μM) as a fluorescent label and mounted in the perfusion chamber. The vacuum seal was applied, and the chamber was primed with 37°C culture medium. A suspension of either MB_{ICAM} or $MB_{Control}$ (3.33×10^6 MBs/mL) in culture medium was actively perfused through the system at a flow rate corresponding to a wall shear rate of 100 s^{-1} for 3 min, followed by a 3 min MB-free wash at 100 s^{-1}. Each coverslip of ECs was either normal or IL-1β-activated. Immediately after each perfusion, 20 randomly selected microscopic fields were imaged at 1000X and the number of ECs and adhered microbubbles quantified.

7.2.5 Heterotopic Rat Heart Transplant Model

In this cardiac transplantation model, first described by Ono and Lindsey [227] in 1969, the heart of the donor rat is harvested, implanted into the abdomen of the recipient animal, and anastomosed to the recipient's abdominal aorta and vena cava. If the donor and recipient rats are of the same strain, then the transplant is accepted with little reaction. If the donor and recipient are of differing strains, however, the transplant will cause fulminant acute rejection within days, because the two strains of rats are mismatched at the major histocompatibility loci. Experiments were approved by the Institutional Animal Care and Use Committee at the University of Pittsburgh.

Inbred male Brown Norway (BN) (150-190g) and Lewis (L) (280-310g) rats were chosen, as they are widely used for acute transplant rejection studies due to their strong immunogenic response. A total of 23 transplants were performed: the rejecting group comprised 12 BN→L allografts, and the control group comprised 6 BN→BN and 5 L→L isografts.

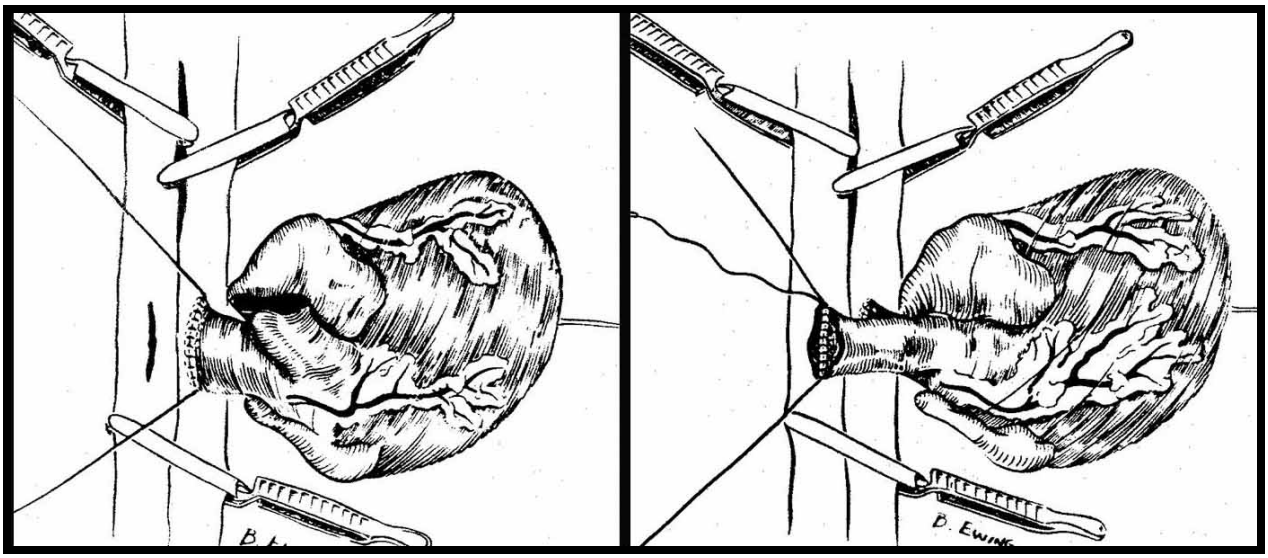

Figure 7-1 Heterotopic heart transplantation in the rat, using the method of Ono and Lindsey [227]. The explanted donor heart is implanted into the abdomen of the recipient animal, and the donor aorta is anastomosed end-to-side to the recipient abdominal aorta (left image). The donor pulmonary artery is then anastomosed to the recipient inferior vena cava (right image). Drawings from [227].

The transplantation surgery proceeded as follows, using a modification [228] of the original method of Ono and Lindsey [227]. Donor animals were anesthetized with intraperitoneal sodium pentobarbitol (50 mg/kg), intubated with a 14 gauge angiocatheter, and ventilated at 10 ml/kg/sec (Harvard Rodent Ventilator, Model 683, Harvard Apparatus, Holliston, MA). A small midline abdominal incision was made, and heparin (1000 U/kg) was injected via the inferior vena cava (IVC). The anterior chest wall was separated from the diaphragm, and the anterior rib cage was divided with heavy scissors on both sides of the sternum from lower rib margins to the clavicles, creating a hinged thoracic door that was lifted to expose the heart. The IVC, superior vena cava, and the pulmonary veins were ligated with 4-0

silk, and the ascending aorta and main pulmonary artery were transected about 2-3 mm from the vessel origins. The isolated donor heart was removed and immersed in 4º C normal saline.

Recipient rats were anesthetized, intubated, and ventilated as above. A midline abdominal incision was made and the and the abdominal aorta and IVC were isolated just beneath the renal arteries. The donor heart was placed transversely in the recipient's left abdominal cavity. As seen in Figure 7-1, the donor aorta was anastomosed end-to-side to the recipient abdominal aorta, and the donor pulmonary artery was anastomosed end-to-side to the recipient abdominal IVC with running sutures using 8-0 monofilament nylon. Surgical mortality was 5%; duration of donor heart immersion in saline was 19 ± 5 min; and anastomosis time was 25 ± 1 min. Graft survival was monitored by daily palpation of the donor heart beat [229].

7.2.6 Verification of Acute Rejection

7.2.6.1 Histological Rejection Grading. Following animal sacrifice, native and donor hearts were harvested and fixed overnight in 4% paraformaldehyde, embedded in paraffin (protocol in Appendix B), and cut into 5 μm cross-sections through the short axis of the heart. The tissue sections were stained with hematoxylin and eosin (protocol in Appendix G), and rejection status was assessed microscopically by blinded observers using the International Society for Heart and Lung Transplantation (ISHLT) grading standard [230] (see Table 7-1).

Table 7-1 ISHLT criteria for the scoring of acute transplant rejection. Modified from [230].

ISHLT Grade	Biopsy characterization
0	No rejection.
I	A = Focal infiltrate without necrosis B = Diffuse but sparse infiltrate without necrosis
II	One focus only with aggressive infiltrates and/or focal myocyte damage
III	A = Multifocal aggressive infiltrates and/or myocyte damage B = Diffuse inflammatory process with necrosis
IV	Diffuse aggressive polymorphous ± infiltrate ± edema ± hemorrhage ± vasculitis, with necrosis

7.2.6.2 Immunohistochemical ICAM-1 Scoring. Histological specimens from a separate series of isograft and allograft rats were harvested on various post-op days (n = 3 per rat type per post-op day) and prepared for staining as above. As described in Section 2.2.3, samples were interrogated for ICAM-1 using a polymer-based immunoperoxidase staining kit and the same biotinylated primary anti-rat-ICAM-1 antibody as used for the MBs (clone 1A29).

The specimens were interrogated microscopically for positive endothelial ICAM-1 staining, and scored semi-quantitatively by blinded observers on a scale of 0 (constitutive ICAM-1 only) to 4 (most positive).

7.2.7 Myocardial Contrast Echocardiography

MCE was performed with the Phillips (Hewlett-Packard) Sonos 5500 ultrasound system and the S3 linear-array transducer. Intermittent transabdominal images were acquired in ultraharmonic mode using send/receive frequencies of 1.3 and 3.6 MHz, respectively. The mechanical index, a measure of the transducer's ultrasound output intensity (power), was set at a relatively high value of 1.6. Probe position, gain settings, and focus (mid-field) were initially optimized and maintained throughout each experiment. Five ECG-triggered images of the donor heart in the short axis plane were acquired at baseline (pre-injection), 3 min, and 3 min 20 sec after injection of a microbubble solution. Images were recorded digitally and analyzed offline using customized MCE software (Jiri Sklenar, University of Virginia). Images were aligned and average pixel intensity was measured in regions of interest encompassing the left ventricular myocardium.

The goal of the ultrasound image analysis was to differentiate between the acoustic signal due to adhered microbubbles and the signal due to microbubbles still freely circulating in the bloodstream. Our approach to differentiating between signals from these two microbubble populations was based on previously described principles of ultrasound-induced microbubble destruction and replenishment, and our observations of the *in vivo* bloodstream kinetics of non-targeted microbubbles [97, 231, 232]. In pilot MCE studies in rats receiving Optison (a clinically used echocardiography contrast microbubble) in doses equivalent to those used in the present study, acoustic signal in the myocardium was no longer detectable by approximately 3 min after injection. Based on this observation, we surmised that ultrasound backscatter at 3:00 post-injection of targeted microbubbles would be attributable predominantly to adhered, rather

than freely circulating, microbubbles. Since high mechanical index ultrasound is known to destroy microbubbles within the beam [231], the ultrasound pulse given at 3:00 should destroy these (predominantly adhered) microbubbles in the field. Thus, the acoustic backscatter of the image taken 20 seconds later, at 3:20, should derive only from the few remaining freely circulating microbubbles that were able to replenish the field during the 20 second interval.

Based on the above concepts, the difference in myocardial videointensity between the initial 3:00 frame (adhered + circulating microbubbles) and the initial 3:20 frame (predominantly circulating microbubbles) was defined as the signal attributable to microbubble adhesion only. We generated an additional index, $VI_{targeted}$, calculated as the mean VI difference for MB_{ICAM} injections minus the VI difference for $MB_{Control}$ injections in the same rat, resulting in a measure that reflected only the videointensity due to specific adhesion of targeted microbubbles to ICAM-1.

$$VI_{targeted} = [\ VI_{3:00,ICAM} - VI_{3:20,ICAM}\ ] - [\ VI_{3:00,Control} - VI_{3:20,Control}\ ]$$

7.2.8 Ultrasound Imaging Protocol

Ultrasound imaging of the *in vivo* transplanted heart was performed on post-op day 5. Animals were anesthetized, intubated, and ventilated as described above (Section 7.2.5). A 22 gauge catheter was placed in the right jugular vein for administration of saline and microbubble solutions. Anesthesia was maintained with intravenous pentobarbitol (15 mg/kg, every 15-30 min). The animal was placed in a prone position on a scaffold with an open window cut-out under the abdomen to allow for placement of the ultrasound probe. Pilot studies were conducted with Optison to determine a dosing strategy, and revealed that a single intravenous bolus

injection of 2.5 x 10^6 microbubbles was sufficient to generate myocardial opacification that was reproducible and of adequate videointensity.

Rats were given an initial bolus injection of 2.5 x 10^6 Optison microbubbles in 0.05 mL saline, during intermittent MCE imaging, to verify adequate probe position, optimize image settings, and verify homogeneous perfusion of the donor myocardium. Donor hearts with obvious myocardial perfusion defects or segmental wall motion abnormalities were excluded from the study. Such defects were most likely due to infarction secondary to operative complications such as inadequate tissue preservation, peri-operative coronary artery occlusion, or embolism.

Following complete washout of the Optison (about 8 min), an intravenous injection of 2.5 x 10^6 MB_{ICAM} or $MB_{Control}$ in 0.05 mL saline was administered as a bolus followed by a 0.2 mL saline flush during simultaneous MCE imaging. Five ECG-triggered frames were captured at baseline, 3:00, and 3:20 post-injection (see Figure 7-2). Each rat received paired injections of MB_{ICAM} and $MB_{Control}$, in random order. The animals were euthanized, and myocardial tissue was harvested and prepared for histology as described above.

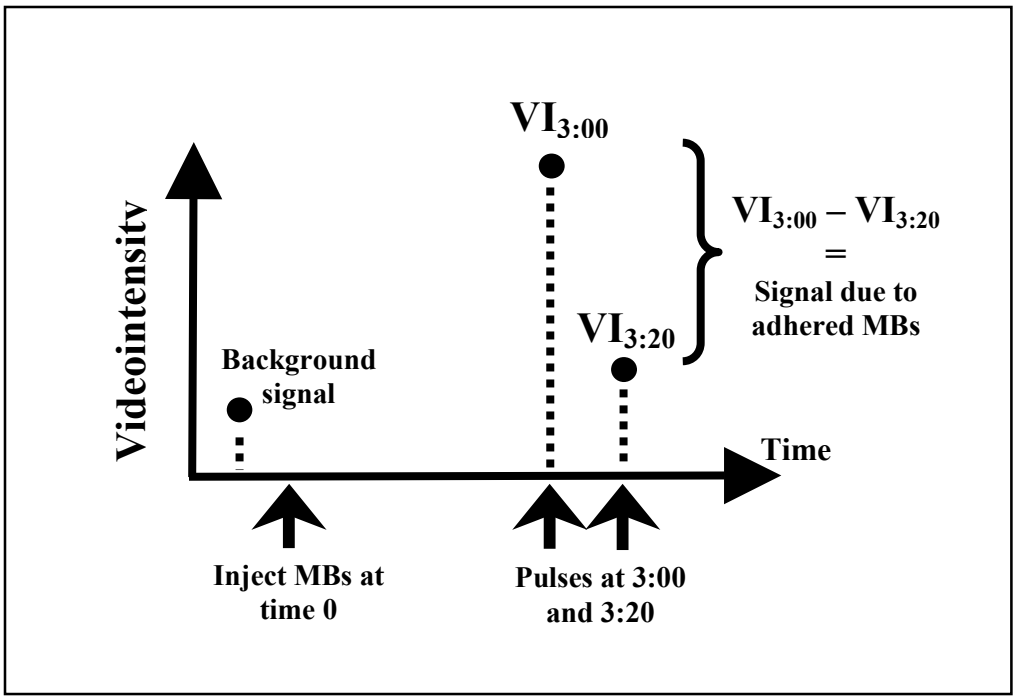

Figure 7-2 Protocol for the *in vivo* ultrasound contrast imaging of transplanted hearts in rats. Microbubbles (either MB_{ICAM} or $MB_{Control}$) were injected at time zero. Ultrasound pulses were given at 3 min and 3 min 20 sec post-injection. The videointensity of the tumor region of interest at 3:20 was subtracted from the videointensity at 3:00 to achieve the acoustic signal attributable only to adhered microbubbles.

7.2.9 Statistics

Results are expressed as mean ± standard deviation. Data were analyzed with two-tailed Student's t-tests, and with two-way ANOVA. Between-group regression coefficients were compared via ANCOVA with dummy variables. Statistical significance was defined as $p<0.05$.

7.3 Results

7.3.1 *In Vitro* Experiments

By flow cytometry, IL-1β activation increased the mean ICAM-1 signal on cultured rat ECs from a baseline of 20 ± 10 up to 180 ± 60 intensity units, as seen in Figure 7-3 and Figure 7-4. Thus the surface expression of ICAM-1 is approximately 8 times higher on the inflammatory ECs than the normal, resting ECs.

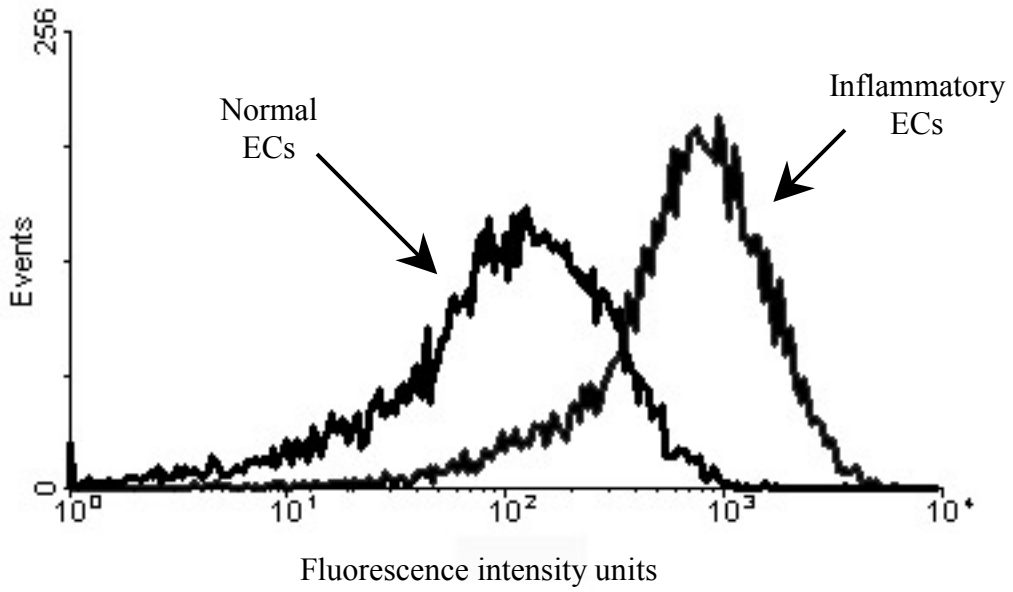

Figure 7-3 Flow cytometry sample data using cultured rat ECs with fluorescently-labeled ICAM-1. Inflammatory cultured rat ECs expressed substantially more ICAM-1 than normal ECs.

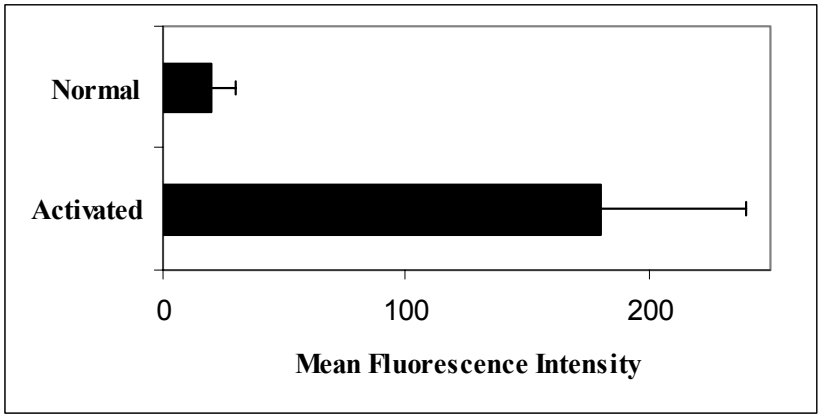

Figure 7-4 Mean fluorescence intensity of ICAM-1-labeled ECs. ICAM-1 expression was approximately 8 times higher on IL-1β-activated ECs than normal ECs. (Mean ± SD).

Data from coverslips of rat ECs perfused with MB_{ICAM} or $MB_{Control}$ are shown in Figure 7-5. Adherence of $MB_{Control}$ was minimal to both normal and inflammatory ECs (0.2 ± 0.1 and 0.3 ± 0.1 MBs/EC). Adherence of MB_{ICAM} was significantly greater to IL-1β-activated ECs than normal ECs (11 ± 3 vs. 3 ± 2 microbubbles/EC, $p<0.005$). Figure 7-6 shows brightfield micrographs of coverslips of inflammatory and normal ECs perfused with both species of microbubbles. ICAM-1-targeted microbubbles clearly adhere preferentially to inflamed (left upper panel) versus normal (right upper panel) endothelium. Isotype control microbubbles adhered only minimally to both cell types (lower panels).

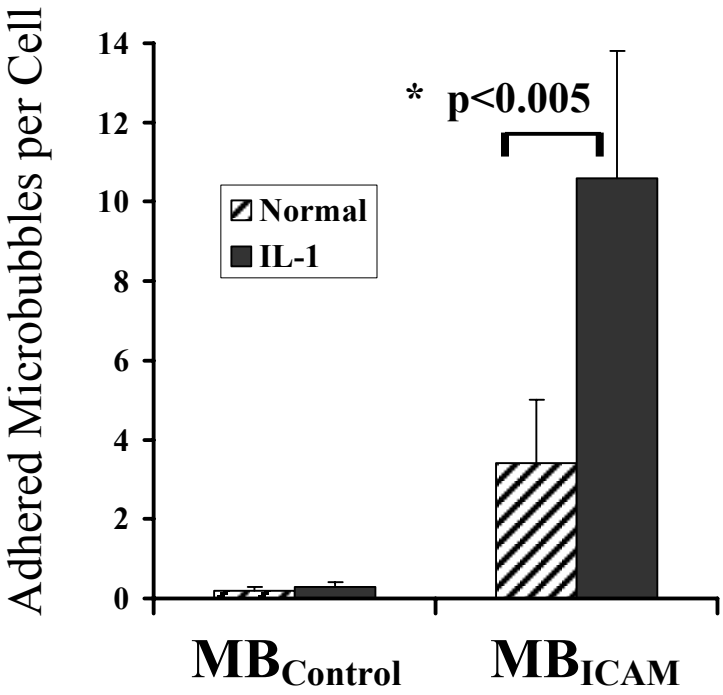

Figure 7-5 *In vitro* adherence of targeted microbubbles to cultured rat endothelial cells. Adherence of control microbubbles ($MB_{Control}$) was minimal to both cell types, whereas adhesion of ICAM-1-targeted microbubbles (MB_{ICAM}) was significantly higher to interleukin-activated cells than normal cells (Mean ± SD).

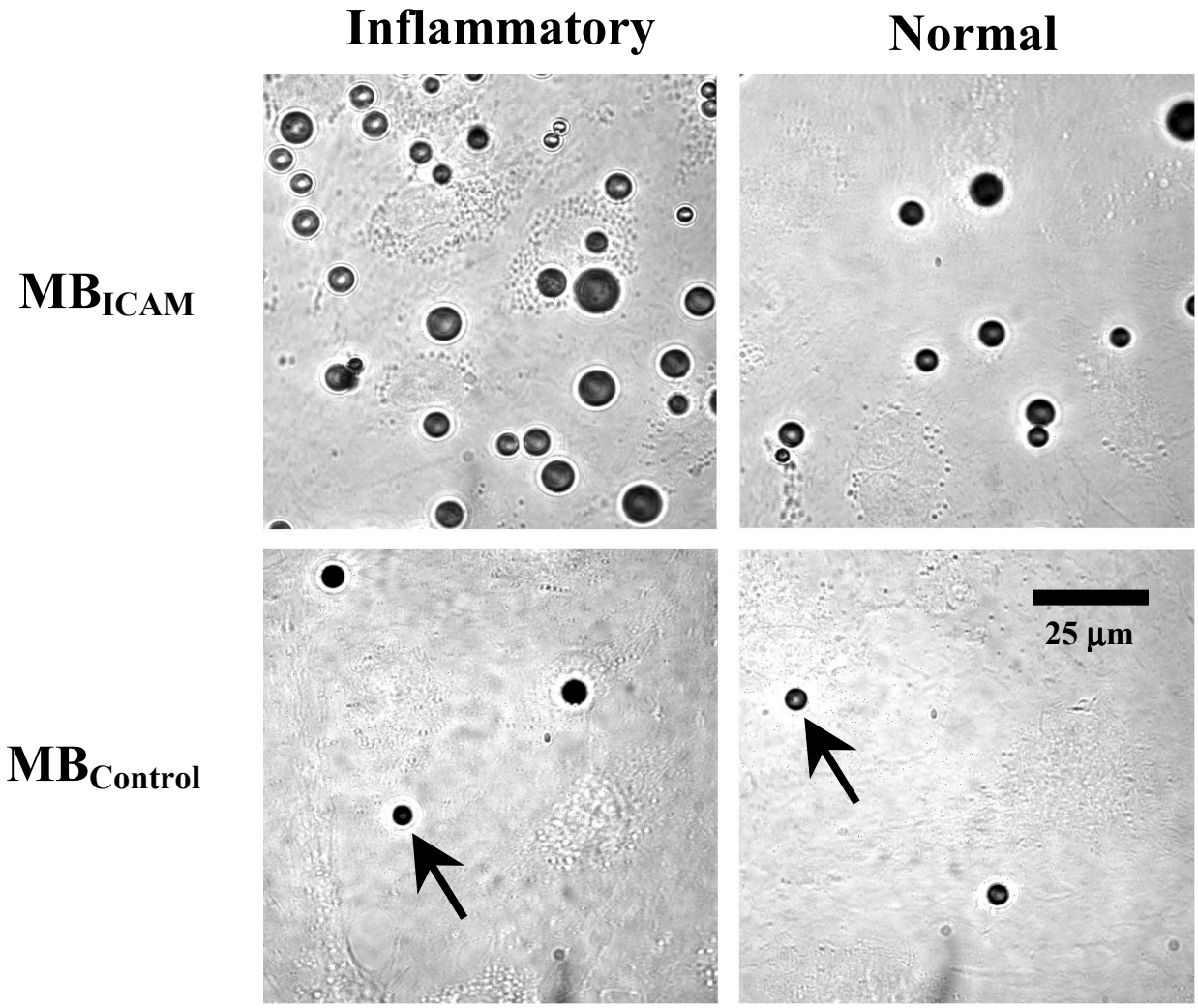

Figure 7-6 Brightfield micrographs of IL-1β-activated (left panels) and normal (right panels) cultured rat ECs after exposure to ICAM-1-targeted microbubbles (MB_{ICAM}, upper panels) and isotype control microbubbles ($MB_{Control}$, lower panels). Each image shows approximately 6-8 ECs in the background, and adhered microbubbles (arrows). There was significantly greater adhesion of MB_{ICAM} to activated versus normal ECs. Adhesion of $MB_{Control}$ to both cell types was minimal.

7.3.2 *In Vivo* Experiments

7.3.2.1 Histology. All 8 allografts (BN→L) showed histologic evidence of ISHLT grade III or IV acute rejection, whereas the 7 isograft rats (4 BN→BN and 3 L→L) were all histologically normal. Figure 7-7 shows typical micrographs from isograft (panel A) and allograft (panel B) myocardium. Whereas panel A shows normal histology, panel B shows the typical features of acute rejection including lymphocytic infiltration, edema, fibrosis, and myocyte damage [230].

ICAM-1 expression as a function of post-op day measured on a semi-quantitative scale for both allograft and isograft donor hearts is shown in Figure 7-8. In both types of tissue, endothelial ICAM-1 levels increased with post-op time. The slope of the linear fit was significantly higher for the allografts than the isografts ($p<0.01$), indicating accelerated ICAM-1 upregulation in rejecting tissue. On post-op day 5, rejecting hearts had a significantly higher ICAM-1 score compared to the normal hearts (3.7 ± 0.6 vs. 0.7 ± 0.6, $p<0.005$).

Figure 7-9 shows brightfield micrographs of normal (panel A) and rejecting (panel B) rat myocardium on post-op day 5, stained for ICAM-1, indicating intense ICAM-1 staining (red-brown) in the microcirculation of the rejecting tissue.

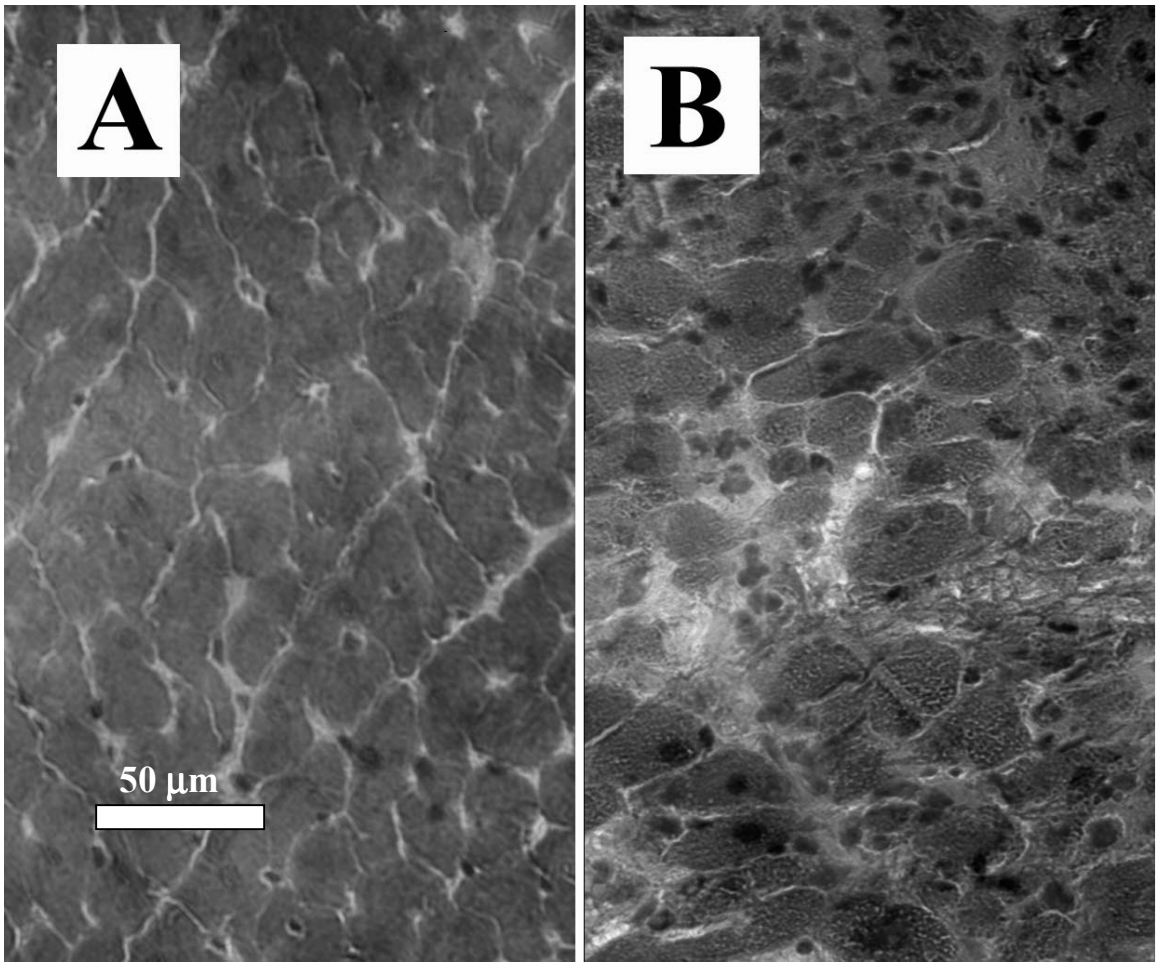

Figure 7-7 Brightfield micrographs of examples of isograft (panel A) and allograft (panel B) rat myocardium stained with hematoxylin and eosin. The isograft tissue was histologically normal, while the allograft tissue was characterized by indicators of acute rejection including edema, lymphocytic infiltration, and myocyte damage. The color version of this figure is shown in Appendix K-7.

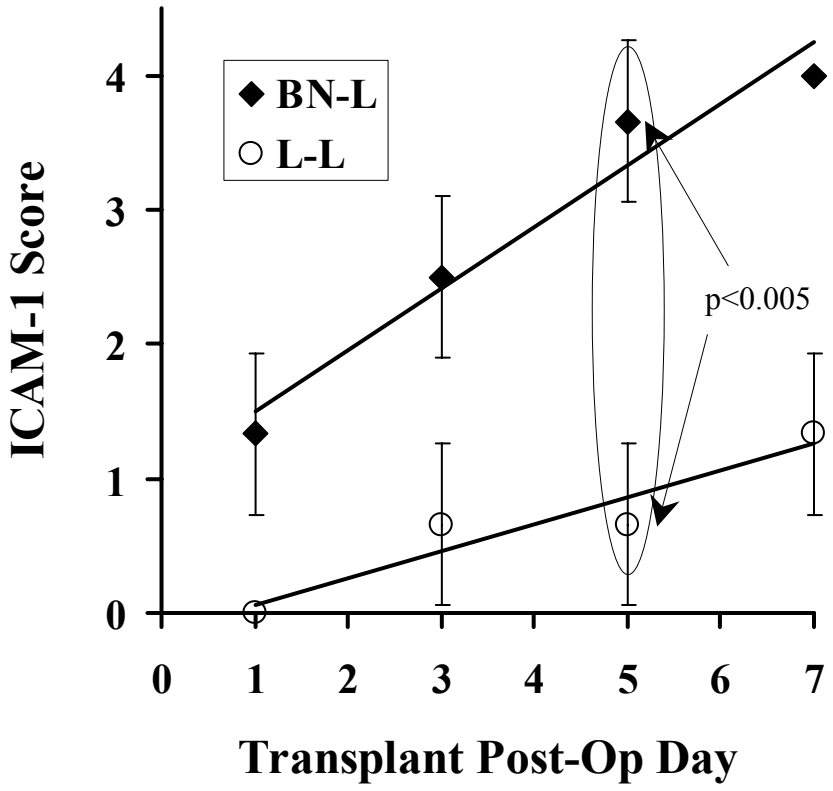

Figure 7-8 Endothelial ICAM-1 expression in BN→L allograft and L→L isograft rat hearts versus post-op day. ICAM-1 expression was scored by blinded observers on a scale of 0 (constitutive ICAM-1 only) to 4 (most positive). The qualitative ICAM-1 score increased more quickly in the allografts than isografts ($p<0.01$), and at post-op day 5 was significantly higher for allograft than isograft rats ($p<0.005$). (Mean ± SD).

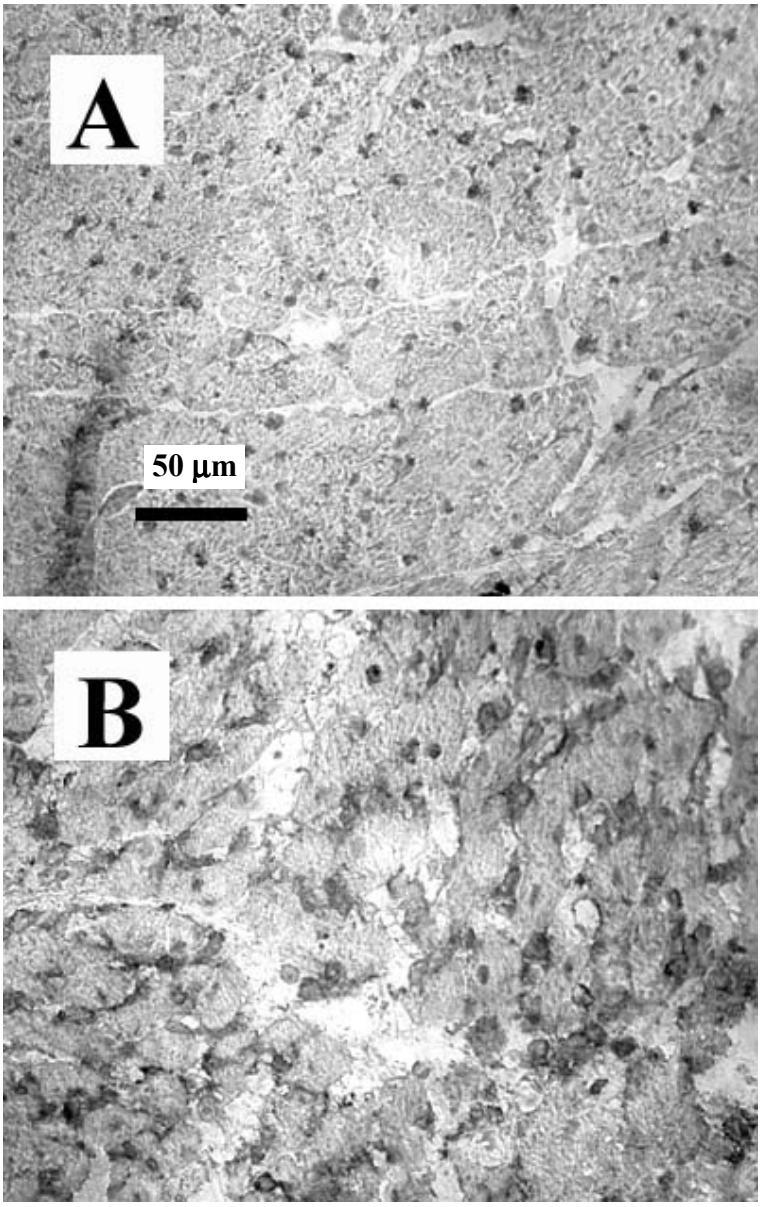

Figure 7-9 Brightfield micrographs of isograft (panel A) and allograft (panel B) rat myocardium stained for ICAM-1 (reddish-brown). The isograft tissue showed only a small amount of constitutively expressed vascular ICAM-1, whereas the rejecting allograft tissue showed dramatic upregulation of endothelial ICAM-1 expression in the microcirculation. (Same as **Figure 2-4**). The color version of this figure is shown in Appendix K-8.

7.3.2.2 Myocardial Contrast Echocardiography. Of the 23 recipient rats used, 1 died during transplantation surgery, and 4 died on post-op day 5 from anesthetic complications prior to complete data collection. Three rats were excluded from the study due to poor perfusion of the donor myocardium as qualitatively visualized by MCE during the initial Optison injection.

Figure 7-10 shows representative *in vivo* ultrasound images obtained at 3:00 (left panels) and 3:20 (right panels) after injection of MB_{ICAM} in a rejecting BN-L rat (upper panels) or control L-L rat (lower panels). Figure 7-11 shows the corresponding images obtained with $MB_{Control}$ in the same rejecting and control rats as Figure 7-10. At 3 min after MB_{ICAM} injection there was intense myocardial opacification (high acoustic signal) in the rejecting rat (Figure 7-10-A) that was not seen in the control rat (Figure 7-10-C). The corresponding images at 3 min for $MB_{Control}$ showed only mild myocardial contrast in the rejecting rat (Figure 7-11-A), of an intensity much lower than that seen after MB_{ICAM} injection in this same rat (Figure 7-10-A). There was no significant myocardial opacification 20 seconds later in any of the injections (Figure 7-10-B and D, Figure 7-11-B and D), confirming that there were few remaining freely circulating microbubbles by this time, and thus any acoustic signal acquired at 3:00 was due predominantly to adhered, rather than circulating microbubbles.

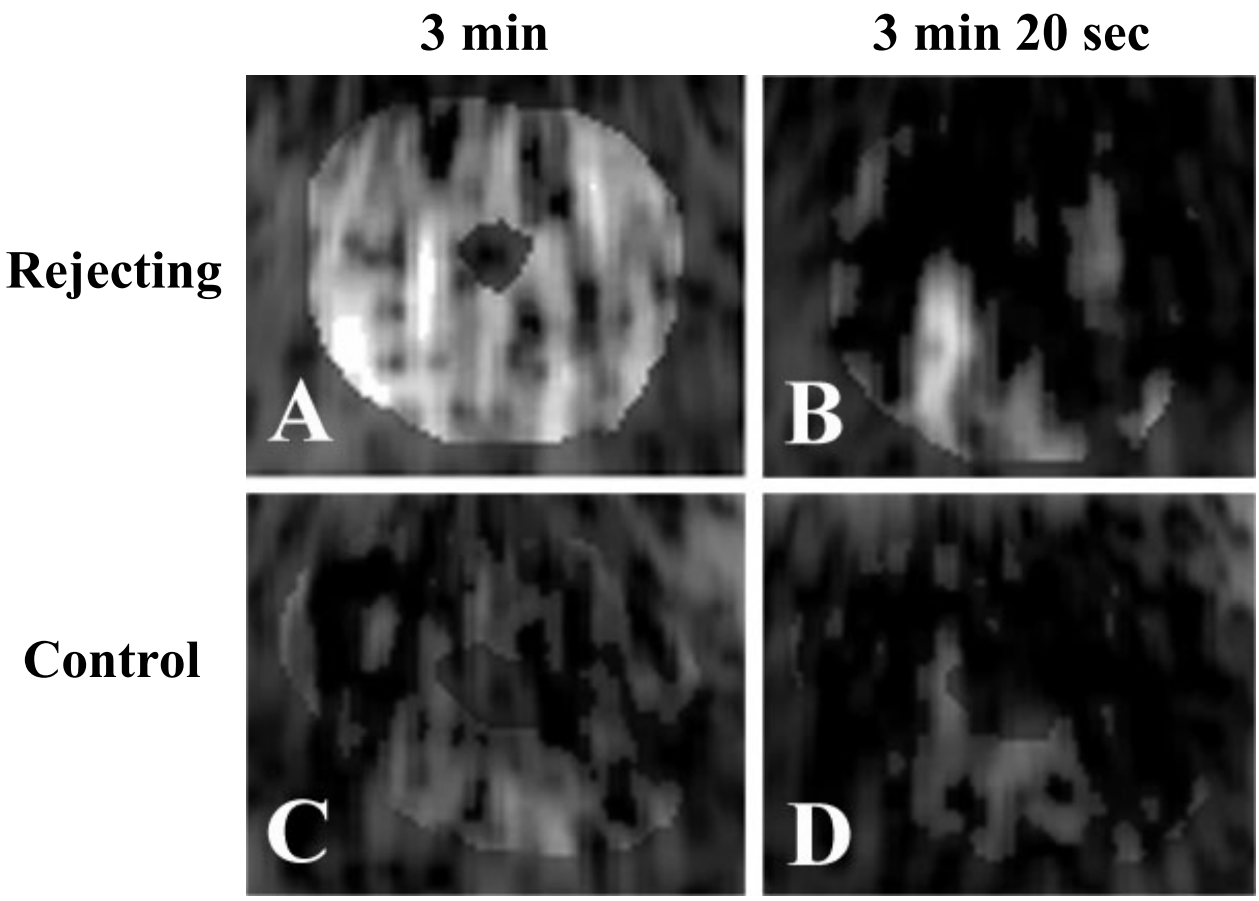

Figure 7-10 Background-subtracted, color-coded ultraharmonic ultrasound images acquired after injection of ICAM-1-targeted microbubbles (MB_{ICAM}) in the donor myocardium of a rejecting allograft rat (upper panels) and control isograft rat (lower panels). Gradations from red → orange → yellow → white denote increasing opacification. Ultrasound contrast enhancement by MB_{ICAM} in the rejecting myocardium (panel A) was greater than in the control myocardium (panel C). There was minimal contrast in both hearts at 3:20. The color version of this figure is shown in Appendix K-9.

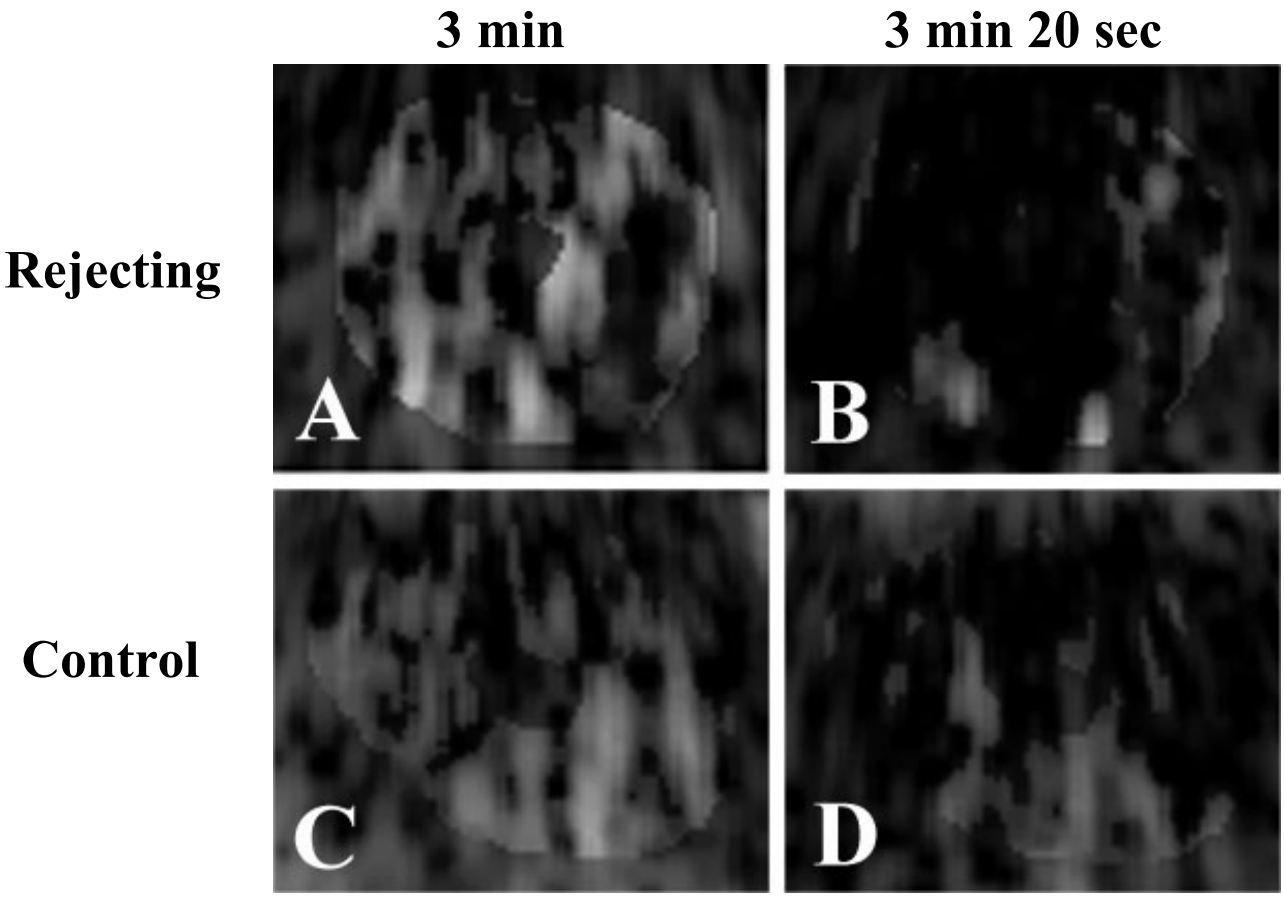

Figure 7-11 Corresponding ultrasound images acquired after injection of isotype control microbubbles ($MB_{Control}$) in the donor myocardium of the same rejecting (upper panels) and control (lower panels) rats as in **Figure 7-10**. Gradations from red → orange → yellow → white denote increasing opacification. Ultrasound contrast enhancement by $MB_{Control}$ was minimal in both rejecting and normal myocardium. The color version of this figure is shown in Appendix K-10.

Table 7-2 Graft myocardial videointensity (VI) measurements for ICAM-1-targeted microbubbles (MB_{ICAM}) and isotype control microbubbles ($MB_{Control}$) for each of the 15 completely analyzed rats. Mean VI's were calculated as the average pixel intensity within the left ventricular region of interest in the first frame at 3:00 minus the average intensity in the first frame at 3:20. The $VI_{targeted}$ index is defined in the text.

Rat #	Transplant Type	MB_{ICAM} Mean VI (3:00 – 3:20)	$MB_{Control}$ Mean VI (3:00 – 3:20)	$VI_{targeted}$	Mean $VI_{targeted}$
C1	BN-BN	17.5	11.3	6.2	1 ± 4 (Control)
C2	BN-BN	1.0	0.0	1.0	
C3	BN-BN	12.5	19.0	-6.5	
C4	BN-BN	13.6	9.3	4.3	
C5	L-L	15.3	14.7	0.6	
C6	L-L	10.4	8.9	1.5	
C7	L-L	19.5	20.6	-1.1	
R1	BN-L	9.2	4.0	5.2	10 ± 4 (Rejecting)
R2	BN-L	40.6	25.7	14.9	
R3	BN-L	31.2	21.3	9.9	
R4	BN-L	25.1	12.9	12.2	
R5	BN-L	25.3	15.4	9.9	
R6	BN-L	28.0	24.5	3.5	
R7	BN-L	28.1	12.5	15.6	
R8	BN-L	21.4	14.8	6.6	

Table 7-2 lists the quantitative videointensity (VI) data for each of the 15 completely analyzed rats. The VI was measured over the left ventricular myocardium for each image, and the VI difference between the 3:20 image and the 3:00 image for each injection in each rat was calculated.

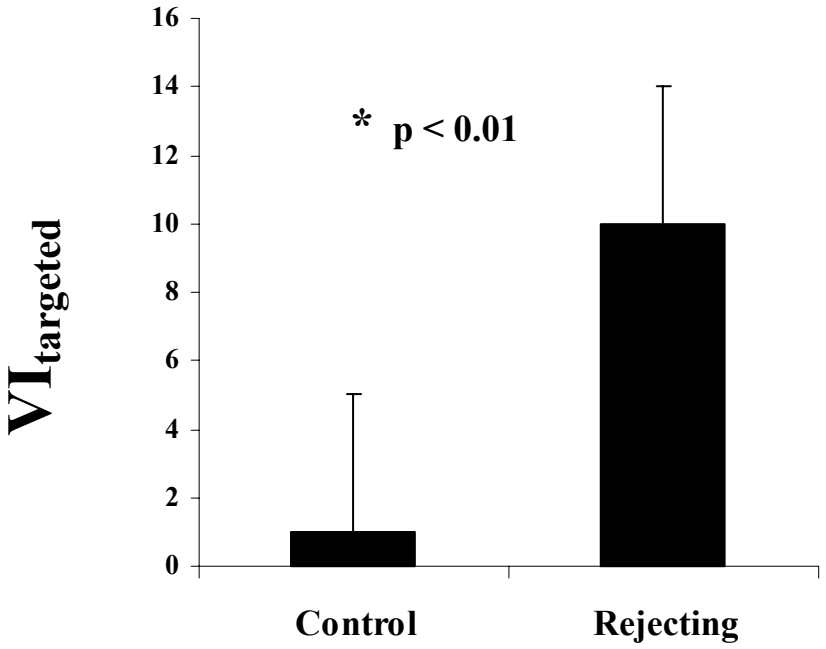

Figure 7-12 Mean $VI_{targeted}$ for control (isograft) vs. rejecting (allograft) donor hearts (n = 7 and 8, respectively). The $VI_{targeted}$ compares the signal due to adhered MB_{ICAM} with the signal due to adhered $MB_{Control}$ to give a measure of the signal attributable to specific microbubble adhesion to vascular ICAM-1. The $VI_{targeted}$ for allograft rats was significantly higher than the $VI_{targeted}$ for isograft rats. (Mean ± SD).

Figure 7-12 summarizes the data for all 15 rats in terms of the $VI_{targeted}$ index. The mean $VI_{targeted}$ for the 7 control isograft transplants was 1 ± 4 intensity units, which was not significantly different from zero. The mean $VI_{targeted}$ for the 8 rejecting allograft transplants was 10 ± 4 intensity units, which was both significantly higher than zero ($p<0.01$) and significantly higher than the isograft $VI_{targeted}$ ($p<0.01$).

7.4 Discussion

The main finding of the work in this chapter is that ultrasound using contrast microbubbles targeted to ICAM-1 can non-invasively detect acute cardiac allograft rejection. The *in vitro* data demonstrate that ICAM-1-targeted MBs preferentially adhere to inflammatory versus normal cultured rat endothelial cells, and the *in vivo* data show that this phenomenon results in increased opacification during myocardial contrast echocardiography. These studies uniquely investigate targeted acoustic agents in cardiac tissue, and are the first to demonstrate the noninvasive assessment of acute organ transplant rejection using ultrasound. These findings advance the development of targeted ultrasound contrast agents for the assessment of endothelial dysfunction, which has applications for the diagnosis of acute cardiac allograft rejection in particular, and all inflammation-linked disease processes in general.

7.4.1 Targeted Adhesion to Cultured Rat Endothelium

In vitro experiments utilized the parallel plate perfusion apparatus, allowing us to establish that microbubbles targeted via conjugation with anti-rat-ICAM-1 antibody are capable of binding to rat endothelium. This was a necessary first step towards the *in vivo* experiments, as

all of our previous *in vitro* studies had been accomplished using anti-human antibodies on the microbubble shell, and studied adhesion to human cells.

Flow cytometric measurements verified that our cell culture model of inflammation did in fact overexpress the inflammatory marker of interest, ICAM-1, increasing its expression approximately 8-fold in response to interleukin stimulation. A positive relationship was found between ICAM-1 expression and MB_{ICAM} adhesion. The observed adherence of MB_{ICAM} to normal cells is likely due to the constitutive expression of ICAM-1 even on resting ECs (as described in chapter 4). MBs conjugated to a nonspecific isotype control antibody ($MB_{Control}$) showed minimal adherence to both cell types, suggesting that neither the presence of immunoglobulin on the MB surface nor the lipid components of the microbubble shell were responsible for the observed adhesion.

These *in vitro* tests demonstrated that (1) the adhesion of MBs targeted to rat ICAM-1 depends on the level of ICAM-1 expression on the rat endothelial cell surface, (2) targeted MBs are capable of binding to ICAM-1 on rat endothelium under physiologically relevant shear conditions, and (3) the adhesion of these targeted MBs is due to specific binding interactions of the antibody with ICAM-1. These points concerning targeted MB adhesion were a necessary prelude to the *in vivo* experiments, and allowed us to interpret the *in vivo* findings in terms of specific adhesion to ICAM-1.

7.4.2 Ultrasound Detection of Allograft Rejection

Abdominal rat heterotopic heart transplantation was shown to be a valid model of acute allograft rejection. By post-op day 5, hetero-strain (BN→L) allografts reliably demonstrated the signs of high-grade acute rejection, while homo-strain (BN→BN or L→L) isografts showed

substantially normal histology, as shown in Figure 7-7. This difference in rejection status was reflected in the level of ICAM-1 expression by the endothelium of the coronary microcirculation, as determined via immunohistochemistry. As seen in Figure 7-8 and Figure 7-9, microvessels of the allograft myocardium strongly expressed ICAM-1, while those in isograft tissue expressed only low, constitutive levels of the marker. Thus, our chosen target is more prevalent in rejecting than non-rejecting myocardium, and we could reasonably hypothesize that ICAM-1-targeted MBs would adhere preferentially to the rejecting tissue.

Having established that the rejection status of the donor heart could be predicted and that our chosen target molecule, ICAM-1, is indeed more prevalent in rejecting myocardium, we performed ultrasound imaging of the *in vivo* donor hearts using our two acoustically active MB species, MB_{ICAM} and $MB_{Control}$. The particular ultrasound machine and probe were chosen because they have ultraharmonic capability, which offers excellent contrast sensitivity, although at the cost of lower spatial resolution. The high sensitivity of ultraharmonics ensured that we could adequately visualize the contrast agent in the myocardium even at relatively low concentrations. A high-MI, destructive imaging technique was chosen because it is the most sensitive method for detecting small numbers of bubbles adhering as a result of our necessarily small volumes of injection into our rats.

The enhanced myocardial contrast seen with MB_{ICAM} in rejecting myocardium demonstrates preferential adhesion of the targeted microbubbles to the inflammatory tissue. The upregulated ICAM-1 expression in these hearts allows for preferential binding of MB_{ICAM} versus $MB_{Control}$, manifested as a high $VI_{targeted}$. Conversely, the control myocardium shows little difference between MB_{ICAM} and $MB_{Control}$ adhesion, as expected due to the low ICAM-1 expression in these isograft transplants. Additionally, from the ultrasound images in Figure 7-10

and from the $VI_{targeted}$ results, it is apparent that there was also at least some MB_{ICAM} adherence to non-rejecting control myocardium; this is likely due to low levels of constitutive ICAM-1 expression, as seen in the *in vitro* studies. There may also have been some adhesion of $MB_{Control}$ to rejecting myocardium, as seen in Figure 7-11. This (minimal) attachment of control microbubbles likely represents binding to activated leukocytes adhered to endothelium, as has been previously shown in models of acute inflammation [83]. The magnitude of the contrast enhancement resulting from such attachment, however, is much lower than that caused by MB_{ICAM} attachment to ICAM-1 on the same rejecting tissue (Figure 7-10). This difference perhaps indicates either greater quantity of ICAM-1 sites compared to leukocytes available for binding microbubbles, and/or greater retention of microbubbles bound via specific antibody/antigen interaction (as in the case of MB_{ICAM}) versus nonspecific interactions (as with $MB_{Control}$). Our data thus suggest that a *targeted* microbubble system is superior to a non-specific, non-targeted microbubble system for detecting acute rejection.

The pattern of microbubble adhesion in some cases appeared patchy, as seen in Figure 7-10. This observed patchiness of opacification is possibly due to two phenomena. First, the endothelial expression of ICAM-1 in the myocardium may be patchy, i.e. the inflammatory process of acute rejection may be inhomogeneous. Second, there could be regional variations in capillary volume within the myocardium, causing heterogeneous perfusion and thus differences in the regional concentration of MB_{ICAM}. We were not able to quantify capillary volume, as doing so would have required continuous non-targeted microbubble infusion, potentially volume-overloading the animal. In addition, the high sensitivity of our ultraharmonic ultrasound technique was achieved at the expense of decreased spatial resolution, rendering us unable to precisely localize the regional distribution of contrast enhancement.

Our data demonstrate a correlation between tissue rejection status, microcirculatory ICAM-1 expression, and targeted ultrasound signal, indicating that MCE using our ICAM-1-targeted microbubbles can successfully detect acute cardiac transplant rejection.

7.4.3 Comparison with Previous Studies

This is the first study to use targeted ultrasound to assess the expression of adhesion molecules in the myocardium, and the first to detect organ transplant rejection. As discussed in Section 1.6, others have demonstrated the specific adhesion of ultrasound agents to various markers of disease. Thrombi have been imaged ultrasonically using a biotinylated microbubble injected after pre-coating of the thrombus with avidin [90], and with a microbubble targeted to fibrinogen [87-89].

Inflammation in particular has been imaged using microbubbles targeted to activated leukocytes in a mouse cremaster model [97] and a canine myocardial reperfusion (post-ischemic) model [98], and microbubbles targeted to p-selectin in a mouse kidney model [96].

Acute transplant rejection has been imaged using a variety of techniques. Scintigraphic approaches include radiolabeled agents targeting apoptosis [129], major histocompatibility complex antigens [133], and ICAM-1 [134, 135]. Such scintigraphic techniques are encumbered by the disadvantages the requirement for radioactive isotopes and poor spatial resolution. Other non-targeted, radiologic approaches include the use of MRI to measure morphologic changes [121] and PET to measure metabolic changes [125, 126] associated with organ transplant rejection. These imaging techniques are limited by the requirement for equipment that is generally available only in tertiary care centers.

Our work advances beyond these previous reports, by making several unique demonstrations. This is the first study to target cell adhesion molecules in the coronary microcirculation, and the first to use ultrasound to detect the presence of ICAM-1 *in vivo*. Combining these with our *in vitro* and histologic findings allowed us to make the first demonstration of the *in vivo* detection of acute cardiac allograft rejection using targeted ultrasound.

7.4.4 Limitations

Our data demonstrate the targeted ultrasonic detection of cardiac allograft rejection using a fulminant model. It is unknown if similar differential adhesion of targeted microbubbles would occur with lesser degrees of inflammation, as seen in lower grade rejection. The *in vitro* data presented in Chapter 6 explored the range of inflammation (as measured by ICAM-1 expression) between normal and peak (fulminant) inflammation, and suggest that the adhesion strength of targeted microbubbles depends linearly on the level of inflammation. Thus, even with lesser degrees of transplant rejection, which express lower amounts of ICAM-1, we would still expect to see increased ICAM-bubble adhesion as compared to normal tissue. However, we need to further investigate this relationship between ICAM-1 expression and targeted microbubble adhesion *in vivo*, to determine if our ultrasound imaging technique can differentiate inflamed versus normal tissue at moderate ICAM-1 levels, such as would be important in monitoring inflammation in response to therapy.

The acoustic signals acquired at 3 min after MB_{ICAM} injection may not have been solely attributable to microbubble adhesion to endothelium, for two reasons. First, it is possible that ICAM-1-targeted microbubbles did not adhere exclusively to endothelium, but rather to other

cells that can express low levels of ICAM-1, including erythrocytes, activated leukocytes, eosinophils, and macrophages [6, 34]. However, had there been significant microbubble adhesion to blood cells, the myocardial opacification at 3:20 after microbubble injection would have been more intense, due to replenishment of the ultrasound imaging field by blood cells carrying adhered microbubbles. Furthermore, the finding that the $VI_{targeted}$ was high in rejecting allograft rats and very low in non-rejecting isograft rats suggests that microbubble interaction with blood cells was minimal compared to targeted microbubble adhesion to vascular ICAM-1. Second, a portion of the signal at 3:00 may have been due to persistently circulating free microbubbles. This possibility is also unlikely, as there was minimal signal 20 seconds later at 3:20, when freely circulating microbubbles would have been expected to replenish the beam. Also, our preliminary experiments using Optison demonstrated that the contrast agent was cleared from the myocardium by 3:00, suggesting that this time frame is adequate to allow washout of non-adherent microbubbles.

As mentioned previously, we were unable to measure myocardial perfusion, which could affect microbubble delivery. The rejecting heart could be hypoperfused compared to normal hearts due to fibrosis and myocyte death, or could be hyperemic due to inflammation. Standard radiolabeled microsphere technologies could not be used to measure regional flow in small specimens such as the rat heart. Continuous ultrasound imaging using continuous infusions of a contrast agent such as Optison could have been used to measure perfusion, but the infusion volume required for such quantification would likely have been so high as to physiologically destabilize the animal preparation. The bolus injection of Optison given at the beginning of each experiment should have been adequate to rule out gross areas of hypoperfusion or infarction, which appeared as myocardial contrast defects, and did in fact result in the exclusion of 3 rats

from the study. Additionally, our use of the $VI_{targeted}$ index in the current study should minimize the dependence of measured microbubble adhesion on myocardial blood flow, by making direct comparisons between the videointensity due to the two different microbubble species, MB_{ICAM} and $MB_{Control}$, in the *same* rat.

Our destructive imaging protocol, which included a 3 min delay between contrast injection and the first ultrasound pulses, may be difficult to translate into clinical application, as precisely locating the heart prior to delivery of the first imaging (destructive) pulse may be a challenge. In the current clinical application of myocardial perfusion imaging using intermittent bubble destruction, there is minimal real-time feedback to allow adjustment of transducer position. However, sonographers in the clinic have already been trained to initially locate an image (in real time) and with the patient lying still, fix the transducer on the chest such that, after a period of "blinded" waiting, the next image can still be accurately registered. Such an approach does present a challenge, though, and equipment manufacturers have begun designing methods to address precisely this issue. For example, ultrasound equipment has been developed that offers high-mechanical index (destructive) triggered imaging along with simultaneous real-time, low-MI (non-destructive) imaging. Such constant low-MI imaging would allow maintenance of an adequate imaging window to allow for transducer adjustments during the microbubble injection protocol. This type of low-MI monitoring could possibly be accomplished even with standard ultrasound equipment, by manually manipulating the MI and pulsing intervals during the imaging protocol.

Further study of the adhesive characteristics of targeted microbubbles is needed to improve their potential utility for *in vivo* imaging, including optimization of shell parameters such as composition, size, and flexibility, and optimization of the imaging protocol.

Experiments similar to those in the current study performed in a larger animal model, either porcine or canine, may lead to even stronger results.

7.4.5 Summary

The data in this chapter have demonstrated for the first time the ability of targeted ultrasound to non-invasively detect acute cardiac allograft rejection *in vivo*. Contrast microbubbles targeted to the inflammatory cell surface marker ICAM-1 were shown to preferentially bind to interleukin-activated cultured rat endothelium. Furthermore, this phenomenon of selective adherence to tissue overexpressing ICAM-1 was exploited to demonstrate the non-invasive ultrasonic detection of acutely rejecting myocardium in a rat heterotopic transplant model.

Such ultrasonic detection of acute rejection could offer an improvement over the current clinical gold standard of endomyocardial biopsy. Additionally, such an ultrasound technique that is able to detect molecular markers of disease in the vasculature may offer promise in other fields, including ischemic heart disease, targeted drug delivery, and oncology.

8.0 APPLICATIONS IN TUMOR ANGIOGENESIS

8.1 Introduction

A unique opportunity was available during the time this dissertation research took place, to investigate the potential of targeted ultrasound contrast agents to offer molecular imaging of tumor angiogenesis. The laboratory of Dr. Michael Wong at the University of Pittsburgh Cancer Institute had recently isolated a series of tumor vasculature-binding peptides, and was interested in translating this finding into an angiogenesis imaging technique. Concurrently, our group was interested in pursuing our targeted ultrasound studies in additional *in vivo* models of endothelial dysfunction. We felt that a collaboration combining the expertise of the two laboratories could yield results that would contribute toward the development of a noninvasive, ultrasonic molecular imaging tool for the assessment of tumor angiogenesis.

As discussed in Section 1.4, angiogenesis is a requirement for the progression of solid tumors to a malignant, metastatically-competent state [138, 141]. Without an adequate vascular supply, the tumor tissue remains restricted to a small volume. In addition, endothelial molecular markers of angiogenesis have been correlated with such prognostic indicators as tumor size and metastatic potential [152, 153]. Thus an imaging technique that can assess the functional status of the tumor endothelium may be valuable for the diagnosis and characterization of solid tumors, and the monitoring of tumor response to therapy.

The work presented in Chapter 7 demonstrated proof-of-principle for the *in vivo* identification of acute cardiac allograft rejection using noninvasive targeted contrast

echocardiography. Based on those previous results, we hypothesized in the current study that contrast microbubbles targeted to tumor angiogenic-specific endothelial markers would preferentially adhere to tumor versus normal endothelium, and that this selective binding phenomenon would result in increased contrast enhancement during ultrasound imaging. These hypotheses were tested by conjugating our lipid-based microbubble to a tumor endothelium-specific binding peptide, and investigating the adhesion properties of this agent to cultured endothelium as well as in a mouse solid tumor model.

8.1.1 MW3 Tumor-Binding Peptide

The tripeptide sequence arginine-arginine-leucine (RRL), designated MW3, is a tumor EC-specific binding peptide that was identified in Dr. Michael Wong's laboratory by using an *in vitro* bacterial peptide display library [233]. Briefly, two different endothelial cell types were used for panning: Matrigel-invading cells, comprised of cells that infiltrate an FGF-doped Matrigel plug, and tumor-derived endothelial cells (TDEC), which were harvested by collagenase digestion from subcutaneous SCC VII squamous cell carcinomas grown in C3H/HeJ mice and isolated using fluorescent cell sorting with an antibody against platelet-endothelial cell adhesion molecule (PECAM, CD31) [234]. These Matrigel-invading cells represent non-tumor angiogenic ECs, while the TDECs represent ECs from a tumor xenograft, and contain tumor-specific markers. A bacterial peptide display library was panned across the Matrigel-invading cells to remove clones with peptides that bind to non-tumor EC markers, and then panned across the TDECs to identify clones that do bind specifically to tumor markers. This negative and positive panning sequence was cycled repeatedly, and those clones that survived the selection

were expanded, and had their peptides isolated. One of the identified recurring sequences was MW3.

Characterization performed by Dr. Wong's group included *in vitro* binding experiments conducted by incubating fluorescently tagged MW3 with either cultured murine TDECs, or murine NIH3T3 cells as a negative cell control. A peptide consisting of only glycines served as a negative peptide control. As seen in Figure 8-, MW3 binds much more strongly to tumor-derived ECs (left upper panel) than control cells (left lower panel), while the glycine control peptide binds minimally to both cell types, thus demonstrating that the MW3 peptide sequence binds specifically to tumor-derived endothelium.

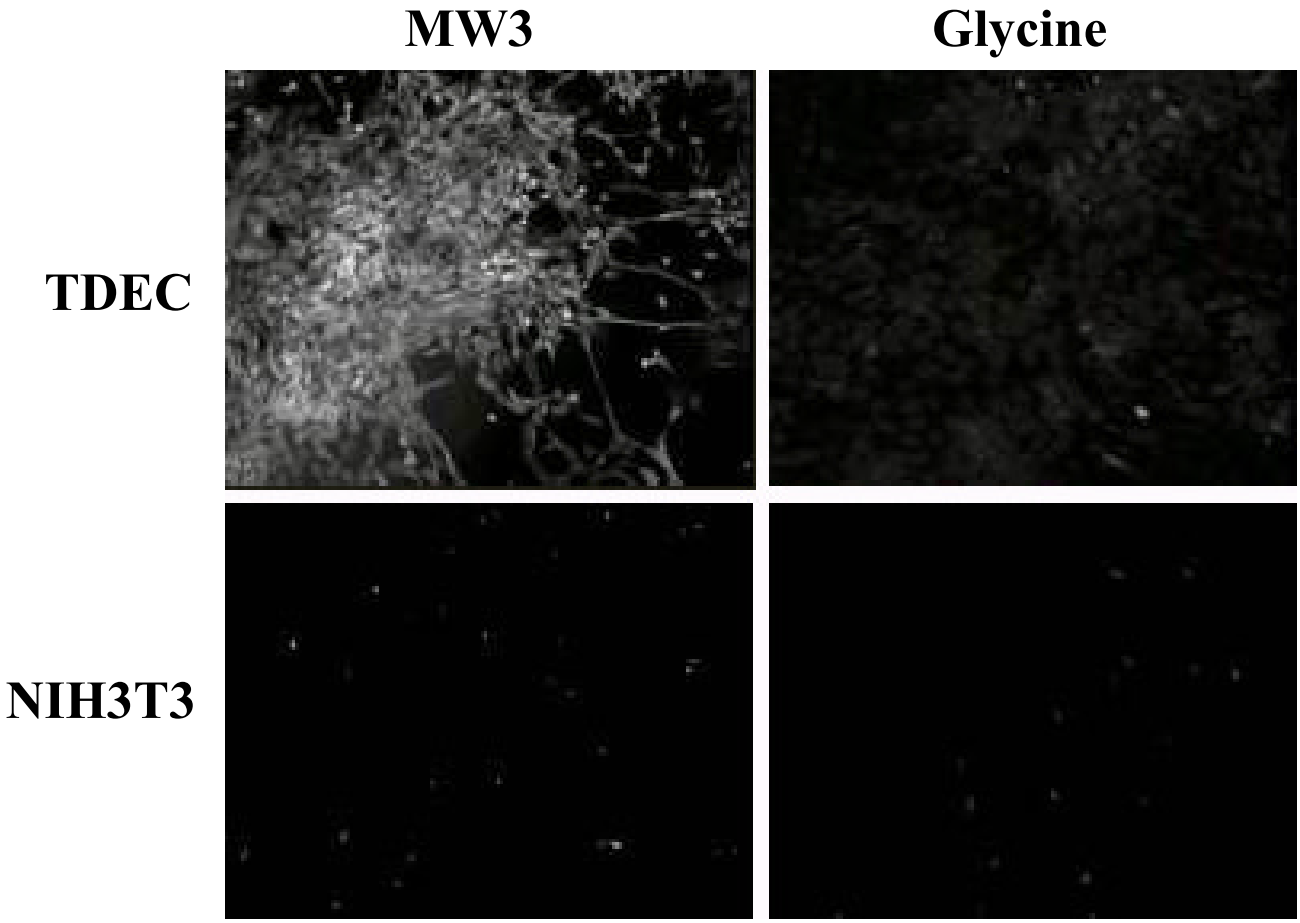

Figure 8-1 Fluorescent micrographs showing that the peptide MW3 (left panels) binds strongly to cultured angiogenic tumor-derived endothelial cells (TDEC, upper panels), but not to control cells (NIH3T3, lower panels). A control peptide composed only of glycines (right panels) shows only minimal binding to both cell types. Courtesy of Dr. Michael K. K. Wong.

In vivo binding characterization utilized mice bearing two types of solid tumors, Clone C and PC3. Clone C cells are derived from NIH3T3 mesenchymal mouse cells, transfected to secrete high levels of FGF. These cells are engineered to grow tumors that are highly vascularized, i.e. very angiogenic. PC3 cells are derived from human prostate tumor. Fluorescently tagged MW3 or glycine control peptides were injected intravenously into these tumor-bearing mice, and the tumors were later harvested, sectioned, and imaged microscopically. Sample fluorescent micrographs are shown in Figure 8-1, demonstrating that MW3 peptide adherence is substantially greater than glycine control peptide adherence to both tumor types.

To summarize, the above previous work from Dr. Wong's laboratory identified a short peptide sequence, MW3, that specifically binds tumor endothelium both *in vitro* and *in vivo*. In the remainder of this chapter will be presented our work investigating the binding properties of acoustically active microbubbles targeted to tumor angiogenesis via conjugation with the MW3 peptide. Such an agent may offer noninvasive functional imaging of tumor angiogenesis, allowing for the assessment of the malignancy potential of solid tumors, and the monitoring of tumor therapy.

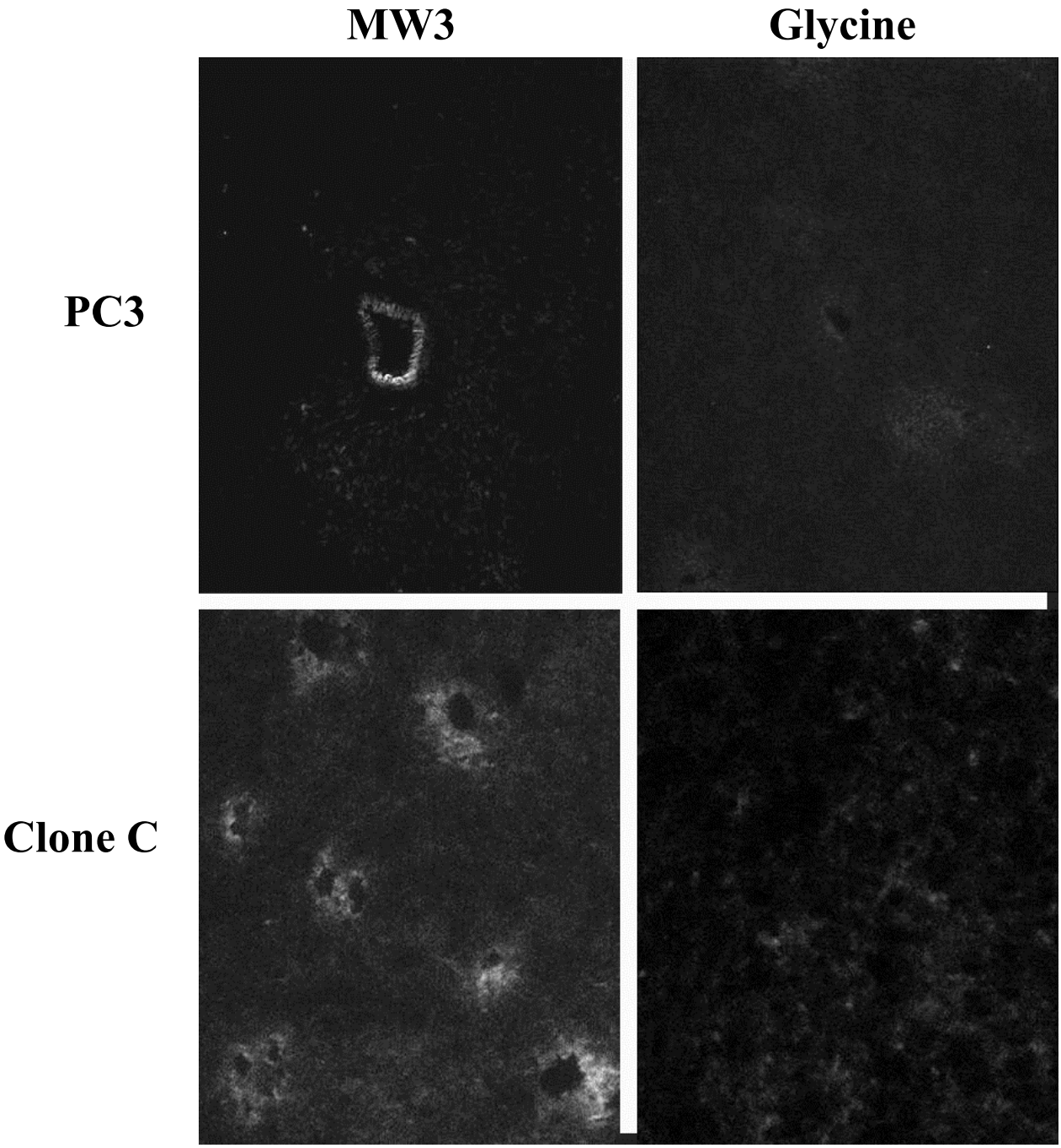

Figure 8-1 Fluorescent micrographs of PC3 (upper panels) and Clone C (lower panels) tumors harvested from mice following *in vivo* intravenous injection of fluorescently-labeled MW3 (left panels) or glycine control peptide (right panels). In comparison to the glycine control, MW3 binds strongly to the tumor vasculature. Courtesy of Dr. Michael K. K. Wong.

8.2 Methods

8.2.1 Targeted Microbubbles

Biotinylated lipid-based microbubbles (MP1950) were conjugated to 9-mer cyclic peptides containing either the MW3 sequence (see Figure 8-2) or a control glycine peptide (see Figure 8-3). The MW3-targeted cyclic peptide comprised the RRL sequence bracketed by glycines, and terminated on both ends with cysteine residues (N'-Cys-Gly-Gly-**Arg-Arg-Leu**-Gly-Gly-Cys-C'), while the control peptide was identical except with the substitution of glycines for the Arg-Arg-Leu sequence (Cys-Gly-Gly-Gly-Gly-Gly-Gly-Gly-Cys); both peptides were biotinylated at the amino-terminal cysteine. Both biotinylated cyclic peptides were custom-synthesized (Genemed Synthesis, South San Francisco, CA), and were courtesy of Dr. Michael K. K. Wong. Disulfide bonds form between the two cysteines residues on each peptide, maintaining the cyclic structure. Biotin is conjugated at one of the cysteines residues, allowing the cyclic peptides to be linked to our microbubbles via avidin/biotin bridging as previously described (see chapter 3). Microbubbles linked to the MW3-containing peptide were designated MB_{MW3}, and those linked to the glycine control peptide were designated $MB_{Glycine}$. Microbubble diameter was 3.2 ± 1.0 μm.

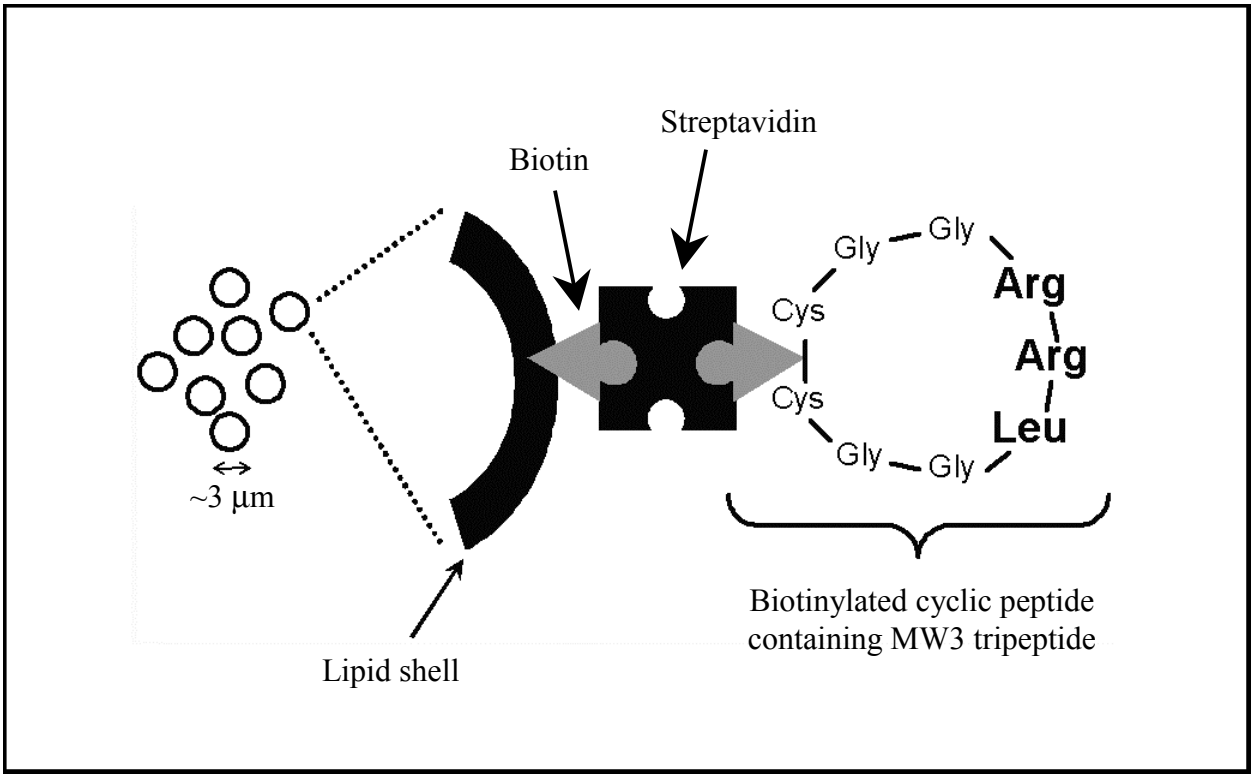

Figure 8-2 Schematic of microbubble conjugation to cyclic peptide containing the MW3 tumor-binding sequence. (Not to scale).

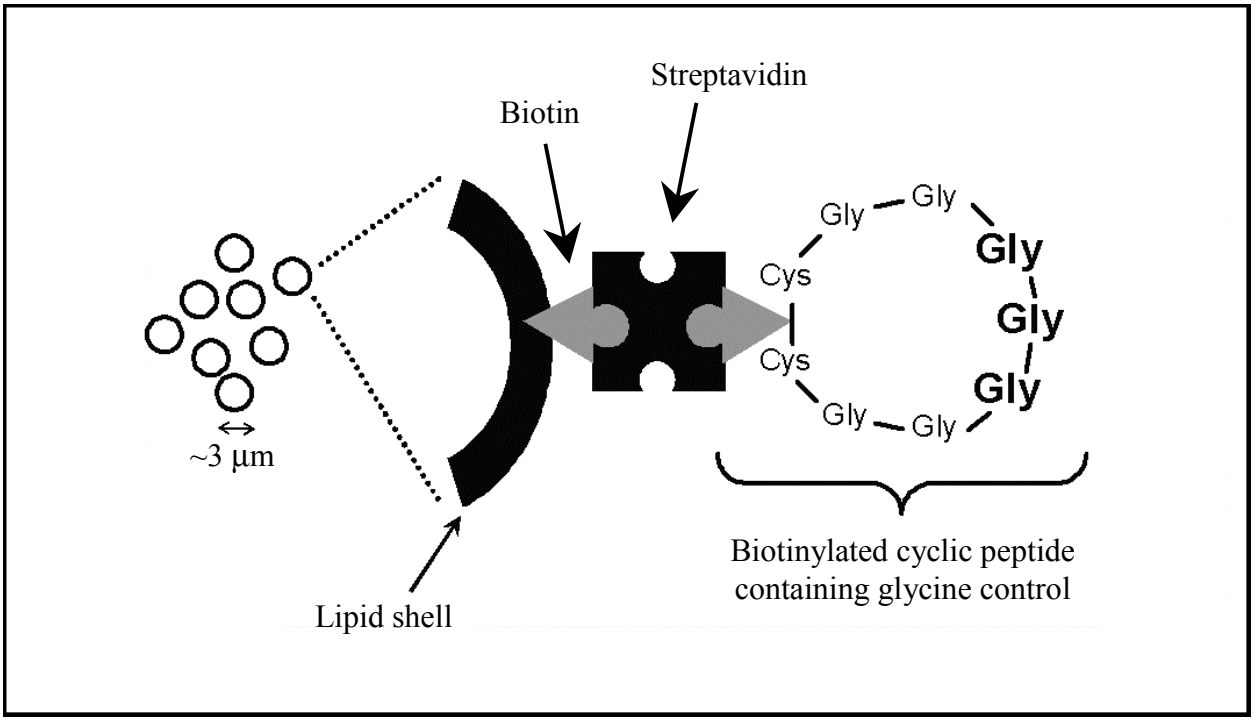

Figure 8-3 Schematic of microbubble conjugation to cyclic peptide containing a glycine control sequence. (Not to scale).

8.2.2 Cell Culture

Mouse tumor-derived ECs (TDECs), originating from a squamous cell carcinoma, (7th-8th passage, courtesy of Dr. Ruth A. Modzelewski) and human coronary artery ECs (HCAECs; 3rd-5th passage) were grown to confluence on glass coverslips in endothelial basal medium supplemented with 5% fetal bovine serum.

8.2.3 *In Vitro* Microbubble Perfusions

The rectangular parallel plate perfusion chamber was used to examine adhesion of microbubbles to cultured tumor-derived and normal ECs. The general setup was as described in Chapter 4. Coverslips of ECs (n = 6-8 per condition) were briefly incubated with quinacrine dihydrochloride (50 μM) as a fluorescent label and mounted in the perfusion chamber. The vacuum seal was applied, and the chamber was primed with 37°C culture medium. A suspension of either MB_{MW3} or $MB_{Glycine}$ (3.33×10^6 MBs/mL) in culture medium was actively perfused through the system at a flow rate corresponding to a wall shear rate of 100 s^{-1} for 3 min, followed by a 3 min MB-free wash at 100 s^{-1}. Immediately after each perfusion, 20 randomly selected microscopic fields were imaged at 1000X and the number adhered microbubbles quantified.

8.2.4 Mouse Tumor Model

Tumorigenic cells were injected into the flanks of nude mice and allowed to expand into solid tumors as our model of tumor angiogenesis. Experiments were approved by the Institutional Animal Care and Use Committee at the University of Pittsburgh.

Approximately two million tumor cells, either PC3 or Clone C, were injected subcutaneously into the flank of the animal, and allowed to expand for 2 to 6 weeks, until the tumor size was about 0.5 cm^3. A total of 11 mice were injected with tumor cells: 5 with Clone C tumors and 6 with PC3 tumors.

8.2.5 Contrast Echocardiography

MCE was performed with the ATL HDI 5000 ultrasound system and the broadband L12-5 transducer. Intermittent transabdominal images were acquired in pulse inversion mode with a mechanical index (MI) of 0.6. A small plastic bag of water was positioned as a standoff between the ultrasound probe and the mouse flank. Probe position, gain settings, and mid-field focus were initially optimized and maintained throughout each experiment. Triggered images of the tumor were acquired at baseline (pre-injection), 120 sec, and 135 sec after injection of a microbubble solution. Images were recorded digitally and analyzed offline, and average pixel intensity was measured in regions of interest encompassing the tumor.

As before, the goal of the ultrasound image analysis was to differentiate between the acoustic signal due to adhered microbubbles and the signal due to microbubbles still freely circulating in the bloodstream. As such, we used a similar approach to differentiating between signals from these two microbubble populations as in the transplant rejection studies. In pilot MCE studies in mice receiving Optison in doses equivalent to those used in the present study,

acoustic signal in the tumor was no longer detectable by approximately 120 sec after injection, and thus 120 sec was chosen as the delay time. Based on concepts of ultrasound-induced microbubble destruction and image field replenishment described in Chapter 7.2.7, the difference in tumor videointensity between the 120 sec frame (adhered + circulating microbubbles) and the 135 sec frame (predominantly circulating microbubbles) was defined as the signal attributable to microbubble adhesion only.

8.2.6 Ultrasound Imaging Protocol

Ultrasound imaging was performed on the *in vivo* tumor with the mouse in a prone position. Animals were anesthetized with intraperitoneal sodium pentobarbitol (25 mg/kg), intubated with a 22-gauge angiocatheter, and ventilated at 0.1 ml x 150 Hz with a Harvard rodent ventilator. A 24-gauge catheter was placed in the right jugular vein for administration of saline and microbubble solutions. Anesthesia was maintained with intravenous pentobarbitol (25 mg/kg, every 15 min as needed). Pilot studies were conducted with Optison to determine a dosing strategy, and revealed that a single intravenous bolus injection of 5×10^6 microbubbles was able to generate opacification of the tumor that was reproducible and of adequate videointensity.

Mice were given an initial bolus injection of 5×10^6 Optison microbubbles in 0.05 mL saline, during intermittent MCE imaging, to verify adequate probe position, optimize image settings, and verify adequate perfusion of the tumor tissue. Mice with tumors that could not be adequately visualized (poor opacification) were excluded from the study.

Following complete washout of the Optison, an intravenous injection of 5×10^6 MB_{MW3} or $MB_{Glycine}$ in 0.05 mL saline was administered as a bolus followed by a 0.2 mL saline flush

during simultaneous MCE imaging. Timer-triggered frames were captured at baseline, 120 sec, and 135 sec post-injection (see Figure 8-4). Each mouse received paired injections of MB_{MW3} and $MB_{Glycine}$, in random order. The animals were euthanized, and tumor tissue was harvested for anatomic analysis.

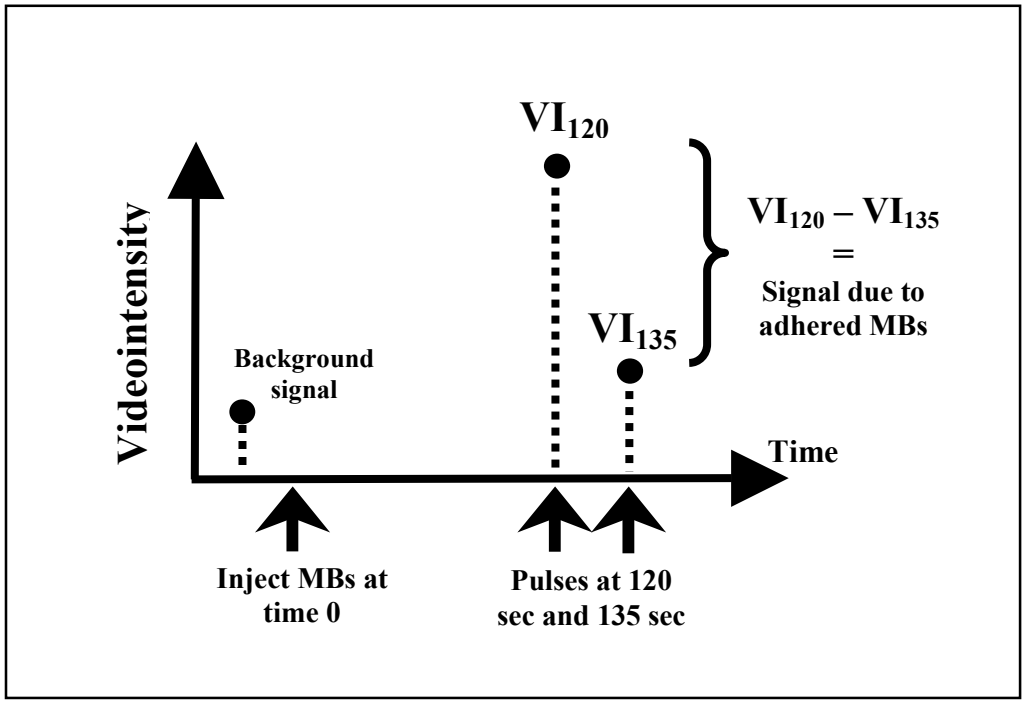

Figure 8-4 Protocol for the *in vivo* ultrasound contrast imaging of tumors in mice. Microbubbles (either MB_{MW3} or $MB_{Glycine}$) were injected at time zero. Ultrasound pulses were given at 120 and 135 sec post-injection. The videointensity of the tumor region of interest at 135 sec was subtracted from the videointensity at 120 sec to achieve the acoustic signal attributable only to adhered microbubbles.

8.2.7 Statistics

Results are expressed as mean ± standard deviation. Data were analyzed with paired two-tailed Student's t-tests, and with two-way ANOVA. Statistical significance was defined as $p<0.05$.

8.3 Results

8.3.1 *In Vitro* Experiments

Figure 8-5 shows brightfield micrographs of coverslips of tumor-derived ECs (TDEC) and normal ECs (HCAEC) perfused with the two species of microbubbles, MB_{MW3} and $MB_{Glycine}$. Microbubbles targeted via the MW3 peptide clearly adhere preferentially to TDEC (left upper panel) versus normal (left lower panel) endothelium. Glycine control MBs adhered only minimally to both cell types (right panels). Quantified data from these *in vitro* perfusions are shown in Figure 8-6. Adherence of $MB_{Glycine}$ was minimal to both TDEC and HCAEC (4 ± 2 and 3 ± 1 MBs/field of view). Adherence of MB_{MW3} was 3-6 times greater than $MB_{Glycine}$ ($p<0.01$), and was significantly greater to TDEC than HCAEC (24 ± 6 vs. 9 ± 1 MBs/field of view, $p<0.01$).

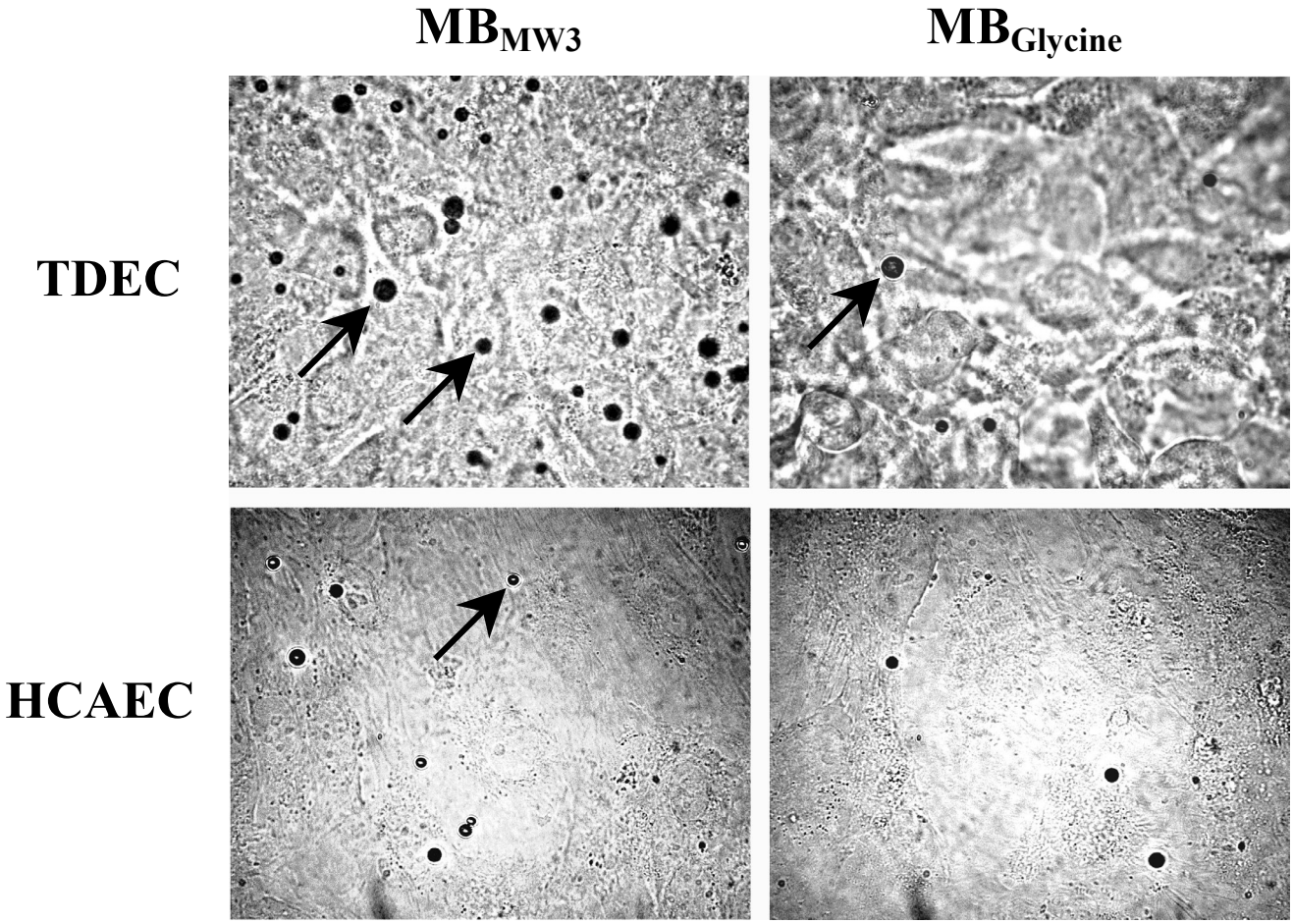

Figure 8-5 Brightfield micrographs of cultured tumor derived endothelial cells (TDEC, upper panels) and normal human coronary artery endothelial cells (HCAEC, lower panels) after exposure to microbubbles conjugated to MW3 (left panels) or a glycine control peptide (right panels). More MB_{MW3} adhered to the tumor-derived cells than to the normal cells. Only a few control microbubbles adhered to either cell type.

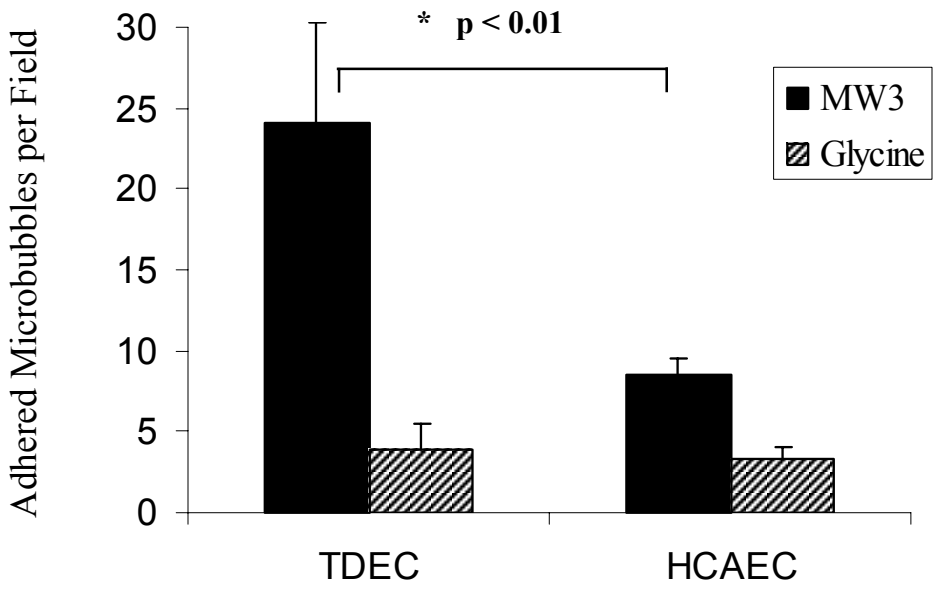

Figure 8-6 *In vitro* adherence of targeted microbubbles to cultured tumor-derived endothelial cells (TDEC) and normal human coronary artery endothelial cells (HCAEC). Adherence of control microbubbles (Glycine) was minimal to both cell types, whereas adhesion of microbubbles targeted via the tripeptide Arg-Arg-Leu (MW3) was significantly higher to tumor-derived cells than normal cells (Mean ± SD).

8.3.2 *In Vivo* Experiments

Of the 11 tumor-bearing mice, 4 were excluded from the study due to inadequate perfusion of the tumor tissue as qualitatively visualized by MCE during the initial Optison injection.

Figure 8-7 shows representative background-subtracted, *in vivo* ultrasound images of a Clone C tumor obtained 120 sec after injection of MB_{MW3} (left panel) or $MB_{Glycine}$ (right panel) into the mouse. Figure 8-8 shows corresponding MB_{MW3} and $MB_{Glycine}$ images from a different mouse, with a PC3 tumor. There was intense contrast enhancement (acoustic signal) in both

tumors after injection with MB_{MW3}. The corresponding images for $MB_{Glycine}$ showed only mild contrast enhancement. There was no significant tumor opacification 15 seconds later in any of the injections (images not shown), confirming that there were few remaining freely circulating microbubbles by this time, and thus any acoustic signal acquired at 120 sec was due predominantly to adhered, rather than circulating microbubbles. It was observed that in the PC3 tumor example, the opacification due to MB_{MW3} (Figure 8-8, left panel) was concentrated in the periphery of the tumor; the central core of the tumor did not appear to be enhanced by the targeted contrast.

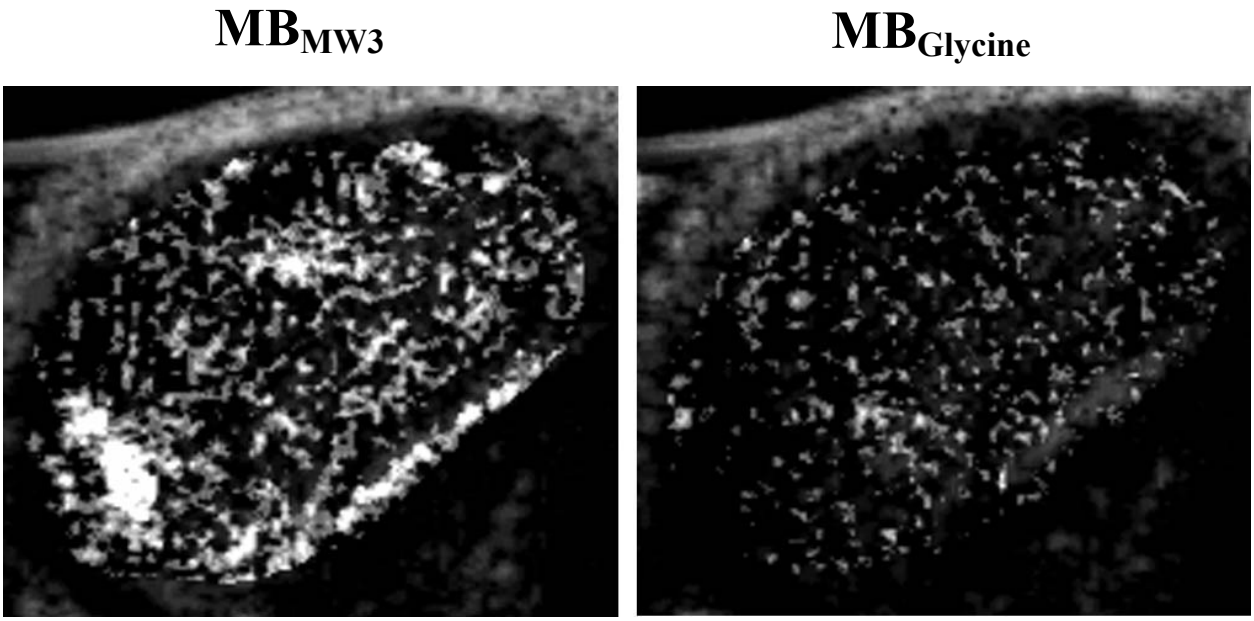

Figure 8-7 Background-subtracted, color-coded ultrasound images taken 120 seconds after injection of microbubbles conjugated to MW3 (left image) or glycine control peptide (right image) into a mouse bearing a Clone C tumor. The region within the tumor has been color-coded. Gradations from red → orange → yellow → white denote increasing opacification. MB_{MW3} resulted in greater contrast enhancement. The color version of this figure is shown in Appendix K-11.

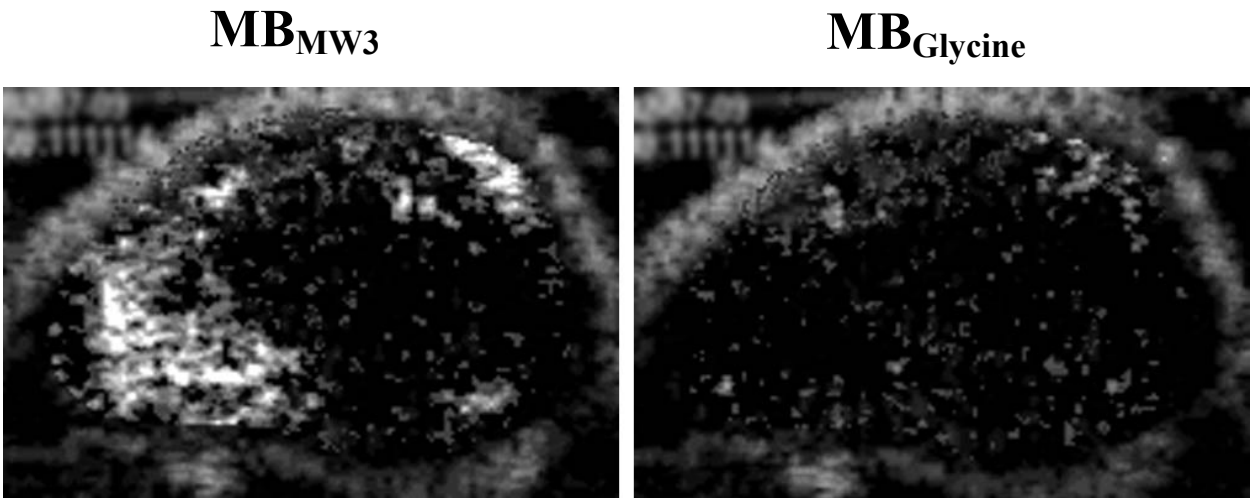

Figure 8-8 Background-subtracted, color-coded ultrasound images taken 120 seconds after injection of microbubbles conjugated to MW3 (left image) or glycine control peptide (right image) into a mouse bearing a PC3 tumor. The region within the tumor has been color-coded. Gradations from red → orange → yellow → white denote increasing opacification. MB_{MW3} resulted in greater contrast enhancement. The color version of this figure is shown in Appendix K-12.

Table 8-1 lists the quantitative videointensity (VI) data for each of the 7 completely analyzed mice. The VI was measured in a region of interest encompassing the entire tumor for each image, and the VI difference between the 120 sec image and the 135 sec image for each injection in each mouse was calculated.

Table 8-1 Tumor videointensity (VI) measurements for microbubbles targeted via the tumor-binding peptide MW3 (MB_{MW3}) and glycine control microbubbles ($MB_{Glycine}$) for each of the 7 completely analyzed mice. Mean VI Differences were calculated as the average pixel intensity within the region of interest encompassing the tumor in the 120 sec frame minus the average intensity in the 135 sec frame.

Mouse #	Tumor Type	MB_{MW3} VI Difference (120 –135 sec)	$MB_{Glycine}$ VI Difference (120 –135 sec)
A	Clone C	7.4	4.6
B	Clone C	4.3	0.0
C	Clone C	6.4	1.3
D	PC3	6.2	0.3
E	PC3	9.6	3.7
F	PC3	11.3	0.1
G	PC3	0.6	2.1
Mean Intensity Units ± SD		7 ± 3	2 ± 2

Figure 8-9 summarizes the data for all 7 mice in terms of the VI difference between the images acquired at 120 and 135 sec. The mean VI difference for all tumors using $MB_{Glycine}$ was 2 ± 2 intensity units, which was not significantly different from zero, suggesting that there was little or no $MB_{Glycine}$ adhesion. The mean VI difference using MB_{MW3} was 7 ± 3 intensity units, which was both significantly higher than zero ($p<0.005$) and significantly higher than that found with $MB_{Glycine}$ ($p<0.02$).

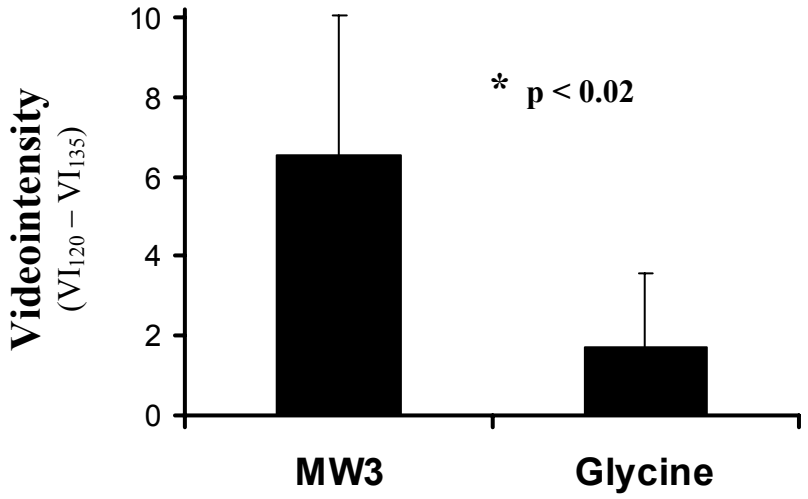

Figure 8-9 Videointensity due to adhered microbubbles (120 sec signal – 135 sec signal). Intensity due to adhesion of microbubbles targeted via MW3 was significantly greater than that due to adhesion of control glycine microbubbles. (n=7 each). (Mean ± SD).

8.4 Discussion

The main finding of the work in this chapter was that contrast microbubbles targeted via the tumor-binding tripeptide MW3 can non-invasively identify tumor vasculature. The *in vitro* studies demonstrated that MB_{MW3} preferentially adhere to tumor-derived versus normal endothelium, while the *in vivo* studies demonstrated that this selective adherence leads to differential contrast enhancement under ultrasound. We have investigated the targeting of acoustic contrast agents to tumor endothelium, and are the first to demonstrate the non-invasive identification of tumor angiogenic vasculature using targeted ultrasound. These data have

implications for the development of a technique that may allow for the non-invasive detection and characterization of tumor angiogenesis, and contribute to the monitoring of anti-tumor (especially anti-angiogenic) therapy.

8.4.1 Targeted Adhesion to Tumor Endothelium

It was first necessary to establish that microbubbles conjugated to MW3 selectively bind to tumor versus normal endothelium. Fluorescent histochemistry studies performed in our collaborator's lab had previously demonstrated that the MW3 cyclic peptide selectively adheres to tumor-derived endothelial cells *in vitro*, and to Clone C and PC3 tumors *in vivo*. Based on these data (see Section 8.1.1), as well as our previous findings using ICAM-1-targeted microbubbles on inflammatory endothelium (see Chapters 4, 5, and 6), it was reasonable to hypothesize that microbubbles targeted via MW3 would adhere preferentially to tumor-derived versus normal cultured endothelial cells.

The *in vitro* experiments again made use of the parallel plate perfusion apparatus. It was shown that MB_{MW3} do in fact demonstrate selective binding to cultured tumor-derived ECs. MBs conjugated to a control glycine peptide ($MB_{Glycine}$) showed only minimal adherence to both cell types, suggesting that neither the presence of the cyclic peptide on the MB surface nor the lipid components of the microbubble shell were largely responsible for the observed adhesion. However, the adhesion level of $MB_{Glycine}$ was higher, relative to MB_{MW3} adhesion, than was the adhesion of isotype control antibody microbubbles ($MB_{Control}$) relative to MB_{ICAM} on inflammatory ECs (see Figure 7-5; $MB_{Control}$ adhesion is close to zero). This may imply some non-specific adhesion due to the presence of the cyclic peptide. The magnitude of this effect, however, is small compared to the specific MW3 adhesive interaction.

These *in vitro* data showed that the adhesion of MBs targeted to tumor angiogenesis via the tumor-binding peptide MW3 selectively adhere to tumor endothelium under physiologically relevant shear conditions, and that the adhesion of these targeted MBs is due to specific binding interactions between the MW3 sequence and its ligand on the endothelial surface. These findings allowed us to proceed to the *in vivo* experiments, by offering a basis by which our ultrasound imaging data could be interpreted in terms of specific microbubble-endothelium interactions.

8.4.2 Ultrasound Imaging of Tumor Angiogenesis

Prior studies by our collaborator's group had established that the MW3 peptide specifically binds to epitopes on the endothelium of two different types of tumors, Clone C and PC3, implanted subcutaneously in mice (see section 8.1.1). We thus chose these two tumor models upon which to perform *in vivo* targeted ultrasound imaging. The two cyclic peptides conjugated to our microbubbles, one containing the MW3 sequence and the other containing a glycine control sequence, likewise were chosen based on their use in previous studies. Two acoustically active MB species, MB_{MW3} and $MB_{Glycine}$, were produced using the avidin/biotin bridging technique introduced in Chapter 3. The particular ultrasound machine and probe were chosen because they have pulse inversion capability, which offers good contrast sensitivity, as well as spatial resolution superior to that available with the ultraharmonics system used in the allograft rejection studies. The high spatial resolution ensured that we could adequately visualize the small subcutaneous tumors. A destructive (high-MI) imaging technique was again chosen because it is the most sensitive method for detecting small numbers of microbubbles adhering as a result of our necessarily small volumes of injection into the mice.

Microbubbles targeted via MW3 demonstrated specific adherence to the tumor vasculature, generating enhanced opacification of the tumor region of interest on MB_{MW3} images as compared to the $MB_{Glycine}$ images. The presence of tumor-specific markers on the tumor endothelium allows for preferential binding of MB_{MW3} versus $MB_{Glycine}$. There was some (low) adhesion of $MB_{Glycine}$ to the tumor tissue, as seen in Figure 8-7 and Figure 8-8, which agrees with our *in vitro* finding that some $MB_{Glycine}$ do adhere to tumor endothelium (see Figure 8-6). This may be due to non-specific interactions between the control peptide and the endothelium, as discussed in Section 8.4.1. Alternatively, this attachment of control microbubbles may represents microbubble binding to activated leukocytes adhered to the endothelium, as mentioned in Section 7.4.2. Regardless of the mechanism, the magnitude of the contrast enhancement resulting from such non-specific attachment is much lower than that generated by MB_{MW3} attachment (Figure 8-9).

As seen in Figure 8-7 and especially Figure 8-8, the pattern of tumor opacification often showed high contrast enhancement in the peripheral zones of the tumor, but little enhancement in the tumor core. This observation was also often noted to some degree during the initial Optison imaging. Such spatial distribution of MB_{MW3} contrast enhancement may be interpreted to indicate that the tumor periphery is more angiogenic, expressing a higher density of the tumor-specific ligand for MW3, than is the tumor core. However, since the same phenomenon was often noted using the non-targeted contrast agent Optison, we believe that the opacification pattern is simply matching the anatomic pattern of the tumor vasculature, i.e. the tumor periphery is highly vascularized, while the tumor core is not. This would agree with previous histologic observations that these tumors usually have necrotic cores. Thus the observed pattern of contrast enhancement was likely due to the lack of vascularity in the necrotic tumor center.

8.4.3 Comparison to Previous Studies

This is the first report of the noninvasive imaging of tumor vasculature via an ultrasonic contrast agent targeted via a tumor-specific peptide. We have uniquely used a tumor endothelium-specific binding peptide to target acoustically active microbubbles to tumor angiogenesis. Based on the growing research into anti-angiogenic cancer therapies, we feel that these data have strong implications for the development of a uniquely benign and inexpensive imaging technique for the assessment and monitoring of tumor angiogenesis.

As discussed in Section 1.4, a number of reports have been published describing methods for the non-invasive imaging of tumor angiogenesis. Some of these techniques rely on anatomic measurements of tumor size, blood flow, and vascular permeability, while a smaller number have used various molecular imaging techniques to assess the functional status of the tumor vasculature in terms of endothelial molecular markers. These functional molecular imaging techniques most often utilize ligands (usually peptides) that bind to tumor- or angiogenesis-specific endothelial markers ("vascular addressing"). These targeting ligands or peptides are visualized by radiolabeling, or conjugation to a contrast agent relevant for the imaging modality. Examples include MRI imaging of tumor angiogenesis using magnetic contrast agents conjugated to anti-$\alpha_v\beta_3$ antibodies [160], PET scanning using ^{F}18-labeled glycopeptides containing the RGD adhesion sequence [170], and ^{99m}technetium-labeled RGD peptide [172].

Most recently, in 2003 Dr. Jonathan Lindner's group demonstrated that echogenic microbubbles targeted to α_v integrins via conjugation to antibodies adhere to FGF-stimulated vessels overexpressing α_v integrins *in vivo* [162]. This adhesion phenomenon resulted in increased contrast enhancement on ultrasound. This study adequately demonstrated the

feasibility of ultrasonic imaging of angiogenesis, but does have limitations and differences from our work. First, no non-angiogenic tissue control was included in the *in vivo* tests; specific adhesion was demonstrated, in that MBs conjugated to the anti-integrin antibody showed more binding than control MBs, but it was not proven that the targeted MBs selectively adhere to angiogenic versus normal endothelium. Second, these MBs were targeted via an antibody, whereas in our studies the MBs were targeted via a short cyclic peptide. Third, in the report from Dr. Lindner's laboratory, MBs are targeted to angiogenesis in general, and adhesion was investigated using FGF-stimulation of angiogenesis in the cremaster muscle and angiogenic invasion into Matrigel plugs. Our studies target MBs to *tumor* angiogenesis, and utilize an *in vivo* tumor model and a targeting agent (MW3) that is specific for tumor angiogenic endothelium.

We believe that targeted contrast ultrasound has advantages over other imaging modalities for the *in vivo* functional assessment of vascular beds. Optical methods using fluorescent-tagged proteins or peptides are generally limited to small animal models, due to high tissue absorption and autofluorescence [235]. MRI generally offers good spatial resolution, but has a poor signal-to-noise ratio, i.e. low sensitivity [235]. Scintigraphic methods generally yield high sensitivity, but poor spatial resolution [146]. Non-contrast ultrasound images only the larger vessels, having limited utility for assessing angiogenesis in the tumor microvasculature [146].

8.4.4 Limitations

These tumor imaging studies have some of the same limitations discussed for the transplant rejection studies in Section 7.4.4. Specifically, these include the limitations

concerning the ability of our ultrasound imaging system to resolve small differences in targeted MB adhesion, the use of a destructive imaging protocol, and the use of a 2 min delay between contrast injection and image acquisition. Additional limitations include the following:

For the *in vitro* adhesion experiments comparing MB_{MW3} binding to tumor-derived versus normal endothelium, the two cell types were of different species origin. The TDECs were murine, while the normal ECs were human. This was a necessary concession, due to the difficulty in acquiring either human tumor ECs or completely normal mouse ECs. Since the MW3 peptide was identified using positive panning against mouse tumor-derived cells, the lower adhesion of MB_{MW3} to the normal human ECs may have been due to the species difference. However, it has been demonstrated that MW3 does species cross-react with some human tumors, including sarcomas and prostate tumors (unpublished data from Dr. Michael K. Wong).

The *in vitro* panning technique used to identify MW3 utilizes cultured TDECs, which may not accurately represent their original *in vivo* tumor EC phenotype. Specifically, due to a lack of continued interaction with the tumor, the cultured TDECs may fail to maintain tumor-specific cell surface markers. To minimize differences between *in vivo* tumor ECs and the TDECs, only low passage (< fifth) TDECs were used during the peptide display library panning process [233]. However, to convincingly demonstrate that microbubbles targeted via MW3 adhere selectively to tumor angiogenic endothelium versus other angiogenic endothelium, further control experiments need to be undertaken using a non-tumor model such as retinal neovascularization [236] or post-ischemic myocardial angiogenesis.

Currently, the *in vivo* tumor imaging experiments have been limited to the Clone C and PC3 tumors grown subcutaneously in mice. We have not yet performed imaging in negative tissue controls, i.e. non-tumor tissues. We have demonstrated that MB_{MW3} specifically adheres

to tumor vasculature *in vivo* (MB_{MW3} adhesion > $MB_{Glycine}$ adhesion), and we have shown that MB_{MW3} selectively adheres to tumor-derived versus normal endothelium *in vitro*, but we have yet to demonstrate this selective adherence *in vivo*. Experiments are currently planned to supply these missing data, by imaging MB_{MW3} and $MB_{Glycine}$ adhesion in mouse kidneys, spleen, or heart. We expect that these non-neoplastic tissues will show minimal MB_{MW3} adhesion.

8.4.5 Summary

The data in this chapter have demonstrated for the first time the ability of targeted ultrasound to non-invasively detect tumor angiogenesis *in vivo*. Contrast microbubbles targeted to tumor endothelium via conjugation with the tumor-binding peptide MW3 were shown to preferentially bind to tumor-derived cultured endothelium. Furthermore, we demonstrated the non-invasive, *in vivo* ultrasonic detection of tumor vasculature in a tumor-bearing mouse model. Such ultrasonic molecular imaging of tumor angiogenesis may offer improved assessment of malignant potential, and improved monitoring of tumor response to anti-angiogenic therapies.

9.0 FUTURE WORK

9.1 Planned Future Work

9.1.1 Multi-targeted MBs

In the multistep model of leukocyte adhesion, described in Section 1.1, different binding interactions occur between different sets of adhesion receptors. Initial leukocyte binding and rolling is mediated by endothelial selectins, while firm adhesion and subsequent migration through the endothelial layer is mediated by interactions between immunoglobulin superfamily receptors and leukocyte integrins. These two types of binding work synergistically to achieve leukocyte capture. Since our LAM-targeted MBs can be interpreted as an attempt to mimic the adherence characteristics of natural leukocytes, it is reasonable to study the potential for targeting multiple ligands simultaneously with a single contrast agent, in an effort to take advantage of possible synergistic effects.

We briefly investigated MBs that were multi-targeted to both ICAM-1 and VCAM-1, by conjugating them to a 50/50 mixture of antibodies against the two LAMs. Hypothesizing that the dual-targeted MBs may achieve greater adhesion strength than their mono-targeted counterparts, we perfused three different species of MBs through the radial flow chamber to measure critical shear rate: 100% anti-ICAM-1 MBs, 100% anti-VCAM-1 MBs, and 50%-anti-ICAM-1 / 50%-anti-VCAM-1 MBs. As seen in Figure 9-1, the adhesion strength of the dual-targeted MB was not greater than that of either of the singly-targeted species, and, in fact, was close to the average of the two singly -targeted species. Flow cytometric Scatchard-type analysis of the two

antibodies used revealed that their affinities were both on the order of 10^{-8} mol/L, differing only by a factor of approximately 5, perhaps explaining the lack of any synergistic adhesion effects. Additionally, in these tests the two binding interactions are antibody/antigen in character, rather than receptor/ligand as in the case of leukocyte/endothelium adhesion.

Future work is planned to investigate dual-targeting against ICAM-1 and selectins, with MBs simultaneously conjugated to anti-ICAM-1 antibodies and sialyl Lewis-x, the selectin ligand. This pairing should more closely resemble the weak versus strong interactions characteristic of natural leukocyte/endothelial binding. Selectin-mediated adhesion of sialyl Lewis-x-coated microspheres has been investigated by Dr. Daniel Hammer's group [237], but a multi-targeted system using both an antibody and the sialyl Lewis-x interactions has yet to be reported, and may prove to be of great interest.

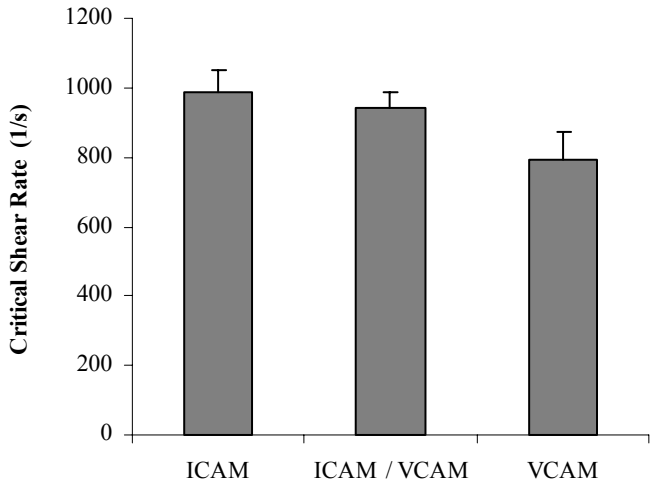

Figure 9-1 Adhesion strength of microbubbles targeted via conjugation with anti-ICAM-1 antibodies only, a 50/50 mix of anti-ICAM-1 and anti-VCAM-1 antibodies, or anti-VCAM-1 antibodies only, respectively.

9.1.2 Tissue Controls for *In Vivo* Tumor Imaging

As discussed in Section 8.4.4, our *in vivo* investigations of targeted tumor imaging had the limitation that negative tissue controls were not performed. MB_{MW3} and $MB_{Glycine}$ were used for contrast-enhanced ultrasound imaging in subcutaneous tumors with vasculatures that are known to bind the MW3 peptide. We demonstrated that MB_{MW3} imaging can detect tumor vasculature, but we have not yet shown that this agent can successfully distinguish normal tissue from tumor endothelium.

Imaging experiments in normal tissue controls are currently planned, visualizing contrast in either the mouse kidney or mouse heart. The previous data from Dr. Michael Wong's lab presented in Section 8.1.1 demonstrated that MW3 does not adhere to non-tumor tissues, so we expect that the non-neoplastic kidney and heart will show minimal MB_{MW3} adhesion.

9.1.3 Additional Angiogenesis Imaging

Experiments have been planned to investigate microbubbles targeted to angiogenesis via conjugation with angiogenic endothelium-specific binding peptides identified by Dr. Erkki Ruoslahti's group [165]. These peptides have been identified in angiogenic tissues other than tumors, so they may be capable of targeting angiogenic endothelium such as that found in or around ischemic cardiac tissue. Additionally, the endothelial ligand for these peptides has been identified, allowing characterization of candidate angiogenic tissues, as well as detailed studies of ligand density and receptor/ligand interaction kinetics.

9.2 Recommendations for Additional Future Work

LAMs other than ICAM-1 should be investigated as potential targets for our contrast agents. Brief *in vitro* preliminary studies investigating microbubbles targeted to VCAM-1 (not presented in this dissertation) indicated that absolute MB adhesion to endothelial VCAM-1 may be greater than with ICAM-1. Additionally, VCAM-1 may serve as a better molecular target because it has lower constitutive expression in the coronary microcirculation than does ICAM-1, and may be a more specific marker of endothelial dysfunction [101]. Other potential targets include PECAM and the receptors in the selectin family.

The effect of MB size on adhesion should be evaluated. The mathematical model by Cozens-Roberts *et al* includes particle radius as a parameter that affects adhesion strength (see Section 4.2.7), and others have shown that particle size is a key design feature [238]. In parallel, ultrasound studies of differently sized MBs would need to be conducted, because MB diameter can dramatically affect acoustic properties [184].

Another MB design parameter that should be investigated is the tether length between the MB shell and the targeting molecule, in our case an antibody. Tether length can be controlled by choosing longer or shorter PEG spacer molecules for the biotin-PEG-DSPE reagent used in MB synthesis (see Appendix F). The length of the tether by which the targeting molecule is attached has been shown to be an important parameter in microsphere and cell adhesion [239, 240]. An interesting recent report by Jeppesen *et al* demonstrated that, in a receptor/ligand binding system in which the ligand molecules are anchored on flexible polymer tethers, efficiency of the interaction depends not on the equilibrium configuration (length) of the tether molecule, but rather on the length of its rare high-energy excursions [240]. Such findings may impact the adhesion strength, and thus the design, of our targeted contrast agent.

Lastly, in regards to imaging studies utilizing *in vivo* transplant rejection models, I would recommend that, in protocols in which LAM-targeted MBs are administered intravenously, other tissues in the animal (besides the graft) be assessed for targeted MB adhesion. Evidence of upregulation of ICAM-1 in organs remote from the transplanted graft during rejection has been reported [241]. Accordingly, non-graft tissues in the transplant model, particularly the lung, may capture more of the targeted agent in rejecting than non-rejecting animals, reducing the amount of microbubbles available to circulate to the graft organ, thus reducing the potential acoustic signal from the graft.

10.0 CONCLUSIONS

Endothelial dysfunction is characterized by the upregulation of cell surface markers including intercellular adhesion molecule-1, and is characteristic of numerous disease processes including inflammation, atherosclerosis, and transplant rejection. A molecular imaging technique utilizing ultrasound contrast microbubbles specifically targeted to cell surface markers of endothelial dysfunction may offer non-invasive assessment of associated disease processes.

Immunohistochemistry demonstrated that our chosen molecular target, ICAM-1, was upregulated on the microvascular endothelium in animal models of inflammation and acute allograft rejection. We were not able to identify relative overexpression of ICAM-1 on samples of human ischemic versus normal myocardium, perhaps due to inadequacy of the normal specimens.

The adhesion characteristics of lipid-based microbubbles targeted to ICAM-1 via conjugation with anti-ICAM-1 antibodies were studied *in vitro*. We were able to quantify the antibody density on the microbubble surface, and demonstrate control over this parameter. Using a parallel plate perfusion chamber, targeted microbubble to cultured endothelium was shown to be dependent on microbubble antibody density, in a relationship that agreed with theoretical predictions. We demonstrated ICAM-1-targeted microbubble adhesion under shear conditions, and showed that the level of adherence was dependent on the wall shear rate.

Using a radial flow chamber, we determined that targeted microbubble adhesion to cultured endothelium was linearly dependent on the level of ICAM-1 expression, which has

important implications for the ability of our targeted ultrasound technique to distinguish not only the presence, but also the severity of endothelial dysfunction-associated disease.

Each of these *in vitro* studies provided results that contribute to the quantitative understanding of targeted microbubble adhesion. Together, they significantly advance the targeted contrast agent literature, which has previously been largely qualitative, in the direction of quantitative analysis.

Ultrasonic detection of adhered targeted microbubbles was investigated using an *in vivo* rat model of cardiac transplant rejection. ICAM-1-targeted microbubbles injected intravenously into rats bearing heterotopic transplants selectively adhered to rejecting versus non-rejecting grafts, successfully demonstrating for the first time a targeted ultrasound imaging technique for the non-invasive detection of acute cardiac allograft rejection.

To study the potential application of our targeted imaging system in oncology, microbubbles were targeted via conjugation with a tumor endothelium-specific binding peptide. Ultrasound imaging of mice bearing subcutaneous solid tumors demonstrated specific adherence of the targeted microbubble to the tumor vasculature, thus showing the feasibility of targeted acoustic contrast agents for the detection of tumor angiogenesis.

These data make substantial contributions towards the development of a targeted, ultrasound-based molecular imaging technique for the non-invasive, functional assessment of endothelial dysfunction.

APPENDICES

APPENDIX A

Protocol for preparation of 1% paraformaldehyde

* Paraformaldehyde is toxic - Use gloves & chemical fume hood

Materials:

Powdered paraformaldehyde

Phosphate-buffered saline (PBS)

Flasks

Heating/stirring plate

pH meter and buffer solutions

0.2 micron sterile filter

1. Weigh out powdered paraformaldehyde (e.g. 1 g for 100 mL of 1% solution).
2. Place paraformaldehyde in Erlenmeyer flask containing desired amount of PBS.
3. Add stirring rod, seal the top of the flask with parafilm.
4. Stir the flask on heat/stir plate, using gentle heat (below 60 °C).
5. If paraformaldehyde has not fully dissolved after 1 hour, add a small amount of NaOH to increase pH.

6. After all paraformaldehyde has dissolved, allow to cool to room temperature.
7. Using pH meter, adjust pH of solution to 7.4.
8. Filter the solution using a 0.2 micron sterile filter.
9. Transfer the solution into a glass container and refrigerate (4 °C).
10. Resuspend Check the pH of the solution weekly, if there is any change discard solution into appropriate container in fume hood.

APPENDIX B

Protocol for paraffin tissue processing

Materials:

1%-4% paraformaldehyde	Xylene
Phosphate-buffered saline (PBS)	Water bath
Paraffin molds	Slide warmer
Paraffin cassettes	Melted paraffin dispenser
EtOH	

Day 1:

1. Harvest tissue samples, fix in paraformaldehyde overnight.

Day 2:

2. Rinse tissue samples quickly in PBS and cut to size.
3. Place sample in labeled paraffin cassette.
4. Place cassettes in beaker with stir bar, take to fume hood, and add washes as follows, stirring slowly:

    a. 100% EtOH x1 hr
    b. 100% EtOH x1 hr
    c. 100% EtOH x1 hr

d. Xylene x30 min
e. Xylene x30 min
f. Melted paraffin x1 hr
g. Fresh melted paraffin x2 hrs – overnight

Day 3:

5. Remove cassettes from paraffin.

6. Fill well of mold with hot paraffin.

7. Place on cold surface to cool paraffin.

8. With tweezers, set tissue sample in cooling paraffin.

9. Place cassette on top of mold, fill with hot paraffin.

10. Set on cold surface for 30 min to solidify paraffin.

11. Pop cassette with tissue out of mold, shave off extra paraffin, and refrigerate or freeze.

Day 4:

12. Using microtome with fresh knife, cut 5µm sections from paraffin-embedded tissue block.

13. Carefully place sections on water surface in water bath for 5-10 sec.

14. Carefully pick up tissue section with microscope slide.

15. Place slide on slide warmer at 40 ºC for 1 hr.

16. Dip slides in sequential washes as follows:

h. Xylene x 4 min.
i. Xylene x 4 min.
j. Xylene x 4 min.
k. 100% EtOH x 2 min.
l. 100% EtOH x 2 min.
m. 95% EtOH x 2 min.
n. dH_2O x 5 min.

17. Proceed with chosen staining protocol.

APPENDIX C

Endothelial Cell Subculturing Procedure

* This procedure must be performed under sterile conditions (sterile biologic hood)

Materials:

25 mL and 10 mL serological pipettes
75 cm^2 culture flasks, multi-well plates, and/or glass coverslips
Endothelial Basal Medium-2 (EBM-2, Clonetics Corp.)
Hepes-buffered saline solution (HBSS)
Trypsin/EDTA (T-E)
Trypsin neutralizing solution (TNS)
} (Clonetics ReagentPack)
15 mL plastic Falcon tube

1. Preheat EBM-2 to 37 ºC.
2. Remove old media from culture flask.
3. Add 5 mL HBSS to flask for ~30 sec, then remove.
4. Add 5 mL T-E to flask, place in 37 ºC incubator for 3-6 min.
5. Add 5mL TNS to flask.
6. Using microscope, confirm that cells have been lifted into solution.
7. Transfer 10 mL contents of flask to 15 mL Falcon tube.
8. Centrifuge 6 min at 250 x g
9. Remove supernatant
10. Resuspend cell pellet in 10 mL EBM-2
11. Split onto new coverslips, wells, or flasks at 1:3 or 1:4 ratio

APPENDIX D

Parallel Perfusion Chamber Calculations

A fluid dynamic analysis of flow in the parallel perfusion chamber based on the Navier-Stokes equation results in an equation that calculates the wall shear rate for each experiment. The wall shear rate is constant over the entire experimental surface area.

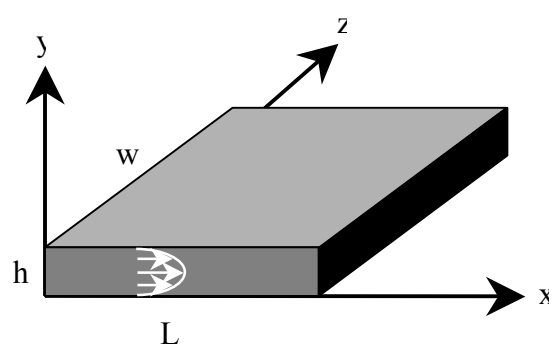

Flow is constrained between two parallel surfaces at z=0 and z=h in the x,y plane. We begin with the continuity equation (D-1) in rectangular coordinates for an incompressible (constant ρ) fluid.

$$\frac{\partial V_x}{\partial x} + \frac{\partial V_y}{\partial y} + \frac{\partial V_z}{\partial z} = 0 \qquad \text{(D-1)}$$

where x = direction of flow, y = height, z = width.

Assuming that the velocities in the y and z directions are zero, equation (D-1) reduces to:

$$\frac{\partial}{\partial x} V_x = 0 \tag{D-2}$$

Assuming that the culture medium perfusate acts in a Newtonian manner, is an incompressible fluid, and has a constant viscosity, the Navier-Stokes equation (D-3) can be employed:

$$\rho[\frac{\partial \bar{V}}{\partial t} + (\bar{V} \bullet \nabla)\bar{V}] = -\nabla P + \mu \nabla^2 \bar{V} + \rho \bar{g} \tag{D-3}$$

We treat the flow as between infinitely wide flat plates, such that flow velocity in the x-direction is a function only of y. Assuming steady flow (no unsteady acceleration) and low Reynolds number (no convective acceleration), and neglecting the effects of gravity, the Navier-Stokes equation (D-3) reduces to the x-component:

$$0 = \frac{-\partial P}{\partial x} + \mu \left[\frac{\partial}{\partial x}\left(\frac{\partial}{\partial x} Vx \right) + \frac{\partial}{\partial y}\left(\frac{\partial}{\partial y} Vx \right) + \frac{\partial}{\partial z}\left(\frac{\partial}{\partial z} Vx \right) \right] \tag{D-4}$$

Substituting equation (D-2) into (D-4) neglecting variation of V_x with z gives:

$$0 = \frac{-\partial P}{\partial x} + \mu \frac{\partial^2 V_x}{\partial y^2} \tag{D-5}$$

Since V_x is a function of y:

$$V_x = f(y) \tag{D-6}$$

$$\frac{\partial^2}{\partial y^2} V_x = \frac{\partial^2}{\partial y^2} f \tag{D-7}$$

Substitute (D-7) into (D-5):

$$0 = \frac{-\partial P}{\partial x} + \frac{\partial^2}{\partial y^2} f \tag{D-8}$$

$$\frac{\partial^2}{\partial y^2} f = \frac{\partial P}{\partial x} = const = c_1 \tag{D-9}$$

$$\frac{\partial}{\partial y} f = c_1 y + c_2 \tag{D-10}$$

$$f = \frac{c_1}{2} y^2 + c_2 y + c_3 \tag{D-11}$$

Evaluate using no-slip boundary conditions at the walls (V_x = 0 at y = 0 and h) and then substitute V_x for f:

$$V_x = \frac{1}{2\mu} \frac{\partial P}{\partial x} (y^2 - hy) \tag{D-12}$$

Volumetric flow rate is defined in rectangular coordinates as:

$$Q = \int_0^h \int_0^w V_x dz dy \tag{D-13}$$

Substitute (D-12) into (D-13) and integrate over the gap (0 to h):

$$Q = \frac{w}{2\mu}\frac{\partial P}{\partial x}\frac{h^3}{6} \tag{D-14}$$

Solve (D-14) for $\frac{\partial P}{\partial x}$ and combine with (D-12) to get an expression for the perfusate velocity in the x-direction:

$$V_x = \frac{6Q}{wh^3}(hy - y^2) \tag{D-15}$$

Of greatest interest is the shear component acting on the y-surface (the coverslip) in the x-direction, hence we start with the shear stress τ_{yx} (under laminar flow conditions) given by Newton's law of viscosity:

$$\tau_{yx} = \mu\frac{\partial Vx}{\partial y} \tag{D-16}$$

Substitute (D-15) into (D-16):

$$\tau_{yx} = \mu\frac{\partial}{\partial y}\left[\frac{6Q}{wh^3}(hy - y^2)\right] \tag{D-17}$$

and differentiate with respect to y and evaluate at the coverslip surface (y=0):

$$\tau_{yx} = \frac{6\mu Q}{wh^2} \tag{D-18}$$

Shear rate is defined as:

$$\overset{\circ}{\gamma} = \frac{\tau}{\mu} \tag{D-19}$$

Substituting (D-18) into (D-19) gives the shear rate equation for the parallel flow chamber:

$$\overset{\circ}{\gamma} = \frac{6Q}{wh^2} \tag{D-20}$$

Equation (D-20) gives the wall shear rate as a function of volumetric flow rate Q, gap height h, and chamber width w. Thus, at a given flow rate, the wall shear rate is constant over the test area of the coverslip, and can be easily calculated.

APPENDIX E

Radial Flow Chamber Calculations

A fluid dynamic analysis of flow in the radial perfusion chamber based on the Navier-Stokes equation results in an equation that calculates the wall shear rate at any radial position on the coverslip.

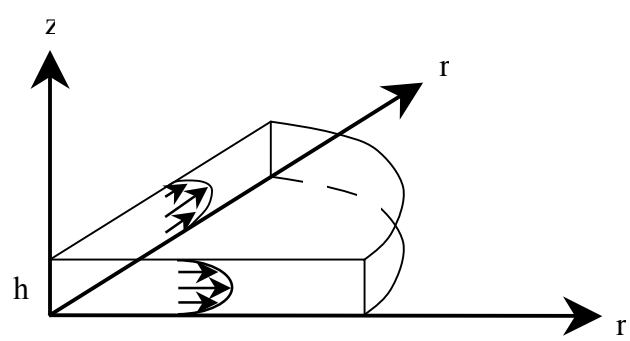

Flow is constrained between two parallel surfaces at z=0 and z=h in the r,θ plane, where r is the radial position, θ is the angle, z is the axial position. We begin with the continuity equation (E-1) in cylindrical coordinates for an incompressible fluid.

$$\frac{1}{r}\frac{\partial}{\partial r}(rV_r) + \frac{1}{r}\frac{\partial V_\vartheta}{\partial \vartheta} + \frac{\partial V_z}{\partial z} = 0 \qquad \text{(E-1)}$$

Assuming that the velocities in the circumferential (θ) and axial (z) directions are zero, equation (E-1) reduces to:

$$\frac{1}{r}\frac{\partial}{\partial r}(rV_r) = 0 \qquad \text{(E-2)}$$

Assuming that the culture medium perfusate acts in a Newtonian manner, is an incompressible fluid, and has a constant viscosity, the Navier-Stokes equation (E-3) can be employed:

$$\rho[\frac{\partial \bar{V}}{\partial t} + (\bar{V} \bullet \nabla)\bar{V}] = -\nabla P + \mu \nabla^2 \bar{V} + \rho \bar{g} \qquad \text{(E-3)}$$

Assuming steady flow (no unsteady acceleration) and low Reynolds number (no convective acceleration), and neglecting the effects of gravity, the Navier-Stokes equation (E-3) reduces to the r-component:

$$0 = \frac{-\partial P}{\partial r} + \mu\left[\frac{\partial}{\partial r}\left(\frac{1}{r}\frac{\partial}{\partial r}(rV_r)\right) + \frac{\partial^2 V_r}{\partial z^2}\right] \qquad \text{(E-4)}$$

Substituting equation (E-2) into (E-4) removes a term and gives:

$$0 = \frac{-\partial P}{\partial r} + \mu\frac{\partial^2 V_r}{\partial z^2} \qquad \text{(E-5)}$$

Since rV_r is a function of z:

$$rV_r = f(z) \qquad \text{(E-6)}$$

$$\frac{\partial^2}{\partial z^2} V_r = \frac{1}{r} \frac{\partial^2}{\partial z^2} f \tag{E-7}$$

Substitute (E-7) into (E-5):

$$0 = \frac{-\partial P}{\partial r} + \frac{\mu}{r} \frac{\partial^2}{\partial z^2} f \tag{E-8}$$

$$\frac{\partial^2}{\partial z^2} f = \frac{r}{\mu} \frac{\partial P}{\partial r} = const = c_1 \tag{E-9}$$

$$\frac{\partial}{\partial z} f = c_1 z + c_2 \tag{E-10}$$

$$f = \frac{c_1}{2} z^2 + c_2 z + c_3 \tag{E-11}$$

Evaluate using no-slip boundary conditions at the walls ($V_r = 0$ at $z = 0$ and h) and then substitute rV_r for f:

$$V_r = \frac{1}{2\mu} \frac{\partial P}{\partial r} (z^2 - hz) \tag{E-12}$$

Volumetric flow rate is defined in cylindrical coordinates as:

$$Q = \int_0^h 2\pi r V_r \, dz \tag{E-13}$$

Substitute (E-12) into (E-13) and integrate over the gap (0 to h):

$$Q = \frac{-1}{6} \frac{\pi r}{\mu} \frac{\partial P}{\partial r} h^3 \tag{E-14}$$

Solve (E-14) for $\frac{\partial P}{\partial r}$ and combine with (E-12) to get an expression for the perfusate velocity in the radial direction:

$$V_r = \frac{3Q}{\pi r h^3}(hz - z^2) \tag{E-15}$$

Of greatest interest is the shear component acting on the z-surface (the coverslip) in the r-direction, hence we start with the shear stress τ_{zr} (under laminar flow conditions) given by Newton's law of viscosity:

$$\tau_{zr} = \mu \frac{\partial V_r}{\partial z} \tag{E-16}$$

Substitute (E-15) into (E-16):

$$\tau_{zr} = \mu \frac{\partial}{\partial z}\left[\frac{3Q}{\pi r h^3}(hz - z^2)\right] \tag{E-17}$$

and differentiate with respect to z and evaluate at the coverslip surface (z=0):

$$\tau_{zr} = \frac{3\mu Q}{\pi r h^2} \tag{E-18}$$

Shear rate is defined as:

$$\overset{\circ}{\gamma} = \frac{\tau}{\mu} \tag{E-19}$$

Substituting (E-18) into (E-19) gives the shear rate equation for the radial flow chamber:

$$\overset{\circ}{\gamma} = \frac{3Q}{\pi r h^2} \tag{E-20}$$

Equation (E-20) gives the wall shear rate as a function of volumetric flow rate Q, gap height h, and radial position r. Thus, at a given flow rate, the wall shear rate varies inversely with radial position on the test area of the coverslip, and this shear rate can be easily calculated.

APPENDIX F

Preparation of Biotinylated Microbubbles

Materials:

Phospholipid DSPC (distearoylphosphatidylcholine), 50 mg

PEG (polyethyleneglycol) stearate as a surfactant, 25 mg

Biotin-PEG-DSPE

(biotinamidocaproyl PEG-distearoylphosphatidylethanolamine), 21.3 mg

Decafluorobutane (perfluorobutane; C_4F_{10})

* Microbubbles must be prepared at or above the phase transition temperature of the lipids before cooling.

1. Mix DSPC, biotin-PEG-PE, and PEG stearate in chloroform/EtOH.
2. Evaporate.
3. Repeat steps 1 and 2 twice.
4. Lyophilize 1 hour.
5. Add 10 mL buffer saline and blend by sonication for 30 sec in the presence of decafluorobutane gas.
6. Separate by flotation or centrifugation at 100 x g for 2 min using buffer saline total of 5 times.

APPENDIX G

Hematoxylin & Eosin Staining Protocol

Materials:

Xylene

Ethanol (100%, 95%, and 30%)

Distilled water (dH_2O)

Harris Hematoxylin

Acid Alcohol

Scott's Solution

Eosin

Permount

* This procedure should be performed in a chemical fume hood.

1. Prepare slides with either frozen or paraffin-embedded tissue samples.
2. Load slides into slide cassette, and dip into the following solutions for the following durations (min:sec):

    a. Xylene (4:00)
    b. Xylene (4:00)
    c. Xylene (4:00)
    d. 100% Ethanol (1:00)
    e. 100% Ethanol (1:00)
    f. 95% Ethanol (1:00)

g. Harris Hematoxylin (4:00)
h. dH_2O (1:00)
i. Acid Alcohol (0:50)
j. dH_2O (1:00)
k. Scott's Solution (0:50)
l. dH_2O (1:00)
m. Eosin (1:30)
n. 30% Ethanol (1:00)
o. 95% Ethanol (1:00)
p. 100% Ethanol (1:00)
q. 100% Ethanol (1:00)
r. Xylene (4:00)
s. Xylene (4:00)
t. Xylene (4:00)

3. Coverslip the slides using Permount, then refrigerate for at least 2 hours before examining on microscope.

APPENDIX H

Conjugation of Phycoerythrin to Antibodies

Materials:

Microcentrifuge tubes

PhycoLink R-PE conjugation kit (Prozyme Inc., San Leandro, CA)

Antibody

Antibody Ultrafiltration (to increase Ab concentration):

1. Add 500 µL antibody solution from vial to ultrafilter (Microcon Millipore)
2. Spin in microcentrifuge at 8,000 rpm for 1-5 min
3. Stop when approximately 50 µL volume remains (i.e. Ab is now 10x concentrated)

Antibody Reduction:

4. Transfer 50 µL Ab to microcentrifuge tube
5. Add 1 µL DTT solution (from kit) for 30 min at room temperature. (This exposes free sulfhydryls).
6. Equilibrate spin column (from kit) with exchange buffer (from kit):
    a. Drain packing buffer into wash tube (from kit), discard buffer
    b. Add exchange buffer, spin at 1000g for 4 min, discard buffer

c. Repeat (b) above, spinning to remove all fluid

7. Set spin column into its collection tube (from kit)

8. Add the Antibody/DTT solution to column

9. Spin at 8,000 rpm for 4 min

Fluorochrome Conjugation:

10. In microcentrifuge tube, add 320 µL activated RPE (from kit) per mg of Ab for 60 min, at room temperature, wrapped in foil to keep light out, on a slow mixer

11. Thaw NEM solution (from kit) to room temperature

12. Add 34 µL NEM solution per mg of Ab for 20 min, at room temperature, wrapped in foil to keep light out, on a slow mixer. (This blocks unreacted free sulfhydryls).

Finishing:

13. Spin above solution 1000g for 30 sec to pellet out insoluble conjugates

14. Equilibrate spin column with storage buffer (from kit)

    a. Drain any buffer into wash tube, discard buffer

    b. Add storage buffer, spin 1000g for 4 min, discard buffer

    c. Repeat (b) above, spinning to remove all fluid

15. Add 100 µL supernatant to spin column, spin 1000g for x 4min

16. Store at 4º C

APPENDIX I

Vectastain Immunoperoxidase Staining Protocol

Materials:

Vectastain Elite ABC kit

PBS

Hydrogen peroxide

Acetone

5% bovine serum albumin (BSA) in PBS

Distilled water (dH_2O)

Gelvatol

1. Prepare slides with 5 µm-thick frozen tissue samples.
2. Fix with 100% acetone (@ -20º C) for 5 min, and wash with PBS.
3. Add 3% hydrogen peroxide for 20 min, wash with PBS, and wash with BSA twice
4. Add blocking antibody from kit for 30 min, and wash with BSA twice.
5. Add primary antibody for 2 hours, and wash with BSA three times.
6. Add biotinylated secondary antibody from kit for 1 hour, wash with BSA, and wash with PBS twice.
7. Add ABC (avidin-biotin complex) reagent for 30 min, and wash with PBS twice.
8. Add AEC (3-amino-9-ethylcarbazole) for 8 min, and wash with dH_20 twice.
9. Coverslip with Gelvatol, and refrigerate.

APPENDIX J

Dako Immunoperoxidase Staining Protocol

Materials:

Dako Envision kit K-1390

PBS

Acetone

Distilled water (dH_2O)

Hematoxylin

1. Prepare slides with 5 μm-thick frozen tissue samples.
2. Air dry at room temperature for 45 min.
3. Fix with 100% acetone (@ -20º C) for 10 min.
4. Air dry at room temperature for 45 min, and wash with PBS three times.
5. Add blocking antibody from kit for 5 min, and wash with PBS twice.
6. Add primary antibody for 10 min, and wash with PBS twice.
7. Add the secondary polymer from kit for 10 min, and wash with PBS twice.
8. Add the substrate DAB (3,3'-diaminobenzidine) for 5 min, to react with the peroxidase on the polymer bound to the primary antibody, forming reddish-brown precipitate.
9. Wash with dH_2O twice.
10. Counterstain with hematoxylin.
11. Coverslip and refrigerate.

APPENDIX K

Color Figures

In this appendix, color versions of the following figures, shown in the preceding chapters, are given.

Figure Number in Preceding Chapters	Figure Number in this Appendix
Figure 1-4	Appendix K-1
Figure 2-1	Appendix K-2
Figure 2-2	Appendix K-3
Figure 2-3	Appendix K-4
Figure 2-4	Appendix K-5
Figure 6-3	Appendix K-6
Figure 7-7	Appendix K-7
Figure 7-9	Appendix K-8
Figure 7-10	Appendix K-9
Figure 7-11	Appendix K-10
Figure 8-7	Appendix K-11
Figure 8-8	Appendix K-12

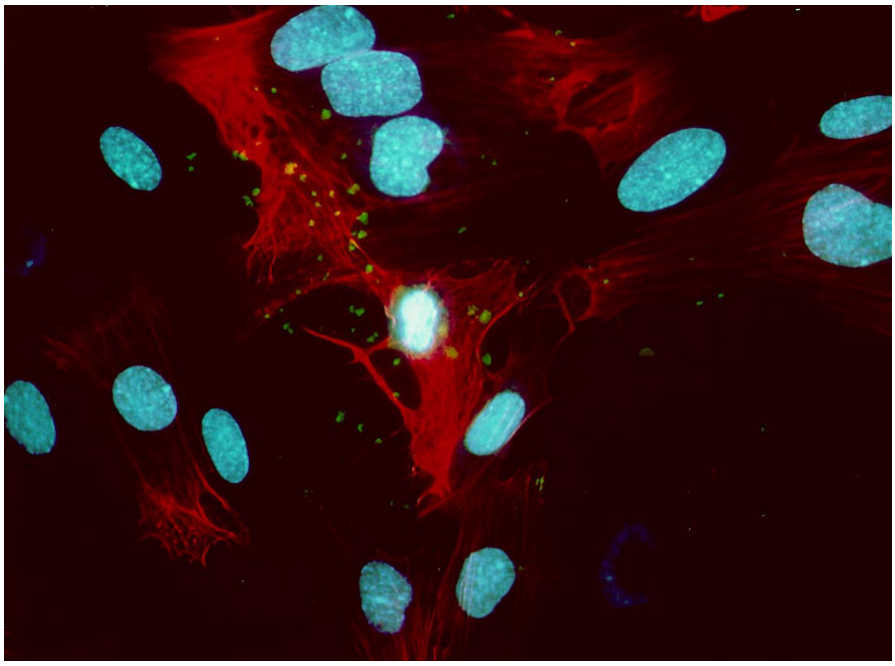

Appendix K-1 Color version of **Figure 1-4**.

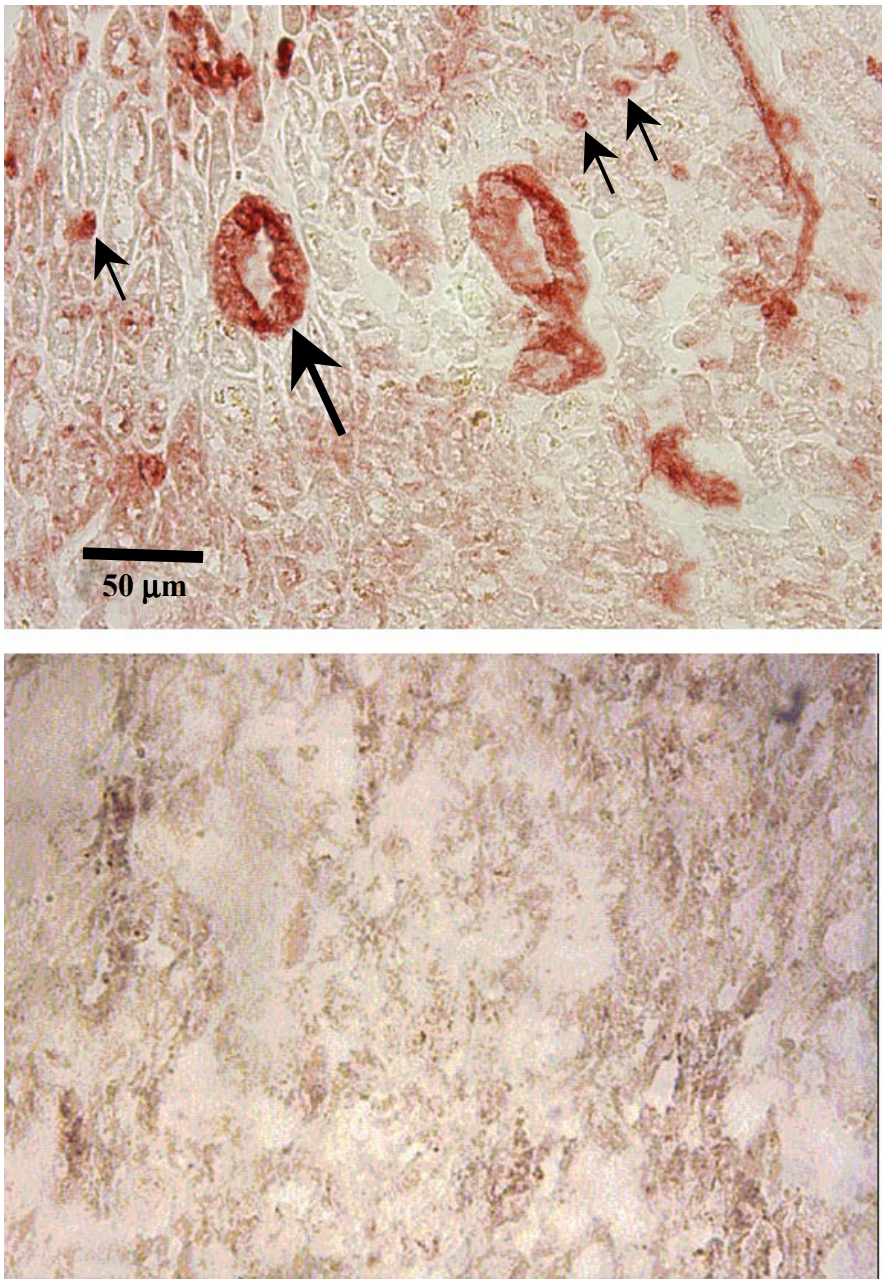

Appendix K-2 Color version of **Figure 2-1**.

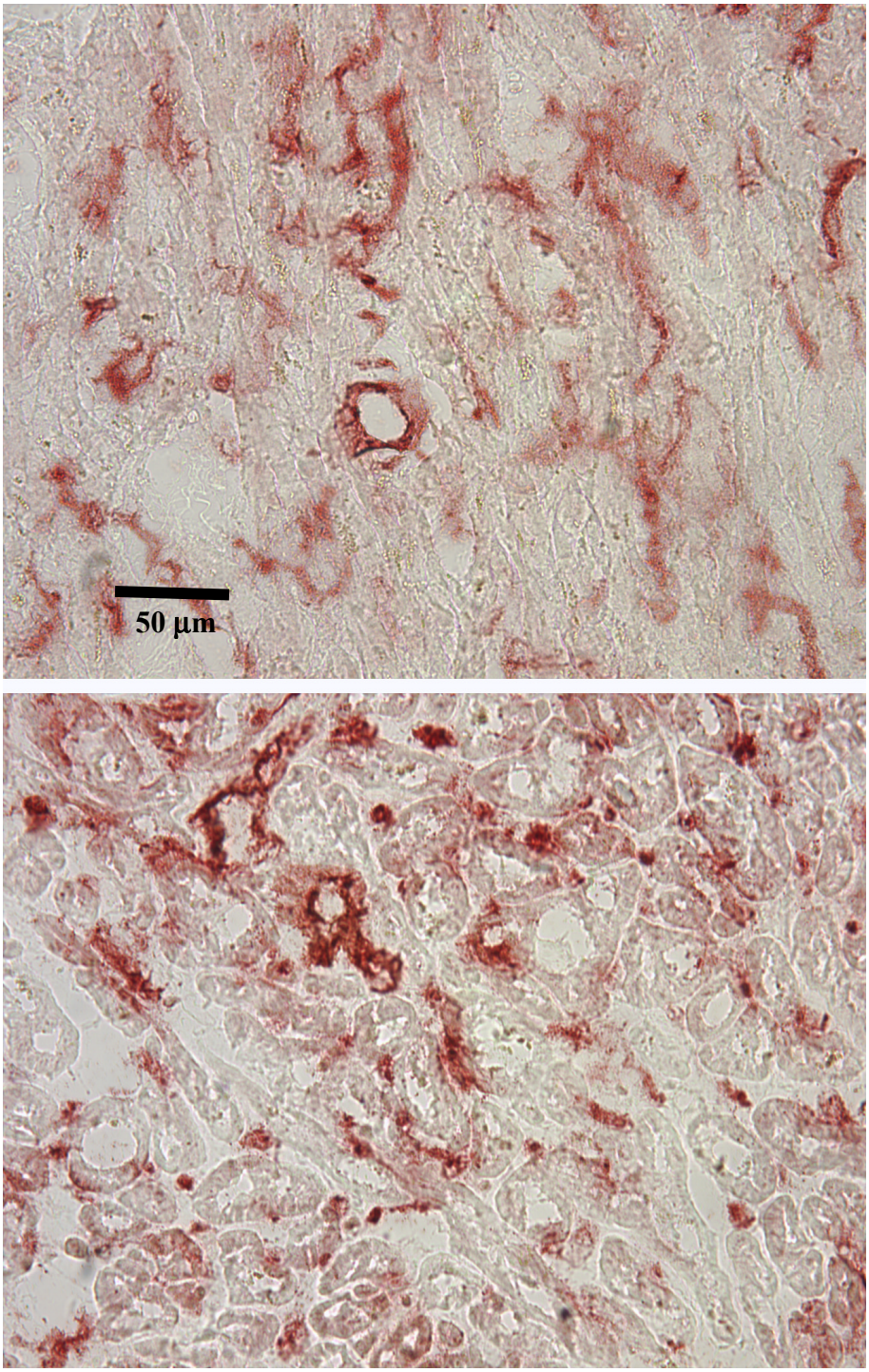

Appendix K-3 Color version of **Figure 2-2**.

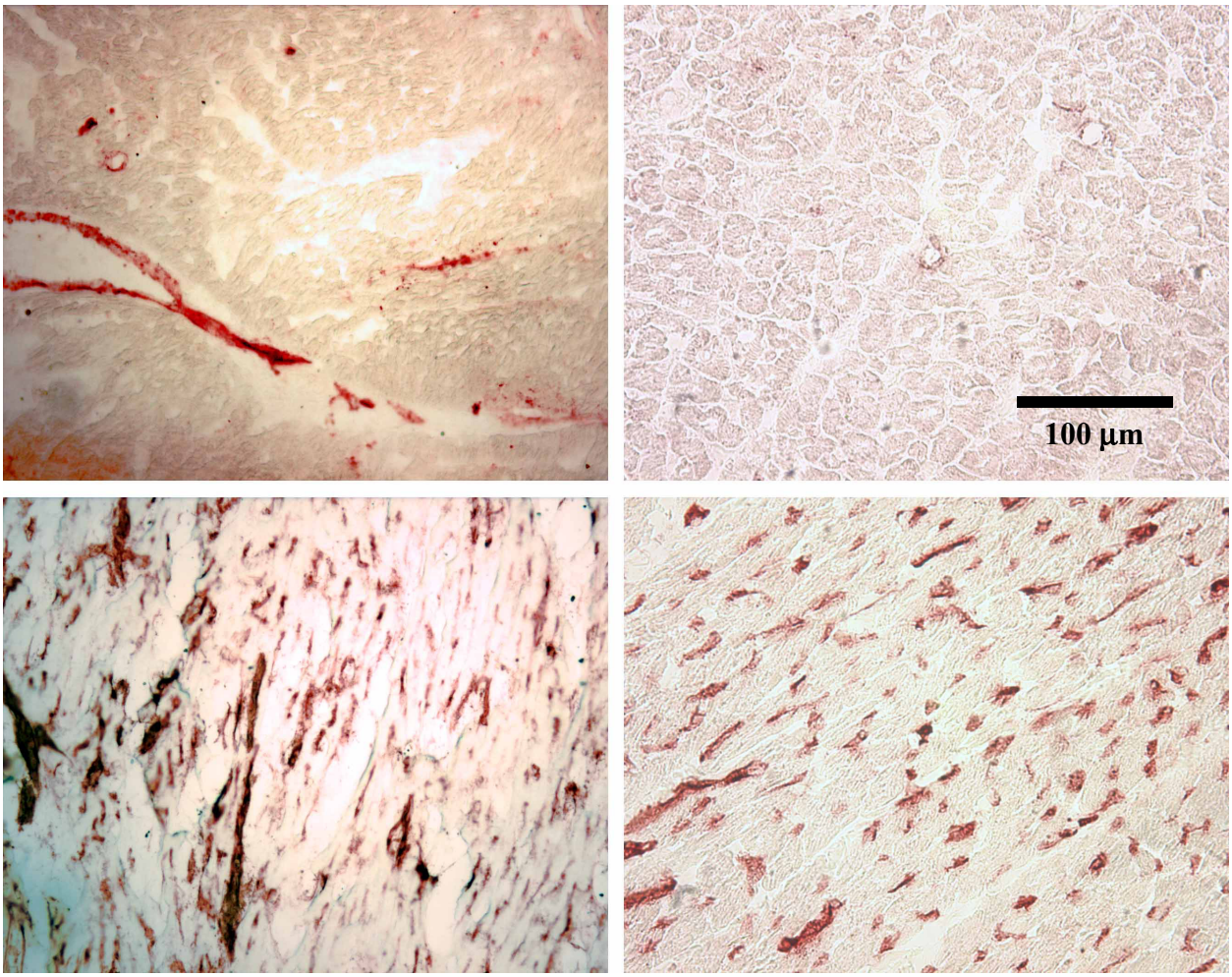

Appendix K-4 Color version of **Figure 2-3**.

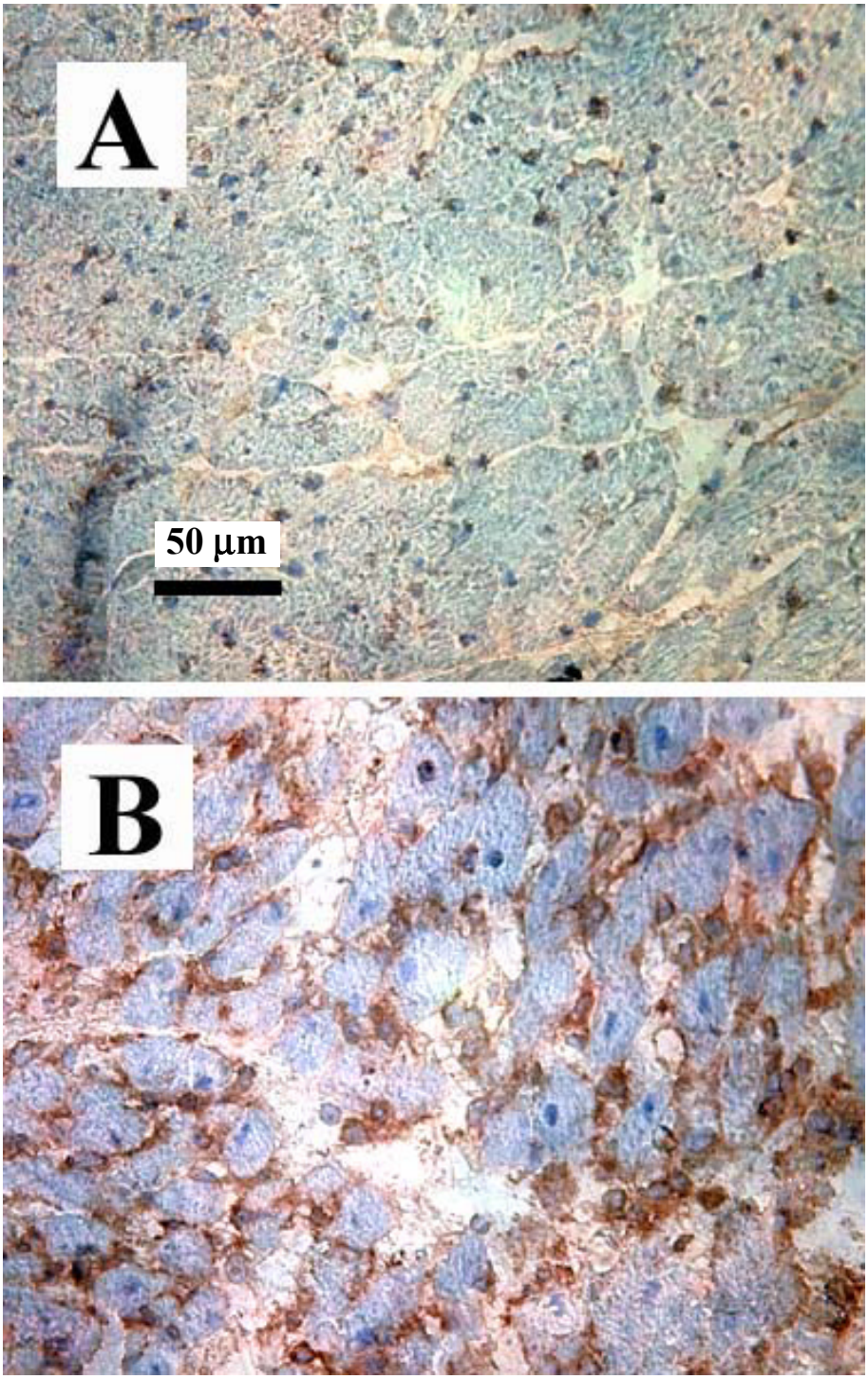

Appendix K-5 Color version of **Figure 2-4**.

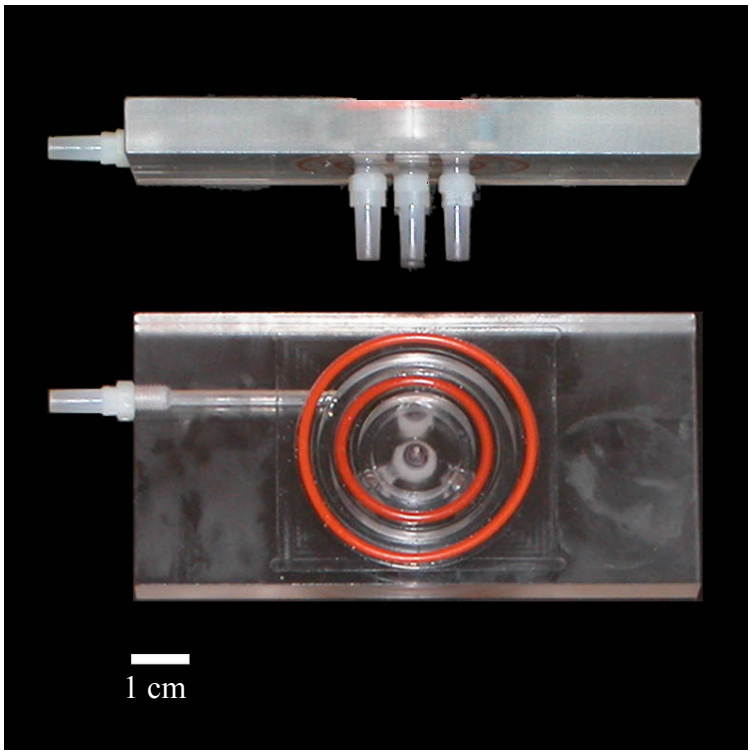

Appendix K-6 Color version of **Figure 6-3**.

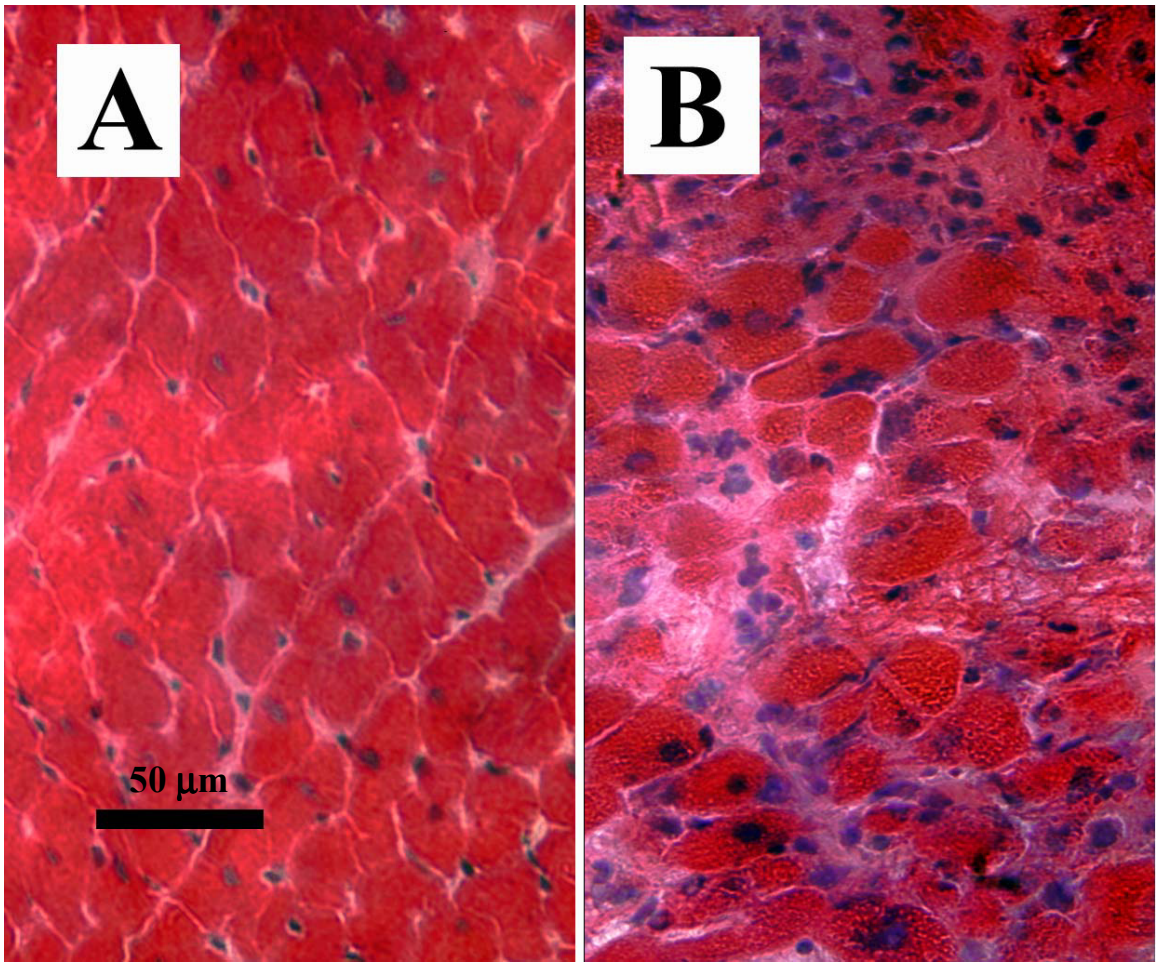

Appendix K-7 Color version of **Figure 7-7**.

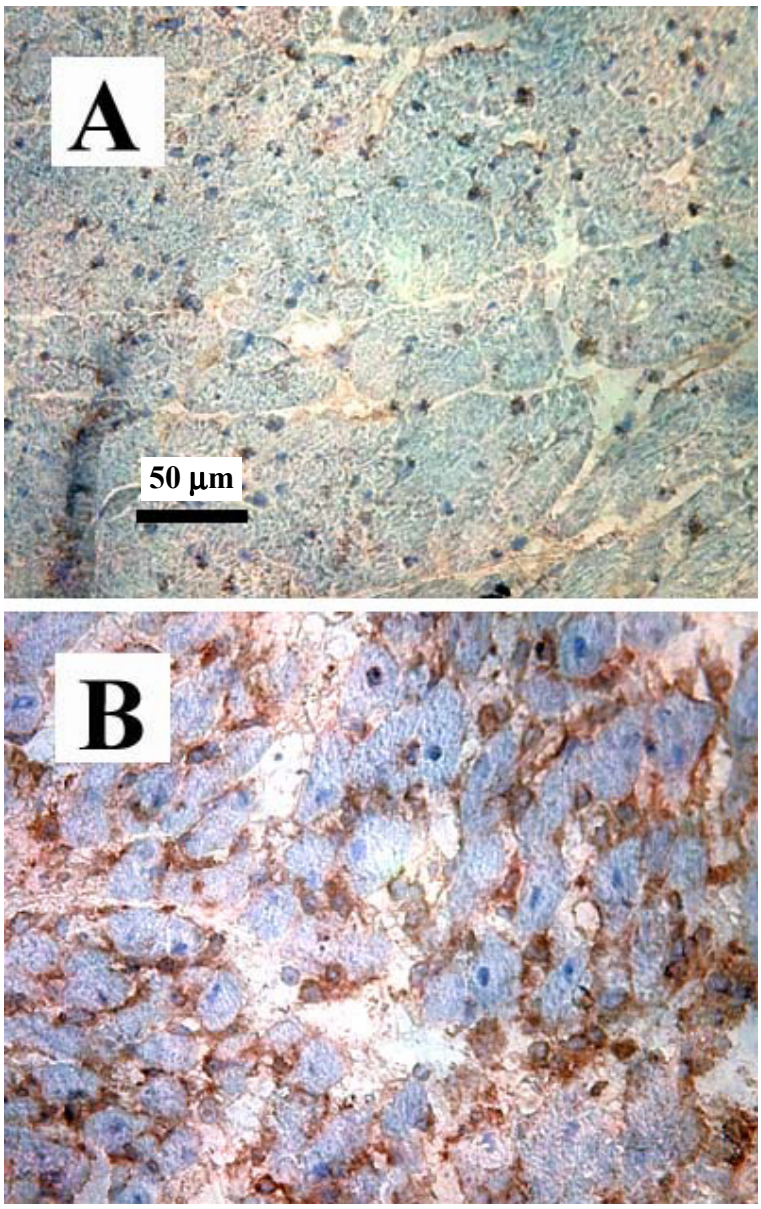

Appendix K-8 Color version of **Figure 7-9**.

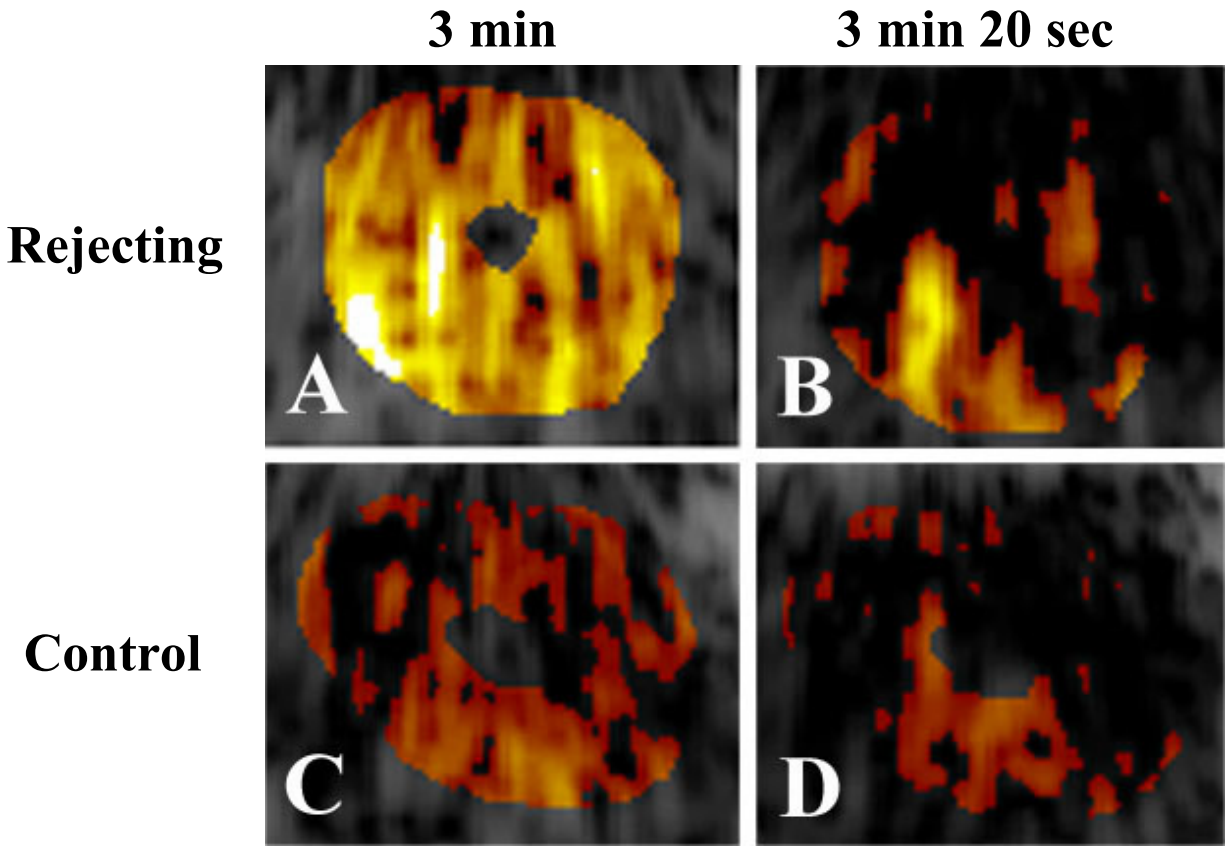

Appendix K-9 Color version of **Figure 7-10**.

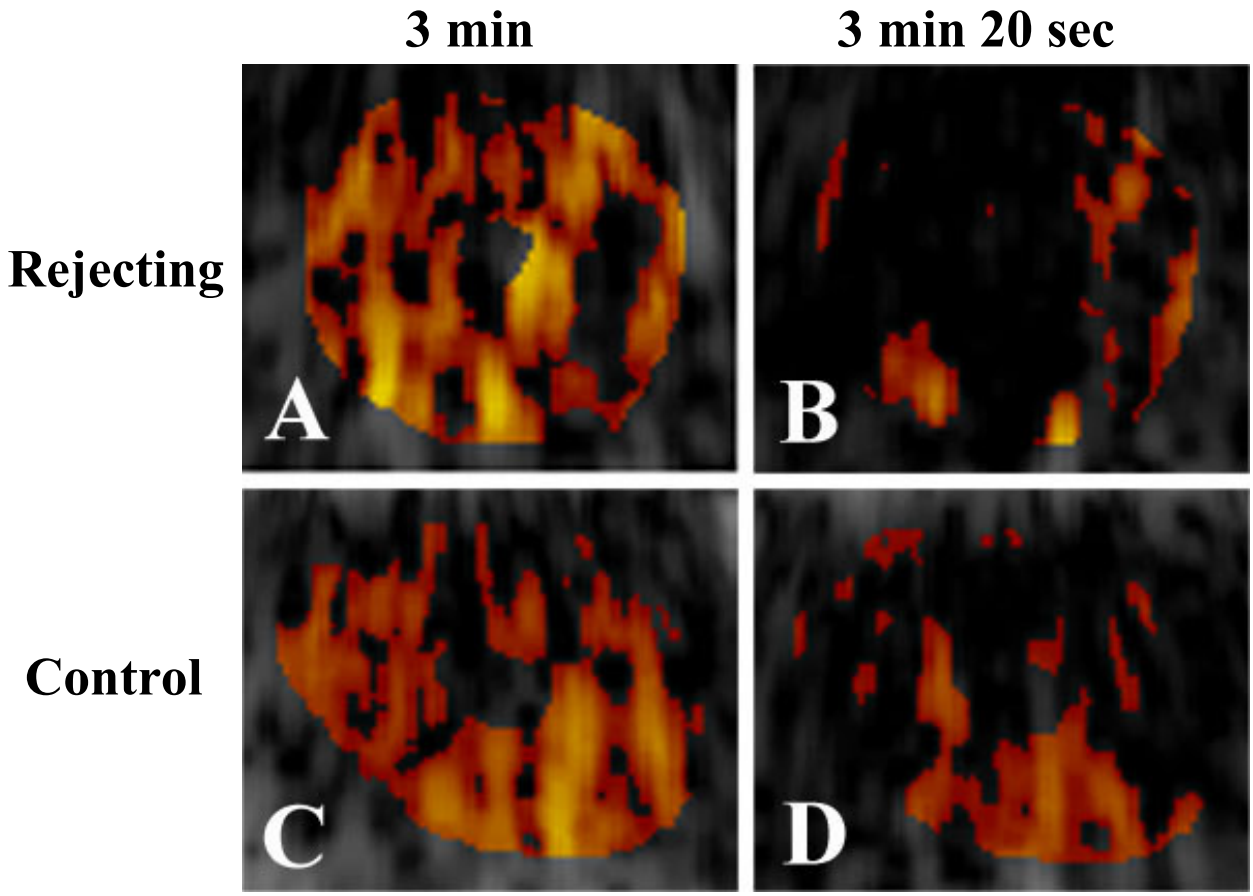

Appendix K-10 Color version of **Figure 7-11**.

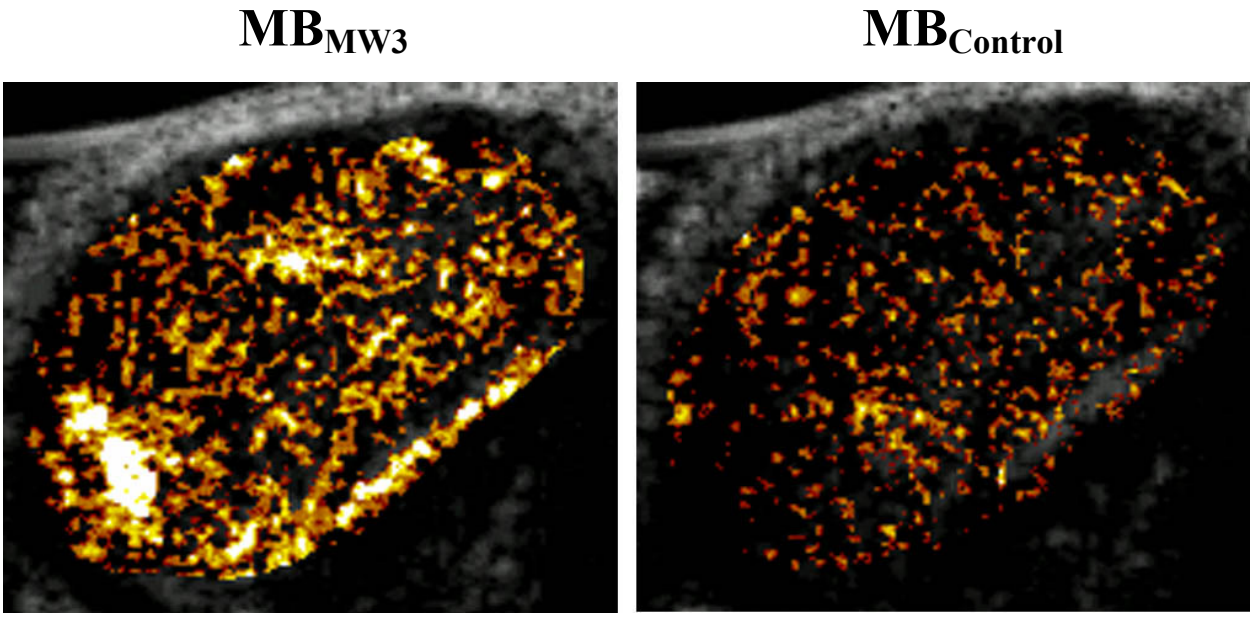

Appendix K-11 Color version of **Figure 8-7**.

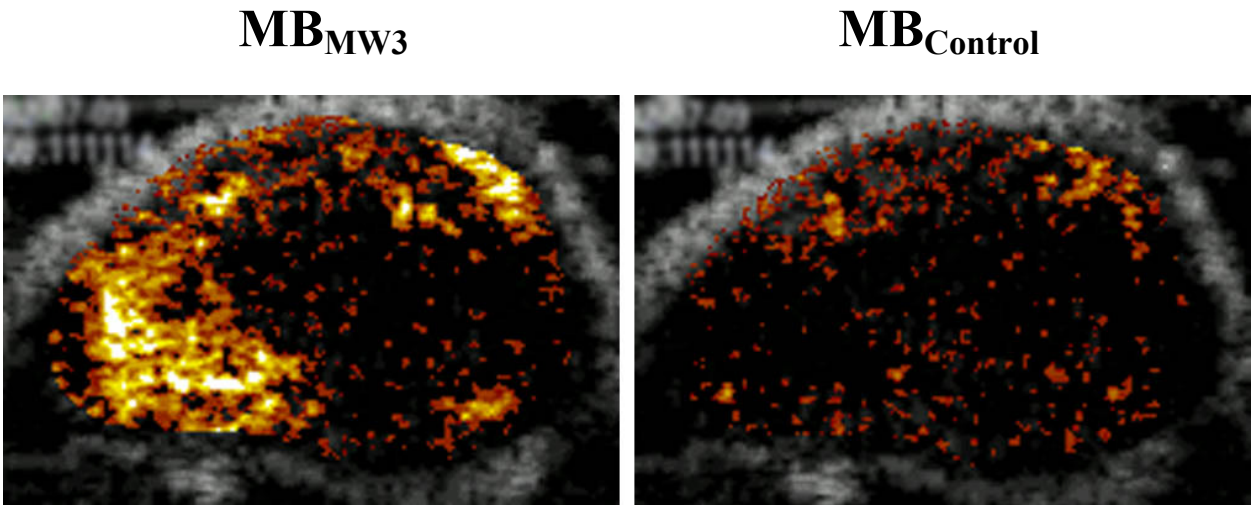

Appendix K-12 Color version of **Figure 8-8**.

BIBLIOGRAPHY

BIBLIOGRAPHY

[1] Meredith IT, Anderson TJ, Uehata A, Yeung AC, Selwyn AP, Ganz P. Role of endothelium in ischemic coronary syndromes. Am J Cardiol. 1993;72:27C-32C.

[2] Gimbrone MA. Vascular endothelium: an integrator of pathophysiologic stimuli in atherosclerosis. Am J Cardiol. 1995;75:67B-70B.

[3] Napoli C, Ignarro LJ. Nitric oxide and atherosclerosis. Nitric Oxide. 2001;5:88-97.

[4] Bevilacqua MP, Pober JS, Wheeler ME, Cotran RS, Gimbrone MA Jr. Interleukin-1 activation of vascular endothelium: Effects on procoagulant activity and leukocyte adhesion. Am J Path. 1985;121:394-403.

[5] Biegelsen ES, Loscalzo J. Endothelial function and atherosclerosis. *Coron Artery Dis*. 1999;10:241-256.

[6] Springer TA. Adhesion molecules of the immune system. Nature. 1990;346:425-434.

[7] Cybulsky MI, Gimbrone MA Jr. Endothelial expression of a mononuclear leukocyte adhesion molecule during atherogenesis. *Science*. 251:788-791, 1991.

[8] Taddei S, Salvetti A. Endothelial dysfunction in essential hypertension: clinical implications. *J Hypertens*. 2002;20:1671-1674.

[9] Bayraktutan U. Free radicals, diabetes and endothelial dysfunction. *Diabetes Obes Metab*. 2002;4:224-38.

[10] Kinlay S, Libby P, Ganz P. Endothelial function and coronary artery disease. *Curr Opin Lipidol*. 2001;12(4):383-389.

[11] Ross R. The pathogenesis of atherosclerosis: a perspective for the 1990s. *Nature*. 1993;362:801-809.

[12] Ross R. Atherosclerosis – an inflammatory disease. *N Engl J Med*. 1999;340:115-126.

[13] Sheridan FM, Cole PG, Ramage D. Leukocyte adhesion to the coronary microvasculature during ischemia and reperfusion in an in vivo canine model. *Circulation*. 1996;93:1784-1787.

[14] Dubina MV, Petrishchev NN, Anisimov VN. Microvascular endothelium dysfunction in rats bearing 1,2-dimethylhydrazine-induced colon tumors. *Cancer Lett*. 1999;144:125-129.

[15] Carlos T, Gordon D, Fishbein D, Himes VE, Coday A, Ross R, Allen MD. Vascular cell adhesion molecule-1 is induced on endothelium during acute rejection in human cardiac allografts. *J Heart Lung Transplant*. 1992;11:1103-1108.

[16] Springer TA. Traffic signals for lymphocyte recirculation and leukocyte emigration: the multistep paradigm. *Cell*. 1994;76:301-314.

[17] Jones DA, Smith CW, McIntire LV. Leucocyte adhesion under flow conditions; principles important in tissue engineering. *Biomaterials*. 1996;17:337-347.

[18] Butcher EC. Leukocyte-endothelial cell recognition: three (or more) steps to specificity and diversity. *Cell*. 1991;67:1033-1036.

[19] Tedder TF, Steeber DA, Chen A, Engel P. The selectins: vascular adhesion molecules. *FASEB J*. 1995;9:866-873.

[20] Carlos TM, Harlan JM. Leukocyte-endothelial adhesion molecules. *Blood*. 1994;84:2068-2101.

[21] Alon R, Hammer DA, Springer TA. Lifetime of the P-selectin-carbohydrate bond and its response to tensile force in hydrodynamic flow. *Nature*. 1995;374(6522):539-42.

[22] Lawrence MB, Springer TA. Leukocytes roll on a selectin at physiologic flow rates: distinction from and prerequisite for adhesion through integrins. *Cell*. 1991;65:859-873.

[23] Davies MJ, Gordon JL, Gearing AJ, Pigott R, Woolf N, Katz D, Kyriakopoulos A. The expression of the adhesion molecules ICAM-1, VCAM-1, PECAM, and e-selectin in human atherosclerosis. *J Pathol*. 1993;171:223-229.

[24] Richardson M, Hadcock SJ, DeReske M, Cybulsky MI. Increased expression in vivo of VCAM-1 and E-selectin by the aortic endothelium of normolipemic and hyperlipemic diabetic rabbits. *Arterioscler Thromb*. 1994;14:760-769.

[25] Toursarkissian B, Schwartz D, Eisenberg PR, Rubin BG. Arterial thrombosis induces early upregulation of intercellular adhesion molecule in the media. *J Vasc Surg*. 1997;26:663-669.

[26] Taylor PM, Rose ML, Yacoub MH, Pigott R. Induction of vascular adhesion molecules during rejection of human cardiac allografts. *Transplantation*. 1992;54:451-457.

[27] Stanimirovic DB, Wong J, Shapiro A, Durkin JP. Increase in surface expression of ICAM-1, VCAM-1, and E-selectin in human cerebromicrovascular endothelial cells subjected to ischemia-like insults. *Acta Neurochir*. 1997;70:12-16.

[28] Del Zoppo GJ. Microvascular responses to cerebral ischemia/inflammation. *Ann N Y Acad Sci*. 1997;823:132-147.

[29] Carlos TM, Clark RS, Franicola-Higgins D, Schiding JK, Kochanek PM. Expression of endothelial adhesion molecules and recruitment of neutrophils after traumatic brain injury in rats. *J Leukoc Biol*. 1997;61:279-285.

[30] McCarron RM, Wang L, Siren AL, Spatz M, Hallenbeck JM. Adhesion molecules on normotensive and hypertensive rat brain endothelial cells. *Proc Soc Exp Biol Med*. 1994;205:257-262.

[31] Cid MC, Grau JM, Casademont J, Tobias E, Picazo A, Coll-Vinent B, Esparza J, Pedrol E, Urbano-Marquez A. Leucocyte/endothelial cell adhesion receptors in muscle biopsies from patients with idiopathic inflammatory myopathies (IIM). *Clin Exp Immunol*. 1996;104:467-473.

[32] Noutsias M, Seeberg B, Schultheiss HP, Kuhl U. Expression of call adhesion molecules in dilated cardiomyopathy: evidence for endothelial activation in inflammatory cardiomyopathy. *Circulation*. 1999;99:2124-2131.

[33] Devaux B, Scholz D, Hirche A, Klovekorn WP, Schaper J. Upregulation of cell adhesion molecules and the presence of low grade inflammation in human chronic heart failure. *Eur Heart J*. 1997;18:470-479.

[34] Van de Stolpe A, Van der Saag PT. Intercellular adhesion molecule-1. *J Mol Med.* 1996;74:13-33.

[35] Rothlein R, Dustin ML, Marlin SD, Springer TA. A human intercellular adhesion molecule (ICAM-1) distinct from LFA-1. *J Immunol*. 1986;137:1270-1274.

[36] Staunton DE, Marlin SD, Stratowa C, Dustin ML, Springer TA. Primary structure of ICAM-1 demonstrates interaction between members of the immunoglobulin and integrin supergene families. *Cell*. 1988;52:925-933.

[37] Bella J, Kolatkar PR, Marlor CW, Greve JM, Rossmann MG. The structure of the two amino-terminal domains of human ICAM-1 suggests how it functions as a rhinovirus receptor and as an LFA-1 integrin ligand. *Proc Natl Acad Sci USA*. 1998;95:4140-4145.

[38] Casasnovas JM, Stehle T, Liu JH, Wang JH, Springer TA. A dimeric crystal structure for the N-terminal two domains of intercellular adhesion molecule-1. *Proc Natl Acad Sci USA*. 1998;95:4134-4139.

[39] Diamond MS, Staunton DE, Marlin SD, Springer TA. Binding of the integrin Mac-1 (CD11b/CD18) to the third immunoglobulin-like domain of ICAM-1 (CD54) and its regulation by glycosylation. *Cell*. 1991;65:961-971.

[40] Hentzen ER, Neelamegham S, Kansas GS, Benanti JA, McIntire LV, Smith CW, Simon SI. Sequential binding of CD11a/CD18 and CD11b/CD18 defined neutrophil capture and stable adhesion to intercellular adhesion molecule-1. *Blood*. 2000;95:911-920.

[41] Marlin SD, Springer TA. Purified intercellular adhesion molecule-1 (ICAM-1) is a ligand for lymphocyte function-associated antigen 1 (LFA-1). *Cell*. 1987;51:813-819.

[42] Neelamegham S, Taylor AD, Burns AR, Smith CW, Simon SI. Hydrodynamic shear shows distinct roles for LFA-1 and Mac-1 in neutrophil adhesion to intercellular adhesion molecule-1. *Blood*. 1998;92:1626-1638.

[43] Languino LR, Plescia J, Duperray A, Brian AA, Plow EF, Geltosky JE, Altieri DC. Fibrinogen mediated leukocyte adhesion to vascular endothelium through an ICAM-1-dependent pathway. *Cell*. 1993;73:1423-1434.

[44] Haraldsen G, Kvale D, Lien B, Farstad IN, Brandtzaeg P. Cytokine-regulated expression of E-selectin, intercellular adhesion molecule-1 (ICAM-1), and vascular cell adhesion molecule-1 (VCAM-1) in human intestinal microvascular endothelial cells. *J Immunol*. 1996;156:2558-2565.

[45] Menger MD, Vollmar B. Adhesion molecules as determinants of disease: from molecular biology to surgical research. *Br J Surg*. 1996;83:588-601.

[46] Van Kempen, Bachert C, Van Cauwenberge P. An update on the pathophysiology of rhinovirus upper respiratory tract infections. *Rhinology*. 1999;37:97-103.

[47] Celi A, Lorenzet R, Furie B, Furie BC. Platelet-leukocyte-endothelial cell interaction on the blood vessel wall. *Sem Hematology*. 1997;34:327-335.

[48] Tamaru M, Tomura K, Sakamoto S, Tezuka K, Tamatani T, Narumi S. Interleukin-1β induces tissue- and cell type-specific expression of adhesion molecules in vivo. *Arterioscler Thromb Vasc Biol*. 1998;18:1292-1303.

[49] Seitz CS, Kleindienst R, Xu Q, Wick G. Coexpression of heat-shock protein 60 and intercellular-adhesion molecule-1 is related to increased adhesion of monocytes and T cells to aortic endothelium of rats in response to endotoxin. *Lab Invest*. 1996;74:241-252.

[50] De Caterina R, Libby P, Peng HB, Thannickal VJ, Rajavashisth TB, Gimbrone MA Jr, Shin WS, Liao JK. Nitric oxide decreases cytokine-induced endothelial activation. Nitric oxide selectively reduces endothelial expression of adhesion molecules and proinflammatory cytokines. *J Clin Invest*. 1995;96:60-8.

[51] Scanlon CE, Berger M, Malcom G, Wissler RW. Evidence for more extensive deposits of epitopes of oxidized low density lipoprotein in aortas of young people with elevated serum thiocyanate levels. *Atherosclerosis*. 1996;121:23-33.

[52] Napoli C, D'Armiento FP, Mancini FP, Postiglione A, Witztum JL, Palumbo G, Palinski W. Fatty streak formation occurs in human fetal aortas and is greatly enhanced by maternal hypercholesterolemia. Intimal accumulation of low density lipoprotein and its oxidation precede monocyte recruitment into early atherosclerotic lesions. *J Clin Invest*. 1997;100:2680-2690.

[53] Ross R, Glomset JA. Atherosclerosis and the arterial smooth muscle cell: Proliferation of smooth muscle is a key event in the genesis of the lesions of atherosclerosis. *Science*. 1973;180:1332-1339.

[54] Sluiter W, Pietersma A, Lamers JMJ, Koster JF. Leukocyte adhesion molecules on the vascular endothelium: their role in the pathogenesis of cardiovascular disease and the mechanisms underlying their expression. *J Cardiovasc Pharm*. 1993;22(Suppl. 4):S37-S44.

[55] Fuster V. Mechanisms leading to myocardial infarction: insights from studies of vascular biology. *Circulation*. 1994;90:2126-2146.

[56] Johnson-Tidey RR, McGregor JL, Taylor PR, Poston RN. Increase in the adhesion molecule p-selectin in endothelium overlying atherosclerotic plaques: coexpression with intercellular adhesion molecule-1. *Am J Path*. 1994;144:952-961.

[57] Poston RN, Haskard DO, Coucher JR, Gall NP, Johnson-Tidey RR. Expression of intercellular adhesion molecule-1 in atherosclerotic plaques. *Am J Path*. 1992;140:665-673.

[58] O'Brien KD, McDonald TO, Chait A, Allen MD, Alpers CE. Neovascular expression of E-selectin, intercellular adhesion molecule-1, and vascular cell adhesion molecule-1 in human atherosclerosis and their relation to intimal leukocyte content. *Circulation*. 1996;93:672-682.

[59] O'Brien KD, Allen MD, McDonald TO, Chait A, Harlan JM, Fishbein D, McCarty J, Ferguson M, Hudkins K, Benjamin CD, et al. Vascular cell adhesion molecule-1 is expressed in human coronary atherosclerotic plaques. *J Clin Invest*. 1993;92:945-951.

[60] Nakashima Y, Raines EW, Plump AS, Breslow JL, and Ross R. Upregulation of VCAM-1 and ICAM-1 at atherosclerosis-prone sites on the endothelium in the ApoE-deficient mouse. *Arterioscler Thromb Vasc Biol*. 1998;18:842-851.

[61] Rohde LE, Lee RT, Rivero J, Jamacochian M, Arroyo LH, Briggs W, Rifai N, Libby P, Creager MA, Ridker PM. Circulating cell adhesion molecules are correlated with ultrasound-based assessment of carotid atherosclerosis. *Arterioscler Thromb Vasc Biol*. 1998;18:1765-1770.

[62] Rohde LE, Hennekens CH, Ridker PM. Cross-sectional study of soluble intercellular adhesion molecule-1 and cardiovascular risk factors in apparently healthy men. *Arterioscler Thromb Vasc Biol*. 1999;19:1595-1599.

[63] Kume N, Cybulsky MI, Gimbrone MA Jr. Lysophospatidylcholine, a component of atherogenic lipoproteins, induces mononuclear leukocyte adhesion molecules in cultured human and rabbit arterial endothelial cells. *J Clin Invest*. 1992;90:1138-1144.

[64] Dietrich H, Hu Y, Zou Y, Dirnhofer S, Kleindienst R, Wick G, Xu Q. Mouse model of transplant arteriosclerosis: role of intercellular adhesion molecule-1. *Arterioscler Thromb Vasc Biol*. 2000;20:343-352.

[65] Labarrere CA, Nelson DR, Faulk WP. Endothelial activation and development of coronary artery disease in transplanted human hearts. *JAMA*. 1997;278:1169-1175.

[66] Kuo L, Davis MJ, Cannon S, Chilian WM. Pathophysiological consequences of atherosclerosis extend into the coronary microcirculation. *Circ Res*. 1992;70:465-476.

[67] Chilian WM, Dellsperger KC, Layne SM, Eastham CL, Armstrong MA, Marcus ML, Heistad DD. Effects of atherosclerosis on the coronary microcirculation. *Am J Physiol*. 1990;258:H529-H539.

[68] Sellke FW, Armstrong ML, Harrison DG. Endothelium-dependent vascular relaxation is abnormal in the coronary microcirculation of atherosclerotic primates. Circulation. 1990;81:1586-1593.

[69] White CW, Wright CB, Doty DB, Hiratza LF, Eastham CL, Harrison DG, Marcus ML. Does visual interpretation of the coronary arteriogram predict the physiologic importance of a coronary stenosis. *N Engl J Med*. 1984;310:819-24.

[70] Corretti MC, Plotnick GD, Vogel RA. Technical aspects of evaluating brachial artery vasodilatation using high-frequency ultrasound. *Am J Physiol*. 1995;268:H1397-H1404.

[71] Villanueva FS, Klibanov A, Wagner WR. Microbubble-endothelial cell interactions as a basis for assessing endothelial function. *Echocardiography*. 2002;19:427-438.

[72] Yuan C, Skinner MP, Kaneko E, Mitsumori LM, Hayes CE, Raines EW, Nelson JA, Ross R. Magnetic resonance imaging to study lesions of atherosclerosis in the hyperlipidemic rabbit aorta. *Magn Reson Imaging*. 1996;14:93-102.

[73] Wong ND, Detrano RC, Abrahamson D, Tobis JM, Gardin JM. Coronary artery screening by electron beam computed tomography. Facts, controversy, and future. *Circulation*. 1995;92:632-636.

[74] Porter TR, Sears T, Xie F, Michels A, Mata J, Welsh D, Shurmur S. Intravascular ultrasound study of angiographically mildly diseased coronary arteries. *J Am Coll Cardiol*. 1993;22:1858-1865.

[75] Reddy KG, Nair RN, Sheehan HM, Hodgson JM. Evidence that selective endothelial dysfunction may occur in the absence of angiographic or ultrasound atherosclerosis in patients with risk factors for atherosclerosis. *J Am Coll Cardiol*. 1994;23:833-843.

[76] Miyasaka M, Kawashima H, Korenaga R, Ando J. Involvement of selectins in atherogenesis: a primary or secondary event. *Ann N Y Acad Sci*. 1997;811:25-34.

[77] Tsimikas S, Palinski W, Halpern SE, Yeung DW, Curtiss LK, Witztum JL. Radiolabeled MDA2, an oxidation-specific, monoclonal antibody, identifies native atherosclerotic lesions in vivo. *J Nucl Cardiol*. 1999;6:41-53.

[78] Tsimikas S. Noninvasive imaging of oxidized low-density lipoprotein in atherosclerotic plaques with tagged oxidation-specific antibodies. *Am J Cardiol*. 2002;90:22L-27L.

[79] Khaw BA, Narula J. Antibody imaging in the evaluation of cardiovascular diseases. *J Nucl Cardiol*. 1994;1:457-476.

[80] Carrio I, Pieri PL, Narula J, Prat L, Riva P, Pedrini L, Pretolani E, Caruso G, Sarti G, Estorch M, Berna L, Riambau V, Matias-Guiu X, Pak C, Ditlow C, Chen F, Khaw BA. Noninvasive localization of human atherosclerotic lesions with indium 111-labeled monoclonal Z2D3 antibody specific for proliferating smooth muscle cells. *J Nucl Cardiol*. 1998;5:551-557.

[81] Kang HW, Josephson L, Petrovsky A, Weissleder R, Bogdanov A Jr. Magnetic resonance imaging of inducible E-selectin expression in human endothelial cell culture. *Bioconjug Chem*. 2002;13:122-127.

[82] Bloemen PG, Henricks PA, van Bloois L, van den Tweel MC, Bloem AC, Nijkamp FP, Crommelin DJ, Storm G. Adhesion molecules: a new target for immunoliposome-mediated drug delivery. *FEBS Letters*. 1995;357:140-144.

[83] Lindner JR, Coggins MP, Kaul S, Klibanov AL, Brandenburger GH, Ley K. Microbubble persistence in the microcirculation during ischemia-reperfusion and inflammation: integrin- and complement-mediated adherence to activated leukocytes. *Circulation*. 2000;101:668-675.

[84] Lindner JR, Dayton PA, Coggins MP, Ley K, Song J, Ferrara K, Kaul S. Noninvasive imaging of inflammation by ultrasound detection of phagocytosed microbubbles. *Circulation*. 2000;102:531-538.

[85] Alkan-Onyuksel H, Demos SM, Lanza GM, Vonesh MJ, Klegerman ME, Kane BJ, Kuszak J, McPherson DD. Development of inherently echogenic liposomes as an ultrasonic contrast agent. *J Pharm Sci*. 1996;85:486-490.

[86] Demos SM, Onyuksel H, Gilbert J, Roth SI, Kane B, Jungblut P, Pinto JV, McPherson DD, Klegerman ME. In vitro targeting of antibody-conjugated echogenic liposomes for site-specific ultrasonic image enhancement. *J Pharm Sci*. 1997;86:167-171.

[87] Demos SM, Dagar S, Klegerman M, Nagaraj A, McPherson DD, Onyuksel H. In vitro targeting of acoustically reflective immunoliposomes to fibrin under various flow conditions. *J Drug Target*. 1998;5:507-518.

[88] Demos SM, Alkan-Onyuksel H, Kane BJ, Ramani K, Nagaraj A, Greene R, Klegerman M, McPherson DD. In vivo targeting of acoustically reflective liposomes for intravascular and transvascular ultrasonic enhancement. *J Am Coll Cardiol*. 1999;33:867-875.

[89] Hamilton A, Huang SL, Warnick D, Stein A, Rabbat M, Madhav T, Kane B, Nagaraj A, Klegerman M, MacDonald R, McPherson D. Left ventricular thrombus enhancement after intravenous injection of echogenic immunoliposomes. *Circulation*. 2002;105:2772-2778.

[90] Lanza GM, Wallace KD, Scott MJ, Cacheris WP, Abendschein DR, Christy DH, Sharkey AM, Miller JG, Gaffney PJ, and Wickline SA. A novel site-targeted ultrasonic contrast agent with broad biomedical application. *Circulation*. 1996;94:3334-3340.

[91] Lanza GM, Wallace KD, Fischer SE, Christy DH, Scott MJ, Trousil RL, Cacheris WP, Miller JG, Gaffney PJ, Wickline SA. High-frequency ultrasonic detection of thrombi with a targeted contrast system. *Ultrasound Med Biol*. 1997;23:863-870.

[92] Lanza GM, Trousil RL, Wallace KD, Rose JH, Hall CS, Scott MJ, Miller JG, Eisenberg PR, Gaffney PJ, Wickline SA. In vitro characterization of a novel, tissue-targeted ultrasonic contrast system with acoustic microscopy. *J Acoust Soc Am*. 1998;104:3665-3672.

[93] Unger EC, McCreery TP, Sweitzer RH, Shen D, Wu G. In vitro studies of a new thrombus-specific ultrasound contrast agent. *Am J Cardiol*. 1998;81:58G-61G.

[94] Wu Y, Unger EC, McCreery TP, Sweitzer RH, Shen D, Wu G, Vielhauer MD. Binding and lysing of blood clots using MRX-408. *Invest Radiol*. 1998;33:880-885.

[95] Villanueva FS, Jankowski RJ, Klibanov S, Pina ML, Alber SM, Watkins SC, Brandenburger GH, Wagner WR. Microbubbles targeted to intercellular adhesion molecule-1 bind to activated coronary artery endothelial cells. *Circulation*. 1998;98:1-5.

[96] Lindner JR, Song J, Christiansen J, Klibanov AL, Xu F, Ley K. Ultrasound assessment of inflammation and renal tissue injury with microbubbles targeted to p-selectin. *Circulation*. 2001;104:2107-2112.

[97] Lindner JR, Song J, Xu F, Klibanov AL, Singbartl K, Ley K, Kaul S. Noninvasive ultrasound imaging of inflammation using microbubbles targeted to activated leukocytes. *Circulation*. 2000;102:2745-2750.

[98] Christiansen JP, Leong-Poi H, Klibanov AL, Kaul S, Lindner JR. Noninvasive imaging of myocardial reperfusion injury using leukocyte-targeted contrast echocardiography. *Circulation*. 2002;105:1764-1767.

[99] Kuby J. Immunology. 3rd ed. W H Freeman & Co., New York, 1997.

[100] Hosenpud JD, Bennett LE, Keck BM, Boucek MM, Novick RJ. The registry of the international society for heart and lung transplantation: eighteenth official report – 2001. *J Heart Lung Transplant*. 2001;20:805-815.

[101] Tanaka H, Sukhova GK, Swanson SJ, Cybulsky MI, Schoen FJ, Libby P. Endothelial and smooth muscle cells express leukocyte adhesion molecules heterogeneously during acute rejection of rabbit cardiac allografts. *Am J Path*. 1994;144:938-951.

[102] Truong L, Shappell S, Solez K. Adhesion molecules as markers of acute cellular rejection of renal allografts. *Transplant Proc*. 1996;28:519-522.

[103] Hill PA, Main IW, Atkins RC. ICAM-1 and VCAM-1 in human renal allografts rejection. *Kidney Int*. 1995;47:1383-1391.

[104] Jeong HJ, Lee HH, Kim YS, Kim SI, Moon JI, Park K. Expression of ICAM-1 and VCAM-1 in renal allograft rejection. *Transplant Proc*. 1998;30:2953-2954.

[105] Kauppinen H, Soots A, Krogerus L, Brummer T, Ahonen J, Lautenschlager I. Different expression of adhesion molecules ICAM-1 and VCAM-1 and activation markers MHC class II and IL-2R in acute and chronic rejection of rat kidney allografts. *Transplant Proc*. 1997;29:3150-3151.

[106] Lemstrom K, Koskinen P, Hayry P. Induction of adhesion molecules on the endothelia of rejecting cardiac allografts. *J Heart Lung Transplant*. 1995;14:205-213.

[107] Hamano K, Ito H, Shirasawa B, Gohra H, Katoh T, Fujimura Y, Esato K. Correlations among expression of intercellular adhesion molecule-1, cellular infiltration, and coronary arteriosclerosis during chronic rejection using the rat heart transplantation model. *Eur Surg Res*. 1998;30:235-242.

[108] Torry RJ, Labarrere CA, Torry DS, Holt VJ, Faulk WP. Vascular endothelial growth factor expression in transplanted human hearts. *Transplantation*. 1995;60:1451-1457.

[109] Herskowitz A, Mayne AE, Willoughby SB, Kanter K, Ansari AA. Patterns of myocardial cell adhesion molecule expression in human endomyocardial biopsies after cardiac transplantation: Induced ICAM-1 and VCAM-1 related to implantation and rejection. *Am J Pathol*. 1994;145:1082-1094.

[110] Steinoff G, Behrend M, Richter N, Haverich A. Endothelial adhesion molecules in human heart and lung transplants. *Transplant Proc*. 1995;27:1274-1276.

[111] Zembala M, Wojnicz R, Zakliczynski M, Wojarski J, Nozynski J, Knapik P, Bialkowski J, Foremny J, Rozek M. Cellular adhesion molecules changes in myocardium during first year post heart transplant. *Ann Transplant*. 1997;2:16-19.

[112] Allen MD, McDonald TO, Himes VE, Fishbein DP, Aziz S, Reichenbach DD. E-selectin expression in human cardiac grafts with cellular rejection. *Circulation*. 1993;88:II243-II247.

[113] Isobe M, Yagita H, Okumura K, Ihara A. Specific acceptance of cardiac allografts after treatment with antibodies to ICAM-1 and LFA-1. *Science*. 1992;255:1125-1127.

[114] Harrison PC, Mainolfi E, Madwed JB. Cyclosporine dosage can be reduced when used in combination with an anti-intercellular adhesion molecule-1 monoclonal antibody in rats undergoing heterotopic heart transplantation. *J Heart Lung Transplant*. 1998;17:150-157.

[115] Yamazaki S, Isobe M, Suzuki J, Tojo S, Horie S, Okubo Y, Sekiguchi M. Role of selectin-dependent adhesion in cardiac allograft rejection. *J Heart Lung Transplant*. 1998;17:1007-1016.

[116] Sadahiro M, McDonald TO, Allen MD. Reduction in cellular and vascular rejection by blocking leukocyte adhesion molecule receptors. *Am J Path*. 1993;142:675-683.

[117] Sadahiro M, McDonald TO, Nelson K, Thomas R, Allen MD. Leukocyte CD18 receptors may be a better target than ICAM-1 ligands for reducing histologic evidence of cellular and vascular rejection in the rabbit. *Transpl Int*. 1995;8:452-458.

[118] Raisanen-Sokolowski A, Glysing-Jensen T, Russell ME. Donor and recipient contributions of ICAM-1 and P-selectin in parenchymal rejection and graft arteriosclerosis: insights from double knockout mice. *J Heart Lung Transplant*. 1999;18:735-743.

[119] Poston RS, Mann MJ, Hoyt EG, Ennen M, Dzau VJ, Robbins RC. Antisense oligodeoxynucleotides prevent acute cardiac allografts rejection via a novel, nontoxic, highly efficient transfection method. *Transplantation*. 1999;68:825-832.

[120] Feeley BT, Park AK, Hoyt EG, Robbins RC. Sulfasalazine inhibits reperfusion injury and prolongs alograft survival in rat cardiac transplants. *J Heart Lung Transplant*. 1999;18:1088-1095.

[121] Beckmann N, Joergensen J, Bruttel K, Rudin M, Schuurman HJ. Magnetic resonance imaging for the evaluation of rejection of a kidney allografts in the rat. *Transpl Int*. 1996;9:175-183.

[122] Walpoth BH, Lazeyras F, Tschopp A, Schaffner T, Althaus U, Billingham M, Morris R. Assessment of cardiac rejection and immunosuppression by magnetic resonance imaging and spectroscopy. *Transplant Proc*. 1995;27:2088-2091.

[123] Kanno S, Wu YJ, Lee PC, Dodd SJ, Williams M, Griffith BP, Ho C. Macrophage accumulation associated with rat cardiac allograft rejection detected by magnetic resonance imaging with ultrasmall superparamagnetic iron oxide particles. *Circulation*. 2001;104:934-938.

[124] Walpoth BH, Tschopp A, Lazeyras F, Galdikas J, Tschudi J, Altermatt H, Schaffner T, Aue WP, Althaus U. Magnetic resonance spectroscopy for assessing myocardial rejection in the transplanted rat heart. *J Heart Lung Transplant*. 1993;12:271-282.

[125] Hoff SJ, Stewart JR, Frist WH, Kessler RM, Sandler MP, Atkinson JB, Votaw J, Carey JA, Ansari MS, Merrill WH. Noninvasive detection of heart transplant rejection with positron emission scintigraphy. *Ann Thorac Surg*. 1992;53:572-577.

[126] Hoff SJ, Stewart JR, Frist WH, Atkinson JB, Kronenberg MW, Votaw J, Kessler RM, Sandler MP. Noninvasive detection of acute rejection in a new experimental model of heart transplantation. *Ann Thorac Surg*. 1993;56:1074-1077.

[127] Puleo JA, Aranda JM, Weston MW, Cintron G, French M, Clark L, Fontanet HL. Noninvasive detection of allograft rejection in heart transplant recipients by use of Doppler tissue imaging. *J Heart Lung Transplant*. 1998;17:176-184.

[128] Angermann CE, Nassau K, Stempfle HU, Kruger TM, Drewello R, Junge R, Uberfuhr P, Weiss M, Theisen K. Recognition of acute cardiac allograft rejection from serial integrated backscatter analyses in human orthotopic heart transplant recipients: comparison with conventional echocardiography. *Circulation*. 1997;95:140-150.

[129] Vriens PW, Blankenberg FG, Stoot JH, Ohtsuki K, Berry GJ, Tait JF, Strauss HW, Robbins RC. The use of technetium Tc 99m annexin V for in vivo imaging of apoptosis during cardiac allograft rejection. *J Thorac Cardiovasc Surg*. 1998;116:844-853.

[130] Blankenberg FG, Katsikis PD, Tait JF, Davis RE, Naumovski L, Ohtsuki K, Kopiwoda S, Abrams MJ, Darkes M, Robbins RC, Maecker HT, Strauss HW. In vivo detection and imaging of phosphatidylserine expression during programmed cell death. *Proc Natl Acad Sci U S A*. 1998;95:6349-6354.

[131] Narula J, Acio ER, Narula N, Samuels LE, Fyfe B, Wood D, Fitzpatrick JM, Raghunath PN, Tomaszewski JE, Kelly C, Steinmetz N, Green A, Tait JF, Leppo J, Blankenberg FG, Jain D, Strauss HW. Annexin-V imaging for noninvasive detection of cardiac allograft rejection. *Nature*. 2001;7:1347-1352.

[132] Isobe M. Scintigraphic imaging of MHC class II antigen induction in mouse kidney allografts: a new approach to noninvasive detection of early rejection. *Transplant Int*. 1993;6:263-269.

[133] Isobe M, Southern JF, Yazaki Y. Scintigraphic detection of early cardiac rejection by iodine 123-labeled monoclonal antibody directed against monomorphic determinant of major histocompatibility complex class II antigens. *Am Heart J*. 1994;127:1309-1317.

[134] Ohtani H, Strauss HW, Southern JF, Tamatani T, Miyasaka M, Sekiguchi M, Isobe M. Intercellular adhesion molecule-1 induction: a sensitive and quantitative marker for cardiac allografts rejection. *J Am Coll Cardiol*. 1995;26:793-799.

[135] Ohtani H, Strauss HW, Southern JF, Tamatani T, Miyasaka M, Isobe M. Imaging of intercellular adhesion molecule-1 induction in rejecting heart: a new scintigraphic approach to detect early allografts rejection. *Transplant Proc*. 1993;25:867-869.

[136] Amano J, Hiroe M, Ohta Y, Ishiyama S, Nishikawa T, Tanaka H, Sunamori M, Suzuki A, Miyasaka M, Marumo F. Uptake of indium-111-anti-intercellular adhesion molecule-1 monoclonal antibody in the allografted rat lung during acute rejection. *J Heart Lung Transplant*. 1996;15:1027-1033.

[137] Padhani AR, Neeman M. Challenges for imaging angiogenesis. *Br J Radiol*. 2001;74:886-890.

[138] Folkman J. Fighting cancer by attacking its blood supply. *Sci Am*. 1996;275(3):150-154.

[139] Risau W. Mechanisms of angiogenesis. *Nature*. 1997;386:671-674.

[140] Folkman J. Clinical applications of research on angiogenesis. *N Engl J Med*. 1995;333:1757-1763.

[141] Folkman J. Angiogenesis in cancer, vascular, rheumatoid, and other disease. *Nat Med*. 1995;1:27-31.

[142] Folkman J. New perspectives in clinical oncology from angiogenesis research. *Eur J Cancer*. 1996;32A:2534-2539.

[143] Li WW. Tumor angiogenesis: Molecular pathology, therapeutic targeting, and imaging. *Acad Radiol*. 2000;7:800-811.

[144] Miles KA, Charnsangavej C, Lee FT, Fishman EK, Horton K, Lee TY. Application of CT in the investigation of angiogenesis in oncology. *Acad Radiol*. 2000;7:840-850.

[145] Brasch RC, Li KC. In vivo monitoring of tumor angiogenesis with MR imaging. *Acad Radiol*. 2000;7:812-823.

[146] Weber WA, Haubner R, Vabuliene E, Kuhnast B, Wester HJ, Schwaiger M. Tumor angiogenesis targeting using imaging agents. *Q J Nucl Med*. 2001;45:179-182.

[147] Gossmann A, Helbich TH, Kuriyama N, Ostrowitzki S, Roberts TP, Shames DM, van Bruggen N, Wendland MF, Israel MA, Brasch RC. Dynamic contrast-enhanced magnetic resonance imaging as a surrogate marker of tumor response to anti-angiogenic therapy in a xenograft model of glioblastoma multiforme. *J Magn Reson Imaging*. 2002;15:233-240.

[148] Ferrara KW, Merritt CR, Burns PN, Foster FS, Mattrey RF, Wickline SA. Evaluation of tumor angiogenesis with US: Imaging, Doppler, and contrast agents. *Acad Radiol*. 2000;7:824-839.

[149] Goertz DE, Yu JL, Kerbel RS, Burns PN, Foster FS. High-frequency Doppler ultrasound monitors the effects of antivascular therapy on tumor blood flow. *Cancer Res*. 2002;62:6371-6375.

[150] Cheng WF, Lee CN, Chu JS, Chen CA, Chen TM, Shau WY, Hsieh CY, Hsieh FJ. Vascularity index as a novel parameter for the in vivo assessment of angiogenesis in patients with cervical carcinoma. *Cancer*. 1999;85:651-657.

[151] Forsberg F, Dicker AP, Thakur ML, Rawool NM, Liu JB, Shi WT, Nazarian LN. Comparing contrast-enhanced ultrasound to immunohistochemical markers of angiogenesis in a human melanoma xenograft model: preliminary results. *Ultrasound Med Biol*. 2002;28:445-451.

[152] Horak ER, Leek R, Klenk N, LeJeune S, Smith K, Stuart N, Greenall M, Stepniewska K, Harris AL. Angiogenesis, assessed by platelet/endothelial cell adhesion molecule antibodies, as indicators of node metastases and survival in breast cancer. *Lancet*. 1992;340:1120-1124.

[153] Meitar D, Crawford SE, Rademaker AW, Cohn SL. Tumor angiogenesis correlates with metastatic disease, N-myc amplification, and poor outcome in human neuroblastoma. *J Clin Oncol*. 1996;14:405-414.

[154] Collins DA, Hogenkamp HP, Gebhard MW. Tumor imaging via indium 111-labeled DTPA-adenosylcobalamin. *Mayo Clin Proc*. 1999;74:687-691.

[155] Rajotte D, Arap W, Hagedorn M, Koivunen E, Pasqualini R, Ruoslahti E. Molecular heterogeneity of the vascular endothelium revealed by in vivo phage display. *J Clin Invest*. 1998;102:430-437.

[156] Auerbach R. Vascular endothelial cell differentiation: organ-specificity and selective affinities as the basis for developing anti-cancer strategies. *Int J Radiat Biol*. 1991;60:1-10.

[157] Ruoslahti E, Rajotte D. An address system in the vasculature of normal tissues and tumors. *Annu Rev Immunol*. 2000;18:813-827.

[158] Folkman J. Angiogenic zip code. *Nat Biotechnol*. 1999;17:749.

[159] Brooks PC, Clark RA, Cheresh DA. Requirement of vascular integrin $\alpha_v\beta_3$ for angiogenesis. *Science*. 1994;264:569-571.

[160] Sipkins DA, Cheresh DA, Kazemi MR, Nevin LM, Bednarski MD, Li KC. Detection of tumor angiogenesis in vivo by $\alpha_v\beta_3$-targeted magnetic resonance imaging. *Nat Med*. 1998;4:623-626.

[161] Hood JD, Bednarski M, Frausto R, Guccione S, Reisfeld RA, Xiang R, Cheresh DA. Tumor regression by targeted gene delivery to the neovasculature. *Science*. 2002;296:2404-2407.

[162] Leong-Poi H, Christiansen J, Klibanov AL, Kaul S, Lindner JR. Noninvasive assessment of angiogenesis by ultrasound and microbubbles targeted to α_v integrins. *Circulation*. 2003;107:455-460.

[163] Pasqualini R, Ruoslahti E. Organ targeting in vivo using phage display peptide libraries. *Nature*. 1996;380:364-366.

[164] Behr TM, Gotthardt M, Barth A, Behe M. Imaging tumors with peptide-based radioligands. *Q J Nucl Med*. 2001;45:189-200.

[165] Pasqualini R, Koivunen E, Kain R, Lahdenranta J, Sakamoto M, Stryhn A, Ashmun RA, Shapiro LH, Arap W, Ruoslahti E. Aminopeptidase N is a receptor for tumor-homing peptides and a target for inhibiting angiogenesis. *Cancer Res*. 2000;60:722-727.

[166] Arap W, Pasqualini R, Ruoslahti E. Cancer treatment by targeted drug delivery to tumor vasculature in a mouse model. *Science*. 1998;279:377-380.

[167] Curnis F, Sacchi A, Borgna L, Magni F, Gasparri A, Corti A. Enhancement of tumor necrosis factor-α antitumor immunotherapeutic properties by targeted delivery to aminopeptidase N (CD13). *Nat Biotechnol*. 2000;18:1185-1190.

[168] Koivunen E, Arap W, Valtanen H, Rainisalo A, Medina OP, Heikkila P, Kantor C, Gahmberg CG, Salo T, Konttinen YT, Sorsa T, Ruoslahti E, Pasqualini R. Tumor targeting with a selective gelatinase inhibitor. *Nat Biotechnol*. 1999;17:768-774.

[169] Ruoslahti E. RGD and other recognition sequences for integrins. *Ann Rev Cell Biol*. 1996;12:697-715.

[170] Haubner R, Wester HJ, Weber WA, Mang C, Ziegler SI, Goodman SL, Senekowitsch-Schmidtke R, Kessler H, Schwaiger M. Noninvasive imaging of $\alpha_v ß_3$ integrin expression using ^{18}F-labeled RGD-containing glycopeptide and positron emission tomography. *Cancer Res*. 2001;61:1781-1785.

[171] Janssen ML, Oyen WJ, Dijkgraaf I, Massuger LF, Frielink C, Edwards DS, Rajopadhye M, Boonstra H, Corstens FH, Boerman OC. Tumor targeting with radiolabeled $\alpha_v ß_3$ integrin binding peptides in a nude mouse model. *Cancer Res*. 2002;62:6146-6151.

[172] Su ZF, Liu G, Gupta S, Zhu Z, Rusckowski M, Hnatowich DJ. In vitro and in vivo evaluation of a technetium-99m-labeled cyclic RGD peptide as a specific marker of $\alpha_v ß_3$ integrin for tumor imaging. *Bioconjug Chem*. 2002;13:561-570.

[173] Haubner R, Wester HJ, Reuning U, Senekowitsch-Schmidtke R, Diefenbach B, Kessler H, Stocklin G, Schwaiger M. Radiolabeled $\alpha_v ß_3$ integrin antagonists: a new class of tracers for tumor targeting. *J Nucl Med*. 1999;40:1061-1071.

[174] Jayaweera AR, Edwards N, Glasheen WP, Villanueva FS, Abbott RD, Kaul S. In-vivo myocardial kinetics of air-filled albumin microbubbles during myocardial contrast echocardiography: comparison with radiolabeled red blood cells. *Circ Res*. 1994;74:1157-1165.

[175] Keller MW, Segal SS, Kaul S, Duling B. The behavior of sonicated albumin microbubbles within the microcirculation: a basis for their use during myocardial contrast echocardiography. *Circ Res*. 1989;65:458-467.

[176] Villanueva FS, Kaul S. Assessment of myocardial perfusion in coronary artery disease using myocardial contrast echocardiography. *Coron Artery Dis*. 1995;6:18-28.

[177] Kaul S. A glimpse of the coronary microcirculation with myocardial contrast echocardiography. *J Investig Med*. 1995;43:345-361.

[178] Keller MW, Spotnitz WD, Matthew TL, Glasheen WP, Watson DD, Kaul S. Intraoperative assessment of regional myocardial perfusion using quantitative myocardial contrast echocardiography. *J Am Coll Cardiol*. 1990;16:1267-1279.

[179] Keller MW, Geddes L, Spotnitz W, Kaul S. Microcirculatory dysfunction following perfusion with hyperkalemic, hypothermic, cardioplegia solutions and blood reperfusion. *Circulation*. 1991;84:2485-2494.

[180] Harjula A, Mattila S, Mattila I, Harkonen M, Myllarniemi H, Nickels J, Merikallio E. Coronary endothelial damage after crystalloid cardioplegia. *J Cardiovasc Surg*. 1984;25:147-152.

[181] Villanueva FS, Jankowski RJ, Manaugh C, Wagner WR. Albumin microbubble adherence to human coronary endothelium: implications for assessment of endothelial function using myocardial contrast echocardiography. *J Am Coll Cardiol*. 1997;30:689-693.

[182] De Jong N. Acoustic properties of ultrasound contrast agents. Zuidam & Zonen, Woerden, 1993.

[183] Burns PN. Microbubble physics and ultrasound – What does an echocardiologist need to know? Proceedings of the Fourth Annual Symposium on Contrast Echocardiography, Washington, D.C., June 1999.

[184] De Jong N, Bouakaz A, Frinking P. Basic acoustic properties of microbubbles. Echocardiography. 2002;19:229-240.

[185] Yao J, Pandian NG. Contrast echocardiography: yesterday, today, and tomorrow. Proceedings of the Fourth Annual Symposium on Contrast Echocardiography, Washington, D.C., June 1999.

[186] Cosgrove DO. "Echo-enhancing (ultrasound contrast) agents," in Ultrasound in Medicine. Duck FA ed. Institute of Physics Publishing, Bristol and Philadelphia. 1998.

[187] Kuersten B, Murthy TH, Li P, Liu Z, Locricchio E, Baisch C, Rafter P, Vannan M. Ultraharmonic myocardial contrast imaging: in vivo experimental and clinical data from a novel technique. *J Am Soc Echocardiogr*. 2001;14:910-916.

[188] Lanza GM, Abendschein DR, Hall CS, Scott MJ, Scherrer DE, Houseman A, Miller JG, Wickline SA. In vivo molecular imaging of stretch-induced tissue factor in carotid arteries with ligand-targeted nanoparticles. *J Am Soc Echocardiogr*. 2000;13:608-614.

[189] Klibanov AL, Lyle LR, Thomas ME. US Patent #6,245,318. Selectively binding ultrasound contrast agents. June, 2001.

[190] Klibanov AL, Gu H, Wojdyla JK, Wible JH Jr., Kim DH, Needham D, Villanueva FS, Brandenburger GH. Attachment of ligands to gas-filled microbubbles via PEG spacer and lipid residues anchored at the interface. Proceedings of the 26th International Symposium on Controlled Release of Bioactive Materials. Boston, 124 –125, 1999.

[191] Klibanov AL, Hughes MS, Marsh JN, Hall CS, Miller JG, Wible JH, Brandenburger GH. Targeting of ultrasound contrast material: an *in vitro* feasibility study. *Acta Radiol Suppl*. 1997;412:113-120.

[192] Green NM. Avidin 1: The use of (14-C)biotin for kinetic studies and for assay. *Biochem J*. 1963;89:585-591.

[193] Green NM. Avidin. *Adv Protein Chem*. 1975;29:85-133.

[194] Rivnay B, Bayer EA, Wilchek M. Use of avidin-biotin technology for liposome targeting. *Methods Enzymol*. 1987;149:119-123.

[195] Savage MD, Mattson G, Desai S, Nielander GW, Morgensen S, Conklin EJ. Avidin-biotin chemistry: a handbook. Pierce Chemical Co, Rockford, IL. 1994.

[196] Bruch RC, White HB 3rd. Compositional and structural heterogeneity of avidin glycopeptides. *Biochemistry*. 1982;21:5334-5341.

[197] Alon R, Bayer EA, Wilchek M. Streptavidin contains an RYD sequence which mimics the RGD receptor domain of fibronectin. *Biochem Biophys Res Commun*. 1990;170:1236-1241.

[198] Gitlin G, Khait I, Bayer EA, Wilchek M, Muszkat KA. Studies on the biotin-binding sites of avidin and streptavidin: A chemically induced dynamic nuclear polarization investigation of the status of tyrosine residues. *Biochem J*. 1989;259:493-498.

[199] Morilla R, Scolnik M. Quantitative flow cytometry. *Proc RMS*. 1998;33:267-270.

[200] Bikoue A, George F, Poncelet P, Mutin M, Janossy G, Sampol J. Quantitative analysis of leukocyte membrane antigen expression: normal adult values. *Cytometry*. 1996;26:137-147.

[201] Taylor AD, S Neelamegham, JH Hellums, CW Smith, SI Simon. Molecular dynamics of the transition from L-selectin to β_2-integrin-dependent neutrophil adhesion under defined hydrodynamic shear. *Biophys J*. 1996;71:3488-3500.

[202] Lawrence MB, McIntire LV, Eskin SG. Effect of flow on polymorphonuclear leukocyte/endothelial cell adhesion. *Blood*. 1987;70:1284-1290.

[203] Van Kooten TG, Schakenraad JM, Van der Mei HC, Busscher HJ. Development and use of a parallel-plate flow chamber for studying cellular adhesion to solid surfaces. *J Biomed Mater Res*. 1992;26:725-738.

[204] Cozens-Roberts C, Quinn JA, Lauffenburger DA. Receptor-mediated adhesion phenomena: Model studies with the radial-flow detachment assay. *Biophys J*. 1990;58:107-125.

[205] Goldman AJ, Cox RG, Brenner H. Slow viscous motion of a sphere parallel to a plane wall – II: Couette flow. *Chemical Engineering Science*. 1967;22:653-660.

[206] Hammer DA, Lauffenburger DA. A dynamical model for receptor-mediated cell adhesion to surfaces. *Biophys J*. 1987;52:475-487.

[207] Bell GI. Models for the specific adhesion of cells to cells. *Science*. 1978;200:618-627.

[208] Goldstein AS, DiMilla PA. Comparison of converging and diverging radial flow for measuring cell adhesion. *AIChE J*. 1998;44:465-473.

[209] Lauffenburger DA, Linderman JJ. Receptors: Models for Binding, Trafficking, and Signaling. New York: Oxford University Press, 1993, 365 pp.

[210] Goetz DJ, Greif DM, Ding H, Camphausen RT, Howes S, Comess KM, Snapp KR, Kansas GS, Luscinskas FW. Isolated P-selectin glycoprotein ligand-1 dynamic adhesion to P- and E-selectin. *J Cell Biol*. 1997;137:509-519.

[211] Barabino GA, McIntire LV, Eskin SG, Sears DA, Udden M. Rheological studies of erythrocyte-endothelial cell interactions in sickle cell disease. *Prog Clin Biol Res*. 1987;240:113-127.

[212] Giavazzi R, Foppolo M, Dossi R, Remuzzi A. Rolling and adhesion of human tumor cells on vascular endothelium under physiological flow conditions. *J Clin Invest*. 1993;92:3038-3044.

[213] Remy M, Valli N, Brethes D, Labrugere C, Porte-Durrieu MC, Dobrova NB, Novikova SP, Gorodkov AJ, Bordenave L. In vitro and in situ intercellular adhesion molecule-1 (ICAM-1) expression by endothelial cells lining a polyester fabric. *Biomaterials*. 1999;20:241-251.

[214] Kuo SC, Lauffenburger DA. Relationship between receptor/ligand binding affinity and adhesion strength. *Biophys J*. 1993;65:2191-2200.

[215] Morigi M, Zoja C, Figliuzzi M, Foppolo M, Micheletti G, Bontempelli M, Saronni M, Remuzzi G, Remuzzi A. Fluid shear stress modulates surface expression of adhesion molecules by endothelial cells. *Blood*. 1995;85:1696-1703.

[216] Goldsmith HL, Turitto VT. Rheological aspects of thrombosis and haemostasis: basic principles and applications. *Thromb Haemost*. 1986;55:415-435.

[217] Pierres A, Benoliel AM, Bongrand P. Measuring the lifetime of bonds made between surface-linked molecules. *J Biol Chem*. 1995;270:26586-26592.

[218] Cozens-Roberts C, Lauffenburger DA, Quinn JA. Receptor-mediated cell attachment and detachment kinetics I: Probabilistic model and analysis. *Biophys J*. 1990;58:841-856.

[219] King MR, Hammer DA. Multiparticle adhesive dynamics: interactions between stably rolling cells. *Biophys J*. 2001;81:799-813.

[220] Fowler WH, McKay AJ. The measurement of microbial adhesion, in Microbial Adhesion to Surfaces. Ellis Horwood, Chichester, England. Pgs 143-161. 1980.

[221] Groves BJ, Riley PA. A miniaturised parallel-plate shearing apparatus for the measurement of cell adhesion. *Cytobios*. 1987;52:49-62.

[222] Dickinson RB, Nagel JA, McDevitt D, Foster TJ, Proctor RA, Cooper SL. Quantitative comparison of clumping factor- and coagulase-mediated *staphylococcus aureus* adhesion to surface-bound fibrinogen under flow. *Infect Immun*. 1995;63:3143-3150.

[223] Moller PS. Radial flow without swirl between parallel discs. *Aeronautical Quarterly*. 1963;14:163-186.

[224] Thurman RG, Bradford BU, Iimuro Y, Frankenberg MV, Knecht KT, Connor HD, Adachi Y, Wall C, Arteel GE, Raleigh JA, Forman DT, Mason RP. Mechanisms of alcohol-induced hepatotoxicity: studies in rats. *Front Biosci*. 1999;4:E42-E46.

[225] Nathens AB, Bitar R, Watson RW, Issekutz TB, Marshall JC, Dackiw AP, Rotstein OD. Thiol-mediated regulation of ICAM-1 expression in endotoxin-induces acute lung injury. *J Immunol*. 1998;160:2959-2966.

[226] Tamatani T, Miyasaka M. Identification of monoclonal antibodies reactive the the rat homolog of ICAM-1, and evidence for a differential involvement of ICAM-1 in the adherence of resting versus activated lymphocytes to high endothelial cells. *Int Immunol*. 1990;2:165-171.

[227] Ono K, Lindsey ES. Improved technique of heart transplantation in rats. *J Thorac Cardiovasc Surg*. 1969;57:225-229.

[228] Araneda D, Padberg WM, Tilney NL. Refined techniques for heterotopic cardiac transplantation in the rat. *Transplant Proc*. 1989;21:2562.

[229] Wada T, Ono K, Hadama T, Uchida Y, Shimada T, Arita M. Detection of acute cardiac rejection by analysis of heart rate variability in heterotopically transplanted rats. *J Heart Lung Transplant*. 1999;18:499-509.

[230] Billingham ME, Cary NR, Hammond ME, Kemnitz J, Marboe C, McCallister HA, Snovar DC, Winters GL, Zerbe A. A working formulation for the standardization of nomenclature in the diagnosis of heart and lung rejection: heart rejection study group. *J Heart Transplant*. 1990;9:587-593.

[231] Wei K, Jayaweera AR, Firoozan S, Linka A, Skyba DM, Kaul S. Quantification of myocardial blood flow with ultrasound-induced destruction of microbubbles administered as a constant venous infusion. *Circulation*. 1998;97:473-483.

[232] Wei K, Skyba DM, Firschke C, Jayaweera AR, Lindner JR, Kaul S. Interaction between microbubbles and ultrasound: in vitro and in vivo observations. *J Am Coll Cardiol*. 1997;29:1081-1088. [ultrasound destroys microbubbles]

[233] Brown CK, Modzelewski RA, Johnson CS, Wong MK. A novel approach for the identification of unique tumor vasculature binding peptides using an E. coli peptide display library. *Ann Surg Oncol*. 2000;7:743-749.

[234] Modzelewski RA, Davies P, Watkins SC, Auerbach R, Chang MJ, Johnson CS. Isolation and identification of fresh tumor-derived endothelial cells from a murine RIF-1 fibrosarcoma. *Cancer Res*. 1994;54:336-339.

[235] Costouros NG, Diehn FE, Libutti SK. Molecular imaging of tumor angiogenesis. *J Cell Biochem*. 2002;Suppl 39:72-78.

[236] Smith LE, Wesolowski E, McLellan A, Kostyk SK, D'Amato R, Sullivan R, D'Amore PA. Oxygen-induced retinopathy in the mouse. *Investig Ophthalmol Vis Sci*. 1994;35:101-111.

[237] Brunk DK, Goetz DJ, Hammer DA. Sialyl Lewis-x/E-selectin-mediated rolling in a cel-free system. *Biophys J*. 1996;71:2902-2907.

[238] Shinde Patil VR, Campbell CJ, Yun YH, Slack SM, Goetz DJ. Particle diameter influences adhesion under flow. *Biophys J*. 2001;80:1733-1743.

[239] Jensen TW, Hu BH, Messersmith PB, Miller WM. Membrane-mimetic culture surface for presentation of hematopoietic cell adhesion molecule ligands. Abstract #344g, presented at AIChE annual meeting, 2002.

[240] Jeppesen C, Wong JY, Kuhl TL, Israelachvili JN, Mullah N, Zalipsky S, Marques CM. Impact of polymer tether length on multiple ligand-receptor bond formation. *Science*. 2001;293:465-468.

[241] Wang CY, Naka Y, Liao H, Oz MC, Springer TA, Gutierrez-Ramos JC, Pinsky DJ. Cardiac graft intercellular adhesion molecule-1 (ICAM-1) and interleukin-1 expression mediate primary isograft failure and induction of ICAM-1 in organs remote from the site of transplantation. *Circ Res*. 1998;82:762-772.

[242] Kaul S, Pandian NG, Okada RD, Pohost GM, Weyman AE. Contrast echocardiography in acute myocardial ischemia, I: in-vivo determination of total left ventricular area at risk. *J Am Coll Cardiol.* 1984;4:1272-1282.

[243] Kemper AJ, O'Boyle JE, Cohen CA, Taylor A, Parisi AF. Hydrogen peroxide contrast echocardiography: quantification in vivo of myocardial risk area during coronary occlusion and of the necrotic area remaining after myocardial reperfusion. *Circulation*. 1984;70:309-317.

[244] Cobb FR, Bache RJ, Rivas F, Greenfield JC Jr. Local effects of acute cellular injury on regional myocardial blood flow. *J Clin Invest*. 1976;57:1359-1368.